

BULGARIAN CHEMICAL COMMUNICATIONS

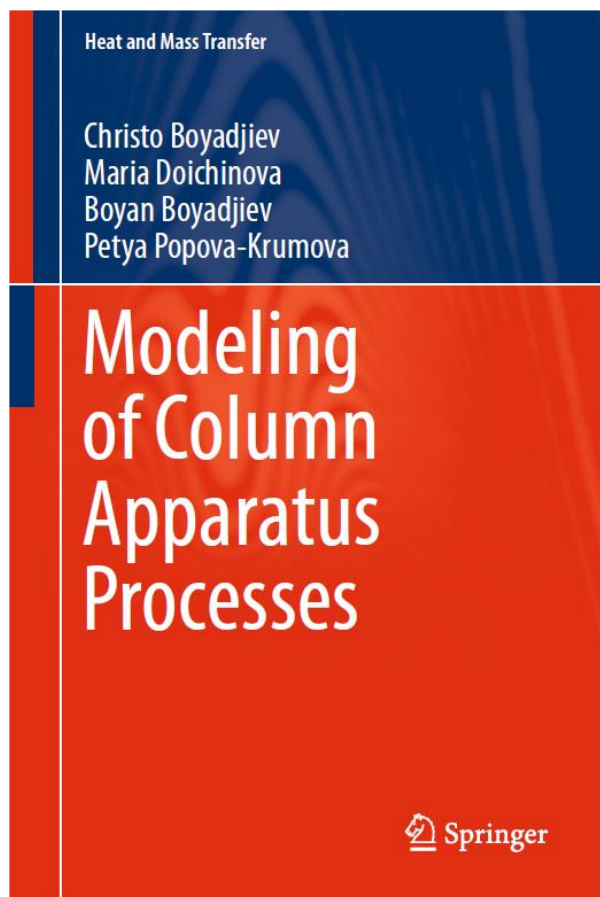
2016 Volume 48 / Number 2

*Journal of the Chemical Institutes
of the Bulgarian Academy of Sciences
and of the Union of Chemists in Bulgaria*

Book Review

Chr. Boyadjiev, M. Doichinova, B. Boyadjiev, P. Popova-Krumova,
“Modeling of Column Apparatus Processes”,
Springer-Verlag, Berlin Heidelberg, 2016.

<http://www.springer.com/gp/book/9783319282572>



In the book is presented a new physically motivated approach for the modeling of column apparatus processes in industrial conditions, using the mechanics of continua. In the Introduction is presented the contemporary, physically motivated, mass transfer theory. The proposed analysis shows that the presented mass transfer theory is not applicable for the modeling of column apparatus processes in industrial conditions, because the velocities in each phase and the phase surfaces in columns are unknown and practically cannot be determined.

The modeling of column apparatus processes in industrial conditions is made, using new type models as convection-diffusion models (for qualitative analysis) and average concentration models (for quantitative analysis), where as an innovation is the process mechanism identification

on the base of the Guhman's generalized model analysis (model analysis in generalized variables). In the book are presented convection-diffusion and average concentration models of one, two and three phase processes.

In the first part of the book are presented the convection-diffusion models and qualitative analysis of the chemical, absorption, adsorption and catalytic processes.

The one-phase processes in column chemical reactors are analyzed in the cases of complex chemical reaction kinetics, two components chemical reactions and pseudo-first-order reactions. It is shown the influence of the velocity radial non-uniformity on the conversion degree. As an innovation is a new explanation of the “back mixing” effect as a reducing of the average residence time of the flow in the column.

The two-phase processes in column apparatuses are analyzed in the cases of absorption processes (physical and chemical absorption), adsorption processes (physical and chemical adsorption), catalytic processes (physical and chemical adsorption mechanism).

The absorption processes are presented in co-current and counter-current gas-liquid flows. As innovations are the presentation of the interphase mass transfer as a volume reaction and the distribution of the interphase mass resistances between the gas and liquid phases.

The adsorption processes are presented in the cases of nonstationary process in the solid phase and quasi stationary process in the gas (liquid) phase. As innovation is the presentation of the adsorption process as a volume reaction.

The catalytic processes are presented as stationary processes in gas-solid systems, where the adsorption of the first reagent is physically or chemically. As innovation is the presentation of the catalytic reaction as a volume reaction.

In the second part of the book are presented the average concentration models and quantitative analysis of the chemical, absorption, adsorption and catalytic processes. The innovations in this part are:

1. The presented theoretical (averaging) procedure.
2. The ability to be used the average concentration models for modeling of the processes at an unknown velocity distribution in the column, which is introduced in the model by two parameters, which can be determined from experimental data.

3. The explanation of the conversion degree decrease as a result of the radial non-uniformity of the velocity distribution.
4. The experimental data, obtained in a short column with real diameter, are useful for the model parameters identification.

In the third part of the book are presented calculation algorithms as innovations.

In many cases the computer modeling of the processes in column apparatuses, made on the base the convection–diffusion and average concentration models, does not allow a direct use of the MATLAB program. In these cases it is necessary to create combinations of appropriate algorithms.

Practically, the new type models are characterized by the presence of small parameters at the highest derivatives. As a result, the use of the conventional software for solving the model differential equations is difficult. This difficulty may be eliminated by an appropriate combination of MATLAB and perturbations method.

In the cases of counter-current gas-liquid or liquid-liquid processes the mass transfer process models are presented in two-coordinate systems, because in a one-coordinate system one of the equations has no solution by reason of the negative value in the equation Laplacian. Thus, a combination of an iterative algorithm and MATLAB has to be used for solving the equations set in different coordinate systems.

In the practical cases of non-stationary adsorption in gas-solid systems, the presence of mobile (gas) and immobile (solid) phases in the conditions of lengthy (long-term) processes leads to a non-stationary process in the immobile phase and a stationary process in the mobile phase. As a result different coordinate systems must be used for the gas and solid phase models. A combination of a multi-step algorithm and MATLAB has to be used for the

solutions of the equations set in different coordinate systems.

Practically, the waste gases purification in the thermal power plants uses absorption methods. The SO₂ absorption intensification needs a quantitative description of the process using a suitable mathematical model, which has to be created on the basis of a qualitative analysis of the process mechanism. The new convection-diffusion and average concentration models lead to the creation of three patents as innovations.

In the cases of comparable interphase mass transfer resistances in the gas and liquid phases, an intensification of the mass transfer should be realized in two phases. In these conditions a new patent is proposed, where the process optimization is realized in a two-zone column, where the upper zone the process is physical absorption in a gas-liquid drops system (intensification of the gas phase mass transfer), while in the lower zone it is a physical absorption in liquid-gas bubbles system (intensification of the liquid phase mass transfer) and the chemical reaction takes place in the column tank.

The waste gases purification from SO₂ is solved in a new patent, using a two-step process – physical absorption of SO₂ by water and adsorption of SO₂ from the water solution by synthetic anionite particles. The adsorbent regeneration is made by NH₄OH solution. The obtained (NH₄)₂SO₃ (NH₄HSO₃) is used (after reaction with HNO₃) for production of concentrated solutions of SO₂ and NH₄NO₃.

The decrease of the column diameter is realized in a new patent, where a co-current SO₂ absorption is used.

The created methods for modeling of column apparatus processes are a base for solution of many industrial problems.

Circadian misalignment and alcohol intake change the oxidative status of rat blood plasma

M. G. Varadinova^{1,*}, M. L. Valcheva-Traykova²

¹ Department of Pharmacology and Toxicology, Medical Faculty, Medical University - Sofia, Bulgaria

² Department of Medical Physics and Biophysics, Medical Faculty, Medical University - Sofia, Bulgaria

Received September 16, 2015, Revised October 25, 2015

Circadian misalignment and chronic alcohol intake often occur together and are known to result in decreased endogenous antioxidant resistance and oxidative stress in human and animal models. This is associated with a myriad of chronic health consequences and thus may have a large-scale financial burden on society and healthcare system. There is evidence for the antioxidant activity of ethanol in model solutions. However, some data suggest that ethanol can display pro-oxidative properties *in vivo*.

The aim of this study was to investigate the effect of *in vitro* ethanol supplementation on the oxidative status of rat blood plasma in models of circadian rhythm disruption (CRD) and chronic alcohol consumption (A). Our results demonstrated that ethanol exhibited pro-oxidative activity in blood plasma. The plasma oxidant status was impaired in both models. Moreover, the combination of CRD and A increased malondialdehyde (MDA) levels nearly twice.

Our data suggest that the combined influence of CRD and A can exacerbate the single adverse effects of each factor on the plasma oxidative status. The explanation of these observations needs further investigation on mechanisms of association between circadian misalignment and chronic alcohol consumption.

Key words: chronic alcohol intake; circadian rhythm disruption; malondialdehyde; oxidative stress.

INTRODUCTION

Epidemiological data reveal that disruption of circadian rhythm due to shift work, jet-lag, sleep disorders, and other modern life style choices and work practices is now very common in our society. Circadian misalignment is associated with a wide variety of adverse health consequences including cancer, metabolic disorders, cardiovascular dysfunction, immune dysregulation, impaired reproduction and neuropsychiatric conditions [1, 2, 3].

Recent studies have reported that disrupted circadian rhythms and increased alcohol consumption are often related [4, 5, 6]. Moreover, it has been suggested that the link is bidirectional [7]. Circadian misalignment and excessive alcohol intake may have considerable harmful effects on molecular and organismal levels [7, 8]. It has been proposed that circadian and redox regulatory systems are tightly interconnected [9]. Experimental evidence demonstrates that circadian misalignment may cause substantial alterations on the redox balance and may enhance susceptibility to lipid peroxidation [10, 11, 12]. In addition, chronic and acute models of alcohol exposure are reported

to produce increased oxidative stress [8, 13, 14].

In the literature, there is a controversy about the pro-oxidative/antioxidative properties of alcohol *in vitro* [15, 16, 17]. Interestingly, the effect of the combination of circadian misalignment and chronic alcohol intake on plasma antioxidant resistance still remains unexplored.

The aim of this study was to investigate the effect of *in vitro* ethanol supplementation on the oxidative status of rat blood plasma in models of circadian rhythm disruption and chronic alcohol consumption. Endogenous lipid peroxidation was assessed by measuring the levels of malondialdehyde (MDA) in blood plasma.

MATERIALS AND METHODS

Chemicals

All chemicals used in the investigation were SIGMA and of finest grade (p.a.). The water was distilled and degassed by sonification, if necessary. The 10% ethanol solution was prepared using 99% ethanol.

Animals

Male Wistar rats (220-240) were housed 1 per standard polypropylene cage and maintained in a temperature (20±0.5°C) and humidity (65±1%) controlled room for 6 weeks. The animals had free access to food (standard rodent chow) and tap water

* To whom all correspondence should be sent:
E-mail: miria@abv.bg

or 10% ethanol solution. 2-3 days before the experiment the animals were handled and then randomly assigned to four groups (n=5).

Group 1 – Control – normal light/dark cycle + tap water *ad libitum*;

Group 2 – Circadian rhythm disruption (CRD) – exposed to light-at-night + tap water *ad libitum*;

Group 3 – Alcohol (A) - normal light/dark cycle + 10% ethanol solution *ad libitum*;

Group 4 – Circadian rhythm disruption + alcohol (CRD+A) - exposed to light-at-night + 10% ethanol solution *ad libitum*.

The experiments were carried out in accordance with the Bulgarian regulations on animal welfare and in conformance with the European Communities Council Directive of 24 November 1986 (86/609/EEC).

The blood was collected in EDTA washed test tubes, and the plasma was separated by centrifugation at 2000XG (4°C) for 30 min. The protein content of the samples was determined using the Biuret method [18]. A 552 UV-VIS spectrophotometer “Perkin-Elmer” with 2 ml quartz cuvettes was used for the spectrophotometric measurements. The *in vitro* ethanol treatment was performed at the following conditions: 50 µl of blood plasma, 300 µl ethanol (10^{-3} M) and 1600 µl PBS were incubated at 37°C for 15 min. The same amount of blood plasma was incubated at the same temperature in 1900 µl PBS. Then the MDA was measured in all samples.

MDA assay

The MDA formation was assessed as described in [19]. The characteristic absorbance of MDA at $\lambda=245$ nm was monitored for 5 minutes at 25°C, in presence (sample) and in absence (blank) of supernatant. One ml of the cuvette contained 0.01 ml supernatant, 0.01 ml $\text{FeCl}_2/\text{EDTA}$ (3 mM FeCl_2 and 0.2 mM EDTA in distilled water), BPS (pH 7.4) and 0.01 ml 0.003M H_2O_2 . Molar extinction coefficient of $13700 \text{ M}^{-1} \text{ cm}^{-1}$ was used to calculate the MDA and after removing blank from sample measurements, the MDA formation was presented in pmoles/mg protein.

- MDA levels determination in the absence of alcohol in the sample: 50 µl of blood plasma and 1900 µl PBS were incubated at 20°C for 15 min. 50 µl FeCl_2 and 10 µl H_2O_2 were added.

- MDA levels determination in the presence of alcohol in the sample: 50 µl of blood plasma, 300 µl ethanol (10^{-3} M) and 1600 µl PBS were incubated at 20°C for 15 min. 50 µl FeCl_2 and 10 µl H_2O_2 were added. For the blank measurement only FeCl_2 and H_2O_2 were added to PBS.

Data presentation

For a better understanding, MDA was presented by its Activity Index (AI), as a percentage of the corresponding marker for the Control group (e.g., $\text{AI} = \text{Marker}_{\text{stress}} * 100 / \text{Marker}_{\text{control}}$). The AI for MDA formation are shown in Figures 1 and 2.

Statistical analysis

Each OS marker was determined three times for each animal. Thus, an oxidative marker of a group was estimated using nine parallel measurements. After elimination of the gross errors *via* the Romanowski test [20], the mean values and standard deviations were calculated. The statistical significance of the differences between the mean data was estimated by the INSTAT program package (Bartlett test for significance of differences among the standard deviations followed by ANOVA and Bonferoni post-test).

RESULTS

There were no statistically significant differences between the MDA levels in the blood samples of all animals, exposed to light at night or receiving ethanol, or both, compared to the control group (Fig.1). The absolute values of our data were in agreement with these described in the literature for a different model of ethanol intake [21]. Figure 2 illustrates that elevated MDA levels were registered in all experimental groups compared to the same groups in the absence of alcohol. The combined effects of circadian disruption and alcohol caused the highest relative increase of MDA in the “CRD+A” group.

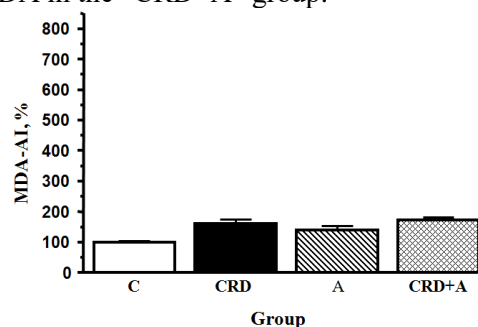


Fig. 1. MDA levels in the blood plasma without alcohol in the sample.

DISCUSSION

The present results demonstrated that, within our model of systemic ethanol intake, there were no significant differences in MDA levels (Fig. 1). The data in Figure 2 show that ethanol *in vitro* supplementation caused increased levels of MDA in all experimental groups compared to the same groups in the absence of alcohol. The increased MDA level indicated more profound lipid

peroxidation due to inefficient antioxidant defense. The lowest relative increase of the MDA level was in the Control group. In agreement with [8] this may be related with the metabolic transformation of ethyl alcohol in the blood plasma of the control animals in conditions of undisturbed antioxidant defense. Disrupted circadian rhythm and chronic ethanol intake, alone and in combination, resulted in a significantly increased level of MDA in rat blood plasma. This may be because of increased free radicals formation, and/or diminished antioxidant defense. Our data also suggest that the combined influence of circadian rhythm disruption and chronic alcohol can exacerbate the single adverse effects of each factor on the plasma oxidative status.

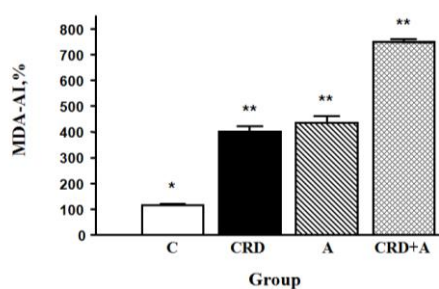


Fig. 2. MDA levels in the blood plasma in the presence of alcohol in the sample.

* $P=0.0063$; ** $P<0.0001$ vs the same group in the absence of alcohol.

Our previous results showed that light at night and chronic alcohol consumption induced significant oxidative stress in the brains of the experimental animals. Furthermore, our data proposed that the combination of circadian misalignment and chronic alcohol might result in significantly higher MDA levels in the rat brain, than any of these models alone [22]. In this investigation, similar effects in rat blood plasma were observed. It may be assumed that the combination of circadian misalignment and chronic ethanol intake compromise the antioxidant defense and result in a massive lipid peroxidation within the entire organism of the model animals.

It is believed that oxidative stress plays a major role in the pathogenesis of a variety of adverse health conditions. In addition, lots of disorders have been found to have strong oxidative stress and circadian rhythm connections, including physical and psychiatric dysfunctions. Reactive oxygen species (ROS) and reactive nitrogen species (RNS) are important regulators of cellular metabolism, signal transduction, and gene expression and they are implicated in the regulation of physiological processes [9]. The exposure to light at night increases the lipid peroxidation in tissues and

decreases both the total antioxidant activity and superoxide dismutase activity [12]. It is proposed that impairment of redox regulation and circadian rhythms may lead to a number of adverse effects on human health [23].

One causative pathway between excessive alcohol consumption and disease may be the circadian misalignment because they are often related [5, 24]. Furthermore, high ethanol consumption significantly enhances endogenous lipid peroxidation resulting in significantly elevated MDA and increased oxidative stress [10, 25]. In addition, exposure of cells to excessive ethanol result in a significant increase in the ROS production [16].

On the other hand, there is evidence for the antioxidant activity of ethanol in experimental models. For instance, Trevithick *et al.* [26] demonstrated antioxidant properties of ethanol *in vivo*, associated with anti-atherosclerotic effects. Also, ethanol protected LDL from oxidation initiated by superoxide and hydroxyl radicals *in vitro* [15]. Additionally, Tyulina *et al.* [17] reported that ethanol caused a decrease in erythrocyte reactive oxygen species levels and displayed protective activity on erythrocytes *in vitro*.

These controversial data gave us a reason to investigate the effects of supplementation of ethanol to plasma in our experimental models. It is known that in pathological conditions the antioxidant system may be overwhelmed. Oxidative stress occurs when ROS outweigh the antioxidant defense. In our experiment ethanol exhibited pro-oxidative activity in blood plasma *in vitro*. In agreement with the abovementioned data and our results, we can speculate that in our models there was increased lipid peroxidation and decreased antioxidant resistance in the blood plasma.

Compelling evidence from experimental and clinical studies links circadian misalignment and chronic alcohol abuse to disruptions in the neuroendocrine, immune and oxidative stress systems. Assessment of various related mechanisms is still a limited and novel field, but may be of considerable clinical relevance, having in mind the increasing number of affected individuals. Our results suggest an interconnection between circadian disruption, alcohol intake and imbalanced oxidative status, due to enhanced lipid peroxidation and/or reduced antioxidant resistance. The explanation of these observations needs further investigation and may contribute to the development of more efficacious preventive and therapeutic approaches for endangered patients.

REFERENCES

1. K. G. Baron, K. J. Reid, *Int. Rev. Psychiatry*, **26**, 139 (2014).
2. J. A. Evans, A. J. Davidson, *Prog. Mol. Biol. Transl. Sci.*, **119**, 283 (2013).
3. A. Knutsson, *Occupat. Med.*, **53**, 103 (2003).
4. A. N. Filiano, T. Millender-Swain, R. Johnson Jr, M. E. Young, K. L. Gamble KL, S. M. Bailey., *PLoS One*, **8**, e71684 (2013).
5. B. P. Hasler, D. B. Clark, *Alcohol Clin. Exp. Res.*, **37**, 558 (2013).
6. H. L. Rogers, S. M. Reilly, *AAOHN J.*, **50**, 449 (2002).
7. R. M. Voigt, C. B. Forsyth, A. Keshavarzian, *Alcohol Res.* 2013; 35(1):87-96.
8. M. Comporti, C. Signorini, S. Leoncini, C. Gardi, L. Ciccoli, A. Giardini, D. Vecchio, B. Arezzini, *Genes Nutr.*, **5**, 101 (2010).
9. M. P. Antoch, R. V. Kondratov, *Circ. Res.*, **106**, 68 (2010).
10. E. B. Kalaz, B. Evran, S. Develi, G. Ö. Erata, M. Uysal, N. Koçak-Toker, *Pathophysiology*, **19**, 49 (2012).
11. N. Krishnan, K. Rakshit, E. S. Chow, J. S. Wentzell, D. Kretschmar, J. M. Giebultowicz, *Neurobiol. Dis.*, **45**, 1129 (2002).
12. I. A. Vinogradova IA, V. N. Anisimov, A. V. Bukalev, V. A. Pyukha, E. A. Khizhkin, T. A. Lotosh, A. V. Semenchenko, M. A. Zabezhinski, *Aging (Albany NY)*, **2**, 82 (2010).
13. A. Dolganiuc, G. Szabo, *World J. Gastroenterol.*, **15**, 1168 (2009).
14. A. Kahraman, H. Çakar, T. Köken, *Mol. Biol. Rep.*, **39**, 2789 (2012).
15. D. Bonnefont-Rousselot, A. Rouscilles, C. Bizard, J. Delattre, D. Jore, M. Gardès-Albert. *Radiat. Res.*, **155**, 279 (2001).
16. K.-M. Lee, H.-S. Kang, C.-H. Yun and H.-S. Kwak, *Biomol. Ther. (Seoul)*, **20**, 492 (2012).
17. O. V. Tyulina, V. D. Prokopieva, R. D. Dodd, J. R. Hawkins, S. W. Clay, D. O. Wilson, A. A. Boldyrev, P. Johnson, *Alcohol Alcohol.*, **37**, 179 (2002).
18. K.C. Bohnstedt, in "Determination of biomarkers for Lipid Peroxidation and Oxidative Stress – development of Catalytical techniques and methods", PhD Thesis, SU, Stockholm, 2005.
19. E. Layne, *Methods Enzymol.*, **10**, 447 (1957).
20. I. Glushtenko. Basics of scientific research (in Russian), Vissha Shkola, Kiev, 1983, p.103.
21. T. Traykov, M. Traykova, L. Astasidi, N. Boyadjieva, *Trakia J. Sci.*, **10**, 326 (2012).
22. M. Varadinova, M. Traykova, N. Boyadjieva, *Am. J. Ther.*, (2015), in press.
23. M. Wilking, M. Ndiaye, H. Mukhtar, N. Ahmad, *Antioxid. Redox. Signal.*, **19**, 192 (2013).
24. S. B. Hammer, C. L. Ruby, A. J. Brager, R. A. Prosser, J. D. Glass, *Alcohol. Clin. Exp. Res.* **34**, 1651 (2010).
25. S. Vasdev, V. Gill, P. K. Singal, *Vasc. Health Risk Manag.*, **2**, 263 (2006).
26. C. C. Trevithick, J. A. Vinson, J. Caulfeild, F. Rahman, T. Derksen, L. Bocksch, S. Hong, A. Stefan, K. Teufel, N. Wu, M. Hirst, J. R., *Redox Rep.*, **4**, 89 (1999).

НАРУШЕНИЯТ ЦИРКАДЕН РИТЪМ И АЛКОХОЛНИЯТ ПРИЕМ ПРОМЕНЯТ ОКСИДАТИВНИЯ СТАТУС НА КРЪВНА ПЛАЗМА НА ПЛЪХ

М. Г. Варадинова¹, М. Л. Вълчева-Трайкова

¹ Катедра по фармакология и токсикология, Медицински факултет, Медицински Университет – София, България

² Катедра по медицинска физика и биофизика, Медицински факултет, Медицински Университет – София, България

Постъпила на 16 септември, 2015 г. коригирана на 26 октомври, 2015 г.

(Резюме)

Нарушеният циркаден ритъм и хроничният алкохолен прием често се съчетават и водят до понижена антиоксидантна защита и оксидативен стрес при човешки и животински опитни постановки. Това се асоциира с редица хронични здравни проблеми, които от своя страна имат сериозни финансови последици върху обществото и системата на здравеопазване.

Съществуват доказателства за антиоксидантна роля на етанол в експериментални модели. Същевременно, редица данни демонстрират про-оксидативни свойства на алкохол в *in vivo* условия.

Цел на настоящето изследване бе да проучи ефекта на етанол *in vitro* върху оксидативния статус на кръвна плазма от плъх при модели на нарушен циркаден ритъм (НЦР) и хроничен алкохолен прием (А). Получените резултати показаха про-оксидативна активност на етанол в кръвна плазма. Оксидативният статус на плазмата бе нарушен и при двата модела. В допълнение, при комбинацията от НЦР и А нивата на малондиалдехид бяха увеличени близо два пъти.

Нашите данни демонстрират, че съчетанието от нарушен циркаден ритъм и хроничен алкохолен прием могат да отежнят самостоятелния отрицателен ефект на всеки от факторите върху оксидативния баланс на кръвна плазма. Обяснението на тези наблюдения изисква по-нататъшни изследвания на механизмите на взаимовръзка между НЦР и продължителен алкохолен прием.

A convenient green protocol for one-pot three-component synthesis of 2-amino-4*H*-chromene derivatives catalyzed by ilmenite (FeTiO₃) as an efficient and reusable catalyst in water

B. Ebadzadeh¹, A. Ramazani^{1*}, V. Azizkhani², H. Aghahosseini¹, S. W. Joo^{3*}

¹Department of Chemistry, University of Zanjan, P O Box 45195-313, Zanjan, Iran

²Department of Chemistry, Payame Noor University, P.O. Box 19395-3697, Tehran, Iran

³School of Mechanical Engineering, Yeungnam University, Gyeongsan 712-749, Republic of Korea

Received July 24, 2014, Revised March 28, 2016

A highly efficient and simple procedure for the synthesis of 2-amino-4*H*-chromene derivatives *via* one-pot, three-component reaction from various aldehydes, malononitrile, and α - or β -naphthol in the presence of a catalytic amount of ilmenite (FeTiO₃) is described. The advantages of this novel protocol include good yield, short reaction time, simple work-up, low toxicity and environmentally friendly catalyst. According to our results, FeTiO₃ (10 mol %) can be used as a catalyst for the synthesis of 2-amino-4*H*-chromene derivatives in water solvent under reflux conditions.

Key words: FeTiO₃, ilmenite, three-component reaction, 2-amino-4*H*-chromene derivatives, malononitrile, aldehydes.

INTRODUCTION

Multicomponent coupling reactions (MCRs) are emerging as useful tools for the carbon–carbon and carbon–heteroatom bond-forming reactions and for the synthesis of small drug-like molecules with several degrees of structural diversity [1]. One-pot multicomponent reactions provide the possibility of directly synthesizing a complex molecule without needing to isolate the intermediates, which has aroused researchers to design such reactions using different catalysts [2,3].

Ilmenite (FeTiO₃) is one of the most common minerals in the earth crust. FeTiO₃ is an interesting wide bandgap (2.58–2.9 eV) antiferromagnetic semiconductor with potential applications in spintronics, optoelectronics, high temperature integrated circuits, chemical catalysts, photo catalysts, etc. [4].

Aminochromenes and their derivatives are of considerable interest as they possess a wide range of biological properties [5], such as spasmolytic, diuretic, anticoagulant, anticancer and antianaphylactic activities [6]. In addition, they can be used as cognitive enhancers for the treatment of neurodegenerative diseases, including Alzheimer's disease, amyotrophic lateral sclerosis, Huntington's disease, Parkinson's disease, AIDS associated dementia and Down's syndrome, as well as for the treatment of schizophrenia and myoclonus [7].

Aminochromenes have been prepared by heating a mixture of malononitrile, aldehydes and activated phenols or naphthols in refluxing DMF or acetonitrile in the presence of hazardous organic bases such as piperidine and triethylamine [8, 9]. In the literature, a lot of synthetic methods for the synthesis of 2-amino-4*H*-chromene derivatives have been reported so far [10-26]. Most of these methods are associated with shortcomings like the use of costly, harmful and non-reusable catalysts, tedious separation procedures, long reaction time, tedious work up and use of toxic organic solvents.

To the best of our knowledge, the use of water as a clean solvent in the presence of ilmenite as a reusable catalyst for the synthesis of 2-amino-4*H*-chromene derivatives has not been reported.

In light of the above reports, and in continuation of our ongoing efforts to develop new methods in organic synthesis [27-38], herein we report our results for the synthesis of 2-amino-4*H*-chromene derivatives *via* a one-pot three-component reaction of various aldehydes (**2**), malononitrile (**3**) and α -, or β -naphthol (**1**) in the presence of FeTiO₃ as an efficient and reusable catalyst in water under reflux conditions (Scheme 1).

RESULTS AND DISCUSSION

As a part of a continuing effort in our laboratory towards the development of new methods in organic synthesis [27-38], in the present paper, a convenient and green protocol for the one-pot three-component synthesis of 2-amino-4*H*-

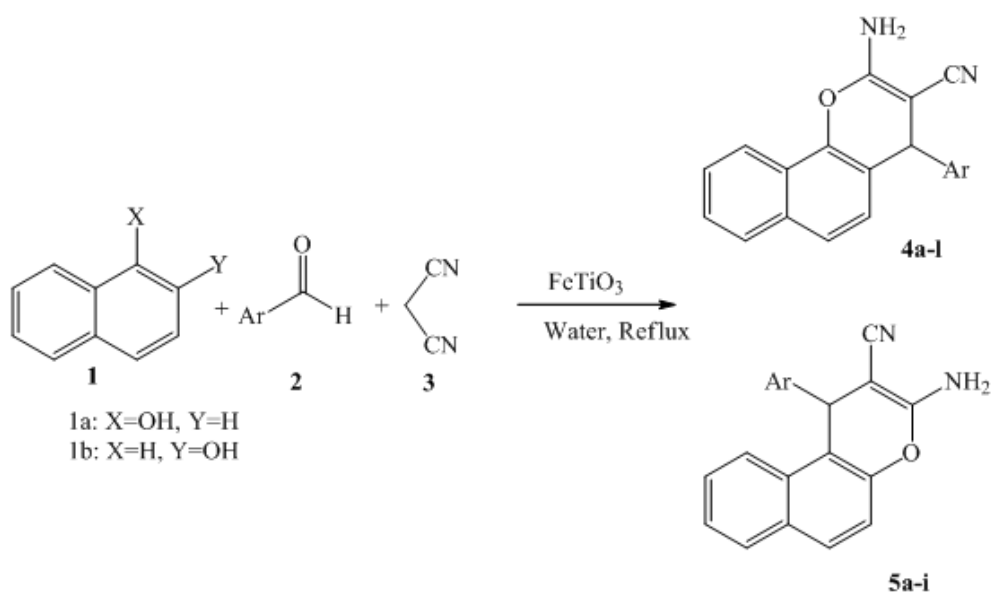
* To whom all correspondence should be sent:
E-mail: aliramazani@gmail.com ; swjoo@yu.ac.kr

chromene derivatives catalyzed by ilmenite as a reusable catalyst in water is described.

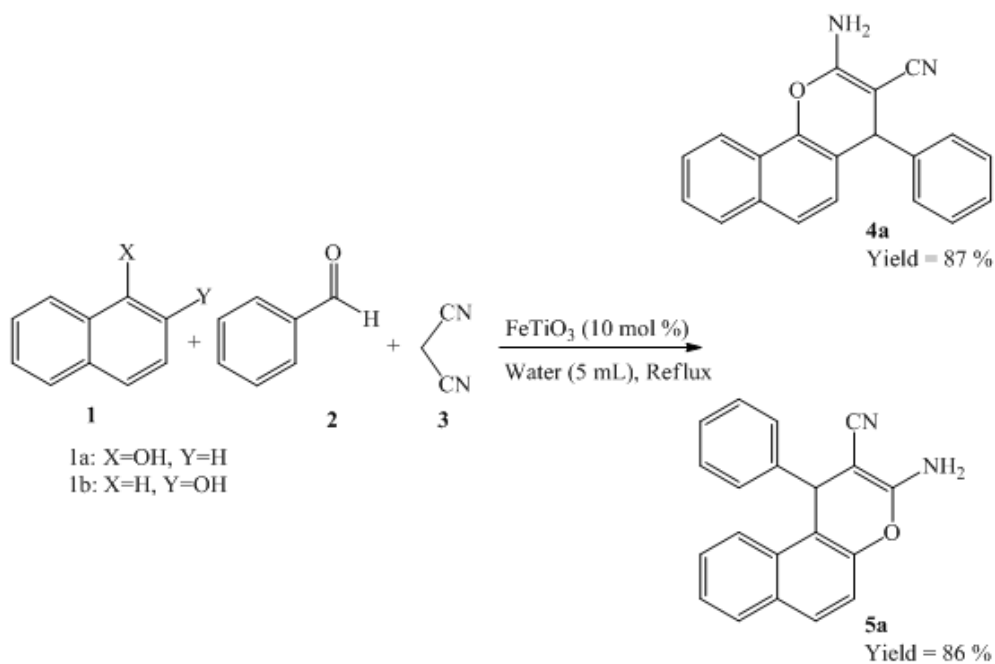
To optimize the reaction conditions, the condensation reaction of α - or β -naphthol (**1**), benzaldehyde (**2**), and malononitrile (**3**) was tested as the model reaction using different amounts of FeTiO₃ at 40 or 100 °C under reflux conditions in the presence of various solvents. As shown in Table 1, FeTiO₃ (10 mol %) as a catalyst under reflux conditions afforded 2-amino-4*H*-chromene

derivatives in 30 min with (**4a** = **87 %**, and **5a** = **86 %**) of yield in water (Table 1, Scheme 2).

In the next section, in order to assess the efficiency and the scope of the catalyst for the preparation of 2-amino-4*H*-chromene derivatives, the reaction of α - or β -naphthol with various aldehydes and malononitrile was examined in the presence of 10 mol% of FeTiO₃ as a catalyst. The corresponding results are displayed in Table 2.



Scheme 1. Synthesis of chromene derivatives from various aromatic aldehydes, malononitrile and naphthols in water.

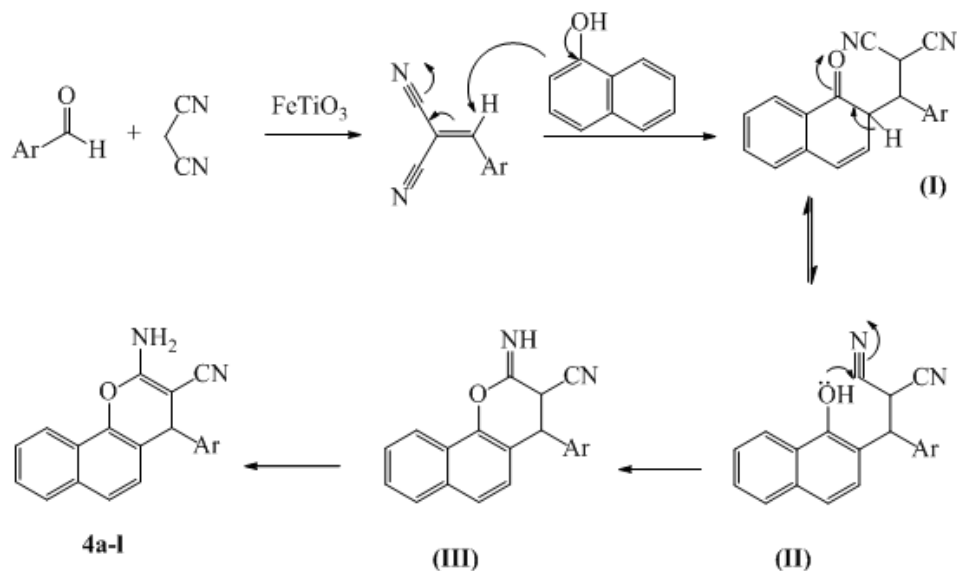


Scheme 2. Preparation of chromene derivatives from benzaldehyde, malononitrile and naphthols in the presence of FeTiO₃ as a catalyst.

Table 1. Optimization of conditions for the synthesis of 2-amino-4*H*-chromene derivatives from 4-chlorobenzaldehyde, malononitrile, and α - or β -naphthol in the presence of different amounts of FeTiO₃ as a catalyst at different temperatures.

Entry	Solvent	Catalyst (mol %)	T (°C)	Time (min)	Yield (%) ^{a,b}	
					4a	5a
1	Ethanol	10	60	35	75	73
2	Methanol	10	60	30	82	81
3	Dichloromethane	10	40	60	52	50
4	Acetonitrile	10	60	40	82	81
5	Water	15	Reflux	30	85	84
			90		79	78
			80		67	63
6	Water	10	Reflux	30	87	86
			90		81	80
			80		70	67
7	Water	5	Reflux	30	72	67
			90		64	62
			80		52	45
8	Water	Catalyst-free	Reflux	6 h	40	36
9	Solvent-free	10	100	60	72	70

^aReaction conditions: α -naphthol (1 mmol), or β -naphthol (1 mmol), benzaldehyde (1 mmol), malononitrile (1 mmol) and solvent (5 mL) in the presence of FeTiO₃ as a catalyst. ^b Isolated yield



Scheme 3 A proposed mechanism for the preparation of 2-amino-4*H*-chromene derivatives from various aldehydes, malononitrile and α -naphthol.

Table 2. Synthesis of 2-amino-4H-chromene derivatives using ilmenite as a catalyst ^a

Entry	Ar	Phenol	Product	Time/min	Yield /% ^b	Mp/°C	Lit ^c Mp/°C
1	C ₆ H ₅	α -Naphthol	4a	30	87	209-211	210-211 [39]
2	4-ClC ₆ H ₄	α -Naphthol	4b	35	91	231-232	231-232 [42]
3	2-ClC ₆ H ₄	α -Naphthol	4c	35	90	237-238	236-237 [11]
4	2,4-Cl ₂ C ₆ H ₃	α -Naphthol	4d	35	91	220-222	222-224 [46]
5	4-NO ₂ C ₆ H ₄	α -Naphthol	4e	37	91	230-232	231-234 [18]
6	3-NO ₂ C ₆ H ₄	α -Naphthol	4f	40	89	208-210	208-211 [24]
7	4-FC ₆ H ₄	α -Naphthol	4g	40	90	228-230	229-231 [42]
8	4-MeOC ₆ H ₄	α -Naphthol	4h	30	85	194-195	195-196 [10]
9	3-OHC ₆ H ₄	α -Naphthol	4i	35	83	230-232	228-232 [46]
10	4-BrC ₆ H ₄	α -Naphthol	4j	30	90	243-244	241-243 [41]
11	4-MeC ₆ H ₄	α -Naphthol	4k	30	84	205-206	205-206 [39]
12	4-HOC ₆ H ₄	α -Naphthol	4l	35	85	244-246	245-247 [43]
13	C ₆ H ₅	β -Naphthol	5a	30	86	279-280	278-280 [42]
14	4-ClC ₆ H ₄	β -Naphthol	5b	35	90	209-210	208-210 [42]
15	2-ClC ₆ H ₄	β -Naphthol	5c	35	91	237-238	274-276 [11]
16	2,4-Cl ₂ C ₆ H ₃	β -Naphthol	5d	35	90	220-222	219-222 [47]
17	4-NO ₂ C ₆ H ₄	β -Naphthol	5e	40	91	230-232	188-189 [42]
18	3-NO ₂ C ₆ H ₄	β -Naphthol	5f	50	94	211-213	210-212 [41]
19	4-FC ₆ H ₄	β -Naphthol	5g	55	94	231-232	232-233 [45]
20	4-MeOC ₆ H ₄	β -Naphthol	5h	30	83	190-192	191-193 [42]
21	4-MeC ₆ H ₄	β -Naphthol	5i	35	82	205-206	270-272 [40]

^a Reaction conditions: α - or β -naphthol (1 mmol), aldehyde (1 mmol), malononitrile (1 mmol) and water (5 mL) in the presence of FeTiO₃ as a catalyst under reflux conditions; ^b Isolated yield; ^c All known compounds were characterized by comparing their spectral (FT-IR) and physical data with those reported.

As shown in Table 2, the presence of electron-donating groups on the aromatic aldehydes resulted in low yields of the corresponding products and the reaction was sluggish. The presence of electron-withdrawing groups, however, resulted in shorter reaction times and higher yields. Using α -naphthol or β -naphthol had no effect on the reaction time or yield of the corresponding products.

The proposed mechanism for the preparation of 2-amino-3-cyano-4-phenyl-4H-benzo[h]chromene from benzaldehyde, malononitrile, and α -naphthol in the presence of FeTiO₃ as a catalyst is depicted in Scheme 3. According to the literature [10-19],

benzylidene malononitrile, containing an electron-poor C=C double bond, is formed quantitatively by Knoevenagel addition of malononitrile to the aromatic aldehyde in the presence of FeTiO₃ as a catalyst. Ortho C-alkylation of the electrophilic C=C double bond by α -naphthol gives the intermediate (I). The latter converts *via* tautomerization to intermediate (II) which is then cyclized by nucleophilic attack of an OH group on the cyano (CN) moiety to give intermediate (III). Subsequent tautomerization produced the 2-amino-3-cyano-4-phenyl-4H-benzo[h]chromene (**4a**).

Reusability is one of the important properties of this catalyst. In order to check the reusability of the catalyst, the reaction of benzaldehyde, malononitrile and α -naphthol was studied under similar conditions in the presence of 10 mol% of FeTiO₃ (Table 2, Entry 1). After the completion of the reaction, the catalyst was separated by an external magnet, and after several washings with acetone and distilled water the activated catalyst was reused to assess its efficiency in subsequent reaction cycles without any appreciable loss of its activity.

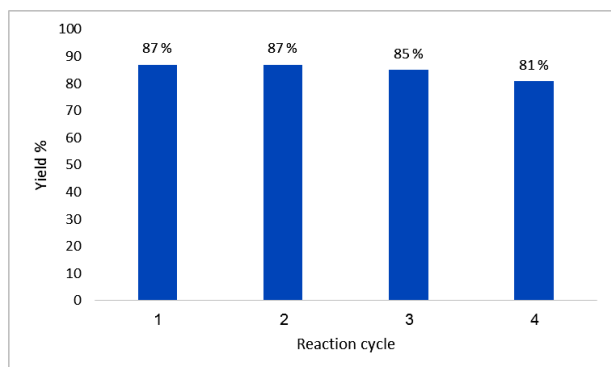


Fig. 1. Recycling of FeTiO₃ as a catalyst investigated for the synthesis of 2-amino-4H-chromene derivatives by the reaction of benzaldehyde, malononitrile and α -naphthol as a model reaction.

CONCLUSIONS

To summarize, herein, an efficient and eco-compatible method for the synthesis of 2-amino-4H-chromene derivatives via a one-pot three-component reaction of α - or β -naphthol with malononitrile and aromatic aldehydes in the presence of FeTiO₃ as a catalyst was developed. The operational simplicity, easy work-up, short reaction time, together with the use of non-toxic and commercially available catalyst are the remarkable features of the procedure.

EXPERIMENTAL

Starting materials and solvents were obtained from Merck (Germany) and Fluka (Switzerland) and were used without further purification. Melting points were measured on an Electrothermal 9100 apparatus and are uncorrected. IR spectra were measured on a Jasco FT-IR 6300 spectrometer. All obtained products are known compounds and were identified by comparing their physical and spectral data (FT-IR) with those reported in the literature. The progress of reactions was monitored by thin layer chromatography (TLC).

Synthesis of 2-amino-4H-chromene derivatives catalyzed by FeTiO₃. General procedure: A mixture of aldehyde (1 mmol), malononitrile (1 mmol), α - or β -naphthol (1 mmol) and FeTiO₃ (10 mol %) was added to a test tube and was heated in an oil bath under reflux conditions in water (5 mL) for the appropriate time (Table 2). After the completion of the reaction (monitored by TLC), the mixture was allowed to cool and the catalyst was removed by an external magnet. Then, the solvent was evaporated and the solid residue was recrystallized from ethanol (95%) to afford the pure 2-amino-4H-chromene derivatives.

Acknowledgments: This work is funded by the grant NRF-2015-002423 of the National Research Foundation of Korea.

REFERENCES

1. J. Montgomery, *Acc. Chem. Res.*, **33**, 467 (2000).
2. L. Chen, X.-J. Huang, Y.-Q. Li, W.-J. Zheng, *Monatsh. Chem.* **140**, 45 (2009).
3. S.J. Mohr, M.A. Chirigos, F.S. Fuhrman, J.W. Pryor, *Cancer Res.* **35**, 3750 (1975).
4. A.T. Raghavender, N. H. Hong, K. J. Lee, M.-H. Jung, Z. Skoko, M. Vasilevskiy, M. F. Cerqueira, A. P. Samantilleke, *J. Magn. Magn. Mater.* **331**, 129 (2013).
5. G. R. Green, J. M. Evans, A. K. Vong, in: *Comprehensive Heterocyclic Chemistry II*, A. R. Katritzky, C. W. Rens, E. F. V. Scriven, (Eds), vol. 5, Pergamon Press: Oxford, UK, 1995, p. 469.
6. (a) W. O. Foye, *Principi Di Chemico Farmaceutic*; Piccin: Padova, Italy, 1991; p 416. (b) E. C. Witte, P. Neubert Roesch, A. Ger, D.E. Offen, *Chem. Abstr.*, **104**, 224915f (1986).
7. C. S. Konkoy, D. B. Fisk Cai, S. X. Lan, N. C. Keana, *Chem. Abstr.*, **134**, 29313a (2001).
8. G. A. Elagamay, F. M. A. A. El-Taweel, *Indian J. Chem., Sect. B*, **29**, 885 (1990).
9. M. M. Heravi, B. Baghernejad, H. A. Oskooie, *J. Chin. Chem. Soc.*, **55**, 659 (2008).
10. M. M. Heravi, K. Bakhtiari, V. Zadsirjan, F. F. Bamoharram, O. M. Heravi, *Bioorg. Med. Chem. Lett.*, **17**, 4262 (2007).
11. R. Ballini, G. Bosica, M. L. Conforti, R. Maggi, A. Mazzacani, P. Righi, G. Sartori, *Tetrahedron*, **57**, 1395 (2001).
12. L. Chen, X.-J. Huang, Y.-Q. Li, M.-Y. Zhou, W.-J. Zheng, *Monatsh. Chem.*, **140**, 45 (2009).
13. J. Albadi, A. Mansournezhad, M. Darvishi-Paduk, *Chin. Chem. Lett.*, **24**, 208 (2013).
14. M. Kidwai, S. Saxena, M. K. R. Khan, S. S. Thukral, *Bioorg. Med. Chem. Lett.*, **15**, 4295 (2005).
15. H. M. Al-Matar, K. D. Khalil, H. Meier, H. Kolshorn, M. H. Elnagdi, *Arkivoc*, **xvi**, 288 (2008).
16. B. S. Kumar, N. Srinivasulu, R. H. Udupi, B. Rajitha, Y. T. Reddy, P. N. Reddy, P. S. Kumar, *Russ. J. Org. Chem.*, **42**, 1813 (2006).
17. S. R. Kolla, Y. R. Lee, *Tetrahedron*, **67**, 8271 (2011).

18. D. Kumar, V. B. Reddy, B. G. Mishra, R. K. Rana, M. N. Nadagoudac, R. S. Varma, *Tetrahedron*, **63**, 3093 (2007).
19. B. Datta, M. A. Pasha, *Ultrason. Sonochem.*, **19**, 725 (2012).
20. S. Makarem, A. A. Mohammadi, A. R. Fakhari, *Tetrahedron Lett.*, **49**, 7194 (2008).
21. R. A. Mekheimer, K. U. Sadek, *Chin. Chem. Lett.*, **20**, 271 (2009).
22. S. Khaksar, A. Rouhollahpour, S. M. Talesh, *J. Fluorine Chem.*, **141**, 11 (2012).
23. M. P. Surpur, S. Kshirsagar, S. D. Samant, *Tetrahedron Lett.*, **50**, 719 (2009).
24. D. S. Raghuvanshi, K. N. Singh, *Arkivoc*, **x**, 305 (2010).
25. J. M. Khurana, B. Nand, P. Saluja, *Tetrahedron*, **66**, 5637 (2010).
26. A.V. Borhade, B. K. Uphade, D. R. Tope, *J. Chem. Sci.*, **125**, 583 (2013).
27. (a) H. Ahankar, A. Ramazani, K. Ślepokura, T. Lis and S. W. Joo, *Green Chem.*, **18**, DOI: 10.1039/C6GC00157B (2016). (b) A. Souldozi, A. Ramazani, N. Bouslimani, R. Welter, *Tetrahedron Lett.* **48**, 2617 (2007).
28. M. R. Ganjali, S. Aghabalazadeh, M. khoobi, A. Ramazani, A. R. Foroumadi, A. Shafiee, P. Norouzi, *Int. J. Electrochem. Sci.*, **6**, 52 (2011).
29. (a) A. Ramazani, A. R. Kazemizadeh, *Curr. Org. Chem.*, **15**, 3986 (2011). (b) A. Ramazani, M. Khoobi, A. Torkaman, F. Zeinali Nasrabadi, H. Forootanfar, M. Shakibaie, M. Jafari, A. Ameri, S. Emami, M. A. Faramarzi, A. R. Foroumadi, A. Shafiee, *Eur. J. Med. Chem.*, **78**, 151 (2014). (c) A. R. Kazemizadeh, A. Ramazani, *Curr. Org. Chem.* **16**, 418 (2012). (d) A. Ramazani, M. Rouhani, E. Mirhadi, M. Sheikhi, K. Ślepokura, T. Lis, *Nano. Chem. Res.* **1**, 87 (2016). (e) A. Ramazani, A. Bodaghi, *Phosphorus, Sulfur, Silicon Relat. Elem.*, **179**, 1615 (2004). (f) A. Ramazani, M. Rahimifard, *Phosphorus, Sulfur, Silicon Relat. Elem.*, **181**, 2675 (2006). (g) A. Ramazani, A. Souldozi, *Phosphorus, Sulfur, Silicon Relat. Elem.*, **180**, 2801 (2005). (h) A. Ramazani, A. Souldozi, *Phosphorus Sulfur, Silicon Relat. Elem.*, **178**, 1325 (2003). (i) A. Ramazani, H. Ahankar, *Phosphorus, Sulfur, Silicon Relat. Elem.*, **170**, 181 (2001). (j) I. Yavari, A. Ramazani, *Synth. Commun.*, **27**, 1385 (1997). (k) F. Z. Nasrabadi, A. Ramazani, Y. Ahmadi, *Mol. Divers.*, **15**, 791 (2011). (l) A. Ramazani, A. Souldozi, *Phosphorus, Sulfur, Silicon Relat. Elem.*, **179**, 529 (2004). (m) A. Ramazani, A. Souldozi, *Phosphorus, Sulfur, Silicon Relat. Elem.*, **178**, 1329 (2003). (n) M. Khoobi, S. Emami, G. Dehghan, A. R. Foroumadi, A. Ramazani, A. Shafiee, *Arch. Pharm.*, **344**, 588 (2011). (o) M. Khoobi, A. Foroumadi, S. Emami, M. Safavi, G. Dehghan, B. Heidary Alizadeh, A. Ramazani, S. A. Ardestani A. Shafiee, *Chem. Biol. Drug. Des.*, **78**, 580 (2011). (p) A. Ramazani, A. Souldozi, *Phosphorus, Sulfur, Silicon Relat. Elem.*, **178**, 2663 (2003). (q) M. H. Gonbari, A. Ramazani, A. Souldozi, *Phosphorus, Sulfur, Silicon Relat. Elem.*, **184**, 309 (2009). (r) R. Arabian, A. Ramazani, B. Mohtat, A. Azizkhani, S. W. Joo, M. Rouhani, *J. Energ. Mater.*, **32**, 300 (2014). (s) S. Shokrollahi, A. Ramazani, S. J. Tabatabaei Rezaei, A. Mashhadi Malekzadeh, P. Azimzadeh Asiabi, S. W. Joo, *Iran. J. Cat.*, **6**, 65 (2016).
30. (a) A. Ramazani, M. Rouhani and S. W. Joo, *Ultrason. Sonochem.*, **28**, 393 (2016); (b) M. Rouhani, A. Ramazani and S. W. Joo, *Ultrason. Sonochem.*, **22**, 391 (2015); (c) M. Rouhani, A. Ramazani and S. W. Joo, *Ultrason. Sonochem.*, **21**, 262 (2014); (d) R. Moosavi, A. R. Abbasi, M. Yousefi, A. Ramazani and A. Morsali, *Ultrason. Sonochem.*, **19**, 1221 (2012); (e) A. R. Abbasi, H. Kalantary, M. Yousefi, A. Ramazani and A. Morsali, *Ultrason. Sonochem.*, **19**, 853 (2012); (f) M. Rouhani, A. Ramazani, S. W. Joo and Younes Hanifehpour, *Bull. Korean Chem. Soc.*, **33**, 4127 (2012); (g) A. Ramazani, M. Rouhani, F. Zeinali Nasrabadi, F. Gouranlou, *Phosphorus, Sulfur, Silicon Relat. Elem.*, **190**, 20 (2015).
31. H. Karami, A. Yaghoobi, A. Ramazani, *Int. J. Electrochem. Sci.*, **5**, 1046 (2010).
32. A. Ramazani, Sh. Hamidi, A. Morsali, *J. Mol. Liq.*, **157**, 73 (2010).
33. H. Ahankar, A. Ramazani, I. Amini, Y. Ahmadi, A. Souldozi, *Heteroat. Chem.*, **22**, 612 (2011).
34. A. Ramazani, A. Farshadi, A. Mahyari, K. Ślepokura, T. Lis, M. Rouhani, *J. Chem. Crystallogr.*, **41**, 1376 (2011).
35. A. Ramazani, V. Azizkhani, F. Gouranlou, *Phosphorus, Sulfur, Silicon Relat. Elem.*, **185**, 719 (2010).
36. A. Ramazani, K. Dastanra, F. Zeinali Nasrabadi, Z. Karimi, M. Rouhani, M. Hosseini, *Turk. J. Chem.*, **36**, 467 (2012).
37. A. Ramazani, A. Mahyari, *Helv. Chim. Acta*, **93**, 2203 (2010).
38. A. Ramazani, A. Mahyari, H. Lashgari, K. Ślepokura, T. Lis, *Helv. Chim. Acta.*, **94**, 611 (2011).
39. T. S. Jin, J. C. Xiao, S. J. Wang, T. S. Li, X. R. Song, *Synlett.*, **13**, 2001 (2003).
40. T. S. Jin, J. C. Xiao, S. J. Wang, T. S. Li, *Ultrason. Sonochem.*, **11**, 393 (2004).
41. R. Maggi, R. Ballini, G. Sartori, R. Sartorio, *Tetrahedron Lett.*, **45**, 2297 (2004).
42. K. Gong, H. L. Wang, D. Fang, Z. L. Liu, *Catal. Commun.*, **9**, 650 (2008).
43. Y. -M. Ren, C. Cai, *Catal. Commun.* **9**, 1017 (2008).
44. S. Kumar, N. Srinivasulu, R. H. Udipi, *Russ. J. Org. Chem.*, **42**, 1813 (2006).
45. Q. Shi, Z. Zhang, S. J. Tu, *Chin. J. Org. Chem.*, **23**, 809 (2003).
46. S. Balalaie, S. Ramezanpour, M. Bararjanian, J. H. Gross, *Synth. Commun.*, **38**, 1078 (2008).
47. X. S. Wang, G. S. Yanga, G. Zhao, *Tetrahedron*, **19**, 709 (2008).

УДОБЕН ЗЕЛЕН ПРОТОКОЛ ЗА ЕДНО-СТАДИЙНА ТРИ-КОМПОНЕНТНА СИНТЕЗА
НА 2-АМИНО-4H-ХРОМЕНИ ПРОИЗВОДНИ, КАТАЛИЗИРАНИ ОТ
ИЛМЕНИТ(FeTiO₃) КАТО ЕФЕКТИВЕН И МНОГОКРАТНО УПОТРЕБЯВАН
КАТАЛИЗАТОР ВЪВ ВОДНА СРЕДА

В. Евадзаде¹, А. Рамазани^{1*}, В. Азизхани², Х. Агахосеини¹, С. В. Джу^{3*}

¹Департамент по химия, Университет Занджан, 45195-313 Занджан, Иран

²Департамент по химия, Университет Паяме Нур, 19395-3697 Техеран, Иран

³Училище по механично инженерство, Университет Юнгнам, Гьонгсан 712-749, Република Корея

Постъпила на 24 юли, 2014 г.; Приета на 28 март, 2016 г.

(Резюме)

Описана е високо-ефективна и проста процедура за синтезата на 2-амино-4H-хроменови производни чрез едностадийна трикомпонентна реакция от различни алдехиди, малонитрил и α - или β -нафтол в присъствие на катализатор от илменит (FeTiO₃). Предимствата на новия протокол включват добър добив, кратко време, просто изпълнение, ниска токсичност и екологично съобразен катализатор. Според нашите резултати FeTiO₃ (10 % мол.) може да се използва за тази синтеза във водна среда с рефлукс.

Theoretical research of inulin's pharmacological activity by combining DFT with concept DFT methods

W. Long*, Y.K. Li, J.X. Ma, Y.B. Wang

School of Chemistry and Chemical Engineering, University of South China, Hengyang Hunan, 421001 P.R. China.

Received October 16, 2014; Revised May 20, 2015.

The molecular parameters of glucose, pyran-fructose, furfuran-fructose and inulin molecules were investigated by the density functional theory B3LYP method on the 6-311+g(d, p) basis set level. The calculated results indicate that the molecular stability order is: furfuran-fructose>pyran-fructose>glucose>inulin. Using the concept DFT method we found that inulin has the maximum chemical potential, the minimum chemical hardness and the maximum electrophilic index. The Fukui function scanning shows that the C₂ atom of the inulin molecule has strong electron-losing ability, so it is the active site of the inulin molecule. The E_{BDE} calculations show that O₂-H is the easiest position which could be broken off because the bond energy is only 94.65 kcal·mol⁻¹, which is far less than the adiabatic ionization potential value. A reasonable theoretical model was established for the pharmacological activity of inulin.

Keywords: Pharmacological Activity, Inulin, DFT and DRFT, Fukui Function.

INTRODUCTION

There is currently a considerable interest to inulin due to its pharmacological activities [1-6]. Jerusalem artichoke, which is abundant of inulin, is a large-area plant in China. Many kinds of fungi also contain inulin. We found that the plant containing inulin is wild reproductive and highly adaptable, so inulin shows the unique advantage of high resistance to pest invasion. It is easy to reach bumper harvest without manual weeding and fertilization, which attracted many scientists' attention. Jerusalem artichoke tubers contain glucose and a large amount of inulin, which has better resist pest invasion owing to the magical ingredient. There are many experiments [7-10] about inulin in order to research its magical function, but no theoretical research about inulin has been reported so far.

The clinical pharmacology of non-toxic inulin includes blood detoxifying, diuretic, detumescent, antibacterial and antiphlogistic function, so it is widely used in the cure of diseases such as fever, diarrhea and many others [11,12]. It has a magical two-way regulating blood pressure function: when hypertensive patients are cured by inulin, it effectively reduces blood sugar concentration; when hypotensive patients are cured by inulin, it distinctly raises blood glucose concentration [13]. Stevioside (CAS number 57817-89-7) is a macromolecular system with the formula C₃₈H₆₀O₁₈

shown in Figure 1(a). Inulin can be obtained by hydrolysis of stevioside. Chi [14] found that inulin has good oxidation resistance and it can play selective catalytic function superior to that of free radicals as (•OH) and super oxide anion free radical as (O₂•) in the human body, but the real process is not clear. Nieto-Nieto [15] found that a small amount of inulin can greatly increase (from 13.93 to 22.98 kPa) the compressive stress of the gels prepared at pH 7 in order to increase the apparent protein concentration. Aidoo [16] pointed out that inulin and polydextrose mixtures could be used for sugar-free chocolate manufacture with satisfactory physicochemical properties when sweetened with stevia or thaumatin extracts. Hu [17] also made the important conclusion that inulin has good antioxidant activities against hydroxyl radicals (•OH), super oxide radicals (O₂•) and DPPH radicals (DPPH•). In short, there are a lot of experimental reports about inulin, and it is very essential to do some theoretical chemical research in order to explain its magical pharmacological activity.

Predicting drug activity by the theory of chemical simulation calculation have been widely reported [18,19]. We chose *D*-marigold sugar (CAS number 87-81-0, formula C₆H₁₂O₆) to research its pharmacological activity, which can be contrasted to glucose, pyran-fructose, fructose, and furfuran-fructose. We compared the differences in their pharmacological activity by the concept DFT activity index [20-21]. The charge scanning of the inulin molecule was done by the Fukui function [22], which can predict the active position and

* To whom all correspondence should be sent:
E-mail: usclw2013@163.com

many different abilities.

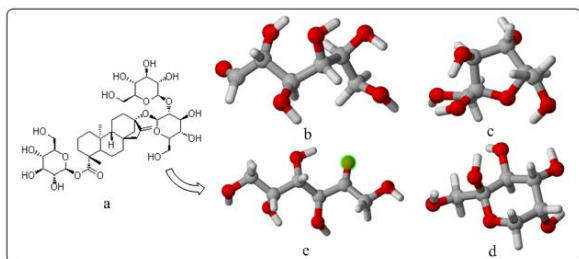


Fig. 1. Structure of the five molecules

THEORY AND CALCULATION METHODS

The geometry optimization of each species selected is carried out using DFT/B3LYP method with 6-311+g(d,p) basis sets [23]. The vibration frequencies are calculated at the B3LYP/6-311+g(d,p) level of theory for the optimized structure and the obtained frequencies are scaled by 0.9613 [24]. The other calculations are performed by the same method with the same basis set. We found that all vibration frequencies of each molecule are positive through vibration frequency analysis, which could certify that all calculated details are effective and credible.

In order to study the magical structure of the inulin molecule, taking into account the different solubility, we chose the PCM model solvent construction by water. At the same time, we performed molecular orbital analysis and charge distribution in the different systems. Also we obtained the charge value using natural bond orbital (NBO) analysis [25]. Density functional activity index is very effective in predicting the pharmacological activity and local selectivity [26]. In DFRT framework, the global reaction indices such as chemical potential μ and chemical hardness η are defined as:

$$\mu = -\chi = (\partial E / \partial N)_v$$

$$\eta = (\partial^2 E / \partial N^2)_v = (\partial \mu / \partial N)_v$$

E is the total energy of the system, N is the total number of electrons in the system, v is the external potential energy, μ can be defined as the negative value of electron negativity χ . According to the principle of Mulliken [27], $\mu = -\chi = -(I+A)/2$. Pearson [28] suggested that $\eta = I-A$, where I is the first ionization potential and A is the electron affinity. According to the closed shell theory, $I \approx -E_{\text{HOMO}}$ and $A \approx -E_{\text{LUMO}}$, where E_{HOMO} is the highest occupied molecular orbital energy, and E_{LUMO} is the lowest occupied molecular orbital energy. Parr and Liu [29] proposed the electric affinity index as $\omega = \mu^2 / 2\eta$, the force affinity index as $\Delta E_n = -A + \omega = (\mu + \eta)^2 / 2\eta$, and the electric affinity

index as $\Delta E_e = I + \omega = (\mu - \eta)^2 / 2\eta$.

Localized reaction index can be described by the Fukui function [29] which is the first order derivative between electron density (R) and the electron number (N). Because the Fukui function is discontinuous, we simplified the affinity electric Fukui function as $f^-(r)$, the affinity nuclear Fukui function as $f^+(r)$ and the free radical Fukui function as $f^0(r)$.

$$f(r) = (\partial \rho(r) / \partial N)_v$$

$$f^-(r) = \rho_{N(r)} - \rho_{N-1(r)}$$

$$f^+(r) = \rho_{N+1(r)} - \rho_{N(r)}$$

$$f^0(r) = (f^+(r) + f^-(r)) / 2$$

where $\rho_{N(r)}$ is the electron density of neutral molecules, $\rho_{N-1(r)}$ is the electron density of cation and $\rho_{N+1(r)}$ is the electron density of anion. We studied the chemical activity of hydroxyl in order to certify the better oxidation resistance of inulin. There are two kinds of molecular reaction mechanisms [30,31] about free radical scavenging tioxide ants: (1) in a nonpolar solvent, the straight pull hydrogen abstraction reaction could achieve the purpose, so the theoretical parameter is O-H bond dissociation energy (bond dissociation enthalpy, referred to as BDE); when E_{BDE} is lower, the reaction could take place more easily; (2) in a polar solvent, a proton-electron transfer reaction could take place and the theoretical parameter is the ionization potential (IP), when IP is lower, the reaction could take place more easily. As the human body is more complex, oxidation resistance performance of hydroxyl often need combine the measurement of E_{BDE} and IP parameters.

$$E_{\text{BDE}} = H_f + H_h - H_p = (\text{SPE}_f + \text{ZPVE}_f \times v + 3/2RT + 3/2RT + RT) + H_h - (\text{SPE}_p + \text{ZPVE}_p \times v + 3/2RT + 3/2RT + RT)$$

$$= (\text{SPE}_f + \text{ZPVE}_f \times v) + H_h - (\text{SPE}_p + \text{ZPVE}_p \times v)$$

$$\text{IP} = H_c - H_p$$

SPE is the electron energy, ZPVE is the zero point energy, v is a correction factor of 0.9804, H_p is the enthalpy of the parent molecule, H_h is the enthalpy of one hydrogen atom (0.49764 a.u.), H_f is the enthalpy of the free radical obtained when the parent molecule loses one hydrogen atom, H_c is the formation enthalpy of the radical cation in response. All calculations are done by the Gaussian 03 program [32]. Taking into account the really existent state of molecules, we have constructed the solvent model (PCM) with water as the solvent. Part of the images were analyzed and plotted through Gaussian-view, NBO and Multiwfn 2.5 program [33].

RESULTS AND DISCUSSION

Geometry Optimization

As shown in Figure 1, **a** is a stevioside molecule, **e** is a *D*-Marigold-inulin molecule obtained by hydrolysis from **a**, **b** is a glucose molecule, **c** is a pyran-fructose molecule, and **d** is a furfuran-fructose molecule. They all have hydroxyl groups, the molecular formula is $C_6H_{12}O_6$, and all of them can be dissolved in water and be absorbed into the cell. A carbon atom ring is involved in the **c** and **d** molecules, a carbonyl radical ($C=O$) in the **e** molecule, and an aldehyde radical ($-CHO$) in the **b** molecule. In order to compare the different molecular structures, we chose the B3LYP/6-311+g(d,p) method combined with the PCM solvent model (solvent is water) to optimize the molecular geometrical structure. We also analyzed the harmonic frequency vibration after the stable structure has been found. All results are positive which indicates that the molecular structure is stable.

As shown in Table 1 (the carbon atom number is shown in Fig.2), we found that the bond lengths in the four isomeric molecules are almost equal, the molecules are stable, and the C-C bond lengths in furan-fructose and pyran-fructose are the same as in the chain molecule, but the molecular intra angle is 110° . This is close to the straight chain molecule's angle of 119° , which leads to molecular stability. It is shown that the covalent radius of the carbon atom is 0.077 nm and the covalent radius of the oxygen atom is 0.066 nm [35], so the bond length of $C=O$ should be less than 0.143 nm. We found that the bond length of $C_1=O$ is 0.1200 nm in the **b** molecule, the bond length of $C_2=O$ is 0.1220 nm in the **e** molecule, both are less than 0.143 nm because of the different aldehyde radical effects. The bond angle data differing from 120° near the C_2 are due to the group electron attraction of the oxygen atom in the **e** molecule. As there are experimental results [36,37] for these molecules, we found that the error between calculated data and experimental data [35] is very small, so our calculations are credible and reasonable.

Infrared Spectroscopy

After single frequency analysis of the four molecules by the Gaussian 03 program [32], we found that all vibration frequencies are positive. The simple harmonic vibrations are attached by the Gauss-View program, we drew the infrared spectra of the four molecules as shown in Figure 3, and the

results are reasonable. Molecular vibration fingerprint peaks appeared between 400 and 1300 cm^{-1} due to the vibration of the total molecule. The absorption peaks between 1000 and 1400 cm^{-1} are due to the stretching vibration of the C-O bond in the molecules (including primary alcohol, secondary alcohol and tertiary alcohol). A strong absorption peak is observed at 1100 cm^{-1} in the **c** or **d** molecules due to the asymmetric stretching vibration of C-O-C bonds. A similar picture is observed for the **b** molecule. There is one strong absorption peak at 1700 cm^{-1} in the **e** molecule due to the vibration of the carbonyl $C=O$ bond, and several strong absorption peaks appeared at 2900 cm^{-1} in the **b** molecule due to the vibration of C-H bonds. There are some uncorrected results at a frequency about 2820 cm^{-1} . There are two areas of many small absorption peaks after 3000 cm^{-1} , which are mainly due to the expansion of C-H bond and the stretching of O-H bond.

NBO Analysis

In order to compare the atomic contribution in the four molecules, we performed atom charged scanning by the NBO program. The distribution of natural charges belonging to an atom is shown in Table 2. It is seen that both the C_1 atom in the **b** molecule and the C_2 atom in the **e** molecule show a strong positive charge owing to the strongly electronegative attraction of the oxygen atom in the $C=O$ bond. The atomic charge of the carbon atom is accounted for by the connected number of oxygen atoms and hydrogen atoms. The atomic charge of the C_5 atom is 0.5616e and 0.5492e in the **c** and **d** molecule, respectively, which is due to the lack of a hydrogen atom contributing a positive charge. The carbon atoms of the primary alcohol generally show more negative charges because of the steric effect, such as the C_6 atom in the **b** molecule and the C_1 atom in the **e** molecule. The oxygen atom shows a negative charge in all molecules. The maximum value of the negative charge has the oxygen atom attached to C_6 in the **b** molecule but not the oxygen atom in $C=O$, which is affected by the contribution of the electron cloud and the steric hindrance. The oxygen atom in C-O-C at both **c** and **d** molecules shows -0.6114e and -0.5560e respectively, which indicate that the connection tension between the ring atoms is suitable. The charge distribution may not explain the overall stability, and we have to judge by the natural orbit and the two-order perturbation stabilization energy, the related data are listed in Table 3.

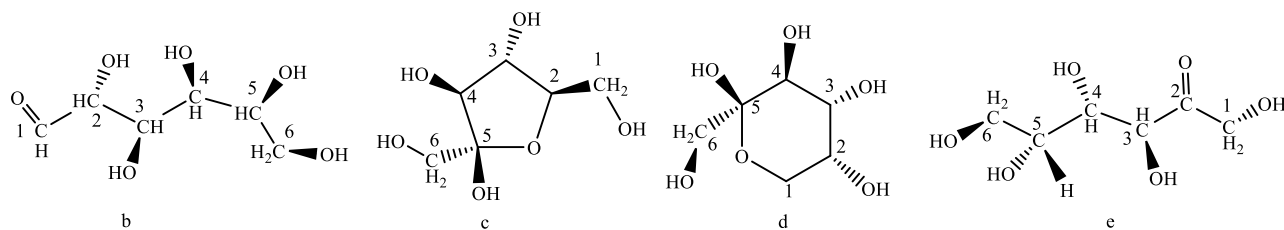


Fig. 2. The carbon atom number in the molecule.

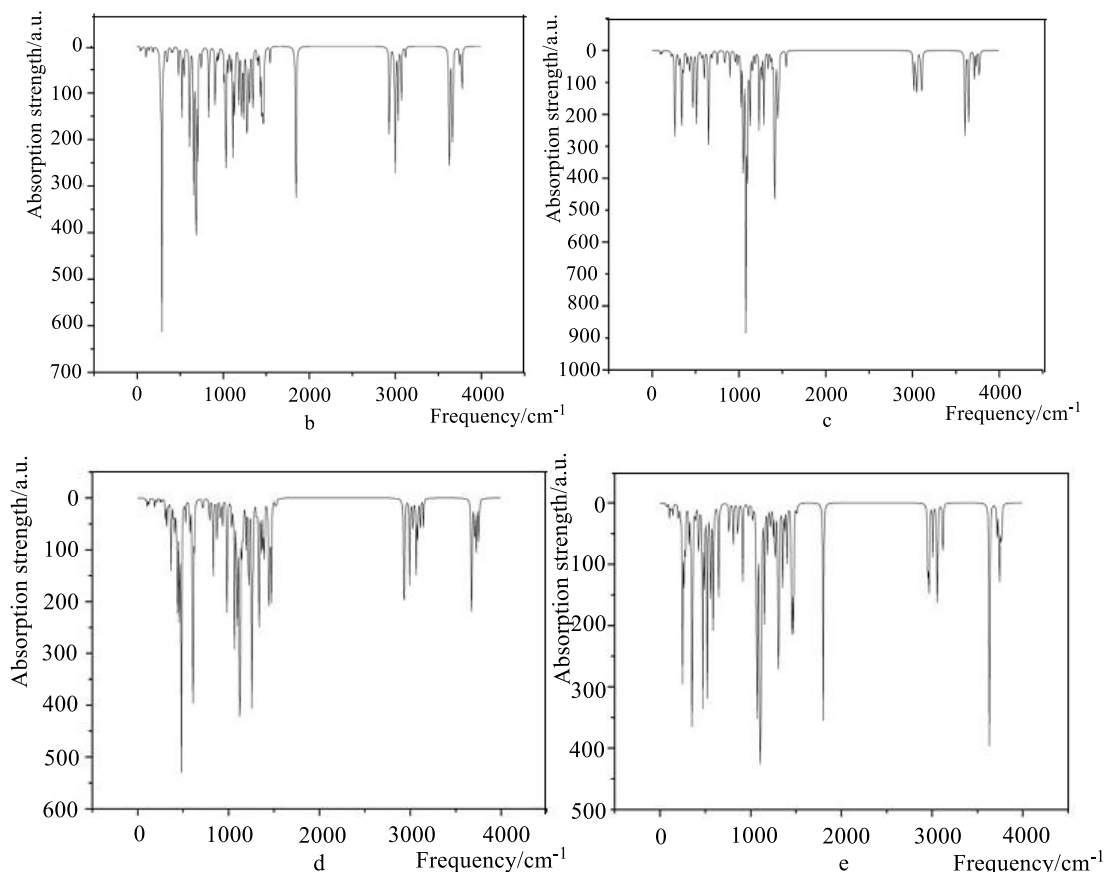


Fig. 3. Infrared spectra of the four molecules.

Table 1. Partial bond lengths (nm) and bond angle ($^{\circ}$) data.

Length	C ₁ -C ₂	C ₂ -C ₃	C ₃ -C ₄	C ₄ -C ₅	C ₅ -C ₆	C ₁ -O	C ₂ -O	C ₃ -O	C ₄ -O	C ₅ -O	C ₆ -O
b	0.1520	0.1550	0.1540	0.1550	0.1530	0.1200	0.1410	0.1430	0.1430	0.1430	0.1430
c	0.1530	0.1530	0.1540	0.1560	0.1530	0.1420	0.1450	0.1430	0.1410	0.1420	0.1430
d	0.1530	0.1530	0.1530	0.1550	0.1540	0.1430	0.1420	0.1420	0.1440	0.1430	0.1410
e	0.1520	0.1530	0.1550	0.1540	0.1530	0.1400	0.1220	0.1430	0.1410	0.1430	0.1420
Angle	$\angle(\text{O}-\text{C}_1-\text{C}_2)$	$\angle(\text{C}_1-\text{C}_2-\text{O})$	$\angle(\text{C}_1-\text{C}_2-\text{C}_3)$	$\angle(\text{C}_2-\text{C}_3-\text{O})$	$\angle(\text{C}_2-\text{C}_3-\text{C}_4)$	$\angle(\text{C}_3-\text{C}_4-\text{O})$	$\angle(\text{C}_3-\text{C}_4-\text{C}_5)$	$\angle(\text{C}_4-\text{C}_5-\text{O})$	$\angle(\text{C}_4-\text{C}_5-\text{C}_6)$	$\angle(\text{C}_5-\text{C}_6-\text{O})$	$\angle(\text{C}_5-\text{C}_6-\text{O})^*$
b	124.9	110.2	109.1	104.8	112.8	109.7	114.4	108.0	114.7	106.4	106.3
c	110.5	108.4	115.1	107.4	103.1	109.8	103.2	110.1	114.3	106.8	106.7
d	112.7	109.3	109.3	107.7	110.6	105.4	111.3	108.7	112.9	111.6	112.1
e	109.3	122.2	117.5	113.1	109.0	108.7	111.2	112.7	113.1	110.2	110.3

* from the experimental data in [34].

Table 2. Natural charge of atoms in the four molecules.

Molecule	C ₁	C ₂	C ₃	C ₄	C ₅	C ₆
b	0.3936	-0.0168	0.0635	0.0390	0.0351	-0.1281
c	-0.1043	0.0635	0.0462	0.0176	0.5616	-0.1252
d	-0.1199	0.0195	0.0474	-0.0063	0.5492	-0.1131
e	-0.1581	0.4679	-0.0238	0.0426	0.0423	-0.0981
Molecule	C ₁ -O	C ₂ -O	C ₃ -O	C ₄ -O	C ₅ -O	C ₆ -O
b	-0.5089	-0.7565	-0.7546	-0.7751	-0.7685	-0.7768
c	-0.7547	-0.6114	-0.7589	-0.7381	-0.7478	-0.7737
d	-0.5560	-0.7737	-0.7703	-0.7491	-0.7416	-0.7372
e	-0.7223	-0.4818	-0.7246	-0.7440	-0.7688	-0.7637

Table 3. Partial results by NBO analysis and the second-order perturbation energy.

Molecule	Donor NBO _(i)	Acceptor NBO _(j)	Stabilization energy E ₍₂₎ cal•mol ⁻¹
B	LP (C ₁ -O)	BD*C ₁ -C ₂	21.88
	LP (C ₁ -O)	BD*C ₁ -H	21.39
C	LP (C ₂ -O)	BD*C ₅ -O	12.95
D	LP (C ₃ -O)	BD*(C ₂ -O)-H	21.16
	LP (C ₁ -O)	BD*C ₅ -O	12.69
E	LP (C ₂ -O)	BD*C ₁ -C ₂	12.28
	LP (C ₂ -O)	BD*C ₂ -C ₃	11.26
	BD (C ₁ -H)	BD*(C ₃ -O)-H	10.22

If the two-order perturbation stabilization energy ($E_{(2)}$) is sourced from an isolated electron pair, this could indicate that the other repel force of bonds is small, so the molecular stability is high. The maximum value of $E_{(2)}$ is followed as Donor NBO_(i)→Acceptor NBO_(j). It is found that $E_{(2)}$ between the lone pair of electrons of the oxygen atom and the antibonding orbital has the maximum value in the **b**, **c**, **d** molecules which indicate that the three molecules are stable. $E_{(2)}$ value between the C₁-H bond and BD* of C₃-O-H in the **e** molecule is as large as 10.22 cal•mol⁻¹ and cannot be neglected. So the formation of molecular intra hydrogen bond on C₁-H in the **e** molecule may proceed under the effect of the oxygen atom attached to the C₃ atom. This influence may bring the inulin molecule in a stable state.

Molecular Energy and Frontier Orbit

In order to assess the different stability of the four molecules, we calculated the energy data at 0K which are listed in Table 4. We found that E_0 of the furan-fructose molecule has the lowest value, which is because the ring built of six atoms could better accommodate many electrons. The molecular energy data indicate that the furan-fructose molecule is the most stable one, the relative isomerism energy of the glucose molecule is 50.6721kJ•mol⁻¹, and the relative isomerism energy of the inulin molecule is 43.3208 kJ•mol⁻¹. The reason for this phenomenon is that the linear

molecule could cause molecular volume expansion, and the scope expansion of the electronic motion leads to an energy increase. In order to assess the electronic transitions and chemical energy, we calculated the energy level of the frontier molecular orbital, which is shown in Figure 4. HOMO is the highest molecular orbital, and LUMO is the lowest unoccupied molecular orbital. The HOMO-LUMO gap is used as a direct indicator of kinetic stability. A large HOMO-LUMO gap implies high kinetic stability and low chemical activity because it is energetically unfavorable to add electrons to a high-lying LUMO orbit [38] or to extract electrons from a low-lying HOMO orbit [39]. ΔE is the value of the HOMO-LUMO gap, and for lower ΔE the electron transition is easier and the molecule is more unstable.

It is shown that the inulin molecule is more unstable than the other ones because its $\Delta E=3.75\text{eV}$ which is the lowest value in Figure 4, and one electron could easily transit from the primary alcohols at the end of the molecule to the carbonyl bond (C=O), so the atom of the right hydroxy radical is the best active site which could easily lose one electron. The activity of the molecule is mainly controlled by the aldehyde radical which has a large contribution to the HOMO orbit and LUMO orbit. It is shown that the electronic transition of pyran-fructose is very difficult because its $\Delta E=7.51\text{eV}$ is the maximum energy gap among the others. The track comparison of LUMO orbit is dispersed,

covering the total pyran ring, which can indicate that the molecule has a better ability to accept electrons. Furan-fructose's frontier orbit is shown as **d** in Figure 4, the HOMO orbital distribution is relatively dispersed, and the value of ΔE is 6.81eV, so the electronic transition is not easy. LUMO orbital is almost contributed by the oxygen atom orbit which is connected to the C₄ atom. There is the same linear structure in the **b** and **e** molecules, but one aldehyde radical in the **b** molecule differs from that in the **e** molecule, so the energies are different in the **b** and **e** molecules. In contrast to the value of ΔE , we derived the stability of molecules as: $e < b < d < c$; the pyran-fructose molecule is the most stable one.

Table 4. Electronic energy, zero point energy and relative energy.

Molecule	$E_0(\text{a.u.})$	$E_{ZPE}(\text{a.u.})$	$E_{\text{tot}}(\text{a.u.})$	$\Delta E(\text{kJ}\cdot\text{mol}^{-1})$
b	-687.1257	0.1952	-686.9305	50.6721
c	-687.1446	0.1971	-686.9475	6.0387
d	-687.1478	0.1980	-686.9498	0
e	-687.1279	0.1946	-686.9333	43.3208

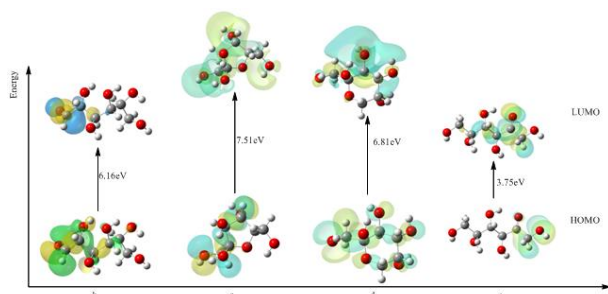


Fig.4. Diagram of the frontier orbital energy.

Concept DFT and Fukui Index Calculations

Recently, concept DFT active index (μ , η , ω , ΔE_n , ΔE_e) are applied widespread [20,21,40] both in inorganic and organic chemical field. If the molecule is in a transition state, the value of chemical potential μ would be the great, and the value of chemical hardness η would be small, so the molecule is in an unstable state. The opposite case is when the molecule is in a steady state, then the value of chemical potential μ would be small, and the value of chemical hardness η would be great. The electrophilic index ω could show the binding degree of a molecule with an electrophilic reagent, also the nucleophilic force differential index ΔE_n . The electrophilic force differential index ΔE_e is indicated as the activity degree of nucleophilic or electrophilic attack. All concept active indices are listed in Table 5. We found that the volume and the specific surface area of the **c** and **d** molecules decreased because of the formation of a cyclic

structure in the molecules, but the molecular volume and surface area of the **b** and **e** molecules are still large because of the straight chain. The order of the ionization potentials is $c > b \approx d > e$, and the ionization potential value of the inulin molecule is the lowest one. This conclusion is not the same as the former one, which is a result of not accurate correction. We also found that the same values of inulin's related indices are obtained using different methods, but this does not effect the final conclusion. Electron affinity values of **c** and **d** molecules are negative, which indicate that their energy would decrease after accepting one electron into the anion, but the electron affinity value of the **e** molecule is much larger than that of the **b** molecule, which could indicate that its energy would increase after accepting an electron into the anion and the stability of the anion has become weak. The chemical potential μ of the **e** molecule is the maximum one and the chemical hardness η is the lowest sample, which could certify that the **e** molecule is in a relatively stable state; the chemical potential μ of the pyran-molecule is lower and the chemical hardness η is maximal, which is probably because the whole molecule structure is unstable and the tension of the ring is so large that it could easily accommodate electrons. The electrophilic index ω of the **e** molecule is maximal, which points to its best activity and better electrophilic capability. Comparing ΔE_n and ΔE_e , we found that the value of ΔE_n of the **e** molecule is the maximal and the value of ΔE_e of the **e** molecule is the minimum, so the inulin molecule has better nucleophilic ability and it can become a good antioxidant drug.

In order to comprehensively understand the molecular activity, we performed local atomic Fukui index calculation on the inulin molecule, and the results are listed in Table 6. Obviously, the $f_{(r)}^-$, $f_{(r)}^+$, $f_{(r)}^0$ values of the six carbon atoms in the inulin molecule are different. The $f_{(r)}^+$ value of the C₂ atom is maximal, so its ability of gaining one electron is stronger than that of the other atoms, while the $f_{(r)}^+$ values of the C₄, C₅, C₆ atoms are negative, i.e., gaining one electron is impossible. The $f_{(r)}^-$ value of the C₂ atom is maximal, i.e., losing one electron is easy, so all carbon atoms except the C₃ atom could lose one electron. In contrast to the $f_{(r)}^+$ value, the electronic contribution is more distinct, the total molecule could easily lose one electron. Analysis of the $f_{(r)}^0$ values of all carbon atoms showed that the most active position is at the C₂ atom. Both $f_{(r)}^-$ value and $f_{(r)}^+$ value of the oxygen atom attached to the C₆ atom are the maximal, so it is able to easily capture one electron. The $f_{(r)}^+$ value of the oxygen atom attached to the C₂ atom is the

Table 5. Concept DFT indices of the four molecules.

Molecule	V Bohr ³	SA Bohr ²	I eV	A eV	μ eV	η eV	ω eV	ΔE_n eV	ΔE_e eV
b	1358.18	707.21	6.52	0.36	3.44	6.16	0.96	7.48	0.60
c	1287.23	669.13	6.72	-0.77	3.48	7.49	0.81	8.03	1.07
d	1313.91	666.31	6.50	-0.29	3.11	6.79	0.71	7.22	1.00
e	1329.88	708.32	6.45	2.71	4.58	3.74	2.80	9.25	0.09

Table 6. Fukui function analysis of key atoms in the inulin molecule.

Atom	$\rho_{N(r)}$	$\rho_{N-1(r)}$	$\rho_{N+1(r)}$	$f^-(r)$	$f^+(r)$	$f^0(r)$
C ₁	0.1581	0.1698	0.1448	0.0117	0.0133	0.0125
C ₂	0.4679	0.5677	0.1925	0.0998	0.2754	0.1876
C ₃	0.0238	0.0023	0.0088	-0.0215	0.0150	-0.0033
C ₄	0.0426	0.0731	0.0701	0.0305	-0.0275	0.0015
C ₅	0.0423	0.0457	0.0490	0.0034	-0.0067	-0.0017
C ₆	0.0981	0.1264	0.1081	0.0283	-0.0100	0.0092
C ₁ -O	0.7223	0.7123	0.7316	-0.0100	-0.0093	-0.0097
C ₂ -O	0.4818	0.3757	0.7650	-0.1061	-0.2832	-0.1947
C ₃ -O	0.7246	0.7175	0.7908	-0.0071	-0.0662	-0.0367
C ₄ -O	0.7440	0.6914	0.8052	-0.0526	-0.0612	-0.0569
C ₅ -O	0.7688	0.7348	0.7926	-0.0340	-0.0238	-0.0289
C ₆ -O	0.7637	0.5236	0.7756	-0.2401	-0.0119	-0.1260

Table 7. E_{BDE} energy of the different hydrogen atoms

Molecule	SPE _f (a.u.)	ZPV _p (kJ•mol ⁻¹)	O—H E _{BDE} (kJ•mol ⁻¹)
	-687.127937	511.068278	—
1-H	-686.459871	470.287437	407.471927
2-H	-686.465734	474.290536	396.003258
3-H	-686.454712	473.926642	424.585545
4-H	-686.459414	473.009817	411.340801
5-H	-686.456683	471.023627	416.563519

lowest one so that it is difficult for the C₂ atom to accept one electron but it could lose one electron, which makes the inulin's real molecular structure magical.

Evaluation of the Antioxidant Ability

In pharmacological aspect, the inulin molecule shows very good antioxidant properties [41,42]. It is known that inulin could exert pesticide effect by reacting with the hydroxyl free radical (\bullet OH) or the super oxide anion free radical ($O_2\bullet$). The reaction mechanism of disposal of free radicals mainly depends on the role of hydroxyl dehydrogenation, which could be assessed by the E_{BDE} and IP parameters. Therefore, we calculated the E_{BDE} value of the different hydrogen atoms on the basis of the molecular stable structure which has been optimized by the B3LYP method. Every hydrogen atom in the inulin molecule is numbered as shown in Figure 5, and the E_{BDE} values of the different

hydrogen atoms are listed in Table 7.

It is shown that the E_{BDE} values of hydrogen atoms at different positions are different. When the E_{BDE} value is lower, this position can more easily provide a hydrogen atom, so the antioxidant ability is stronger. We found that 2-H is most easily broken because its E_{BDE} value is the lowest one, which is due to the strong electronic contribution of carbonyl (C=O). But the E_{BDE} value of the 3-H atom is by approximately 28.5800 kJ•mol⁻¹ higher than that of the 2-H atom. We calculated the vertical ionization energy and the adiabatic ionization energy of the inulin molecule by the same method, the values are 196.5600 kcal•mol⁻¹ and 183.1500 kcal•mol⁻¹, respectively. Both ionization energies are very high, so the E_{BDE} value is reasonable to explain the antioxidant activity.

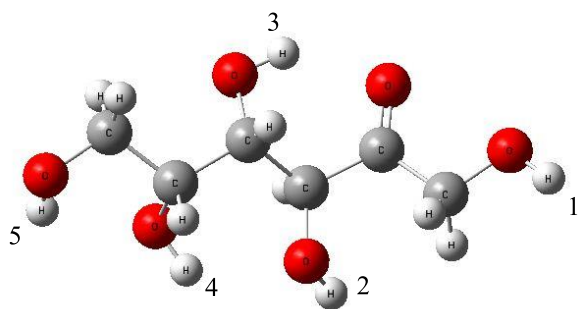


Fig.5. Hydrogen atom numbers in the inulin molecule.

CONCLUSIONS

We found that the stability order is furan-fructose>pyran-fructose>glucose>inulin through geometrical structure optimization, frequency analysis, infrared spectroscopy, atom charge population, NBO analysis, and frontier orbital energy calculation by the DFT method. On this basis, we chose the concept DFT activity index method to analyze the various parameters of inulin molecule. The chemical potential and the electrophilic index of the inulin molecule are great, but the chemical hardness is small. The C₂ atom is the active center of the whole molecule because it is the easiest position for losing one electron through the Fukui index scanning. Calculations of E_{BDE} showed that 2-H is the most easily broken off position because the value is far less than the adiabatic ionization potential. All these can form a reasonable theoretical model to explain the magical pharmacological activity of the inulin molecule.

REFERENCES

1. H.Y. Zhang, L.F. Wang, Y.M. Sun, *Bioorganic & Medicinal Chemistry Letters*, **13**, 909 (2003).
2. J.H. Roe, J.H. Epstein, N.P. Goldstein, *J. Biol. Chem.*, **178**, 839 (1949).
3. Y. Zhang, T.H. Chen, J.T. Sun, *Chemistry Bulletin*, **65**, 12 (1998).
4. G.R. Gibson, E.R. Beatty, X. Wang, *Gastroenterology*, **108**, 975 (1995).
5. R.A.A. Muzzarelli, J. Boudrant, D. Meyer, *Carbohydrate Polymers*, **87**, 995 (2012).
6. S. Stoyanova, J. Geuns, E. Hideg, *Int. J. Food Sci. & Nutr.*, **62**, 207 (2011).
7. P. Andrewes, J.L.H.C. Busch, T. Joode, *J. Agric. & Food Chem.*, **51**, 1415 (2003).
8. K. Seki, K. Haraguchi, M. Kishimoto, S. Koboyashi and K. Kainuma, *Agric. Biol. Chem.*, **53**, 2089 (1989).
9. Y.J. Zhang, *Anal. Chem.*, **5**, 167 (1977).
10. Y.M. Sun, H.Y. Zhang, D.Z. Chen, *Org. Letters*, **4**, 2909 (2002).
11. J. Luo, S.W. Rizkalla, C. Alamowitch, *Am. J. Clin. Nutr.*, **96**, 939 (1996).
12. M.L. Jose, T. Elad, P. Raymond, D.M. Glahn, *Food Chem.*, **109**, 122 (2008).

13. K.G. Jackson, G.R. Taylor, A.M. Clohessy, *Brit. J. Nutrition*, **82**, 23 (1999).
14. Z.M. Chi, T. Zhang, T.S. Cao, *Biol. Tech.*, **102**, 4295 (2011).
15. T.V. Nieto-Nieto, Y.X. Wang, L. Ozimek, L.Y. Chen. *Food Hydrocolloids*, **50**, 116 (2015).
16. R.P. Aidoo, E.O. Afoakwa, K. Dewettinck. *LWT-Food Science and Technology*, **62**, 592 (2015).
17. Y.X. Hu, J. Zhang, C.W. Yu, Q. Li, F. Dong, G. Wang, Z.Y. Guo. *International Journal of Biological Macromolecules*, **70**, 44 (2014).
18. L.J. Pauling, *J. Am. Chem. Soc.*, **62**, 2643 (1940).
19. M. Azenha, P. Kathirvel, P. Nogueira, *Biosens. & Bioelectron.*, **23**, 1843 (2008).
20. A.D. Becke, *J. Chem. Phys.*, **97**, 9173 (1992).
21. R.G. Parr, W. Yang, *J. Am. Chem. Soc.*, **106**, 4049 (1984).
22. K. Fukui, *J. Phys. Chem.*, **74**, 4161 (1970).
23. M.P. Andersson, P. Uvdal, *J. Phys. Chem. A*, **109**, 2937 (2005).
24. A.P. Scott, L. Random, *J. Phys. Chem.*, **100**, 16502 (1996).
25. M. Szafram, A. Komasa, E.B. Adamska, *J. Mol. Struct.*, **827**, 101 (2007).
26. B. Miehlich, B., A. Savin, A., H. Stoll, H. Preuss, *Chem. Phys. Letters*, **157**, 200 (1989).
27. Y. Li and J.N.S. Evans, *J. Am. Chem. Soc.*, **117**, 7756 (1995).
28. R.G. Pearson, Springer-Verlag: Berlin, **22**, 101 (1993).
29. S.B. Liu, *Acta Phys.-Chim. Sin.*, **25**, 590 (2009).
30. G.T. Head, G.M. Head, M.J. Frisch, *J. Am. Chem. Soc.*, **113**, 5989 (1991).
31. R.B. Ammar, W. Bhourri, M.B. Sghaier, *Food Chem.*, **116**, 258 (2009).
32. M.J. Frisch, G.W. Trucks, H.B. Schlegel, Gaussian 03, Revision D.02; Gaussian Inc.: Pittsburgh, PA, 2003.
33. T. Lu, F.W. Chen, *J. Comp. Chem.*, **33**, 580 (2012).
34. M.Z. Saavedra-Leos, C. Leyva-Porras, E. Martínez-Guerra, S.A. Pérez-García, J.A. Aguilar-Martínez, C. Álvarez-Salas. *Carbohydrate Polymers*, **105**, 10 (2014).
35. J.A. Dean Ed. Lang's Handbook of Chemistry, Thirteenth Edition. McGraw-Hill Book Company, 1985.
36. L. Santiago-Rodríguez, M. M. Lafontaine, C. Castro, J. Méndez Vega, M. Latorre-Esteves, E. J. Juan, C. Rinaldi, *J. Mater. Chem. B*, **22**, 2807 (2013).
37. K.D.O. Vigier, A. Benguerba, A. Barrault, *J. Green Chem.*, **14**, 285 (2012).
38. F. Russo, C. Clemente, M. Linsalata, M. Chiloiro, A. Orlando, E. Marconi, *Europ. J. Nutr.*, **50**, 271 (2011).
39. R.M. Yosadara, *J. Phys. Chem., A*, **106**, 11283 (2002).
40. P. Geerlings, F. Deproft, W. Langenaeker, *Chem. Rev.*, **103**, 1793 (2003).
41. E.M. Dewulf, P.D. Cani, A.M. Neyrinck, *J. Nutr. Biol. & Chem.*, **22**, 712 (2011).
42. B.S. Reddy, R. Hamid, C.V. Rao, *Carcinogenesis*, **18**, 1371 (1997).

ТЕОРЕТИЧНО ИЗСЛЕДВАНЕ НА ФАРМАКОЛОГИНАТА АКТИВНОСТ НА ИНУЛИН ЧРЕЗ КОМБИНАЦИЯ НА DFT С КОНЦЕПТУАЛНИ DFT-МЕТОДИ

В. Лонг*, И.И. Ли, Дж.С. Ма, И.Б. Ванг

Училище по химия и химично инженерство, Южнокитайски университет, Хенгян, Юнан, 421001 Китай

Постъпила на 16 октомври, 2014 г.; Коригирана на 20 май, 2015 г.

(Резюме)

Молекулните параметри на глюкозата, пирано-фруктозата, фурфуран-фруктозата и на инулина са изследвани с помощта на DFT –теорията по метода B3LYP на базата на 6-311+g(d, p)–ниво. Изчислителните резултати показват, че редът на молекулна стабилност е: фурфуран-фруктоза>пиран-фруктоза>глюкоза>инулин. С помощта на концептуален DFT-метод намерихме, че инулинът има максимален химичен потенциал, минимална химическа устойчивост и максимален електрофилен индекс. Сканирането чрез функция на Fukui показва, че C₂-атомът в инулиновата молекула има силна склонност към отдаване на електрони и затова е активната ѝ част. E_{BDE} –изчисленията показват, че връзката O₂-H е най-лесна за разкъсване понеже енергията ѝ е само 94.65 kcal•mol⁻¹, което е много по-малко от потенциала за адиабатична йонизация. Съставен е подходящ теоретичен модел за фармакологичната активност на инулина.

Suffering water of Pakistan: arsenic – A major threat

M. Parvez¹, M. Akram^{2*}

¹Department of Chemistry, Govt. Degree College for Women Lodhran, Pakistan

²Department of Environmental Sciences, COMSATS Institute of Information Technology, Vehari Pakistan

Received December 11, 2014, Revised December 22, 2015

Arsenic which is known as ‘Sinkhia’ in Pakistan is notorious as a king of poisons. It is commonly found in water, mostly originating from geological sources and pollutes the environment. It is the 12th most common element in nature. It can be found in the earths’ crust, atmosphere, rocks, soil, organisms and natural water. Studies show that 60% of the arsenic is introduced into the atmosphere by anthropogenic activities. It can combine with other elements to form inorganic and organic arsenic compounds. The important inorganic species are arsenate (As V) and arsenite (As III). Inorganic arsenic compounds may include oxygen, sodium, copper, potassium, chlorine, sulphur and iron, while arsenic combines with carbon and hydrogen to form organic arsenic in plants and animals. The three basic pathways of arsenic or sources of ingested arsenic include, water, food (fish, sea food, cereals and algae) and air (smelting, coal-fired power generation). Out of these sources long term exposure to arsenic in drinking water is the greatest threat to human health. Because of daily and widespread consumption, the presence of arsenic in drinking water has been documented as a major public health concern in many parts of the world in recent years. The worst health effects due to arsenic are directly related to the dose and duration of exposure. Dermatological effects are the characteristics of chronic or severe exposure to arsenic. The dermatological effects include Melanosis (pigmentation) and Keratosis (rough, dry skin lesions) which may be spotted or diffuse. Arsenic’s chronic exposure may result in neurological, reproductive, cardiovascular, haematological, respiratory and diabetic effects in humans. Like other parts of the world in Pakistan too, people are exposed to arsenic by different ways like by the intake of contaminated water or food, by the use of arsenic containing medicinal preparations, by inhalation or by homicidal or suicidal ingestion of arsenic compounds. Data regarding arsenic contamination in drinking water is lacking in Pakistan. It is essential that strategies are made available to tackle the health hazards caused by arsenic contaminated water. This review is an attempt to cover the available data concerning arsenic contamination, particularly in Punjab and Sindh and generally in Pakistan.

Key words: Arsenic hazards, contaminated drinking water, Arsenic in Pakistan

ARSENIC – THE HISTORY

Arsenic has been derived from the Greek word ‘Arsenikon’ which means ‘Yellow Orpiment’ [1]. It was first discovered by Albertus Magnus in 1250. Arsenic is a metalloid existing in more than 200 different forms whereby 60% are arsenates, 20% sulphosalts, sulphides and arsenite, oxides, arsenide, silicates and elemental arsenic constituting the remaining 20%, which exhibit different grades of toxicity [2]. Arsenic which is known as ‘Sinkhia’ in Pakistan is notorious as a king of poisons. It is commonly found in water, mostly originating from geological sources and pollutes the environment [3]. It is the 12th most common element in nature. It can be found in the earth crust, atmosphere, rocks, soils, organisms and natural water. Studies show that 60% of arsenic is introduced into atmosphere by anthropogenic activities. It can combine with other elements to

form inorganic and organic arsenic compounds [4]. The important inorganic species are arsenate (As V) and arsenite (As III) [1]. Inorganic arsenic compounds may include oxygen, sodium, copper, potassium, chlorine, sulphur and iron, while arsenic combines with carbon and hydrogen to form organic arsenic in plants and animals. Organic arsenic present in foods is harmless and easily removed from the body but inorganic arsenic is very toxic and can result in acute, sub-acute or chronic affects. Due to long term exposure it can be deposited in the body and once concentrated it can cause long term damage [2].

SOURCES OF ARSENIC

The three basic pathways of arsenic or sources of ingested As include:

1. Water
 2. Food (fish, sea food, cereals and algae)
 3. Air (smelting, coal-fired power generation)
- [5].

Out of these sources long term exposure of arsenic in drinking water is the greatest threat to

* To whom all correspondence should be sent:
E-mail: akramcp@gmail.com

human health. Because of daily and widespread consumption, presence of arsenic in drinking water has been documented as a major public health concern in many parts of world in recent years [6]. Similarly Bangladesh, in recent years, witnessed a mass poisoning of population because of arsenic contaminated ground water [7]. The average concentration of arsenic in sea water may be as high as 2.6 µg/L and in fresh water is nearly 0.4 µg/L [8]. An extreme level of up to 225mg/L, as in the case of drinking well water in Bangladesh can also be reached [9].

ARSENIC – A USEFUL ELEMENT

The initial use of arsenic as a medicine was for curing breathing problems and dates back to around 2500 years ago. Arsenic trioxide (As₂O₃), one of the common forms of arsenic is used in agriculture and for medical purposes such as the treatment of promyelocytic leukemia. During 1970 arsenic was mainly used as an insecticide to kill insects [2].

ARSENIC – A TOXIC, HAZARDOUS CHEMICAL

The worst health effects of arsenic are directly related to the dose and duration of exposure. The dermatological effects are characteristic of chronic or severe exposure to arsenic. The dermatological effects include Melanosis (pigmentation) and Keratosis (rough, dry skin lesions) which may be spotted or diffuse. Chronic exposure to arsenic may result in neurological, reproductive, cardiovascular, haematological, respiratory and diabetic effects in humans [10]. As arsenic is colorless, odorless and tasteless so its exposure is mostly un-noticed especially in drinking water. The International Agency of Research on Cancer (IARC) has classified arsenic as a class I human carcinogen. The skin and many types of intestinal causes like bladder, liver, kidney, prostate and lungs are also linked to arsenic ingestion [5]. A variety of substances coming from different sources can be added to the soil, water, air and the food chain. It can easily accumulate in biological samples such as nails, hair, skin, urine and blood [11]. The nails and hair are considered as the most acceptable biomarkers as arsenic can persist in these biosamples for longer periods of time [12].

DRINKING WATER CRITERIA FOR ARSENIC

The arsenic (As) in drinking water can affect human health and is considered as one of the most important environmental causes of cancer in the world. Thus, it is essential to record the levels of As

in the drinking water, its chemical composition and to establish the regulatory standards and guiding principles [13]. According to FAO (Food and Agriculture Organization) the health limit for As in groundwater is 50 µg/L, but in view of recent incidences of As poisoning in the Indian subcontinent, a decrease to 5–10 µg/L is being considered by a number of regulatory bodies throughout the world. The temporary World Health Organization (WHO) guideline for As in drinking water is also 10 µg/L. This is based on the skin cancer risk, which is much higher than the factor usually used to protect human health. However, the WHO states that the health-based drinking water guideline for As should in reality be 0.17 µg/L [14].

Nevertheless, the current drinking water guideline for As adopted by both the WHO and the US EPA is 10 µg/L. This is higher than the proposed Canadian and Australian maximum permissible concentrations of 5 and 7 µg As/L, respectively.

ARSENIC IN PAKISTAN – THE CURRENT SCENARIO

Though a significant proportion of ground water in South Asia is contaminated with arsenic, Pakistan has low levels of arsenic in the ground water as compared to Bangladesh, India and China [15]. The expected increase of population in Pakistan is from 180 million to 221 million by 2025. This represents a threat for the available fresh water supply which is drops from 5600 m³ to 1000 m³ per capita. The quality of the water supply in different cities in Pakistan is also deteriorating fast [16]. In Pakistan the screening of water for arsenic contamination started relatively late in the year 2000. It is essential that strategies are built to tackle the health hazards caused by arsenic contaminated water. A record of the data with the arsenic contamination levels in different areas of Pakistan would be helpful to address further contamination [2].

Like other parts of the world in Pakistan too, people are exposed to arsenic by different ways such as by the intake of contaminated water or food, by the use of arsenic containing medications, by inhalation or by homicidal or suicidal ingestion of arsenic compounds. But the arsenic present in the water or food does not evaporate into air [15].

In the Southern part of Sindh, Pakistan 61-73% of the population is facing chronic arsenic toxicity. Almost the same situation prevails in the Punjab province. With a huge outbreak of arsenic contamination in different villages of the Kasur district. The results of the study show that the water

supply schemes of Kasur fail to fulfill the water quality standards and due to the high concentration of arsenic and the people of Kasur face the threat of various diseases like skin cancer, skin irritation and chronic inflammation of the kidneys [16].

Ground water is the main source of drinking water in Pakistan which is pumped out by electric pumps or hand pumps [2]. Another important aspect was revealed in a study which showed, that geographically, more arsenic containing ground water and associated diseases are found along the coastline, suggesting a strong link between arsenic contamination of the ground water and presence of the Arabian Sea. It was found that for the coastal population, the toxicity of arsenic varies with the health of the people, their meal composition, their diet as well as the location of their drinking water storage tanks, overhead or underground. As arsenic is cumulative, its level can be easily determined in hair, urine, nails or skin through which it slowly leaves the body and these studies showed an increasing risk from arsenic in Pakistan [15].

Matiari a district of Sindh, Pakistan is also witnessing the presence of arsenic in the drinking water. As in other parts of Pakistan, here too the ground water is the main source of drinking water that can be extracted by motor pump or hand pump. In this area the presence of arsenic in the ground water can be related to three theories or facts:

1. Use of phosphatic fertilizer that may release arsenic due to phosphorus.
2. Oxidation of pyrite
3. Due to a reductive dissolution of metal oxy-hydroxide desorption of arsenic.

In this area phosphate fertilizers are extensively used on cotton and sugar cane crops which can be a reason for the elevated concentration of arsenic as found in many studies [17]. The emerging health problems of arsenic contaminated water are more prominent in Southern Punjab. The most affected areas are located near the Indus River like Rajan Pur, Rasul Pur in the district Rahim Yar Khan. In some rural villages the ‘Curse of God’ name is given to “Arsenicosis”, indicating the physical pain and sufferings. Again, the main cause of the arsenic contamination of the ground water is the extensive use of fertilizers as Rahim Yar Khan is an important agriculture production land [18]. Initially only eight districts out of 34 in Punjab were screened for arsenic contamination by the PCRWR (Pakistan Council of Research in Water Resources) and the UNICEF (United Nations Children's Fund) and then in 2004-05 all the remaining districts were also covered. It was found that six districts namely Bahawalpur, Layyah, Multan, Muzaffar Garh, Okara

and Sahiwal are at high risk. The water samples collected from these districts had the alarming arsenic level of 250-500µg/L (Fig. 1) while samples from 60% of the area of Punjab had an arsenic level of less than 10µg/L i.e. within safe limits.

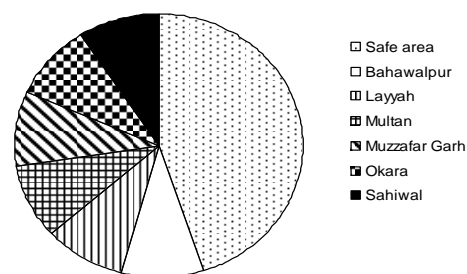


Fig.1. Districts at high risk of the arsenic level in Punjab Pakistan.

ARSENIC IN NEIGHBORING COUNTRIES

The arsenic contamination scenario has changed remarkably in Asian countries in the near past. Before the year 2000, only five major incidents of arsenic contamination of ground water were reported in Bangladesh, West Bengal, India and China among Asian countries. During 2000-2005 new sites were reported having ground water contaminated with arsenic in Mongolia, Cambodia, Myanmar, Nepal, Pakistan and Afghanistan [19]. Here the main focus is on Afghanistan, India and Bangladesh. According to the World Health Organization (WHO) in Bangladesh 42 districts have ground water contaminated with arsenic, greater than the permissible limits of 50 µg/L. Nail, hair and urine samples of the people living in the arsenic contaminated villages were analyzed and the people were found to suffer from arsenical skin lesions. The study revealed that adults can be afflicted by arsenical skin lesions if the water contained arsenic above 300µg/L; the average water intake for adults is 4L/day. Interestingly, if the nutrition status is poor then even low arsenic levels can cause arsenical skin lesions, while if the nutrition status is good even 400µg/L cannot generate the disease [20].

In Afghanistan, the Water and Sanitation group (WSG) of Afghanistan did the screening of the rural water supply schemes for arsenic in different villages with the help of UNICEF. Under this program they tested 647 wells out of which 565 were found to be arsenic free, 74 wells contained arsenic and 56 had arsenic ranging from 10-500µg/L. The predictable number of people at risk was about 500,000 [10].

In India, the Lower Ganga plain of West Bengal was initially found to be severely affected by

arsenic contamination, but later Bhojpur District, Bihar which is in the Middle Ganga plain was also found to be contaminated with arsenic. In a study conducted in these areas, water from 206 tube wells was analyzed for arsenic content and it showed that 56.8% had an arsenic concentration exceeding 50µg/L to 300µg/L. In the same study 390 adults and 160 children were medically examined and showed that 13% of the adults and 6.3% of the children had skin lesions, especially the children were more affected, which can be linked to malnutrition [21].

LESSONS LEARNT

There is a lot which can be learnt from the neighboring countries as they fight arsenic contamination. The public and private sector in Pakistan can both play a very effective role in this together so that they could educate and train the natives of affected areas in taking preventive measures against arsenic contamination.

An inspiring success story, in this regard, comes from West Bengal, India. There the Public Health Engineering (PHE) Department, with the collaboration of the UNICEF and local NGOs set up arsenic testing labs. The lab employees and trainee female members of the local population not only educate their communities about Arsenic contamination but also regularly collect samples from tube wells which are the common source of drinking and domestic-usage of water for the local people. If samples from a tube well give positive results for Arsenic, the PHE teams (trained local women) inform the local population about it and encourage them to collectively buy Activated Alumina Arsenic Filters for the affected tube well. In addition to employing local women as awareness and sampling resources, the PHE has also trained around 300 local women to work as tube well mechanics. These lady mechanics act on a self-help basis to repair tube wells and install and replace As Filters whenever needed. This makes it very cost effective for the local communities and affordable to maintain the arsenic free tube wells. This strategy has really helped the PHE in fighting Arsenic contamination on a war footing [22].

In Bangladesh, through the conducted survey of the rural communities the level of awareness was gauged and prevailed amongst the local community members as regards arsenic contamination through the water and soil. Throughout the survey it was ensured that native members of rural community were kept on board, educated and consulted to promote arsenic awareness. Gatherings amongst the village residents were organized to talk about the

As hazards and public networks such as radio and TV were engaged to disseminate information regarding the adverse long term effects of Arsenic contamination. These activities drastically improved the household perceptions about the health impacts of arsenic contamination. Furthermore, different methods and technologies were identified for fighting arsenic contamination. Rural residents were not only educated about these methodologies but were also informed about the merits and demerits of each. This infused interest into the community members and encouraged their positive involvement [23].

The methods and technologies identified to fight back Arsenic were:

1. Three Kolshi (Pitcher) Method
2. Dugwell
3. Activated Alumina Method
4. Deep Tubewell

Similar strategies and models can be adopted in the affected rural areas of Pakistan and with the support of public-private partnerships.

Apart from Pakistan's neighboring countries, lessons can be learnt from other nations which have been successfully fighting this menace too. In Cambodia private philanthropists have taken it upon themselves to discover new ways of understanding and combating arsenic effectively. To improve the lives of the local rural community in this regard, these researchers test all the existing wells for arsenic contamination. If the test comes negative, they install another tube well in the vicinity and hand it over to the local community for domestic use. In case the test results show positive signs of Arsenic, the team finances the local community to buy a locally made rainwater-harvesting unit. Thus, not only helping them meet their domestic water needs but also providing them with a water resource free of arsenic [19].

ENDING NOTE

Keeping in view of the whole scenario, the following practices should be adopted:

1. Screening of the ground water / tube wells should be undertaken on a regular basis to keep an eye on the rise of arsenic contamination.
2. Provision of low cost testing facilities or apparatus.
3. Areas which are at a high risk like the Southern Punjab and also some sites in Sindh must be monitored and the arsenic removal systems should be made using locally available materials such as water filtering mediums.
4. Social awareness is a must. It can be done through print and electronic media. Besides that

volunteers should be employed to educate the masses in the affected villages about the harmful affects. More importantly the sources/ tube wells/ wells that have been screened and found contaminated should be marked or painted as 'Red' indicating the use of water as risky and those not contaminated by arsenic should be painted as 'Green' indicating 'safe' for drinking.

5. As the ground water is more contaminated, alternative water supply options should be introduced.

6. To determine the health risks associated with and caused by arsenic, the Government Health department should take steps so that the Epidemiological survey in various areas can be carried out as early as possible.

7. The health hazards caused by arsenic like 'Arsenicosis' and all the related study materials should be included in the curricula of the medical institutes.

REFERENCES

1. S. Akhtar, A. Shoiab, *J. Animal and Plant Sci.*, **22**(3), 659 (2012).
2. K. T. Lim, M. Y. Shukor, H. Wasoh, *BioMed Research International*, Volume 2014, Article ID 503784, doi 10.1155/2014/503784, (2014).
3. M. Siepak, P. Niedzielski, K. Bierla, *Polish J. Env. Studies* **13**(6), 709 (2004).
4. I. A. Toor, N. A. Tahir, *Polish J. Env. Studies* **18**(5), 907 (2009).
5. V. D. Martinez, E. A. Vucic, D. D. Becker-Santos, L. Gil, W. L. Lam, *Journal of Toxicology*, Volume 2011, Article ID 431287, doi 10.1155/2011/431287 (2011).
6. D. N. G. Mazumder, WHO, Geneva, Switzerland, 2000, p. 655.
7. A.H. Smith, M. Goycolea, R. Haque, M. L. Biggs, *American J. Epidemiology*, **147**(7), 660 (1998).
8. W. R. Cullen, K. J. Reimer, *Chem. Rev.* **89**(4), 713 (1989).
9. M. Kato, M. Y. Kumasaka, S. Ohnuma, A. Furuta, Y. Kato, H. U. Shekhar, M. Kojima, Y. Koike, N. D. Thang, N. Ohgami, T. B. Ly, X. Jia, H. Yetti, H. Naito, G. Ichihara, I. Yajima, *PLOS ONE*, **8**, 1 (2013).
10. A. Mukherjee, M.K. Sengupta, M. A. Hossain, S. Ahamed, B. Das, B. Nayak, D. Lodh, M. M. Rahman, D. Chakraborti. *J. Health, Population and Nutrit.* **24**(2), 142 (2006).
11. <http://www.sciencedirect.com/science/article/pii/S0039914002000942>.
12. S. H. Frisbie, R. Ortega, D. M. Maynard, B. Sarkar, *Env. Health Perspect.*, **110**(11), 1147 (2002).
13. A. H. Welch, D. B. Westjohn, D. R. Helsel, R. B. Wanty, *Ground Water*, **38**(4), 589 (2000).
14. US EPA. US EPA Drinking Water Regulations and Health Advisories; EPA 822-B- 96-002, Washington, DC, 1996.
15. S. S. Ali, N. Karim, A. B. Munshi, I. Siddique, F. A. Khan, *J. water resource and protection*, **5**, 1235 (2013).
16. S. A. Ahmad, A. Gulzar, H. Rehman, Z. A. Soomro, M. Hussain, M. U. Rehman, M. A. Qadir, *World Applied Sci.*, **24**, 634 (2013).
17. A. A. Uqaili, A. H. Mughal, B. K. Maheshwari, *Int. J. Chemical and Env. Engineering*, **3**(4), 1 (2012).
18. I. ul Haq, W. Hanif, G. Hasnain, S. Durez, *Sustainable Agriculture Research*, **1**(2), 100 (2012).
19. <http://www.sciencedaily.com/releases/2009/03/090325091830.htm>.
20. U. K. Chowdhury, B. K. Biswas, T. R. Chowdhury, G. Samanta, B. K. Mandal, G. C. Basu, C. R. Chanda, D. Lodh, K. C. Saha, S. K. Mukherjee, S. Roy, S. Kabir, Q. Quamruzzaman, D. Chakraborti, *Env. Health Perspect.*, **108**, 393 (2000).
21. D. Chakraborti, S.C. Mukherjee, S. Pati, M. K. Sengupta, M. Rahman, U. K. Chowdhury, D. Lodh, C. R. Chandra, A. K. Chakraborti, G. K. Basu. *Env. Health Perspect.*, **111**, 1194 (2003).
22. http://www.wunrn.com/news/2008/12_08/12_01_08/120108_india.htm.
23. http://www.wsp.org/sites/wsp.org/files/publications/51200762900_Fighting_Arsenic_Listening_to_Rural_Communities_Dec_2002.pdf.

ВОДНИЯТ ПРОБЛЕМ НА ПАКИСТАН: АРСЕНЪТ КАТО ГЛАВНА ЗАПЛАХА

М. Парвез¹, М. Акрам^{2*}

¹Департамент по химия, Дамски правителствен колеж, Лодхран, Пакистан

²Департамент по екологични науки, Институт по информационни технологии COMSATS, Вехари, Пакистан

Постъпила на 11 декември, 2014 г., коригирана на 22 декември, 2015 г.

(Резюме)

Арсенът (известен като 'Sinkhia' в Пакистан) се определя като най-опасната отрова. Обикновено той се среща във водите, главно от геологически източници или от замърсявания на околната среда. Като химичен елемент той е на 12-то място по разпространение в природата. Намира се в земната кора, атмосферата, скалите, живите организми и в природните води. Изследванията показват, че наличието му в атмосферата е с антропогенен произход. Арсенът образува неорганични и арсен-органични съединения. Най-важните неорганични вещества са арсенатите (As^{V}) и арсенитите (As^{III}). Неорганичните арсенови съединения могат да включват кислород, натрий, мед, калий, сяра и желязо, а органичните се образуват при взаимодействието му с въглерод и водород в органичните на растенията и животните. Известни са три основни пътища за приемане на арсена: чрез водата, храната (риба, морски храни, житни култури и водорасли) и въздуха (дишане, емисии от изгаряне на въглища). Освен тях най-сериозна заплаха за човешкото здраве представлява дългосрочното наличие на арсен в питейните води. В последните години това се смята за най-голямата заплаха в много части по света. Най-лошите въздействия се дължат на дозите и продължителността на въздействието. Те се проявяват дерматологични смущения при хронично или краткотрайно излагане на въздействието на арсен. Дерматологичните ефекти включват меланози (пигментация) и кератози (втвърдяване, загрубяване на места от кожата) като петна или дифузно разпространени. Хроничното излагане на въздействие може да причини неврологични, репродуктивни, сърдечно-съдови, хематологични, дихателни и диабетични ефекти върху хората. Както и в други места по света и в Пакистан хората са изложени на въздействието на арсена по различни начини: чрез приемане на храна, медицински препарати, вдишване и пр. В Пакистан няма достатъчно данни по отношение замърсяването с арсен на питейните води. Те са необходими за изработването на стратегия за решаване на здравните проблеми, причинени от водите, замърсени с арсен. Този обзор е опит за да се разгледат достъпните данни относно замърсяването с арсен в Пунджаб и Синдх и изобщо в Пакистан.

Nano-structure zinc and cadmium azide and thiocyanate complexes: Synthesis, characterization, thermal, antimicrobial and DNA interaction

S. A. Musavi¹, M. Montazerzohori^{1*}, M. Nasr-Esfahani¹, R. Naghiha², M. Montazer Zohour³

¹Department of Chemistry, Yasouj University, Yasouj 75918-74831, Iran.

²Department of Animal Sciences, Faculty of Agriculture, Yasouj University, Yasouj, Iran.

³Genetics of Non-Communicable Disease Research Center, Zahedan University of Medical Sciences, Zahedan, Iran

Received January 2, 2015, Revised July 3, 2015

Three nano-structure azide and thiocyanate zinc and cadmium complexes of a Schiff base ligand were prepared and characterized by conductivity measurements, elemental analysis, IR, UV–Visible, ¹H and ¹³C NMR Spectroscopy and thermo-gravimetric studies. Detectable changes in the spectral data suggested coordination of ligand to zinc and cadmium ions. The proposed formula structure of the complexes was found to be MLX₂. Nano-size structure of the complexes was confirmed by transmission electron microscopy (TEM). The average particle sizes of the complexes were found to be in the range of 25.32 - 85.11 nm. Thermal analyses of the complexes was carried out. The thermal curves showed that zinc thiocyanate was decomposed via six thermal steps while cadmium azide and thiocyanate complexes were thermally degraded via three steps. Moreover some activation thermodynamic parameters such as the activation energy, enthalpy, entropy and Gibbs-free energy of activation and the Arrhenius constant were calculated based on TG/DTG curves. The antimicrobial behavior with respect to bacteria of *Escherichia coli*, *Pseudomonas aeruginosa*, *Staphylococcus aureus*, *Bacillus subtilis* and a fungus (*Candida albicans*) was investigated. ZnL(NCS)₂ was found to have more antifungal activity against *Candida albicans* than others. Finally, the interaction of the complexes with DNA (pMalC₂X DNA of *Escherichia coli*) was checked to investigate their cleavage potential.

Keywords: Schiff base, antimicrobial, thermal, transmission electron microscopy, nano-structure.

INTRODUCTION

Metal complexes including a central metal atom or ion is surrounded by a series of ligands and play an important role from an inorganic chemistry point of view especially for elements of the d-block. Recently various organic ligands containing N, O and S donor atoms have been used for preparation of metal complexes. Schiff base ligands have an important role in the development of the field of coordination chemistry [1-7]. Such ligands and their complexes are of interest due to their catalytic activity in some reactions such as epoxidation, carbonylation, oxidation and carbon-carbon coupling reactions. The other reason of importance of these types of compounds is their biological activity in containing anti-inflammatory activity, antibiotic activity, antimicrobial activity and antitumor activity. The DNA binding or cleavage interaction of Schiff base complexes is the other major application of these compounds in the field of biochemistry [8-19]. Nowadays the synthesis of nanostructure coordination compounds is of interest for many researchers. This interest may be due to specific properties as compared with bulk compounds. The notable characteristics of nano-

structure compounds originate from their large surface area with respect to bulk materials. Various methods are used for the preparation of nano-structure compounds and synthesis under ultrasonic conditions is one of the common techniques.

As part of our continued work in the synthesis of metal complexes of Schiff base ligands [20-23], herein we report on the synthesis and characterization of three nano structure zinc and cadmium azide and thiocyanate complexes of a Schiff base ligand (L) with the general formula MLX₂ whereas X= SCN⁻ and N₃⁻. These compounds have been characterized by physical and spectral data including elemental analysis, conductance data, FT-IR, UV-Vis, ¹H and ¹³C-NMR spectroscopy. TEM images were used to confirm the nano-size structure of all complexes. Furthermore, the DNA interaction, antimicrobial activities and thermal behavior of the complexes were investigated.

EXPERIMENTAL MATERIALS AND METHODS

All solvents used in the synthesis and analysis of N'-(2-Amino-ethyl)-ethane-1,2-diamine and 4-nitrobenzaldehyde were purchased from Aldrich and Merck and used without any further purification. In biological tests, Nutrient agar (Merck, Germany)

* To whom all correspondence should be sent:
E-mail: mmzohory@yahoo.com

was used to prepare nutrient plates while Mueller Hinton broth (Scharlab) was used for the liquid culture media. The *Escherichia coli* (ATCC 25922), *Pseudomonas aeruginosa* (ATCC 9027), *Staphylococcus aureus* (ATCC 6538) and *Bacillus subtilis* (ATCC 6633) were used for antibacterial and *Candida albicans* for the antifungal investigations. The FT-IR spectra were recorded on the JASCO-680 model in the range of 400-4000 cm^{-1} using KBr discs. Elemental analyses data (C, H and N) were obtained by a CHNS-932 (leco) elemental analyzer. UV-Visible spectra were recorded using a JASCO-V570 spectrometer of DMF solution in the 200-800 nm range. ^1H and ^{13}C NMR spectra were recorded using a Bruker DPX FT-NMR spectrometer at 400 MHz in DMSO-d_6 using TMS as the internal standard. Molar conductance data of the ligand and their metal complexes were measured in DMF (1.0×10^{-3} M) at room temperature using a SelectaLab ECW 312 microprocessor conductivity meter. The ultrasonic instrument used in the synthesis process was an ultrasonic bath (Tecno-Gasz SPA, Parma, Italy) with a frequency of 40 kHz and 130 W. The melting points ($^{\circ}\text{C}$) of the complexes were recorded on a Kruss instrument. The TG/DTG curves were obtained from a Diamond TGA PerkinElmer 60 Hz. The transmission electron microscopy (TEM) images were recorded on a Zeiss EM900 transmission electron microscope with an accelerating voltage of 80 kV.

Synthesis of Schiff base ligand

The Schiff base of (E)-N-(4-nitrobenzylidene)-2-(2-(4-nitrophenyl)imidazolidine-1-yl)ethanamine(L) was synthesized by a condensation reaction between 2 mmol of 4-nitro-benzaldehyde and 1 mmol of N'-(2-Amino-ethyl)-ethane-1,2-diamine in 30 mL methanolic solution according to our previous report²³. After 2h, the ligand was filtered as cream precipitate and washed twice with cooled methanol and then dried on the vacuum apparatus. The characteristic data of IR, UV-Visible, ^1H NMR and ^{13}C NMR have been tabulated as table 1, 2 and 3.

Preparation of nano-structure MLX_2 complexes ($M = \text{Zn(II)}$ and Cd(II) and $X = \text{SCN}^-$ and N_3^-)

At first, ethanolic solution of zinc and cadmium thiocyanate or azide were prepared by a reaction between zinc or cadmium nitrate (1 mmol) and potassium thiocyanate or sodium azide (2 mmol) in 20 mL ethanol and then filtration. For preparation of the nano-structure complexes, 15 mL of fresh ethanolic solution of MX_2 was placed in an

ultrasonic condition at a temperature of 60°C . Into this solution, 15 mL of a methanolic solution of the Schiff base ligand was added drop wise in a 1:1 molar ratio. After 1 h, the precipitate was filtered off, washed with cooled ethanol and then dried in the vacuum apparatus.

Antimicrobial activity assay procedure

To investigate the activity of the titled compounds as antibacterial and antifungal agents *in vitro* four bacteria and a fungus species were selected. The disk diffusion technique was employed for biological studies on *Escherichia coli* and *Pseudomonas aeruginosa* as Gram negative; *Staphylococcus aureus* and *Bacillus subtilis* as Gram positive and *Candida albicans* as a fungus. The stock solution of each compound was prepared in DMSO solvent ($500 \mu\text{g/mL}$). Muller Hinton broth was used for preparation of the basal media for the organisms. For preparation of solid media by the disk diffusion method, 15 mL of sterilized nutrient agar (NA) and Sabouraud dextrose agar (SDA) for antibacterial and antifungal studies respectively were poured and solidified into each petri plate. The suspension of the test microorganisms (0.1 mL) was swabbed by a sterile glass spreader on to individual media plates. A sterile paper disk (6mm in diameter) was saturated with a solution of the test compound and placed over the media surface and the petri dishes were incubated at 37°C . The diameter of the inhibition zone was measured after incubation for 24 h. The minimum inhibitory concentration (MIC) values of the ligand and its complexes were also determined. The MIC value is defined as the lowest concentration of compound that prevents the visible growth of bacteria after the incubation period. In the MIC method, test solutions of each compound in DMSO were prepared by serially diluting the stock solution ($500 \mu\text{g/mL}$). A set of tubes containing Mueller-Hinton broth medium, different concentration of compounds and inoculums of the microorganism (18h old culture) were incubated at 37°C for 24 hours to determine the MIC values.

DNA cleavage experiments

Investigation of the DNA cleavage activity of the ligand and its complexes were performed by agarose gel electrophoresis using plasmid DNA of supercoiled pMalC₂X of *E. Coli*. Plasmid DNA was extracted using the DNA Mini Prep Extraction Kit (BIONEER, Korea) according to the manufacturer's instructions and the plasmid were kept at -40°C for the following tests. For the extraction of plasmid DNA, the LB protocol [Pepton water: 10 g/L; Yeast

extract: 5 g/L; NaCl: 10 g/L and/or Agar: 1.5%] were used for culturing TG1 strain of *E. coli* (carried pMalC₂X DNA). 30 mL of LB broth medium was prepared and autoclaved for 20 min. at 121°C under a pressure of 15 lb. After cooling, 50 µL of Ampiciline (100ug/ul for 1 liter) and TG1 strain were inoculated and incubated at 37°C for 24 h. After cooling, the seed culture, 50 µL of Ampiciline was added and incubated for 24 h at 37 °C. The fresh bacterial culture was centrifuged to obtain the Pellet. The agarose gel for electrophoresis was prepared by dissolving 500 mg of agarose in 50 mL of TAE buffer (40mM Tris base, pH 8.0; 40mM Acetic acid; 1mM EDTA) under a boiling condition. When the temperature of the solution reached 55 °C, 10 µL of ethidium bromide was added and poured into the gel cassette, fitted with a comb and allowed to solidify. After solidification, the comb was carefully removed. The solid gel was placed in the electrophoresis chamber flooded with a TBE buffer. The gel electrophoresis experiment was performed by incubation of the samples containing 4 µL of 5 mg per mL of each compound in DMSO and 4 µL of plasmid DNA for 2 h at 37 °C. After incubation, the samples were mixed with bromophenol blue dye and along with Plasmid DNA alone, the mixture of DNA and H₂O₂ and a DNA ladder were carefully loaded into wells of the instrument. Electrophoresis was performed at a constant 100 V of electricity for about 30 min. The resulting bands of electrophoresis were visualized by UV light and then photographed.

RESULTS AND DISCUSSION

The nano-structure complexes with the general formula of [MLX₂] were synthesized by reaction between the Schiff base ligand (E)-N-(4-nitrobenzylidene)-2-(2-(4-nitrophenyl)imidazolidin-1-yl) ethanamine (L) and thiocyanate and azid salts of zinc and cadmium metals under ultrasonic conditions. The Ligand and its complexes were obtained as stable powders at room temperature. The titled compounds were characterized by physical (elemental analysis, molar conductance values) and spectral (FT-IR, ¹H and ¹³C NMR and UV-Visible) data. The molar conductivity values of the complexes were obtained in 10⁻³ M DMF solutions. Low molar conductivities of them in the range 5.22-13.97 cm² Ω⁻¹M⁻¹ indicate that the complexes are non-electrolytes and stable against dissociation in DMF (Table 1) [24]. The decomposition temperatures of the titled complexes are in the range of 143-185°C. Figure 1 illustrates the suggested structures of the free ligand and its

complexes. The experimental data are in good agreement with the suggested structures for them. The TEM images of the complexes (Figure 2) well approve their nano- structure character. TEM images analyses suggested average particle sizes of 85.11, 25.32 and 39.78 nm for zinc thiocyanate, zinc azide and cadmium thiocyanate complexes respectively.

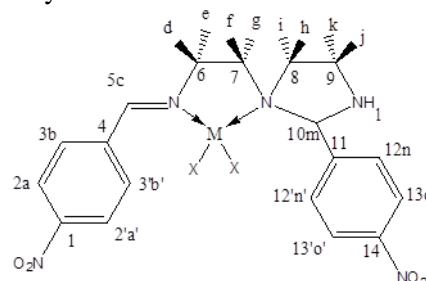


Fig. 1. Proposed structure for the azide and thiocyanate complexes with the general formula of MLX₂ wherein M= zinc(II), cadmium(II) and X= SCN⁻ and N₃⁻.

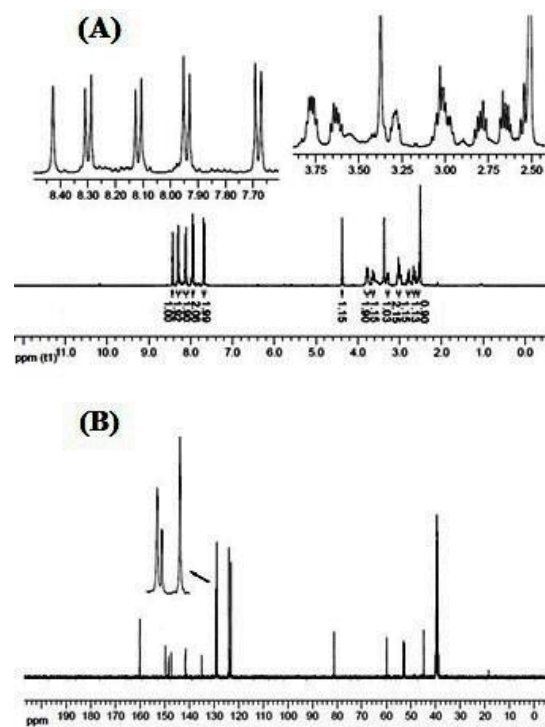


Fig. 2. ¹H NMR (A) and ¹³C NMR (B) of ZnL(NCS)₂ respectively.

Infrared and UV-Visible spectra

The characteristic IR spectral data of the complexes as compared with the ligands have been listed in Table 2. The IR spectrum of the Schiff base ligand exhibited a sharp peak at 1645 cm⁻¹ assigned to the vibration frequency of the azomethine group [25]. Appearance of the C=N vibration frequency and absence of the absorption bands of the starting materials including aldehyde

and amine at 1703 and 3100–3300 cm^{-1} provides evidence to successfully synthesis of the Schiff base ligand. The azomethine signal in the infrared spectra of all complexes shifted to the lower frequencies by 6-9 cm^{-1} toward lower energies [26-28]. The red shift of the azomethine peak indicates that the imine nitrogen atom is well bound to the central metal ions. This red shift may be due to π -back bonding of metal to ligand orbitals after coordination that reduces the bond order of the iminic bond leading to vibration at lower energies. The ligand spectrum shows a stretching vibration frequency of N-H at 3210 cm^{-1} as a broad peak due to widely internal hydrogen bonding which is observed in the complexes spectra at 3216-3268 cm^{-1} as a medium intensity band. This change in the shape and intensity of the vibration frequency of the N-H peak in the spectra is considered as confirmation of the coordination of ligand to metal ions [29]. The absorption peaks at (3101 and 3071), (2941 and 2886) and 2848 cm^{-1} are assigned to the stretching frequencies of aromatic, aliphatic and iminic CH bonds respectively. After coordination, these peaks shifted to the higher of the lower wave numbers. The stretching vibration bands of asymmetric (ν_{asym}) and symmetric (ν_{sym}) $-\text{NO}_2$ groups were observed at 1518 and 1346 cm^{-1} [30] respectively. These strong peaks shifted to another position after coordination. In the spectra of $\text{ZnL}(\text{SCN})_2$ and $\text{ZnL}(\text{N}_3)_2$, the absorption peaks at 2077 and (2088 and 2063) were assigned to the coordination of SCN^- (N-coordination) and N_3^- to zinc ions [30-34]. In the IR spectra of the cadmium thiocyanate complex, the appearance of two absorption peaks at 2089 and 2066 cm^{-1} for coordinated thiocyanate may be assigned to coordinated thiocyanate in $[\text{CdL}(\text{NCS})_2]$. Finally, the appearance of some weak absorption peaks in the range 482-495 cm^{-1} in the complexes spectra were

assigned to the M-N bond that is considered as another evidence for the synthesis of the complexes [35-37].

Electronic spectra of the ligand and its complexes were recorded in DMF at room temperature and their spectral data including the λ_{max} values are listed in Table 2. A band at 278 nm attributed to the π - π^* transition (iminic and benzene ring) is observed in the electronic spectra of the ligand and after formation of the complexes, this band shows a blue shift to a lower value of wavelength at 267 nm suggesting the coordination of the iminic nitrogen to the metal ions [19-23]. Other possible transitions such as the d-d transition and the metal to ligand charge transfers (MLCT) or ligand to metal charge transfers (LMCT) were not observed probably due to its overlap with the π - π^* transitions of the ligand.

¹H and ¹³C NMR spectra

¹H and ¹³C NMR spectra were recorded at 400 MHz, using DMSO-d_6 solvent for the complexes and CDCl_3 solvent for the ligand. The signal positions observed in the complexes spectra as compared with the ligand are given in Table 3. The ¹H and ¹³C NMR of the ligand and $\text{ZnL}(\text{NCS})_2$ as typical spectra are exhibited in Figure 3. The assignments of ¹H and ¹³C NMR spectral data based on Figure 1, confirm the structures of the ligand and its complexes. In the ¹H NMR spectrum of the ligand, the resonance of H_m appeared at 4.40 ppm shifted to 4.37-4.38 ppm in the complexes spectra. In the ¹³C NMR spectrum of the ligand, the signal at 82.37 ppm is attributed to the C_{10} of the imidazolidine ring [38] that is blue shifted to 81.24-81.38 ppm in the azide and thiocyanate complexes spectra proving the coordination of the ligand with a retained structure.

Table 1. Analytical and physical data of the Schiff base ligand (L) and its azide and thiocyanate complexes.

Run	Compound	Color	Melting point (dec.)	Yield (%)	Found (Calcd.) (%)			Δ_M ($\text{cm}^2 \Omega^{-1} \text{M}^{-1}$)
					C	N	H	
1	Ligand	cream	108	65	58.3 (58.53)	18.8 (18.96)	5.1 (5.18)	5.22
2	$\text{ZnL}(\text{NCS})_2$	cream	185	78	43.5 (43.60)	17.7 (17.85)	3.40 (3.56)	13.80
3	$\text{ZnL}(\text{N}_3)_2$	cream	143	72	41.5 (41.67)	29.6 (29.70)	3.8 (3.69)	6.20
4	$\text{CdL}(\text{NCS})_2$	cream	153	80	40.2 (40.17)	16.6 (16.40)	3.4(3.20)	13.97

Table 2. Vibrational (cm^{-1}) and electronic (nm) spectral data of the Schiff base (L) and its complexes.

Compound	ν_{NH}	$\nu_{\text{CH}_{\text{arom.}}}$	$\nu_{\text{CH}_{\text{aliph}}}$	$\nu_{\text{CH}_{\text{imin}}}$	$\nu_{\text{C=N}}$	N ($-\text{NO}_2$)	N ($-\text{SCN}$)	$\nu(-\text{N}_3)$	$\nu_{\text{M-N}}$	λ_{max}
$\text{ZnL}(\text{NCS})_2$	3259	3108, 3070	2929, 2881	2854	1638	1523, 1346	2077	-	482	267
$\text{ZnL}(\text{N}_3)_2$	3216	3108, 3062	2918	2879	1639	1525, 1342	-	2088, 2063	495	267
$\text{CdL}(\text{NCS})_2$	3268	30104, 3064	2929	2871	1636	1528, 1344	2089, 2066	-	484	267

In the ^1H NMR spectrum of the ligand, the azomethine proton (H_c) is affected by complexation so that it shifts to the weaker fields from 8.33 to 8.42-8.43 ppm as a singlet indicating coordination of azomethine nitrogen to metal ions. The signals of aromatic hydrogens of free ligand were observed in the 7.69-8.30 ppm that they were found at 7.68-8.31 ppm in the azide and thiocyanate complexes spectra.

$\text{H}_{a, a'}$ protons were found as a doublet signal at 8.30 ppm due to coupling with $\text{H}_{b, b'}$ appearing at 7.88 ppm as doublet signals. In the complexes spectra, these signals appeared as doublets at similar chemical shifts or at up/downfield positions. $\text{H}_{o, o'}$ protons were observed as a doublet peak at 8.18 ppm due to coupling with $\text{H}_{n, n'}$ and appeared at 7.69 ppm. Shifts of these signals to up or downfield regions are another evidence for the coordination of the ligand. Also, the signals of ethylenic hydrogens were seen in the 2.61-3.76 ppm range as eight individual multiple peaks due to the formation of a imidazolidine ring in the structure of the free ligand while these signals are shown as several multiple signals in the range of 2.53-3.78 ppm in the complexes. The signal of H_{NH} appeared as a multiple in the range of 2.6-2.78 ppm in the spectrum of the ligand that shifts to 2.99-3.02 ppm in the complexes spectra. In the ^{13}C NMR spectrum of the ligand, the iminic carbon resonance was observed at 159.59 ppm shifts to 159.98-160.02 ppm in the complexes spectra. This difference in the location of carbon resonance for the complexes with respect to the free ligand suggests good ligation to the central metal. The resonances of the aromatic carbons appeared at 148.56 for C1 and C14, 141.44 ppm for C4 and 11, 129.98 for C12, 129.81 ppm for C12', 128.70 ppm for C3 and 3', 123.98 for C2 and 2' and 123.72 ppm for C13 and 13'.

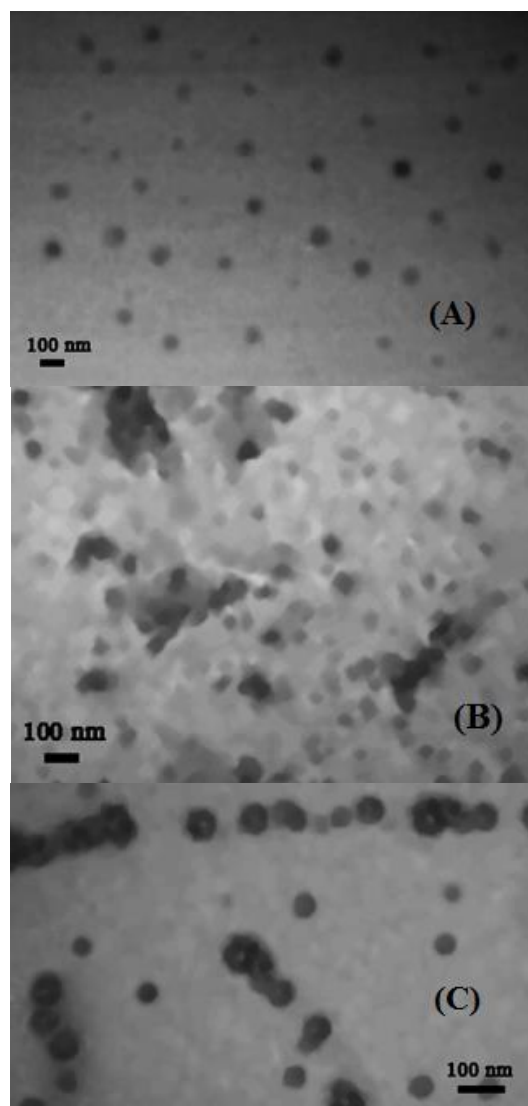


Fig. 3. TEM Images of (A) $\text{ZnL}(\text{NCS})_2$, (B) $\text{ZnL}(\text{N}_3)_2$ and (C) $\text{CdL}(\text{NCS})_2$.

Table 3. ^1H NMR and ^{13}C NMR chemical shifts of ligand and its zinc(II), cadmium(II) complexes in ppm.

Compounds		Proposed assignment of the protons and carbons
$\text{ZnL}(\text{NCS})_2$	^1H -NMR	8.42(s, 1H), 8.31(d, 2H, J= 8.80 Hz), 8.11(d, 2H, J= 8.80 Hz), 7.94(d, 2H, J= 8.80 Hz), 7.68(d, 2H, J= 8.80 Hz), 4.37(s, 1H), 3.77(m, 2H), 3.63(m, 1H), 3.29(m, 1H), 3.02(m, 2H), 2.79(m, 1H), 2.65(m, 1H), 2.54(m, 1H).
	^{13}C -NMR	160.02, 149.18, 148.44, 147.14, 141.59, 134.86, 129.19, 129.10, 128.77, 123.87, 123.09, 81.24, 59.88, 53.09, 52.70, 44.76.
$\text{ZnL}(\text{N}_3)_2$	^1H -NMR	8.43(s, 1H), 8.30(d, 2H, J= 8.80 Hz), 8.11(d, 2H, J= 8.80 Hz), 7.95(d, 2H, J= 8.80 Hz), 7.68(d, 2H, J= 8.40 Hz), 4.38(s, 1H), 3.78(m, 2H), 3.64(m, 1H), 3.26(m, 1H), 3.00(t, 2H), 2.80(m, 1H), 2.66(m, 1H), 2.53(m, 1H).
	^{13}C -NMR	160.01, 149.87, 148.44, 147.02, 141.60, 129.28, 129.09, 128.78, 123.88, 123.06, 81.32, 59.99, 53.28, 52.94, 44.73.
$\text{CdL}(\text{NCS})_2$	^1H -NMR	8.43(s, 1H), 8.31(d, 2H, J= 8.80 Hz), 8.10(d, 2H, J= 8.80 Hz), 7.94(d, 2H, J= 9.20 Hz), 7.68(d, 2H, J= 8.40 Hz), 4.38(s, 1H), 3.76(m, 2H), 3.64(m, 1H), 3.24(m, 1H), 2.99(t, 2H), 2.80(m, 1H), 2.66(m, 1H), 2.53(m, 1H).
	^{13}C -NMR	159.98, 150.34, 148.44, 146.94, 141.60, 132.47, 129.04, 128.85, 128.77, 123.88, 123.03, 81.38, 60.05, 53.39, 53.09, 44.73.

After formation of complexes, these signals are shifted to down or up fields and exhibited at 149.18-150.34(C1), 148.44(C14), 146.94-147.14(C4), 141.59-141.60(C11), 129.04-129.28(C12), 128.85-129.10(C12'), 128.77-128.78(C3 and 3'), 123.87-123.88(C2 and 2') and 123.03-123.09(C13 and 13'). The ligand spectrum showed four individual peaks for C8, C6, C9 and C7 as aliphatic carbons at 61.10, 53.51, 53.46 and 45.30 ppm respectively. The coordination of the ligand with the metal ions leads to changes in their chemical shifts so that they appeared at 57.60-60.05 ppm for C8, 53.09-53.28 ppm for C6, 52.70-53.09 ppm for C9 and 44.60-44.73 ppm for C7 in the spectra of all complexes. In the spectrum of $ZnL(NCS)_2$ and $[CdL(SCN)_2]$, the signal of the carbon resonance of $-SCN$ anions appeared at 134.86 and 132.47 ppm respectively [19-23]. Finally it is obvious that the resultant data obtained from the 1H and ^{13}C NMR spectra well confirms the suggested structure of the complexes as shown in Figure 1.

Thermal analysis

Thermogravimetric and differential thermogravimetric analysis (TG/DTG) of the complexes were studied under an N_2 atmosphere from room temperature to 900 °C (Fig. 4). Thermal studies of the solid complexes were performed to show more insight into the structure of the reported complexes. The thermal analyses of the data including the temperature range, the mass loss (%) and the thermodynamic activation parameters of the decomposition steps of the complexes are listed in Table 4. The decomposition of $ZnL(NCS)_2$ occurred in six successive thermal steps and in the final step, the percentage of mass loss was 69.78%. It seems that the thiocyanate groups and the organic segment are eliminated respectively. A limited amount of zinc-organic compound is left at the final step. Major mass loss of $ZnL(NCS)_2$ occurred at 510-680 °C with a weight loss of 41.93%. The TG plots of $ZnL(N_3)_2$ and $CdL(NCS)_2$ showed three successive thermal degradation steps and the total mass loss(%) at the end of the thermal decomposition was 82.03% and 61.47% and the major decomposition occurred at the third thermal step 390-900 °C and 430-600 °C respectively. Likewise in these complexes, azide and thiocyanate as well as organic parts are the major lost segments such that zinc and cadmium metals are major residuals at the final step. The thermodynamic activation parameters of the decomposition processes of the complexes including the Arrhenius constant (A), the activation energy (E^*), enthalpy (ΔH^*), entropy (ΔS^*) and Gibbs free energy of

decomposition (ΔG^*) were evaluated based on plots using the Coats–Redfern relation [39-41].

The Coats-Redfern equation for the first order process is in the form:

$$\log[\log\{W_f/(W_f-W)\}/T^2]=\log [AR/\Theta E^*(1-2RT/E^*)]-(E^*/2.303RT) \quad (\text{Eq. 1})$$

Where W_f is the mass loss at the completion of the reaction, W is the mass loss up to temperature T ; ($W_f=W_f-W$), R is the gas constant, E^* is the activation energy in $J\ mol^{-1}$, Θ is the heating rate. Since $1-2RT/E^* \approx 1$, a plot vs. $1/T$ was drawn and E^* was calculated from the slope and the A (Arrhenius constant) was found from the intercept. Fig. 5 shows the plots of three steps of decomposition for $CdL(NCS)_2$.

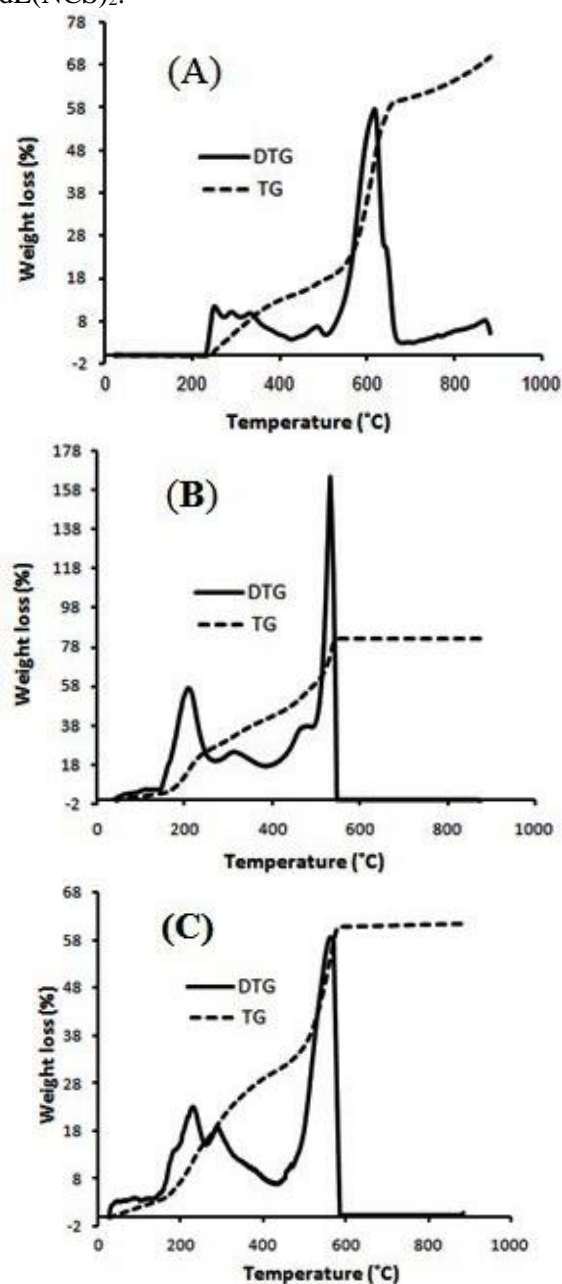


Fig. 4. TG diagrams of the $ZnL(SCN)_2$ complex(A), $ZnL(N_3)_2$ complex(B) and $CdL(NCS)_2$ complex (C).

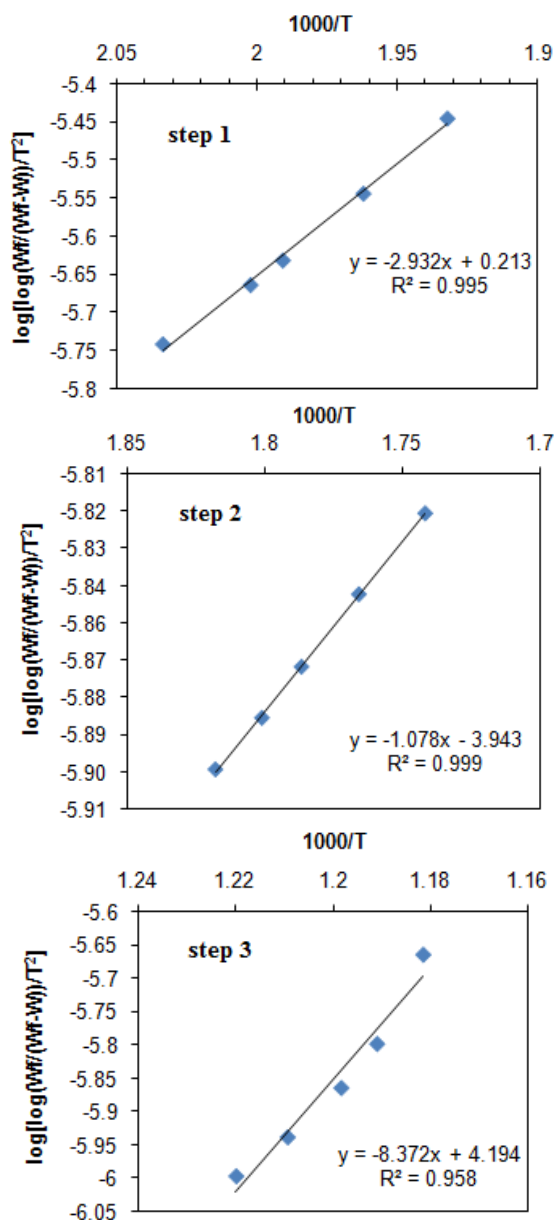


Fig. 5. Coats-Redfern plots of the three decomposition steps of CdL(NCS)₂ complex.

The equations used to calculate the activation entropy ΔS^* , the activation enthalpy ΔH^* and the free energy of activation ΔG^* are:

$$\Delta S^* = 2.303[\log(Ah/kT)R] \quad (\text{Eq. 2})$$

$$\Delta H^* = E^* - RT \quad (\text{Eq. 3})$$

$$\Delta G^* = \Delta H^* - T\Delta S^* \quad (\text{Eq. 4})$$

where k and h are the Boltzmann and Planck constants respectively.

The resultant data listed in table 4 is found in the range 20.64-422.96 k J mol⁻¹ for energies (E^*) at different steps of thermal decomposition indicating relative thermal stability for the complexes. Except for two steps, the entropy of activation (ΔS^*) is negative and the value of ΔS^* is recorded in the range -271-509 kJ mol⁻¹. As reported in the literature, the negative values suggest an associated

mechanism at the rate determining step of thermal degradation. On the other hand the negative values may be due to a lower rate of thermal decomposition than the normal decomposition process [39, 40]. The values of ΔH^* and ΔG^* are evaluated in the range 16.055 - 418.591 kJ.mol⁻¹ and 138 - 330 kJ.mol⁻¹ respectively. The positive values for ΔH^* and ΔG^* at all steps indicate the endothermic character of thermal decomposition for these compounds.

Antibacterial and antifungal activity

The biological activities of the complexes as compared with the ligand were investigated by two methods containing disk diffusion and minimum inhibitory concentration (MIC) techniques against *Escherichia coli* and *Pseudomonas aeruginosa* as Gram negative; *Staphylococcus aureus* and *Bacillus subtilis* as Gram positive and *Candida albicans* as a fungus. The experimental results have been tabulated as Table 5. All tested compounds showed a notable antimicrobial activity. Comparing the biological activity of the Schiff base ligand with respect to its complexes showed that metal complexes potentially have more antibacterial and anti-fungal activity against the microorganisms as mentioned above. In general, the metal complexes are more active than the ligands because metal complexes may serve as a vehicle for activation of the ligand as the principle cytotoxic species [42]. According to Overton's concept and Tweedy's chelation theory [43, 44], the overlap of the ligand orbitals and metal ion valence orbitals leads to π -electron delocalization in the ligand and considerably reduces the polarity of the metal ion and therefore increases the lipophilic character of the compound that causes more diffusion into the cell membranes. In this way, the growth of bacteria and/or fungi can be disturbed by blocking the metal coordination sites of the bacteria and/or fungi enzymes. The MIC method was also carried out for all the compounds using 15.63, 31.25, 62.50, 125, 250, 500 $\mu\text{g/mL}$ concentrations. The MIC value of the ligand for all bacteria is 500 $\mu\text{g/mL}$. After coordination of the ligand to metal ions, the most efficient value was found for CdL(NCS)₂(125 $\mu\text{g/mL}$) with respect to *Staphylococcus aureus* as Gram positive bacteria. In the disk diffusion method, the diameter zone of the inhibitory effect was recorded in millimeters. For all complexes against all microorganisms, this value was more than the parent Schiff base ligand.

Table 4. Thermal analysis data including the temperature range, mass loss(%) and thermodynamic activation parameters of the decomposition steps of the complexes

Compound	Temperature step(°C)	~Mass loss(%)	Total Mass massloss(%)	E*(kJmol ⁻¹)	A(s ⁻¹)	ΔS*(kJmol ⁻¹)	ΔH*(kJmol ⁻¹)	ΔG*(kJmol ⁻¹)
ZnL(NCS) ₂	230-275	2.92	69.78	422.96	3.96×10 ³⁹	5.09×10 ²	418.591	1.51×10 ²
	275-315	3.47		102.265	1.07×10 ⁷	-1.16×10 ²	97.577	1.63×10 ²
	315-430	7.47		46.413	1.25×10 ¹	-2.30×10 ²	41.368	1.81×10 ²
	430-510	3.87		89.532	6.33×10 ³	-1.80×10 ²	83.214	2.20×10 ²
	510-680	41.93		167.729	2.00×10 ⁷	-1.14×10 ²	160.318	2.62×10 ²
	680-900	10.12		228.425	2.01×10 ⁸	-9.72×10 ¹	218.921	3.30×10 ²
ZnL(N ₃) ₂	120-270	27.07	82.03	60.477	7.61×10 ³	-1.75×10 ²	56.520	1.39×10 ²
	270-385	13.85		20.641	1.03×10 ⁻¹	-2.69×10 ²	16.055	1.64×10 ²
	390-900	41.11		226.319	4.06×10 ¹²	-1.03×10 ¹	220.748	2.28×10 ²
CdL(NCS) ₂	120-260	15.87	61.47	56.139	2.14×10 ³	-1.85×10 ²	52.192	1.40×10 ²
	260-430	14.77		20.641	8.49×10 ⁻²	-2.71×10 ²	16.055	1.65×10 ²
	430-600	30.19		160.300	5.40×10 ⁷	-1.04×10 ²	154.728	2.24×10 ²

Table 5.Antibacterial and antifungal activities of 25 µg/disks of the Schiff based ligand and its complexes based on the zone of inhibition, the growth of microorganisms(mm) and MIC(µg/mL).

Compound	Gram negative bacteria				Gram positive bacteria				Candida albicans
	Escherichia coli		Pseudomonas aereuginosa		Bacillus subtilis		Staphylococcus aureus		
	MIC (µg/mL)	zone (mm)	MIC (µg/mL)	zone (mm)	MIC (µg/mL)	zone (mm)	MIC (µg/mL)	zone (mm)	
Ligand	500	11.50	500	6.80	500	14.46	500	10.00	17.40
ZnL(NCS) ₂	250	15.50	500	8.44	250	17.00	250	12.00	24.80
ZnL(N ₃) ₂	500	12.20	500	7.90	500	15.00	500	11.50	21.80
CdL(NCS) ₂	250	15.20	500	8.60	500	14.80	125	16.20	18.50

As seen in Table 5, all compounds have the lowest inhibition effect with respect to *Pseudomonas aereuginosa* among tested bacteria.

The bioassay data for ligands showed maximum and minimum efficiency with respect to *Bacillus subtilis* with inhibition zone of 14.46 mm and *Pseudomonas aereuginosa* with inhibition zone of 6.80 mm respectively. A comparable investigation between all the complexes indicated that the growth of bacteria is more inhibited by ZnL(NCS)₂ for *Escherichia coli* and *Bacillus subtilis*. CdL(NCS)₂ efficiently stopped the growth of *Pseudomonas aereuginosa* and *Staphylococcus aureus*. The growth inhibition effects of the ligand and its complexes with respect to *Candida albicans*, as a fungus, were studied and ZnL(NCS)₂ with inhibition zone of 24.80 mm was selected as an efficient antifungal as compared with the free ligand.

DNA cleavage efficiency

The DNA cleavage ability of the complexes as compared with the free ligand was monitored by the agarose gel electrophoresis method with respect to pMalC₂X DNA of *E. Coli*. Three forms of DNA

containing a supercoiled form (Form I), open circular (nicked) form (Form II) and the linear form (Form III) were separated based on the difference in the rate of migration by electrophoresis. When the original supercoiled form (Form I) of plasmid DNA is nicked, an open circular relaxed form (Form II) will be exist in the system and the linear form (Form III) can be found upon further cleavage. The compact Form I migrates relatively faster while the nicked Form II migrates slowly, and the linearized form (Form III) migrates between Forms I and II. The nuclease activity of the complexes as compared with the free ligand have been assessed by their ability to convert supercoiled pMalC₂X DNA from Form I to Form II and Form III. All the metal complexes and free ligands were able to convert supercoiled DNA into an open circular and linear form of DNA. These changes were illustrated in gel electrophoresis by the intensity of the bands. The results of DNA cleavage are given in Figure 5. In this figure L, X and C are attributed to the ladder, mixture of DNA, H₂O₂ and control DNA respectively. The lanes 1 to 4 are attributed to mixtures of DNA with a ligand,

ZnL(NCS)₂, ZnL(N₃)₂ and CdL(NCS)₂ respectively.

The effect of the compounds in cleavage of the supercoiled DNA to the form II and III is determined by diminishing in intensity of the band of the supercoiled pMalC₂X DNA. It seems that ZnL(NCS)₂ and CdL(NCS)₂ are more efficient for the cleavage of the supercoiled form to the linear form of DNA as compared with the other tested compounds. The DNA cleavage ability of the complexes may depend on the binding of the DNA molecule to the metal complexes. However, the nature of the reactive intermediates involved in the DNA cleavage by the complexes is not clear. According to the experimental data from the DNA cleavage studies, it may be correct to say that the cleavage of genome is responsible for the death of some of the studied microorganisms [45].

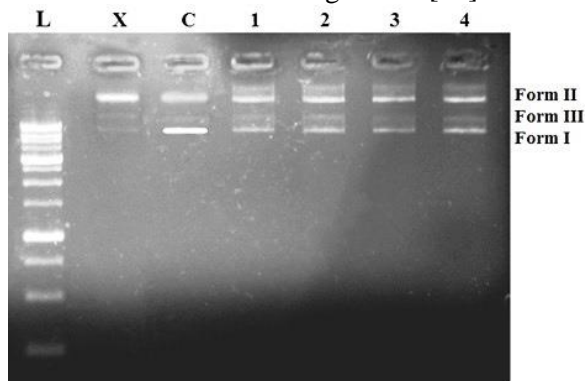


Fig. 6. Gel electrophoresis diagram for DNA cleavage activity of ligand and its complexes. lane L: ladder, lane X: DNA + H₂O₂; lane C: control DNA, lanes 1 to 4: ligand, ZnL(NCS)₂, ZnL(N₃)₂ and CdL(NCS)₂ respectively.

CONCLUSION

In this research three new azide and thiocyanate complexes of an imidazolidine Schiff base ligand were synthesized and characterized by spectral (IR, UV-Visible, ¹H and ¹³C NMR) and physical techniques. The observable changes in IR and NMR spectra in the complexes with respect to the free ligand well suggest the formation of the mentioned complexes. IR peaks appeared for azide and thiocyanate well confirm the coordination of these anions to metal centers in the inner coordination sphere. The spectral data suggest the formula structure of MLX₂ for the complexes. The nano-size character of the synthesized complexes was confirmed by the TEM images. Moreover the thermal behavior of the complexes was studied by their thermal analysis and then some activation thermodynamic parameters such as A, E*, ΔH*, ΔS* and ΔG* were calculated based on the thermal analysis plots of TG/DTG. The antimicrobial

behaviors of the complexes against the *Escherichia coli*, *Pseudomonas aeruginosa*, *Staphylococcus aureus* and *Bacillus subtilis* and a fungus entitled as *Candida albicans* were investigated. Finally, the DNA interaction of the compounds with pMalC₂X DNA of *Escherichia coli* was investigated and it was revealed that ZnL(NCS)₂ and CdL(NCS)₂ are more successful for the cleavage of DNA than other compounds.

Acknowledgement: This work was partially supported by Yasouj University.

REFERENCES:

1. A.K. Sharma, S. Chandra, *Spectrochim. Acta A*, **78**, 337 (2011).
2. P.M. Vimal Kumar, P.K. Radhakrishnan, *Inorg. Chim. Acta*, **375**, 84 (2011).
3. M. Sutradhar, T.R. Barman, M.G.B. Drew, E. Rentschler, *J. Mol. Struct.*, **1041**, 44 (2013).
4. B. Gao, M. Wan, J. Men, Y. Zhang, *Appl. Catal. A: General*, **10**, 156 (2012).
5. M. H. Habibi, E. Shojaei, G. S. Nichol, *Spectrochim. Acta A*, **98**, 396 (2012).
6. B. P. Baranwal, K. Tripathi, A. K. Singh, S. Tripathi, *Spectrochim. Acta A*, **91**, 365 (2012).
7. S. Ershad, L. Sagathforoush, G. Karim-nezhad, S. Kangari, *Int. J. Electrochem. Sci.*, **4**, 846 (2009).
8. G. Grivani, G. Bruno, H.A. Rudbari, A.D. Khalaji, PegahPourteimouri, *Inorg. Chem. Commun.*, **18**, 15 (2012).
9. J. Li, J. Hu, Y. Gu, F. Mei, T. Li, G. Li, *J. Mol. Catal. A: Chem.*, **340**, 53 (2011).
10. W. Zeng, J. Li, S. Qin, *Inorg. Chem. Commun.*, **9**, 10 (2006).
11. M. M. Tamizh, R. Karvembu, *Inorg. Chem. Commun.*, **25**, 30 (2012).
12. D. Arish, M. Sivasankaran Nair, *Spectrochim. Acta A*, **82**, 191 (2011).
13. G. Hu, G. Wang, N. Duan, X. Wen, T. Cao, S. Xie, W. Huang, *Acta Pharma. Sin. B*, **2**, 312 (2012).
14. S. Sathiyaraj, K. Sampath, R.J. Butcher, R. Pallepogu, C. Jayabalakrishnan, *Eur. J. Med. Chem.*, **64**, 81 (2013).
15. S. Akine, T. Taniguchi, W. Dong, S. Masubuchi, T. Nabeshima, *J. Org. Chem.*, **70**, 1704 (2005).
16. W. K. Dong, Y. X. Sun, Y. P. Zhang, L. Li, X. N. He, X. L. Tong, *Inorg. Chim. Acta*, **362**, 117 (2009).
17. M. F. Summers, L.G. Marzilli, N. Bresciani-Pahor, L. Randaccio, *J. Am. Chem. Soc.*, **106**, 4478 (1984).
18. A. K. Singh, O. P. Pandey, S. K. Sengupta, *Spectrochim. Acta A*, **85**, 1 (2012).
19. M. Daszkiewicz, *CrystEngComm*, **15**, 10427 (2013).
20. M. Montazerzohori, S. Zahedi, A. Naghiha, M. Montazer Zohour, *Mater. Sci. Eng. C*, **35**, 195 (2014).
21. M. Montazerzohori, S. Zahedi, M. Nasr-Esfahani, A. Naghiha, *J. Ind. Eng. Chem.*, **20**, 2463 (2014).
22. M. Montazerzohori, S.A. Musavi, A. Naghiha, M. Montazer Zohour, *Spectrochim. Acta A*, **129**, 382 (2014).

23. M. Montazerzohori, S.A. Musavi, A. Naghiha, S. Veyseh, *J. Chem. Sci.*, **126**, 227(2014).
24. Y. Harinath, D. H. K. Reddy, B. N. Kumar, Ch. Apparao, K. Seshaiiah, *Spectrochim. Acta A*, **101**, 264 (2013).
25. A. DehnoKhalaji, G. Grivani, M. Seyyedi, K. Fejfarovac, M. Dusek, *Polyhedron*, **49**, 19 (2013).
26. M. Shebl, *Spectrochim. Acta A*, **73**, 313 (2009).
27. A. DehnoKhalaji, G. Grivani, M. Rezaei, K. Fejfarovac, M. Dusek, *Polyhedron*, **30**, 2790 (2011).
28. S. Chandra, S. Bargujar, R. Nirwal, N. Yadav, *Spectrochim. Acta A*, **106**, 91 (2013).
29. B. Dede, F. Karipcin, M. Cengiz, *J. Hazard. Mater.*, **163**, 1148 (2009).
30. M. Montazerzohori, S.A. Musavi, *J. Coord. Chem.*, **61**, 3934 (2008).
31. B. Samanta, J. Chakraborty, C.R. Choudhury, S.K. Dey, D.K. Dey, S.R. Batten, P. Jensen, G.P.A. Yap, S. Mitra. *Struct. Chem.*, **18**, 33 (2007).
32. C. Zhang, G. Tian, B. Liu. *Transition Met. Chem.*, **25**, 377 (2000).
33. S. Sen, P. Talukder, G. Rosair, S. Mitra. *Struct. Chem.*, **16**, 605 (2005).
34. N.A. Illan-Cabeza, F. Hueso-Urena, M.N. Moreno-Carretero, J.M. Martinez-Martos, M.J. Ramirez-Exposito, *J. Inorg. Biochem.*, **102**, 647 (2008).
35. L.P. Nitha a, R. Aswathy a, Niecy Elsa Mathews a, B. Sindhukumari b, K. Mohanan, *Spectrochim. Acta A*, **118**, 154 (2014).
36. G. Grivani, V. Tahmasebi, K. Eskandari, A. DehnoKhalaji, G. Bruno, H. AmiriRudbari, *J. Mol. Struct.*, **100**, 1054 (2013).
37. Y. Harinath, D. H. K. Reddy, B. N. Kumar, Ch. Apparao, K. Seshaiiah, *Spectrochim. Acta A*, **101**, 264 (2013).
38. F. Yue, L. Gang, T. Xiu-Mei, W. Ji-De, W. Wei, *Chin. J. Struct. Chem.*, **27**, 455 (2008).
39. A. A. Soliman, *J. Therm. Anal. Calorim.*, **63**, 221 (2001).
40. R.R. Zaky, T.A. Yousef, K.M. Ibrahim, *Spectrochim. Acta A*, **97**, 683 (2012).
41. S. Sen, P. Talukder, G. Rosair, S. Mitra, *Struct. Chem.*, **16**, 605 (2005).
42. D.H. Petering, H. Sigel, Metal Ions in Biological Systems, vol. 2, Marcel Dekker, New York, 1973, p. 167.
43. B.G. Tweedy, *Phytopathology*, **55**, 910 (1964).
44. J.W. Searl, R.C. Smith, S.J. Wyard, *Proc. Phys. Soc.*, **78**, 1174 (1961).
45. A. Kulkarni, S.A. Patil, P.S. Badami, *Eur. J. Med. Chem.*, **44**, 2904 (2009).

НАНО-СТРУКТУРИРАНИ ЦИНКОВ И КАДМИЕВ АЗИД И ТИОЦИАНАТНИ КОМПЛЕКСИ: СИНТЕЗА, ХАРАКТЕРИЗИРАНЕ, ТЕРМИЧНИ, АНТИМИКРОБНИ И ДНК-ВЗАИМОДЕЙСТВИЯ

С. А. Мусави¹, М. Монтазерзохори^{1*}, М. Наср-Есфакхани¹, Р. Нагиха², М. Монтазер Зохоур³

¹Департамент по химия, Университет Ясудж, Ясудж 75918-74831, Иран

²Департамент по зоология, Земеделски факултет, Университет Ясудж, Ясудж, Иран.

³Изследователски център по генетика на неинфекциозните заболявания, Медицински университет в Захедан, Иран

Постъпила на 2 януари, 2015 г.; приета на 3 юли, 2015 г.

(Резюме)

Приготвени са три нано-структурирани азиди и тиоцианати на цинка и кадмия и техни комплекси с бази на Schiff като лиганди. Те са охарактеризирани чрез измервания на проводимостта, елементарен анализ, IR, UV-Visible, ¹H и ¹³C ЯМР-спектроскопия и термо-гравиметрични изследвания. Забележимите промени в спектралните данни предполагат координиране на лигандите към цинковия и кадмиевия атом. Предлага се следната емпирична формула на комплексите: MLX₂. Нано-размерната структура на комплексите се потвърждава чрез трансмисионна електронна микроскопия (ТЕМ). Средният размер на комплексите е определен в интервала на 25.32 - 85.11 nm. Резултатите от термичния анализ показват, че цинковият изоцианат се разпада на шест последователни стъпки, докато кадмиевите комплекси се разлагат на три етапа. От термогравиметричните криви и от диференциално-термогравиметричния анализ са определени термодинамични параметри, като активиращата енергия, енталпията, ентропията, свободната енергия на активация по Гибс, както и константата на Арениус. Изследвана е антимикробната активност спрямо бактериите *Escherichia coli*, *Pseudomonas aeruginosa*, *Staphylococcus aureus*, *Bacillus subtilis* и гъбичките *Candida albicans*. ZnL(NCS)₂ има най-висока анти-гъбична активност спрямо *Candida albicans* сравнение с останалите комплекси. Накрая е изпитано взаимодействието на комплексите с ДНК (pMalC2X DNA от *Escherichia coli*) за да се изследва потенциала на разкъсване.

The study on D-aminoacylase gene synthesis via chemical and enzymatic combined method

X. Hou¹, J. Li¹, Z. Nuo¹, Y. Ren¹, C. Gao^{1,2,3*}

¹ Schools of Life Science, Jilin University, Changchun, Jinlin Province, People's Republic of China;

² National Engineering Laboratory for AIDS Vaccine, School of Life Science, Jilin University, Changchun, Jinlin Province, People's Republic of China;

³ Key Laboratory for Molecular Enzymology and Engineering, the Ministry of Education, School of Life Science, Jilin University, Changchun, Jinlin Province, People's Republic of China

Received July 8, 2015, Revised October 6, 2015

According to the amino acid sequence, the codons of D-aminoacylase gene from *Alcaligenes A-6* were superseded by the most abundant codon in *E. coli*. The method is performed to avoid the rare codons and the lower abundance which can affect the expression of heterologous proteins. The total length of the synthesized gene is 1479 bp. 52 oligonucleotides were designed and synthesized by the phosphoramidite four-step chemical method. A three-stage assembling method was applied to assemble the whole DNA fragment. The reduction of the template complexity in the reaction system had a significant effect on reducing the number of byproducts to quickly obtain the synthetic gene. The synthesized DNA was connected to pET32a, and then put into *E. coli* BL21 (DE3) for expression. After induction by IPTG, the codon optimized D-aminoacylase gene can be expressed more efficiently in *E. coli* BL21 (DE3), accounting for 78% of total bacterial protein compared to 56% of codon unoptimized gene. The N-acetyl-D-valine amidohydrolase activity was assayed by measuring the D-valine formed using the fermentation bacterial cell to catalyze the N-acetyl-D,L-valine, the fermentation activity of strain *E. coli* BL21 (DE3) harboring pET-dan, which reaches 98 U/ml.

Keywords D-aminoacylase; *Alcaligenes A-6*; Gene synthesis; Expression.

INTRODUCTION

D-amino acids are involved in the synthesis of antibiotics, pesticides, and other products including food and agrochemical industries [1]. D-amino acids occur naturally in bacterial cell walls, some microbial metabolites including peptide toxins and antibiotics, plants, peptides from frogs and molluscs, several insects, earthworms and other animals [2]. But the D-enantiomers of amino acids are far less abundant in nature than the corresponding L-enantiomers, which are the predominant form occurring in biological molecules [3]. Since fermentation is not an efficient method of producing D-amino acids, the D-amino acids are produced in two ways, by direct organic asymmetric synthesis and by enzymatic resolution of racemates. In recent years, much attention has been paid to using N-acyl-D-amino acid amidohydrolase for the production of D-amino acids [4]. N-acyl-D-amino acid amidohydrolase (3.5.1.81) catalyzes the hydrolysis of N-acyl derivatives of various D-amino acids to D-amino acids and fatty acids, and is used for the

optical resolution of DL-amino acids [5, 6]. N-acyl-D-amino acid amidohydrolase (D-aminoacylase) that acts on N-acyl derivatives of various neutral D-amino acids has been reported from *Alcaligenes*, *Pseudomonas*, *Streptomyces*, *Sebekia*, *Variovorax*. D-aminoacylase from *Alcaligenes xyloxydans* subsp. *xyloxydans* A-6 (*Alcaligenes A-6*) has been produced and sold by Amano Enzyme Co. as a commercial enzyme (D-aminoacylase "Amano") for the manufacture of neutral D-amino acids [6]. But the D-aminoacylase gene from *Alcaligenes A-6* using to construct engineering bacteria *E. coli*, has some rare codons of host bacteria, which can affect the expression of heterologous proteins. Therefore, improving the expression of D-aminoacylase is a main goal which needs to be addressed.

The original purpose of this study was to synthesize an *Escherichia coli* codon optimized D-aminoacylase gene. After induction by IPTG, the codon optimized D-aminoacylase gene can be expressed more efficiently in *E. coli* BL21 (DE3), accounting for 78% of total bacterial protein and contrasted with 56% of codon unoptimized gene. The N-acetyl-D-valine amidohydrolase activity was assayed by measuring the D-valine formed

* To whom all correspondence should be sent:

using the fermentation bacterial cell to catalyze the N-acetyl-D,L-valine, the fermentation activity of strain *E. coli* BL21 (DE3) harboring pET-dan which can reach 98U/ml.

MATERIALS AND METHODS

Materials

E. coli BL21(DE3), *E. coli* JM109, pUC18, pET-32a were obtained from ATCC. *EcoR* I, *Xba* I, *BamH* I, *Bgl* II, *Xho* I, dNTP, T4 DNA ligase, *pfu* DNA polymerase, DNA marker were purchased from Fermentas, USA.

Gene and Oligonucleotide Design

The synthesis of D-aminoacylase gene was designed according to the literature [3,6] and retrieved database [7] information.

Chemical synthesis of oligonucleotides

The phosphoramidite four-step method was applied for chemical synthesis of oligonucleotides, which uses the reaction of acid-activated deoxynucleoside phosphoramidites with solid-phase tethered deoxynucleoside. The oligonucleotides were synthesized using the Biolytic Oligo Synthesizers Dr. Oligo-192 by BGI-Shenzhen at the 20 nmol scale, and PAGE method was used for purification.

Enzymatic assembly of oligonucleotides

In each DA-PCR reaction, a mixed solution of 5 μ L was used in 50 μ L of reaction solution; thus, the final concentration of each inner oligonucleotide in the PCR reaction mixture was 40 nmol/L, and the outer oligonucleotide was 0.2 μ mol/L. DA-PCR reaction was carried out in 25 cycles of denaturing at 94°C for 30 s, annealing at 53°C for 30 s, and extension at 72°C for 90 s. In each OE-PCR reaction, the final concentration of the template block or fragment in the PCR reaction mixture was 40 nmol/L. The two outermost oligonucleotides as amplification primers, were used at a final concentration of 0.2 μ mol/L. OE-PCR reaction was carried out in 25 cycles of denaturing at 94°C for 1 min, annealing at 58°C for 1 min, and extension at 72°C for 3 min [7-9]. All PCR reactions were performed on a PTC-200. PCR products were purified using an agarose gel extraction kit.

Cloning and sequencing

The whole DNA fragment purified by agarose gel electrophoresis was connected into pUC18, constructed the pUC-dan recombinant plasmids and then transformed into *E. coli* JM109. After

identification, the positive clones were sequenced by Sangon Biotech (Shanghai) Co., Ltd. Using other synthesized amplification primers with *Nde* I and *Bgl* II restriction sites, the D-aminoacylase gene was amplified from pUC-dan. Amplification fragments were purified and cloned into *Nde* I and *BamH* I sites of pET32a. After identification, the plasmids pET-dan were put into *E. coli* BL21 (DE3) for enzyme expression.

Induced expression and activity assay

Strain of *E. coli* BL21 (DE3) harboring pET-dan, was inoculated into 4 ml LB medium containing 100 mg ampicillin/L (LB/Amp) and were incubated at 37°C for 12 h. The inoculum (1%, v/v) was added to 100 ml LB/Amp and cultured at 37°C to an OD₆₀₀ of 0.6, after which protein production was induced by adding 0.1 mM IPTG and incubating at 37 °C for 3 h.

N-acyl-D-amino acid amidohydrolase activity was assayed by measuring D-amino acids formed from the hydrolysis of N-acetyl-D-amino acids as previously described [3-4]. One unit of enzyme activity was defined as the amount of enzyme that catalyzed the formation of 1 μ mol D-amino acid per min.

RESULTS AND DISCUSSION

Gene and oligonucleotide design

D-aminoacylase gene (*dan*) from *Alcaligenes* A-6 has been reported by M. Moriguchi in 1993 [10]. The whole sequence can be found in GenBank using accession number D45918, containing 1455 nucleotides, which can be encoded as 484 amino acids.

To synthesize an *Escherichia coli* codon optimized D-aminoacylase gene, the codons were chosen to have either 1/3 or 2/3 GC content to ensure that the resulting GC content of the optimized DNA was between 40% and 60%. The codons encoding each amino acid were superseded by the most abundant codon in *Escherichia coli*[11] to avoid the rare codons which can affect the expression of heterologous proteins [12].

Adding the *EcoR* I and *Xba* I restriction endonuclease sites in the 5' and 3' end, the whole DNA fragment was 1479 bp in length. The design of the synthetically assembled oligonucleotides was that the length of each oligonucleotide was 50 bases and the overlapping region was 18 bases, therefore, 14 nt gaps between overlapping regions, 52 oligonucleotides were designed using Genedesign.

Oligonucleotide assembly

Chemically synthesized oligonucleotides were assembled by DNA polymerase based on polymerase chain reaction. *Taq* polymerase lacks 3'-5' exonuclease activity and is known to be error-prone, and therefore, the *pfu* polymerase is used in this assembly process. Using a three-stage assembling method the 52 oligonucleotides were assembled into a full-length gene. The first stage used DA-PCR, and the second and the third stage used OE-PCR. The schematic diagram is shown in Fig.1.

In the first stage, six single-stranded oligonucleotides as a group were assembled into an intermediate fragment forming a block. The 1-48 oligonucleotides were assembled into block 1-8, the last four oligonucleotides 49-52 were assembled into block 9. In the second stage, three double-stranded block DNA as a group were assembled into a longer intermediate fragment forming a fragment. The 1-9 blocks were assembled into fragment 1-3. In the third stage, three double-stranded DNA fragments were assembled into the whole D-aminoacylase gene (Fig.2).

Cloning and sequencing

The whole DNA fragment purified by agarose gel electrophoresis was connected into pUC18, constructed the pUC-*dan* recombinant plasmids and then was transformed into *E.coli* JM109. After identification, five positive clones were sequenced by Sangon Biotech (Shanghai) Co., Ltd. The sequencing results showed that two of them were confirmed to be the correct products which have the accurate sequence with the design. Unfortunately, one of the five positive clones has the major bands error after the final amplification step appeared to be the correct size. There were total 5 base errors in the sequence of two clones which have no major bands error. It contained two base deletions, one single base insertion and two single point mutations. The average error rate determined by sequencing was approximately 0.68‰.

Induced expression

The strain of *E. coli* BL21 (DE3) harboring pET-*dan*, and the strain of *E. coli* BL21 (DE3) harboring pET-*dan*-N (D-aminoacylase gene amplified from *Alcaligenes* A-6, codons not optimized) were induced by 1 mM IPTG in LB/Amp medium and incubated at 37°C. The expressed codon optimized and unoptimized D-aminoacylase genes were detected by 10%

SDS-PAGE (Fig.3).

The codon unoptimized D-aminoacylase gene efficiently expressed in *E. coli* BL21 (DE3), accounted for 56% of total bacterial protein. Correspondingly, the codon optimized D-aminoacylase gene synthesized in this paper, expressed more efficiently in *E. coli* BL21 (DE3), accounted for 78% of total bacterial protein (Tab. 1). Another better way is to directly express the D-aminoacylase gene in *E. coli* Rosetta 2 which harbors pRARE2 providing all the rare codon tRNAs for *E. coli*. The codon unoptimized D-aminoacylase gene can be efficiently expressed in *E. coli* Rosetta 2, accounting for 64% of total bacterial protein (Tab. 1). This shows that rare codon and codon abundance in the host affect the exogenous gene expression.

Activity assay

D-aminoacylase from *Alcaligenes* A-6 acts preferentially on N-acyl derivatives of d-Met, d-Phe, and d-Leu, and less effectively on those of d-Trp, d-Ala, and d-Val. We are using N-acetyl-D, L-valine as the substrate to assess the recombinant enzyme catalytic activity of the fermenting bacterial cell. The N-acetyl-D-valine amidohydrolase activity was assayed by measuring D-valine formed from the hydrolysis of N-acetyl-D-valine. The fermentation activity of the strain of *E. coli* BL21 (DE3) harboring pET-*dan* can reach 98 U/ml, higher than the wild type strain *Alcaligenes* A-6 (Tab. 2). The codon unoptimized D-aminoacylase gene can be expressed efficiently in *E. coli* Rosetta 2, accounting for 83 U/ml (Tab. 2).

Table 1. The expression of D-ANase synthetic D-aminoacylase gene in *E. coli* BL21 (DE3).

Number (% of)	1	2	3	4	5	Average value
Codon unoptimized	59	51	54	58	58	56
Codon optimized	63	68	65	61	63	64
Rosetta Express	78	84	72	76	80	78

Table 2. Fermentation enzyme activity of D-ANase.

Number (U/ml)	1	2	3	4	5	Average value
Codon unoptimized	68	59	66	74	78	70
Codon optimized	95	101	102	97	95	98
Rosetta Express	80	82	84	86	83	83

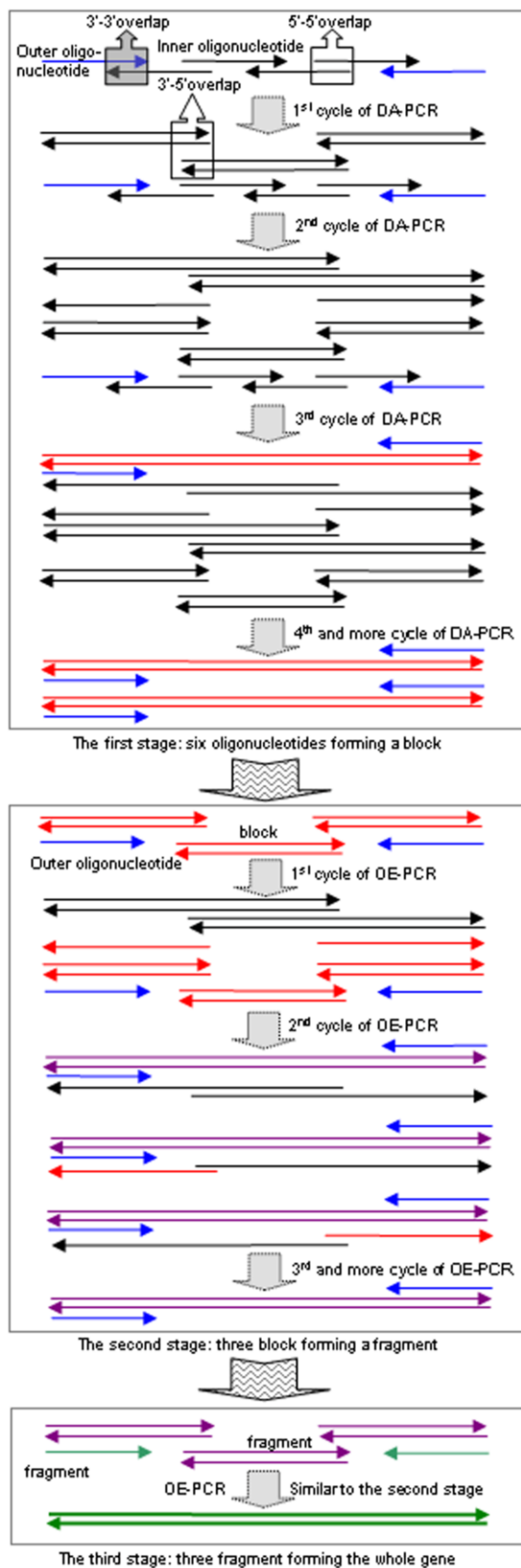


Fig. 1. Schematic diagram of the three-stage assembling method.

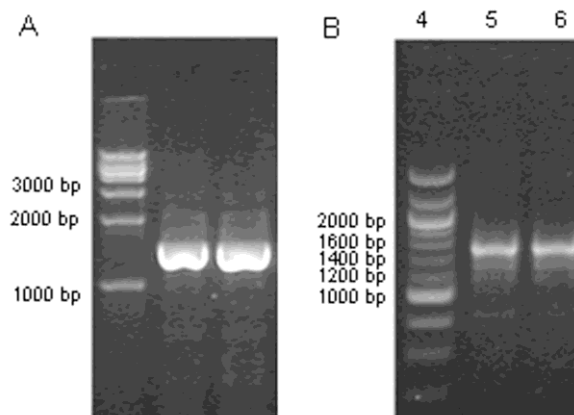


Fig. 2. Oligonucleotide assembly results. (A) three-stage assembling method. Lane 1: 100bp DNA marker, lane 2-3: synthesized D-aminoacylase gene; (B) two-stage assembling method. Lane 4: 1000bp DNA marker, lane 5-6: synthesized D-aminoacylase gene.

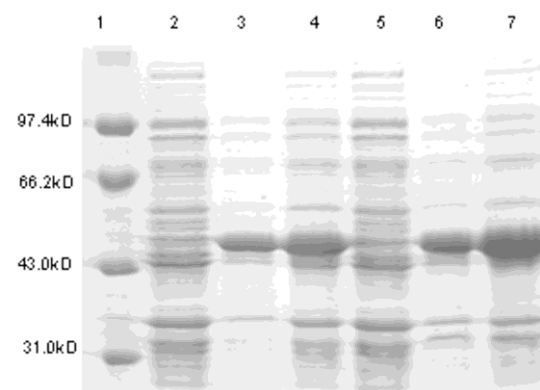


Fig. 3. SDS-PAGE analysis of the codon optimized and unoptimized D-aminoacylase gene expression. Lane 1: protein marker; lane 2-4: pET-dan-N induced by IPTG for 0, 1.5 and 3 h; lane 5-7: pET-dan induced by IPTG for 0, 1.5 and 3h.

D-aminoacylase chromatographic purification process

The 100 ml induced expression of *E.coli* BL21/pET-dan fermentation broth was centrifuged at 4000 rpm and 4°C for 10 min. After collecting the precipitated bacteria and weighing (wet weight), 20 mmol / L PBS buffer (pH 5.0) was added according to the proportion of 1g:10 mL. After mixing in an ice bath for ultrasound breaking (breaking conditions: output power 300W, breaking time 5 s, interval of 5 s times, 200 times), the supernatant was collected at 10000 rpm and 4°C for 10 min. After the supernatant was filtered through a 0.45 μm filter, the buffer solution was used to replace the buffer solution in the 8000 Da. Non fusion expression of D-ANase was purified by DEAE-FF anion exchange chromatography, CM-52 cation exchange chromatography and

Table 3. Separation and purification of non-fusion D-ANase.

Purification steps	Protein content (mg)	Total activity (U)	Specific activity (U/mg)	Recovery rate (%)	Total yield (%)	Purification rate
1. Before breaking	1564.3	6897.5	4.41			
2. Crude enzyme liquid	946.7	8254.3	8.72	120	120	
3.DEAE-FF	216.8	2137.8	9.86	26	31	1.13
4. CM-52	63.2	1769.1	27.99	83	26	2.84
6. Superdex-200	1.3	1489.6	1145.85	84	22	40.93

superdex200 AKTA-FPLC gel filtration chromatography. D-ANase was purified through multiple steps of chromatography, the final product recovery rate was 84% and the specific activity for 1145.85 (U/mg), purification rate was 40.93 times. The results of the chromatographic purification and detection of the various stages are shown in Table 3. The purity of D-ANase protein obtained by SDS-PAGE was higher, and the molecular weight of the protein was about 52 kDa (Fig.3).

CONCLUSIONS

The three-stage assembling method used in this paper includes a phase DA-PCR and two-stage OE-PCR [13]. Irrespectively of the stage, the heating step causes DNA melting of the DNA template by disrupting the hydrogen bonds between complementary bases, yielding single-stranded DNA molecules. Then the reaction solution became a complex system of single-stranded DNA molecules, including the chemically synthesized oligonucleotides, the longer single-stranded fragments being assembled by DNA polymerase. The cooling step causes the primers or the overlapping segments containing sequences complementary to the target region by the stable DNA-DNA hydrogen bonds to form a local double-stranded DNA molecule. The annealing method yielded 3'-3'overlap, 3'-5'overlap and 5'-5'overlap. The DNA polymerase bound to the 3'-3'overlap and 3'-5'overlap double-stranded, synthesized a new DNA strand complementary to the DNA template strand by adding dNTPs that are complementary to the template in 5' to 3' direction, condensing the 5'-phosphate group of the dNTPs with the 3'-hydroxyl group at the end of the nascent (ex-

tending) DNA strand. The oligonucleotides alternate between sense and antisense directions, and the overlapping segments determine the order of the PCR fragments, thereby selectively producing the final long DNA product.

Considering the length of overlapping region of only 18 bases in average, the annealing of long single-stranded DNA molecules may easily produce a mismatch, so that assembling into full-length genes containing too many byproduct bands can be connected into a plasmid. Using the three-stage assembling method, the nine-block assembly by OE-PCR splits into two phases, reducing the complexity of the template in the reaction system, yielding single product bands, and reducing the workload of screening, by quickly producing the synthetic genes.

Acknowledgements: This work was supported by the Specialized Research Fund for the Doctoral Program of Higher Education of China (20100061120076); the Fundamental Research Funds for the Central Universities and the Special Fund Project for the Scientific Research of the Forest Public Welfare Industry (201204614).

REFERENCES

1. D. L. Zhang, F. U. Zhu, W. H. Fan, R. Sh. Tao, H. Yu, Y. L. Yang, W. H. Jiang, Sh. Yang, *Appl. Microbiol. Biotechnol.*, **90**(4), 1361 (2011).
2. H. Lindner, S. Hopfner, M. Tafler-Naumann, M. Miko, Konrad L., Rohm K. H., *Biochimie*, **82**(2), 129.(2000)
3. V. Vranova, H. Zahradnickova, D. Janous, K. R. Skene, A. S. Matharu, K. Rejsek, P. Formanek, *Plant and Soil*, **354**(1), 21 (2012).
4. M. Moriguchi, K. Sakai, Y. Katsuno, T.i Maki, M. Wakayama, *Biosci., Biotechnol., Biochem.*, **57**(7),

- 1145 (1993).
5. Yoshimune K., Ninomiya Y., Wakayama M., Moriguchi M., *J. Ind. Microbiol. Biotechnol.*, **31**(9), 421 (2004).
 6. R. Nandakumar, K. Yoshimune, M. Wakayama, M. Moriguchi, *J. Mol. Catal. B-Enzym.*, **23**(2-6), 87 (2003).
 7. C. H. Gao, X. Y. Shi, X. T. Hou, Q. F. Meng, Y. J. Zhang, L.R. Teng, *Chem. Res. Chinese U.*, **24**(4), 487 (2008).
 8. D. An, X. H. Zhao, M. Zhou, Z. W. Ye, *Chemical Journal of Chinese Universities*, **35**(2), 275 (2014).
 9. Young L. Dong Q. H., *Nucleic Acids Res.*, **32**(7) e59, DOI: 10.1093/nar/gnh058 (2004).
 10. M. Wakayama, Y. Katsuno, S. Hayashi, Miyamoto Y., K. Sakai, M. Moriguchi, *Bioscience, Biotechnology and Biochemistry*, **59**(11), 2115. (1995).
 11. S. L. Shi, Y. R. Jiang, Y. Q. Liu, R. X. Xia, L. Qin, *Virus genes*, **46**(1), 10 (2013).
 12. X. Y. G. C. H. Zhao, L. Jin, X. Wang, Q. F. Meng L.R. Teng, *Chemical Journal of Chinese Universities*, 29(10), 1995 (2008).
 13. K. Yoshimune, Y. Ninomiya, M. Wakayama, M. Moriguchi, *J. Ind. Microbiol. Biotechnol.*, **31**(9), 421 (2004).

СИНТЕЗА НА ГЕН ЗА D-АМИНОАЦИЛАЗА ПО ХИМИЧЕН И КОМБИНИРАН ЕНЗИМЕН МЕТОД

Кс. Хоу¹, Дж. Ли¹, Жай Нуо¹, И. Рен¹, К. Гао^{1,2,3*}

¹ Училищц по науки за живота, Университет Жилин, Чангчун, Провинция Жилин, Китайска НР

² Национална лаборатория за СПИН-ваксини, Училищц по науки за живота, Университет Жилин, Чангчун, Провинция Жилин, Китайска НР

³ Ключова лаборатория по молекулярна ензимология и инженерство, Министерство на образованието, Училищц по науки за живота, Университет Жилин, Чангчун, Провинция Жилин, Китайска НР

Постъпила на 8 юли, 2015 г.; коригирана на 6 октомври, 2015 г.

(Резюме)

Според секвенцията на аминокиселините кодонт на гена за D-аминоацилаза в в щама *Alcaligenes A-6* се замества от по-разпространения кодонт в *E. coli*. Представеният метод позволява да се избегнат редки кодони и слабото разпространение, които могат да повлияят на експресията на хетероложни протеини. Общата дължина на синтезирания ген е 1479 бр. Петдесет и два олигонуклеотида са конструирани и синтезирани чрез четири-степенен химичен метод с фосфорамидит. Три-степенен метод е проложен за асемблирането на целия ДНК-фрагмент. Намалването на сложността на темплейта в реакционната система има значителен ефект за намаляването броя на страничните продукти за бързото получаване на синтетичния ген.

Синтезираната ДНК е свързана с рЕТ32а, след което е вкарана в *E. coli* BL21 (DE3) за експресия. След индукция с IPTG кодонт-оптимизираният ген за D-аминоацилаза може да бъде експресиран по-ефективно в *E. coli* BL21 (DE3) с 78% общ бактериален протеин, при 56% при кодонт-неоптимизиран ген. Определена е активността на N-ацетил-D-валин амидохидазата чрез измерване на D-валина, образуван при хидролизата на N-acetyl-D,L-valine от щама *E. coli* BL21 (DE3) harboring рЕТ-dan. Концентрацията на D-валина достига 98 U/ml.

Room temperature acetone vapor - sensing properties of a mesoporous zinc stannate layer

I. E. Kononova^{1,2}, D. M. Vorobiev¹, D. Tz. Dimitrov^{3*}, A. Ts. Georgieva⁴, V. A. Moshnikov^{1,5}

¹ Department of Micro- and Nanoelectronics, Saint-Petersburg State Electrotechnical University, Saint-Petersburg 197376, Russia

² Department of Machines and Metal Forming Technology, Saint-Petersburg State Polytechnical University, Saint-Petersburg 195251, Russia

³ Laboratory of Nanoparticle Science and Technology, Department of General and Inorganic Chemistry, Faculty of Chemistry and Pharmacy, University of Sofia, Sofia 1164, Bulgaria

⁴ Particle Engineering Research Center, Materials Science & Engineering Department, University of Florida, Gainesville, FL 32611, USA

⁵ Department of Integrated Electronics, Saint-Petersburg State Polytechnical University, Saint-Petersburg 195251, Russia

Received January 13, 2015, Revised August 18, 2015

Zinc stannate porous nanostructured compositions of nanoparticles are produced in the form of thin films by means of the chemical vapor deposition method. The phase, composition and surface condition of the layers as formed by the above route are investigated. Under the application of an alternating electric field the electrical properties of the layer change under acetone vapor exposure at room temperature. As a result of this interaction the radius of the semi-circle on the Nyquist diagram is reduced and the centre of the semi-circle on the plot is shifted to the higher frequency. To describe the resistance-capacitance properties of the samples the characteristic time of charge accumulation at the atmosphere and under acetone vapor exposure is estimated. The values of the gas sensitivity in the frequency range from 1 Hz to 50 KHz is calculated in two ways based on the real and imaginary components of the complex impedance.

Keywords: nanostructures; thin films; impedance spectroscopy; surface properties.

INTRODUCTION

The gas sensors, intended for the detection of acetone in the air, are widely applied for environmental monitoring, in criminology, in military affairs, in mechanical engineering and for medical non-invasive diagnosis for the analysis of exhaled breath of patients suffering from diabetes. Now-a-days, there is still a need for the creation of nanomaterials for acetone gas sensors, operating at room temperature.

Most sensor materials show acetone vapor detection properties at elevated temperatures in the range 150–450°C [1–6]. There are only a few publications in the world literature at present, devoted to research aimed at the creation of nanomaterials that study the gas sensitive properties of acetone vapor at room temperature. These are ZnO nanorods doped with Ni, the sensitivity of which is enhanced by UV activation [7], CuO nanocrystalline thick films [8] and TiO₂ nanotubes with a certain deviation in stoichiometry [9]. To the best of our knowledge, up to now in the scientific journals there does not exist any information

concerning the measurement of the complex resistivity (conductivity) of a Zinc Stannate Layer in the atmosphere under acetone vapor exposure at room temperature.

Impedance spectroscopy is a favorite tool for materials characterization, useful in gathering both, the kinetic and mechanistic information. A review of the recent progress in evaluating the gas concentration by the impedance change and the establishment of state of the art of impedance-based gas sensors is presented in [10]. Despite the well-known fact that the interaction of the material with a gaseous medium depends on the microstructure and the surface states of the sensing material, to the best of our knowledge, alternating current (AC) measurement has been used for detection of gases only for a few metal oxides. The most important advantage of the alternating current (AC) measurements is that they can distinguish the individual contributions to the electrical conduction or polarization arising from different sources like the bulk and the grain boundaries, the intergranular contact regions, and the electrode-sample interface regions whereas direct current (DC) measurements show only the overall effect of all these contributions [10, 11]. It is worth mentioning that the impedance spectroscopy investigation of:

* To whom all correspondence should be sent:

E-mail: dimitrov2001@yahoo.com

undoped titanium dioxide (TiO_2) polycrystalline thin films as a function of temperature and the surrounding atmosphere are presented in [13], zirconia gas sensors [14], zeolite hydrocarbon sensors with a chromium oxide as the intermediate layer [15], room temperature gas sensing of ultrathin SnO_2 sensors prepared by the Langmuir Blodgett technique [16], WO_3 sensors sensitivity versus time and working temperature [17], SmFeO_3 thin-film sensor [18] and a sensing device based on vanadium oxide (V_2O_5)/porous Si/Si structure [19].

An improvement of the gas-sensitive properties can be achieved by using multi-component metal oxides as the sensor material [20–24]. Increasing the gas sensitivity is possible in principle in the case of the cooperative effect as a result of the separation of the functional properties of adsorption and complete oxidation of the reducing gases at different surface centers of the multicomponent systems. During the last few years there is a growing interest in investigations of the properties of nanostructured $\text{ZnO} - \text{SnO}_2$ materials, which are crystallized into perovskite (ZnSnO_3) [25] and spineli (Zn_2SnO_4) structures [26, 27]. The formation of such mixed oxides leads to the modification of the electronic band structure of the Zn-Sn-O system. This includes changes in the bulk and surface properties. The surface properties are expected to be influenced by new boundaries between the grains of different chemical compositions. These could be stoichiometric ZnSnO_3 and Zn_2SnO_4 compounds or composites. It is anticipated that all these phenomena will contribute advantageously to the gas sensing mechanism [28].

Thin films of ZnSnO_3 structures are very promising in the creation of new lead free ferroelectric materials [29]. Other notable applications of these nanostructured compounds are their utilization in lithium ion batteries [30], piezoelectric transformers [31], transparent conductive coatings and thin film transistors [32–34], electro-luminescence devices for power independent memory cells. Among the above applications, the number of investigations dealing with the formation of zinc stannate layers that have a highly sensing performance is increasing remarkably [35–42]. For such new generation sensing structures it is necessary to develop and evaluate the advanced technological aspects for the formation of nanostructure and nanocomposite layers, including various nanocomposites, modified nanowires, nanorods, nanospheres, nanotubes as well as nanomaterials with hierarchical porous nanostructures [43–55].

The development of three-dimensional (3D) face-centered-cubic ZnSnO_3 into two-dimensional (2D) orthorhombic ZnSnO_3 nanosheets has been observed recently [56]. The synthesis from 3D of 2D nanostructures is realized by the dual-hydrolysis-assisted liquid precipitation reaction and subsequent hydrothermal treatment. The 2D ZnSnO_3 nanosheets should exhibit excellent gas sensing properties of acetone vapor, especially through their ultra-fast response and recovery. The authors [56] show, that the 2D ZnSnO_3 nanosheets consist of smaller sized nanoflakes. This further increases the special specific surface area and facilitates their application in gas sensing.

Never-the-less, in the literature there is a hitherto unreported study devoted to the sensitivity of the ZnSnO_3 layer to acetone vapor at room temperature under the application of an alternating electric field. Thus, the main goal of the presented work is the formation and investigation of the surface morphology, the electrical and acetone gas sensing properties under the application of an alternative electric field at room temperature formed by a chemical vapor deposition nanosized ZnSnO_3 thin film.

EXPERIMENTAL

The metal oxides layers investigated in the current work are formed in a laboratory installation by means of the chemical vapor deposition (CVD) method. There are two zones inside the quartz reactor, in both of which there were boats with inorganic metal salts of tin chloride ($\text{SnCl}_2 \cdot 2\text{H}_2\text{O}$) and zinc nitrate ($\text{Zn}(\text{NO}_3)_2 \cdot 6\text{H}_2\text{O}$) while the third zone is the area of location of the holder with the substrates. The temperature required for the process is maintained in the three areas by using independent heaters. The components of the salts obtained were transferred to the deposition area in the reactor. This is done by the transfer of the vapors of volatile compounds from the areas of the tin chloride and zinc nitrate boats to the area of the holder with the substrates.

The sensing layer structures are formed by using three subsequent processes:

- Decomposition of tin chloride ($\text{SnCl}_2 \cdot 2\text{H}_2\text{O}$) and zinc nitrate ($\text{Zn}(\text{NO}_3)_2 \cdot 6\text{H}_2\text{O}$) at the temperature of 150 °C under an air flow within the quartz reactor;
- After decomposition within the quartz reactor the reaction products are transferred to the substrates;
- The formation of the ZnSnO_3 layer at the temperature of 500 °C from the transferred to the substrate reaction products;

Thermally oxidized silicon was used as a substrate. The thickness of the oxide layer was about 500 nm. Before application the substrates were treated in acetone and isopropyl alcohol in an ultrasonic bath. The thickness of the ZnSnO₃ layers, deposited on the substrates is about 500 nm, estimated by means of ellipsometry measurements.

The investigations of the phase composition of layers formed by the above route are done on a low angle registration electron-diffraction apparatus (SELMI, Ukraine). Electron diffraction [57, 58] is a local (small extinction length) an express (high intensity particle flux) method of structural analysis. The method of electron diffraction is indispensable in the study of near-surface regions, thin films and other nano-objects. The investigation is evaluated by comparison of the diffraction patterns of nonelastically scattered electrons in refraction geometry.

The conductive substrate necessitates the determination of its phase composition by means of a low-angle registering electronograph. Because of this electron diffraction experiments were performed on ZnSnO₃ layers deposited on a non-oxidized silicon substrate. However, to investigate the gas-sensing properties of the ZnSnO₃ layers it was necessary to deposit these on an oxidized silicon substrate. Silicon oxide is an insulating dielectric layer between the silicon and the semiconductor layer of zinc stannate. It was used to avoid the conductive silicon and contributes to the gas sensing properties of zinc stannate.

The investigation of the surface condition of the nanostructured film formed by oxidation of a silicon dielectric layer is done on a nanolaboratory instrument Ntegra Terma (NT-MDT, Zelenograd). It was performed by means of a “semi-contact” vibrational AFM mode. Probe type sensors with cantilevers series NSG 01 in the form of a rectangular cross-section rafter were used in the investigation. This has a resonance frequency of 150 kHz and was purchased from the NT-MDT Company.

The electrical properties of ZnSnO₃ nanostructures are studied by means of impedance spectroscopy measurements. It is well know that this method is widely used to investigate the electrical properties of the grain boundary under the application of an electrical field with an alternative frequency. Measuring the frequency dependences of the complex resistivity modulus and determination of the phase shift angle between the current and voltage in the capacitance circuit were carried out in the frequency range between 1 Hz to 500 kHz with an amplitude of the alternating

voltage equal to 30 mV. On our experimental setup [59] we were able to measure the electrical properties of the nanostructure at the atmosphere and under exposure to acetone vapor in the air. The concentration of acetone was 100, 200 and 300 ppm and at a relative humidity of 80 %.

RESULTS OF THE INVESTIGATION OF THE STRUCTURAL PROPERTIES OF MESOPOROUS ZnSnO₃ LAYERS AND THEIR SENSING PERFORMANCE UNDER THE APPLICATION OF AN ALTERNATING ELECTRIC FIELD

The result of electron diffraction for the zinc stannate layer, deposited on an oxide free silicon wafer is shown on Fig.1. It presents the typical dependence of the signal intensity on the photoelectron multiplier as a function of the interplanar distance *d*. The latter is calculated based on the value of the distance from the central spot. The diffraction peaks for nonelastic scattered electrons, corresponding to the crystallized in perovskite structure nanostructured phase of ZnSnO₃ are marked by solid dots. It is clear, that under the applied technological conditions of chemical vapor deposition, the corresponding ZnSnO₃ crystal phase exhibits only reflections. An electron diffraction image for the same sample is presented in Fig.2.

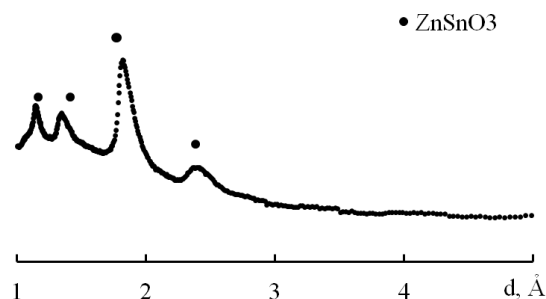


Fig. 1. Cross-section of electron diffraction pattern at radius from the central spot toward the interplanar distance *d* for the based on ZnSnO₃ layer.

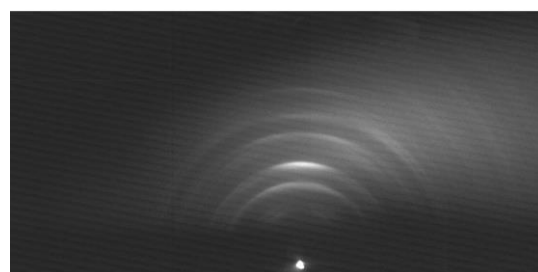


Fig. 2. Electron-diffraction image for the based on ZnSnO₃ layer.

In the current work the AFM images were in the form of a square matrix with the size 256×256 of

the elements. Based on the AFM investigation it was estimated that the produced nanostructured materials are an aggregation of nanoparticles with sizes in the range of 10-100 nm. Into the matrix of the nanoparticles, the pores in size less than 10nm are uniformly distributed. An example for a typical ZnSnO₃ nanostructure, deposited on the substrate of oxidized silicon is presented on Fig.3 for a scanning area of 1µm × 1µm.

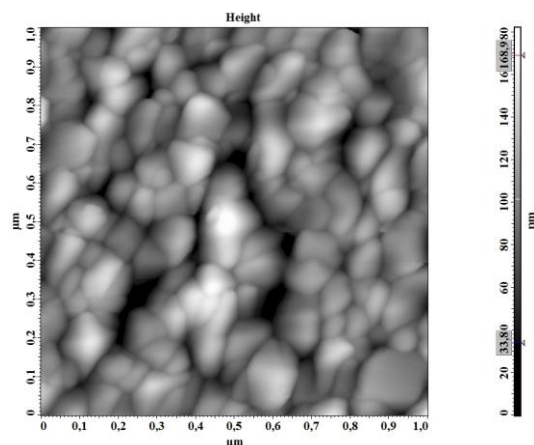


Fig. 3. AFM image of ZnSnO₃ layer

The experimental data measured by means of impedance spectroscopy were evaluated by using a complex plane on which the impedance value and other complex quantity is presented in the form of a dependence of the real and imaginary component of the complex resistivity. The frequency dependences of the real and imaginary components of the complex resistivity for the ZnSnO₃ nanostructure are plotted in semi-logarithmic coordinates and analyzed. It was revealed that the imaginary component of the complex resistivity is going through a maximum when $\omega\tau=1$, where ω is the angular frequency and τ the time of the relaxation polarization. Nyquist diagrams for the nanostructured ZnSnO₃ layer at the atmosphere and under acetone vapor exposure (100, 200, 300 ppm) at room temperature were presented in Fig.4.

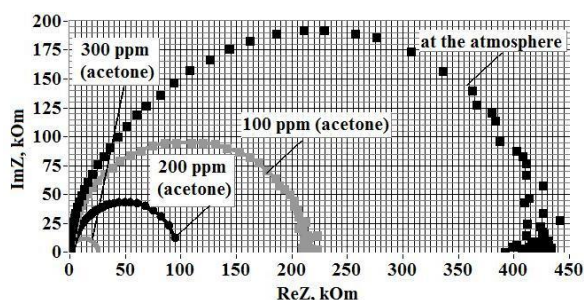
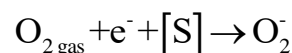


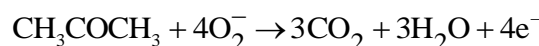
Fig. 4. Nyquist diagram for the nanostructured ZnSnO₃ layer at the atmosphere and under various concentrations of acetone vapour exposure.

DISCUSSION

Basic working principle of operation of the solid state gas sensors is the alternation of semiconductive oxide layer electrical properties under adsorption of gas molecules. Atoms or molecules adsorbed on the nanostructured oxide surface can capture electrons from or inject electrons into the bulk to form localized electron extrinsic energy state at the surface, which can change the concentration of charge carriers into conduction band or valence band. It is known that acetone is an electron-donor molecule, which has two electron pairs on highest occupied molecular orbital (HOMO), which can be donated to form coordinate bond. The lone pairs are relatively high in energy, and are responsible for the well known Lewis base properties of acetone. When the sensor is exposed to acetone vapor, the gas molecules are adsorbed on the surface of the gas-sensing layer and the weak coordinate bonds can be formed between acetone and Sn (IV) ions from the ZnSnO₃ crystal lattice. Similar interaction is in the case when the PbS sensor is exposed to NO₂ or NH₃ gas. Then the gas molecules are adsorbed on the surface of the gas-sensing layer and the weak coordinate bonds is formed between NO₂ or NH₃ and lead(II) in PbS molecules [60]. In our case, electrons are transferred from acetone molecules to the gas-sensing layer and the thickness of surface space depletion layer at the grain boundary of ZnSnO₃ crystallites will be decreased. This will modulate conductive channels at the contacts of the nanocrystalites. The molecules of acetone will interact with oxygen, which is unavoidable existing on ZnSnO₃ crystallites and adsorb there according to the reaction below:



where $O_{2\text{gas}}$ - oxygen molecule in the atmosphere, e^- - free electron at the ZnSnO₃ crystallites surface, $[S]$ - unoccupied center for oxygen chemisorptions, O_2^- - adsorbed on the surface one charged oxygen molecule. Acetone adsorbed on the surface, reacts with the above mentioned molecular oxygen ions and captured by it electrons are released into the layer, according to the reaction:



By this way, no matter that adsorption of one acetone molecule provides two electrons to the ZnSnO₃ layer, after its oxidation four electrons are released into the layer. Consequently, after oxidation of the adsorbed acetone the total effect is

increasing the conductivity of the layer. Under acetone vapor exposure the radius of the semi-circle on the Nyquist diagram is reduced (Fig. 4) and the centre of semi-circle on the plot is shifted to the higher frequency. The reason for this effect is the relaxation maximum shift of the imaginary component of complex resistivity to the area of higher frequencies.

The equivalent electric scheme is used for interpretation of observed capacitance-resistance properties of nanostructured ZnSnO₃ layer. A constant phase element, widely used for modeling impedance of many electrical systems was employed. This scheme describes well the exponential dependence of parameters of chemical-physics processes, related to overcoming energy threshold during the charge transfer and impedance behavior. Also, the scheme is connected to the appearing of fractal properties of investigated structures in particular frequency range. Impedance of the element with constant phase is described by equation: $Z = 1/A(j\omega)^n$, where A - proportionality factor, j - the imaginary unit, n - exponent index, giving the information about the phase shift, $-1 \leq n \leq 1$. Frequency independent factor has physical meaning and dimension of capacitance.

The plotted on Fig.4 impedance hodographs are evaluated for the circuit, constructed of connected in parallel resistance R and the constant phase component. This circuitry can be characterized by resistance and constant phase component of the grain boundary of ZnSnO₃ crystallites. The hodographs consist of semi-circles with center below the horizontal axis. The characteristic time of charge accumulation for the circuit, constructed from connected in parallel resistance R and the constant phase component is expressed by equation $\tau = (R \cdot A)^{1/n} = 1/\omega$, where ω is angular frequency at the point where imaginary component of complex resistivity having maximum value (at the point of relaxation maximum on impedance hodograph).

Let's consider the impedance hodographs in air and in the presence of acetone vapor with concentration of 100 ppm. Values of resistivity R , frequency independent fore-exponential factor A , exponent index n , relaxation maximum frequency f_{max} and time of relaxation polarization τ at the atmosphere and under acetone vapor exposure are calculated. It was revealed that under acetone vapor exposure value of resistivity R is reduced by factor of 1.99; value of frequency independent fore-exponential factor A is reduced by factor of 1.39;

value of relaxation maximum frequency f_{max} is increases by factor of 2.89. It was found that under acetone vapor exposure value of exponent index n is not changed and is 0.94; value of time of relaxation polarization τ is 184 μ sec in the atmosphere and 64 μ sec under acetone vapor exposure.

Based on the above investigations, the value of gas-sensitivity is evaluated in two ways: (i) by the real component of the complex resistivity as $S_{Re} = ReZ_{air}/ReZ_{gas}$, where ReZ_{air} is the real component of the complex resistivity at the atmosphere, ReZ_{gas} is the real component of the complex resistivity under acetone vapor exposure; (ii) by the imaginary component of the complex resistivity as $S_{Im} = ImZ_{air}/ImZ_{gas}$, where ImZ_{air} is the imaginary component of complex resistivity at the atmosphere, ImZ_{air} - is the imaginary component of the complex resistivity under acetone vapor exposure. The estimated value of sensitivity is 2.0, calculated by real component and is 4.2 while calculated by imaginary component. It was revealed that in both cases the maximum of the sensitivity toward acetone vapor is at frequency low than 140 Hz.

Because in the World wide literature to the best of our knowledge does not exist any results of investigation of complex resistivity (conductivity) of Zinc Stannate Layer at the atmosphere and under acetone vapor exposure at room temperature we cannot compare the functional properties of the produced in this work films with similar films of the scientific periodic. At the available literature existing only done at direct current (DC) measurements of gas-sensitive properties of Zinc Stannate Layers [37, 38, 40, 41, 56].

CONCLUSIONS

In this work is presented the procedure of producing zinc stannate based porous nanostructured composition by chemical vapor deposition method. The produced layers are composed from aggregations of nanoparticles 10-100 nm in size. Into the nanoparticles matrix pores are regularly distributed. Under application of alternative electric field the electrical properties of the layer change under acetone vapor exposure at room temperature. Under acetone vapor exposure the radius of the semi-circle on the Nyquist diagram is reduced and the centre of semi-circle on the plot is shifted to the higher frequency. The reason for this effect is the relaxation maximum shift of the

imaginary component of complex resistivity to the area of higher frequencies.

Acknowledgments: D. Dimitrov is thankful for financial support to the Beyond Everest project FP7-REGPOT-2011-1. The Russian researchers are thankful to the grant of Russian Scientific Fund (project №14-15-00324). The authors are grateful to both Dr. Kamilu Gazinyrovich Gareev for help in investigation the phase composition of the nanostructures by electron diffraction measurements.

REFERENCES

1. L. Wang, A. Teleki, S. Pratsinis, P. Gouma, *Chem. Mater.*, **20**, 4794 (2008).
2. K.W. Kao, M.-Ch. Hsu, Yu.-H. Chang, Sh. Gwo, J. A. Yeh, *Sens.*, **12**, 7157 (2012).
3. P. Yu, J. Wang, H.-Yi Du, P.-J. Yao, Y. Hao, X.-G. Li, *J. Nanomater.*, **2013**, 1 (2013).
4. H. Shan, Ch. Liu, L. Liu, Sh. Li, L. Wanga, X. Zhang, X. Bo, X. Chi, *Sens. Actuators B*, **184**, 243 (2013).
5. Yi. Zhang, W. He, H. Zhao, P. Li, *Vacuum*, **95**, 30 (2013).
6. X. B. Li, S. Y. Ma, F. M. Li, Y. Chen, Q. Q. Zhang, X. H. Yang, C. Y. Wang, J. Zhu, *Mater. Lett.*, **100**, 119 (2013).
7. H. Ahn, Y. Wang, S. H. Jee, M. Park, Y. S. Yoon, D.-J. Kim, *Chem. Phys. Lett.*, **511**, 331 (2011).
8. I. Singh, R. K. Bedi, *AIP Conf. Proc.*, **1536**, 1175 (2013).
9. B. Bhowmik, A. Hazra, K. Dutta, P. Bhattacharyya, Device and Materials Reliability, *IEEE Transact.* **PP 99**, 1 (2014).
10. J. M. Rheaume, A. P. Pisano, *Ionics*, **17**, 99 (2011).
11. J. R. Macdonald, *Ann. Biomed. Eng.*, **20**, 289 (1992).
12. O. K. Varghese, L. K. Malhotra, *J. Appl. Phys.*, **87**, 7457 (2000).
13. M. A. Ponce, R. Parra, R. Savu, E. Joanni, P. R. Bueno, M. Cilense, J. A. Varela, M. S. Castro, *Sens. Actuators B*, **139**, 447 (2009).
14. S. Zhuiykov, Electrochemistry of Zirconia Gas Sensors, Taylor Francis Group, USA, 2007.
15. G. Hagen, A. Schulz, M. Knörr, R. Moos, *Sensors (Basel)*, **7**, 2681 (2007).
16. C. A. Betty, S. Choudhury, K. G. Girija, *Sens. Actuators B*, **173** 781 (2012).
17. A. Abidi, C. Jacolin, M. Bendahan, A. Abdelghani, J. Guerin, K. Aguir, M. Maaref, *Sens. Actuators B*, **106**, 713 (2005).
18. T. Tasaki, S. Takase, Y. Shimizu, *J. Sens. Tech.*, **2**, 75 (2012).
19. K. Chebout, A. Iratni, A. Bouremana, K. M'hammedi, H. Menari, A. Keffous, N. Gabouze, The Third International Conference on Sensor Device Technologies and Applications, SENSORDEVICES 2012, Rome, Italy, 2012, p.42.
20. E. H. Espinosa, R. Ionescu, B. Chambon, G. Bedis, E. Sotter, C. Bittencourt, A. Felten, J.-J. Pireaux, X. Correig, E. Llobet, *Sens. Actuators B*, **127**, 137 (2007).
21. G. Lu, J. Xu, J. Sun, Y. Yu, Y. Zhang, F. Liu, *Sens. Actuators B*, **162**, 82 (2012).
22. Y. Gui, S. Li, J. Xu, C. Li, *J. Microelectr.*, **39**, 1120 (2008).
23. D. R. Patil, L. A. Patil, P. P. Patil, *Sens. Actuators B*, **126**, 368 (2007).
24. G. Korotcenkov, Handbook of Gas Sensor Materials: Properties, Advantages and Shortcomings for Applications Volume 1: Conventional Approaches, Springer, 2013.
25. B. Geng, C. Fang, F. Zhan, N. Yu, *Small*, **4**, 1337 (2008).
26. Z. Li, Y. Zhou, C. Bao, G. Xue, J. Zhang, J. Liu, T. Yu, Z. Zou, *Nanoscale*, **4**, 3490 (2012).
27. S. Baruah, J. Dutta, *Sci. Technol. Adv. Mater.*, **12**, 01300410 (2011).
28. K. Zakrzewska, *Thin Solid Films*, **391**, 229 (2001).
29. J. Y. Son, G. Lee, M.-H. Jo, H. Kim, H. M. Jang, Y.-H. Shin, *J. Am. Chem. Soc.*, **131**, 8386 (2009).
30. Z. Y. Yuan, F. Huang, J. T. Sun, Y. H. Zhou, *Chem. Lett.*, **31**, 408 (2002).
31. J. M. Wu, C. Xu, Y. Zhang, Z. L. Wang, *ACS Nano*, **6**, 4335 (2012).
32. Y.-J. Chang, D.-H. Lee, G. S. Herman, C.-H. Chang, *Electrochem. Solid-State Lett.*, **10**, H135 (2007).
33. C.-G. Lee, A. Dodabalapur, *Appl. Phys. Lett.*, **96**, 2435011 (2010).
34. S.-J. Seo, C. G. Choi, Y. H. Hwang, B.-S. Bae, *J. Phys. D*, **42**, 0351061 (2009).
35. S. An, C. Jin, H. Kim, S. Lee, B. Jeong, C. Lee, *Nano*, **7**, 12500131 (2012).
36. A. Sivapunniam, N. Wiromrat, M. T. Z. Myint, J. Dutta, *Sens. Actuators B*, **157**, 232 (2011).
37. B. C. Yadav, R. Singh, S. Singh, P. K. Dwivedi, *Intern. J. Green Nanotechn.*, **4**, 37 (2012).
38. J. Huang, X. Xu, C. Gu, W. Wang, B. Geng, Y. Sun, J. Liu, *Sens. Actuators B*, **171–172**, 572 (2012).
39. H. Fan, Y. Zeng, X. Xu, N. Lv, T. Zhang, *Sens. Actuators B*, **153**, 170 (2011).
40. P. Song, Q. Wang, Z. Yang, *Sens Actuators B*, **156**, 983 (2011).
41. Y. Zeng, K. Zhang, X. Wang, Y. Sui, B. Zou, W. Zheng, G. Zou, *Sens. Actuators B*, **159**, 245 (2011).
42. W. Zeng, T. Liu, Z. Wang, *Mater. Transact.*, **51**, 1326 (2010).
43. W. Zhang, C. Zeng, M. Kong, Y. Pan, Z. Yang, *Sens. Actuators B*, **162**, 292 (2012).
44. H. Men, P. Gao, B. Zhou Y. Chen, C. Zhu, G. Xiao, L. Wanga, M. Zhang, *Chem. Commun.*, **46**, 7581 (2010).
45. J. Chen, L. Lu, W. Wang, *J. Phys. Chem. C*, **116**, 10841 (2012).
46. R. Acharya, Y. Q. Zhang, X. A. Cao, *Thin Solid Films*, **520**, 6130 (2012).
47. K. Saravanakumar, K. Ravichandran, R. Chandramohan, S. Gobalagrishnanc, M. Chavalic, *Superlatt. Microstr.*, **52**, 528 (2012).

48. V. A. Moshnikov, I. E. Gracheva, V. V. Kuznezov, A. I. Maximov, S. S. Karpova, A. A. Ponomareva, *J. Non-Cryst. Solids*, **356**, 2020 (2010) .
49. I. E. Gracheva, V. A. Moshnikov, S. S. Karpova, E. V. Maraeva, *J. Phys. Conf. Ser.*, **291**, 0120171 (2011).
50. I. E. Gracheva, Y. M. Spivak, V. A. Moshnikov, AFM techniques for nanostructures materials used in optoelectronic and gas sensors, IEEE Eurocon-2009, Saint-Petersburg, 2009, p.1250.
51. I. E. Gracheva, V. A. Moshnikov, E. V. Maraeva, S. S. Karpova, O. A. Alexandrova, N. I. Alekseyev, V. V. Kuznetsov, G. Olchowik, K. N. Semenov, A. V. Startseva, A. V. Sitnikov, J. M. Olchowik, *J. Non-Cryst. Solids*, **358**, 433 (2012) .
52. V. A. Moshnikov, I. E. Gracheva, M. G. An'chkov, *Glass Phys. Chem.* , **37**, 485 (2011).
53. A. A. Ponomareva, V. A. Moshnikov, G. Suchaneck, *Mater. Sci. Eng.*, **30** , 0120031 (2012).
54. V. A. Moshnikov, I. E. Gracheva, A. S. Lenshin, Y. M. Spivak, M. G. Anchkov, V. V. Kuznetsov, J. M. Olchowik, *J. Non-Cryst. Solids*, **358**, 590 (2012).
55. N. V. Kaneva, D. T. Dimitrov, C. D. Dushkin, *Appl. Surf. Sci.*, **257**, 8113 (2011).
56. Y. Chen, L. Yu, Q. Li, Y. Wu, Q. Li, T. Wang, *Nanotech.* , **23**, 415501 (2012).
57. L. H. Germer, *Phys. Rev.*, **56**, 58 (1939).
58. A. K. Srivastava, R. Kishore, S. A. Agnihotry, *Indian J. Eng. Mater. Sci.*, **11**, 315 (2004).
59. I. E. Gracheva, V. A. Moshnikov, M. G. An'chkov, *Instrum. Exper. Tech.*, **56**, 209 (2013).
60. T. Fu, *Sens. Actuators B*, **140**, 116 (2009).

ОПРЕДЕЛЯНЕ ПРИ СТАЙНА ТЕМПЕРАТУРА НА СЕНЗОРНИТЕ СВОЙСТВА НА МЕЗОПОРЕСТ СЛОЙ ОТ ЦИНКОВ СТАНАТ ПО ОТНОШЕНИЕ НА ИЗПАРЕНИЯ НА АЦЕТОН

И. Е. Кононова^{1,2}, Д. М. Воробъов¹, Д. Ц. Димитров^{3*}, А. Ц. Георгиева⁴, В. А. Мошников^{1,5}

¹ Катедра по Микро- и Наноелектроника, Санкт-Петербургски държавен електротехнически университет, Санкт-Петербург 197376, Русия

² Катедра по Машины и технологии за формиране на метални детайли, Санкт-Петербургски държавен политехнически университет, Санкт Петербург 195251, Русия

³ Лаборатория за Наука и технология на наночастици, Катедра по Обща и неорганична химия, Факултет по Химия и фармация, Софийски университет, София 1164, България

⁴ Инженерен изследователски център за изследване на свойствата на елементарните частици, Катедра по Материалознание и инженерни науки, Университет на Флорида, Гейнсвил, Флорида 32611, САЩ

⁵ Катедра по Интегрална електроника, Санкт-Петербургски държавен политехнически университет, Санкт Петербург 195251, Русия

Получена на 13 януари 2015, Преработена на 18 август 2015

(Резюме)

Цинк станатни порьозни наноструктурирани композиции от наночастици са получени под формата на тънки слоеве посредством метода химическо отлагане от изпарения. На формираните по гореспоменатия начин слоеве са изследвани фазовия състав и състоянието на повърхността. При прилагане на променливо електрическо поле електрическите характеристики на слоя се измененят под въздействие на изпарения от ацетон при стайна температура. Като резултат на това взаимодействие радиуса на полукръга на диаграмата Найкуист се намалява и центъра на полукръга на графиката се измества към по-висока честота. При описване на резистивно-емкостните свойства на пробите се оценява характерното време на акумулиране на заряд на въздушна атмосфера и при излагане на ацетонови изпарения. Стойностите на чувствителността към изпарения на ацетон в честотния обхват от 1 Hz до 50KHz са изчислени по два начина на базата на реални и имагинерни компоненти на комплексния импеданс.

Concentration of flavonoids in ethanolic extracts from tobacco leaves through nanofiltration

I. Tsibranska^{1*}, V. Karabojikova^{2a}, J. Jeliakov²

¹Institute of Chemical Engineering, Bulgarian Academy of Sciences, 1113 Sofia, Bulgaria

²Department of Chemical Engineering, University of Chemical Technology and Metallurgy, bul. "Kl.Ohridski" 8, 1756 Sofia, Bulgaria

Received November 20, 2014, Revised February 2, 2016

Bioactive compounds (BAC) such as soluble polyphenols and flavonoids, extracted from plant materials, are successfully treated by membrane operations, in view of their separation or concentration. In the present study nanofiltration of ethanolic extracts from tobacco leaves is performed, focusing on concentrating the content of polyphenols and flavonoids (mainly rutin). Membranes DuramemTM 300 and Starmem 240 with molecular weight cut off (MWCO) 300 and 400Da have been used. The obtained rejections with both membranes are about 88%, close to the measured value for the model system rutin-ethanol (92%), and tend slightly to decrease during operation. Observed average flux for real extracts are close to the values for the model system rutin-ethanol: 4.5 – 5.5 vs. 5.3 L/(m².h) for Duramem 300 and somewhat lower for Starmem 240 membrane. The flux vs time evolution for both membranes shows a similar initial decrease and tends to stabilize during longer operation time. The results prove that the two membranes are suitable for concentrating (volume concentration factor 2.5-3.5) extracts from tobacco leaves in terms of flavonoids.

Keywords: nanofiltration, solid-liquid extraction, rutin, tobacco leaves.

INTRODUCTION

Bioactive compounds (BAC) as polyphenols and flavonoids in plant materials, extracted by appropriate solvent and further treated by membrane operations, are promising and intensively investigated area of scientific research in view of BAC separation or concentration. A large number of potential applications are focused on organic solvent nanofiltration (OSN) coupled with solid-liquid extraction of valuable compounds from plant material [1].

The leaves of *Nicotiana tabacum* are not only the most important raw material for the tobacco industry, but also an interesting source of bioactive natural compounds, among which the group of flavonoids is increasingly studied [2-5]. Rutin (C₂₇H₃₀O₁₆, quercetin-3-rutinoside) is one of the major polyphenol components of tobacco leaves with a number of pharmacological activities [6]. Rutin is a low solubility compound (0.125mg/ml in water [6, 7]), which further motivates the search of an optimum extraction method regarding yield and reasonable cost.

A comprehensive overview of the methods applied for rutin extraction from plant materials is

shown in [6, 8, 9]. Either a HPLC component analysis, or total phenolics (TP) and total flavonoids (TF) characterization is used. In the latter case TP are usually referred to the concentration of chlorogenic acid, being highest among the polyphenol compounds in tobacco leaves. Different solvents are reported: water and organic solvents such as methanol, ethanol, acetone, N,N-dimethylformamide etc [10], higher content of polyphenols being obtained with increase in polarity of the solvent. The addition of water (EtOH-H₂O, MeOH-H₂O etc.) usually results in higher polyphenols content than in the pure solvent [10]. Largely varying liquid-solid ratios (10:1 to 90:1) and contact times (most often less than 1h) are reported. Some of the literature data about rutin extraction from tobacco leaves and waste are summarized in Table 1.

Concerning membrane techniques application, concentration of the extract from tobacco leaves has been realized by electrodialysis in combination with filtration through membrane with MWCO of 500 Da, as well as by ion-exchange membranes such as AM-2 and AM-4 [15] (especially for chlorogenic acid, scopoletin and rutin). Concentration or separation of the valuable bioactive components by nanofiltration has not been studied, though OSN has been increasingly investigated in view of treating plant extracts, including separation/concentration of polyphenols

* To whom all correspondence should be sent:

E-mail: tsibranska@ice.bas.bg

^a Actual address Institute of Physical Chemistry, Bulgarian Academy of Sciences, 1113 Sofia, Bulgaria

Table 1. Details of the extraction of flavonoids from milled tobacco leaves/ wastes.

Time [min]	Extracting solvent	Analysis of the chemical composition	Liquid to solid ratio	Extraction mode	Ref. and raw material
15	C ₂ H ₅ OH-H ₂ O 8:2 (v/v)	TP** : UV-vis, Folin–Ciocalteu, ref. compound: chlorogenic acid	10:1	ultrasound assisted	[11] tobacco leaves
-	CH ₃ OH-H ₂ O 7:3 (v/v)	Apigenin, quercetin, rutin :UV-vis, NMR, HPLC	-	conventional	[2] waste tobacco leaves
1	(CH ₃) ₂ CO-H ₂ O, (v/v) 0:1; 3:7; 4:6	Chlorogenic acid UV-vis	40:1	microwaves assisted	[12] tobacco leaves and waste
90 (25)* 120(60)*	H ₂ O C ₂ H ₅ OH (96%)	Total yield, weight analysis.	15:1 -40:1	conventional	[13, 14] tobacco leaves
30	EtOAc- CH ₃ OH 1:1; CH ₃ OH	HPLC	10:1 to 50:1	ultrasound assisted	[5] tobacco leaves and waste
60	C ₂ H ₅ OH (85% in water)	UV-vis: TP (Folin–Ciocalteu , gallic acid), TF** (AlCl ₃)	10:1	heat reflux	[4] tobacco leaves
10-90 (30*)	CH ₃ OH	HPLC	15:1 to 90:1 (45:1)	ultrasound assisted	[7] cigarettes tobacco

* to reach the plateau of the kinetic curve

** TP- total polyphenols; TF – total flavonoids

and flavonoids [16-26]. The method has advantages for multicomponent systems, containing sensitive to elevated temperatures components and allows for the regeneration of the solvent. The technology is especially promising when dealing with extracts from cheap and widely available materials, containing bioactive components that can be concentrated by nanofiltration. The content of some valuable flavonoids (such as rutin) in the tobacco waste in low concentrations makes them a suitable object for concentration by this process.

This study concerns the recovery of rutin from tobacco leaves and waste by solid-liquid extraction and subsequent concentration of the extract by nanofiltration. The molecular weight of most of the important polyphenols components in the extract from tobacco leaves [5] is over 300 Da - chlorogenic acid (C₁₆H₁₈O₉, 354 Da) and its isomers neochlorogenic acid (5-O-caffeoylquinic acid) and 4-O-caffeoylquinic acid, and highest for the flavonoids rutin (quercetin-3-O-rutinoside, MW 610 Da) and kaempferol-3-rutinoside (MW 594). It is expected that nanofiltration using organic solvent resistant (OSR) membranes with MWCO ≥300 Da will allow the successful concentration of the extract in terms of flavonoids. In the present study two OSR membranes were used - Duramem™ (modified polyimide) and Starmem 240 (polyimide) with MWCO 300 and 400 Da respectively.

EXPERIMENTAL

° Extraction

The plant material for extraction was provided by Bulgartabac Sofia - tobacco leaves with defined origin (the region of Petrich) and moisture content 11%. All samples were grounded to powder and then subjected to extraction with ethanol. After batch extraction in a stirred vessel at room temperature 20±1 °C and intensive mixing (stirring speed 300 rpm) the extract was filtered and analyzed. If not additionally treated, the ethanolic extract from tobacco leaves has slightly acidic pH. In our study pH of the extract was 5.93, obtained with liquid/solid ratio 10:1 and 70% ethanol (where highest content of polyphenols is observed), the deviation from neutral being less pronounced for the extracts, obtained with 96% ethanol. The latter were further used in the membrane separation runs with two organic solvent resistant membranes.

The extraction kinetics with 96% ethanol was followed during 12h; the obtained results indicate a contact time of 3h as needed to reach the plateau of the kinetic curve. The recovered amount of flavonoids was 0.8 mg/(g solids) at liquid to solid ratio 10:1. Increasing the latter up to 30:1 allowed evaluating the maximum extractable flavonoids concentration as 1.108 mg/g solid. Further increase of the liquid volume has practically negligible effect on the amount of the extracted target component.

◦ Spectrophotometric analysis

For the spectrophotometric determination of total flavonoids concentration a color reaction with aluminum trichloride was used. According to Ordonez [27] 0.5 ml of the sample was added to 0.5 ml AlCl₃ (2% solution in ethanol). After 1 hour in the dark the absorbance was measured at a wavelength of 425 nm. Three measurements were performed for each sample. The concentrations in the extract (C_f), retentate (C_r) and permeate (C_p) were calculated as rutin equivalent, according eq. (1):

$$\text{Abs} = 10.953 C \quad (R^2 = 0.997) \quad (1)$$

where C [mg/ml] is the concentration of total flavonoids (up to 0.07 mg/ml) and Abs is the measured absorbance. The calibration curve was obtained with model solution of rutin-hidrate in ethanol. Ethanol (96%) was supplied by Valerus (Bulgaria); Aluminium chloride anhydrous and rutin (as rutin hydrate $\geq 94\%$) was supplied by Sigma-Aldrich.

◦ Nanofiltration

Batch nanofiltration in dead-end mode was performed on a laboratory cell (METcell, Evonic MET LTD, UK) with effective surface area of 54 cm² at transmembrane pressure of 20 bar and working volume up-to 200 ml. During nanofiltration flow and rejection evolution over the time of filtration was measured. The concentration of equivalent rutin was determined after each 20 ml permeate.

RESULTS AND DISCUSSION

The permeate flux and rejection evolution during nanofiltration with Duramem 300 (MWCO 300Da) and Starmem 240 (MWCO 400Da) are illustrated in Figs.1 and 2 for similar feed concentrations of rutin (0.022, 0.025 mg/ml respectively, see Fig.2). An initial pronounced flux decrease within the first 3 hours is observed with both membranes. The flux vs time data tend to stabilize within longer operation time (6h), the final flux being in the range of 2 - 3 l/(m².h).

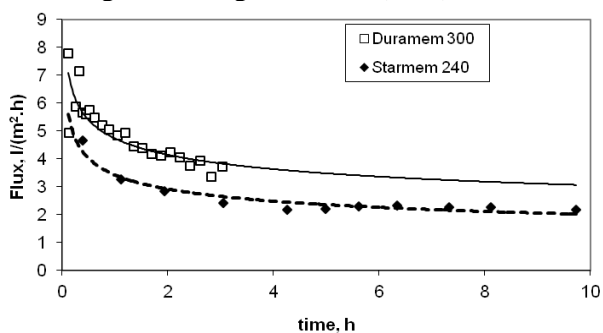


Fig. 1. Measured flux versus time of filtration

A similar tendency is observed in the time evolution of observed rejections, shown in Fig.2. An initial increase is better observed with Duramem 300, corresponding to the more pronounced flux decrease in this period and associated with an increasing membrane resistance. After that the rejection values tend to stabilize and even a slight tendency to decrease can be observed. The two membranes show similar rejections values.

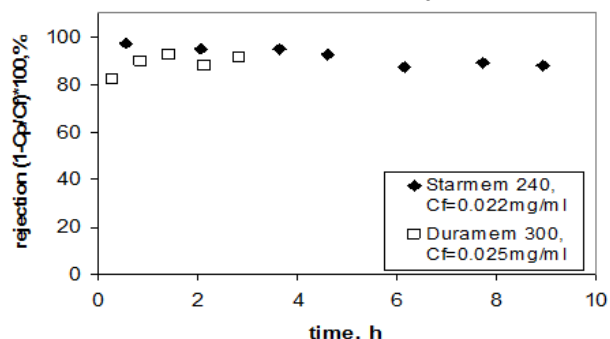


Fig. 2. Measured rejections versus time of filtration

The additional membrane resistance is usually attributed to fouling and related with different phenomena such as concentration polarization, cake layer formation, adsorption of solute molecules inside the pores or pore blocking when the pore size is similar to the molecular dimensions [28].

The four kinetic models commonly used for systems showing flux decline are given in Table 2 together with the calculation results for the first 6 hours of filtration. As can be seen from Table 2, the cake layer formation model gives best correlation, but a statistically good description of the flux decline is also obtained with the rest of the tested models, which rather suggests that fouling phenomenon is not very pronounced under the working conditions (range of feed concentrations in term of flavonoids 0.012 to 0.042 mg/ml).

Similar observations were already reported with nanofiltration of natural extracts containing polyphenols and flavonoids [29, 30], based on the original model, proposed by Hermia to describe the permeate flux decline during constant-pressure filtration [31].

The flux dependence on feed concentration is shown in Fig.3. These results concern average flux values, obtained with Duramem 300 during the initial 3h of filtration, where the flux decline is most pronounced. The volume ratio permeate to feed was kept in the range of 0.6 to 0.7, which defines the limits of the achieved degree of concentration. The feed concentration affects the measured flux, but the latter remains close to the measured value for the model system rutin-ethanol: 4.5 – 5.5 vs. 5.3 L/m².h (model system, R²=0.998).

Table 2. Kinetic models to evaluate flux decline data

Fouling mechanism	Model equation (linearized) [29]	Calculated flux vs time data	R ²
total pore blocking	$\ln(J) = \ln(J_0) - k_1 t$	$\ln(J) = 1.4344 - 0.0737 \cdot t$	0.9043
standard pore blocking model	$J^{-1} = J_0^{-1} + k_2 \cdot t$	$J^{-1} = 0.2354 + 0.0215 \cdot t$	0.9384
intermediate pore blocking	$J^{-1/2} = J_{0/2}^{-1} + k_3 \cdot t$	$J^{0.5} = 0.4868 + 0.0199 \cdot t$	0.9224
cake layer formation	$J^{-2} = J_0^{-2} + k_4 \cdot t$	$J^2 = 0.0534 + 0.0128 \cdot t$	0.9639

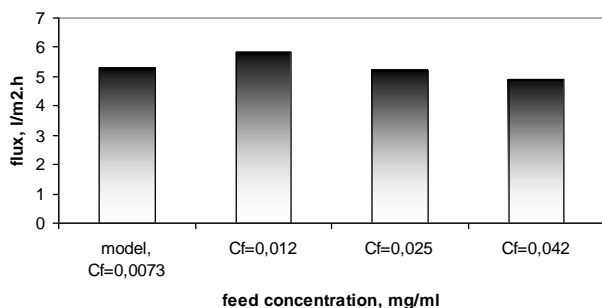


Fig.3. Measured average flux vs feed concentration

The average rejections, obtained with different flavonoids concentrations in the feed are shown on Fig.4. The increase of the feed concentration has a slight effect, resulting in decreasing rejection, whose average value is about 88%. The observed rejections are close to the measured ones for the model system rutin-ethanol (92%). This fact together with the high and approximately constant rejections proves the suitability of the membranes Duramem 300 and Starmem 240 for concentrating natural extracts from tobacco in terms of flavonoids. Both membranes were previously used for nanofiltration of ethanolic extracts from Sideritis [16], where comparable, though higher rejections were observed and the possible reuse of the permeate as extracting agent was proven.

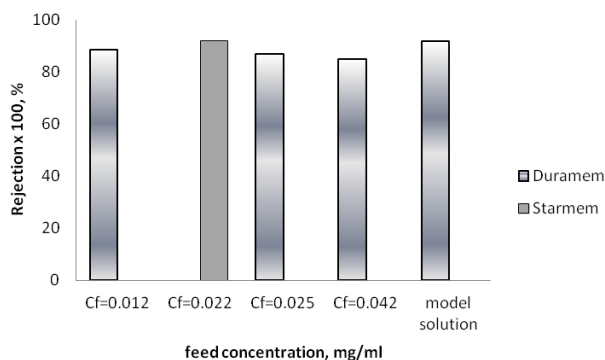


Fig.4. Measured average rejections vs feed concentration

The concentration effect on the rejection is strongly dependent on the mass transfer characteristics of the system [32], which explains

the variety of observations, obtained in the OSN literature – practically constant [24, 33, 34], increasing [35] or decreasing [32] rejections. There are also different reasons for these observations. The constancy is viewed as indication for low membrane solute interaction and stable membrane behavior towards both solute and solvent [23, 36]. Membrane compaction could lead to increasing rejections. Such effect is observed in nanofiltration of ethanolic extracts from *Sideritis* with Duramem™ 500 when the transmembrane pressure increased from 30 to 50 bar [16]. In [28] a decrease of rejection is observed and predicted with the solution-diffusion model. For complex multicomponent solutions (as natural extracts) the analysis of the rejection vs concentration profile is even more difficult to allow for definite conclusions. In order to check the concentration effect nanofiltration was performed at high degree of concentration (permeate to feed ratio up to $V_p/V_f = 0.85$), as well as with model system rutin hydrate - ethanol with maximum feed concentration (determined experimentally 1.49 mg/ml, close to the solubility data found for rutin-3 hydrate in ethanol [39]). In case of pronounced effect of concentration polarization the solute concentration at the membrane surface is expected to be different from the one in the bulk retentate (C_r) and this fact should be taken into account [37]. Otherwise the calculated rejections by eq. (2) and (3) are expected to differ essentially, eq.(3) giving lower rejections than expected from the mass balance [24].

$$R = \left(1 - \frac{C_p}{C_f} \right) \cdot 100, \% \quad (2)$$

$$R = \left(\frac{\ln(C_r / C_f)}{\ln(V_f / V_r)} \right) \cdot 100, \% \quad (3)$$

Here V_f and V_r stand for the respective volumes of the feed and retentate.

Calculations according to eq. (2) and (3) showed comparable rejections close to 80% (77.8% and 79.8% respectively), which supports the absence of an essential concentration effect at the membrane surface. For higher feed concentrations the solubility limit was exceeded in the retentate, the fact being already pointed out in the literature for rutin extraction [38].

CONCLUSION

Extraction with ethanol of tobacco leaves at room temperature shows total flavonoids content 1.1 mg/(g solid) rutin equivalent. About 90% of the flavonoids are extracted during the first 3h, so this time can be considered as sufficient for practical applications.

The nanofiltration of the extracts was studied with OSR membranes Duramem 300 and Starmem 240. Average rejections show small variation with concentration, difficult to separate from the experimental error during the measurements, in view of the solution (natural extract, multicomponent) and the accuracy of the chemical analysis (group analysis, spectrophotometric).

The concentration effect is better seen from the rejection vs time plot. Both membranes show rejections about 88% and tendency to decrease with increasing degree of concentration. This corresponds to observed and predicted rejections in the OSN literature [31].

Permeate flow decreases with increasing concentration, the effect being important in the beginning (the first 3h of operation). Then the flux decline is much less pronounced, tending to stabilize at flux values between 2 and 3 l/m².h. Flux and rejections with real extracts are close to the measured with the model system. The results prove that the two membranes are suitable for concentrating extracts from tobacco leaves in terms of flavonoids.

REFERENCES

1. I. Tsibranska, B. Tylkowski, in "Integrated membrane operations in the food production", Ed. A. Cassano, E. Drioli, chapter 11, p.269-294, De Gruyter, 2014
2. F. Fathiazad, Ab. Delazar, R. Amiri, S.D. Sarker, *Iranian Journal of Pharmaceutical Research* **3**, 222 (2006).
3. J. Chen, H. Leng, Y. Duan, W. Zhao, G. Yang, Y. Guo, Y. Chen, Q. Hu, *Phytochemistry Letters* **6**, 144 (2013).
4. Q.-M. Ru, L.-J. Wang, W.-M. Li, J.-L. Wang and Y.-T. Ding, *Molecules*, **17**, 11281 (2012).
5. M. Docheva, S. Dagnon, St. Statkova-Abeghe, *Natural Product Research*, Taylor & Francis, <http://dx.doi.org/10.1080/14786419.2014.902947>

- (2014).
6. L.S. Chua, *Journal of Ethnopharmacology*, **150**, 805 (2013).
7. Y. Sun, W. Li, J. Wang, J. Bi, Sh. Su, *Molecules*, **17**, 3751 (2012).
8. M. Naczka, F. Shahidi, *Journal of Pharmaceutical and Biomedical Analysis*, **41**, 1523 (2006).
9. I. Ignat, I. Volf, V.I. Popa, *Food Chemistry*, **126**, 1821 (2011).
10. P. Duangsri, K. Juntarapun, C. Satirapipathkul, In *Proceedings of the RMUTP International Conference: Textiles & Fashion* (2012).
11. H. Wang, M. Zhao, B. Yang, Y. Jiang, G. Rao, *Food Chemistry*, **107**, 1399 (2008).
12. Zh. Li, D. Huang, Zh. Tang, Ch. Deng, X. Zhang, *Talanta*, **82**, 1181 (2010).
13. E. Simeonov, I. Tsibranska, A. Minchev, *Chem. Eng. Journal*, **73**, 255 (1999).
14. E. Simeonov, Ch. Chilev, *Journal of Chemical Technology and Metallurgy*, **50**(5), 597 (2015).
15. M. Aider, D. de Halleux, L. Bazinet, *Trends in Food Science & Technology*, **19**, 351 (2008).
16. B. Tylkowski, I. Tsibranska, R. Kochanov, G. Peev, M. Giamberini, *Food and Bioproducts Processing*, **89**(4), 307 (2011).
17. G. Peev, P. Penchev, D. Peshev, G. Angelov, *Chemical Engineering Research and Design*, **89**(11), 2236 (2011).
18. B. Tylkowski, B. Trusheva, V. Bankova, M. Giamberini, G. Peev, A. Nikolova, *Journal of Membrane Science*, **348**(1-2), 124 (2010).
19. M.T. Machado, B.C. Mello, M.D. Hubinger, *Journal of Food Engineering*, **117**(4), 450 (2013).
20. P.C. Pinto, M.I. Mota, J.M. Loureiro, A.E. Rodrigues, *Separation and Purification Technology*, **132**, 234 (2014).
21. D. Peshev, L.G. Peeva, G. Peev, I.I. Baptista, A.T. Boam, *Chemical Engineering Research and Design*, **89**(3), 318 (2011).
22. B.C. Mello, J.C. Petrus, M.D. Hubinger, *Journal of Food Engineering*, **96**(4), 533 (2010).
23. A.P. Prudêncio, E.S. Prudêncio, R.D. Amboni, A.N. Murakami, M. Maraschin, J.C. Petrus, P.J. Ogliari, R.S. Leite, *Food and Bioproducts Processing*, **90**(3), 399 (2012).
24. I. Tsibranska, B. Tylkowski, *Food and Bioproducts Processing*, **91**(2), 169 (2013).
25. A.N. Murakami, R.D. Amboni, E.S. Prudêncio, E.R. Amante, C.B. Fritzen-Freire, B.C. Boaventura, I.B. Muñoz, C.S. Branco, M. Salvador, M. Maraschin, *Food Chemistry*, **141**(11), 60 (2013).
26. B. Díaz-Reinoso, A. Moure, H. Domínguez, J.C. Parajó, *Chemical Engineering Journal*, **175**, 95 (2011).
27. G.J. Ordonez, M.A. Vattuone, M.I. Isla, *Food Chemistry*, **97**, 452 (2006).
28. C. M. Salgado, L. Palacio, P. Prádanos, A. Hernández, C. González-Huerta, S. Pérez-

- Magariño, *Food and Bioproducts Processing*, **94**, 610 (2015).
29. B. C. B. S. Mello, J.C. C. Petrus, M.D. Hubinger, *Studies in Chemical Process Technology (SCPT)* **1**(4), 55 (2013).
30. M.T.C. Machado, B. C.B.S. Mello, M.D. Hubinger, *Food and Bioproducts Processing*, **95**, 304 (2015).
31. J. Hermia, *Chemical Engineering Research and Design*, **60**, 183 (1982).
32. P. Silva, A.G. Livingston, *Journal of Membrane Science*, **280**, 889 (2006).
33. D. Shi, Y. Kong, J. Yu, Y. Wang, J. Yang, *Desalination*, **191**, 309 (2006).
34. B. Su, Zh. Wang, J. Wang, Sh. Wang, *Journal of Membrane Science*, **251**, 189 (2005).
35. J.A. Whu, B.C. Baltzis, K.K. Sirkar, *Journal of Membrane Science*, **170**, 159 (2000).
36. H.J. Zwijnenberg, A.M. Krosse, K. Ebert, K-V. Peinemann, F.P. Cuperus, *JAOCs*, **76**, 83 (1999).
37. D.A. Patterson, L.Y. Lau, Ch. Roengpithya, E.J. Gibbins, A.G. Livingston, *Desalination*, **218**, 248 (2008).
38. E. Miniati, L. Montanari, *Italian Journal of Food Science*, **10**(4), 339 (1998).
39. www.pvp.com.br/EN_rutin_dab_10_technical_data.htm

КОНЦЕНТРИРАНЕ НА ФЛАВОНОИДИ В ЕТАНОЛОВ ЕКСТРАКТ ОТ ТЮТЮНЕВИ ЛИСТА ЧРЕЗ НАНОФИЛТРУВАНЕ

И. Х. Цибранска¹, В. И. Карабожикова², Ж. Желязков²

¹Институт по инженерна химия, Българска Академия на науките, 1113 София, България

²Катедра по инженерна химия, Химико-Технологичен и Металургичен Университет, 1756 София, България

Постъпила на 20 ноември, 2014 г. коригирана на 2 февруари, 2015 г.

(Резюме)

Мембранни процеси на разделяне се прилагат успешно към биоактивни вещества като разтворими полифеноли и флавоноиди, извлечени от растителни материали, с оглед на тяхното концентриране или разделяне. В настоящото изследване е проведено нанofilтруване на етанолови екстракти от тютюневи листа с цел концентриране на съдържанието на полифеноли и флавоноиди (главно рутин). Използвани са мембрани Duramem™ 300 и Starmem 240 с праг на разделяне съответно 300 и 400 Da. Наблюдавано е 88% задържане по общи флавоноиди, близко до измерената стойност за моделна система рутин-етанол (92%), и с тенденция за леко намаляване във времето. Наблюдаваните средни стойности за потока пермеат при реални екстракти са близки до тези за моделната система рутин-етанол: 4.5-5.5 vs. 5.3 L / (m².h) за Duramem 300 и малко по-ниска за Starmem 240. Развитието на потока във времето за двете мембрани показва подобен ход: първоначално намаляване с тенденция към стабилизиране при по-големи времена на филтруване. Резултатите доказват, че двете мембрани са подходящи за концентриране на флавоноиди от екстракти на тютюневи листа в изследваните обемни съотношения захранване спрямо ретенат (2.5-3.5).

Nickel doping effect on the photocatalytic activity of TiO₂/SiO₂ nanocomposite

B. Khodadadi

Department of Chemistry, University of Qom, Qom, Iran

Received January 24, 2015, Revised July 31, 2015

TiO₂/SiO₂ and TiO₂/SiO₂/Ni nanocomposite powders were prepared by a sol-gel technique. Moreover, different concentrations of dopant were added to investigate the effect of the metal doping effect. Structures were characterized by IR spectroscopy, Scanning Electron Microscopy (SEM), Energy Dispersive Analytical X-Ray (EDAX) and X-Ray Diffraction (XRD) methods. Moreover, the absorption coefficients of the samples were analyzed by Tauc's approach and the direct band gaps also were calculated. The photocatalytic activity of all the samples was investigated under UV irradiation in an aqueous medium. The results revealed that metal doping plays an important role in decreasing the particle size. Furthermore, photocatalytic activity improves in the presence of a dopant.

Keywords: Sol-Gel, Nanocomposite, Photocatalytic activity, TiO₂/SiO₂/Ni

INTRODUCTION

Photocatalytic and self-cleaning properties have already become a very interesting subject for researchers and can be used for practical applications regarding environmental decontamination. These properties depend on the relationship between photocatalysis and hydrophilicity, which causes more effective cleaning over the surfaces and is useful for decomposition of organic contaminants. TiO₂ is one of the best materials for self-cleaning purposes due to its thermostability and photocatalytic properties [1,2].

Recently, many researchers have reported replacing TiO₂ by the TiO₂/SiO₂ catalyst, which is an advanced material for self-cleaning and photocatalytic properties, since TiO₂/SiO₂ exhibits different surface chemical and photochemical properties compared to TiO₂ [3, 4]. In order to improve the efficiency of the photocatalytic activity, the TiO₂/SiO₂ catalyst can be modified by the addition of various modifiers, such as metals or metallic oxides by various methods [5-8].

The metal doping process can be performed by the sol-gel method or restricted to the surface by metal deposition. Proportional abundance and low-cost properties are reasons for choosing Nickel in this process [8-11]. The photocatalytic properties are related to the surface structure of the nanocomposite powder [12]. On the other hand, organic polymers are used to prevent agglomeration of TiO₂ powder and modify its photocatalytic activity [13, 14].

Consequently, in this work, we have synthesized TiO₂/SiO₂ nanocomposites, doped with Ni. Moreover, we have investigated the effects of the molar ratio of the dopant on the particle size, structure and photocatalytic activity.

EXPERIMENTAL

Materials and Equipment

Titanium tetra isopropoxide (TTIP) (AR analytical grade, Merck Chemical Company) was used as the titanium source for the preparation of the TiO₂ photocatalysts. Nickel (II). 6 H₂O, Hydroxypropyl cellulose (HPC), HNO₃, SiO₂ colloid solution, absolute ethanol were purchased from the Merck Chemical Company. XRD measurements were performed using a Philips X'Pert PRO MPD diffractometer with CuK_α radiation from 10 to 80 (2θ) at room temperature. The morphology and microanalysis of the samples were observed by a scanning electron microscope (SEM, SEM-4100, Jeol). Ultraviolet-visible (UV-Vis) absorption spectra were obtained by means of a Varian Carry 300. FT-IR spectra were obtained via KBr pellets in the range 500 to 4000 cm⁻¹ using a Thermo Nicolet 870 FT-IR Nexus spectrophotometer.

Preparation of the Samples

All samples were prepared by the Sol-Gel technique using the following procedure:

Preparation of sample 1 (TiO₂/SiO₂ nanocomposite)

A: Preparation of solution I: 0.2 g of (HPC) was added to absolute ethanol and stirred until complete dissolution was achieved. Then, TTIP was

* To whom all correspondence should be sent:
E-mail: bkhodadadi98@yahoo.com; Khodadadi@qom.ac.ir

dissolved in this solution (with a molar ratio TTIP/ethanol = 1/75).

B: Preparation of solution II: HNO₃, deionized water and SiO₂ were dissolved in absolute ethanol (with a molar ratio ethanol /HNO₃/H₂O/SiO₂ = 43/0.2/1/30).

C: Preparation of the TiO₂/SiO₂ nanocomposite: Solution II was added dropwise into solution I and vigorously stirred for 30 min at room temperature. The obtained transparent colloidal suspension was sonicated for 30 min. and aged for 48 h to form a gel. The sample was dried in an oven at 50°C and ultimately calcinated at 500°C for 4 hours.

Preparation of samples 2, 3, 4, and 5 (TiO₂/SiO₂/Ni nanocomposite)

A: Preparation of solution I: Solution A was prepared exactly as sample 1.

B: Preparation of solution II: HNO₃, deionized water and SiO₂ were dissolved in absolute ethanol (with a molar ratio ethanol /HNO₃/H₂O/SiO₂ = 43/0.2/1/30) and then several concentrations of Ni (NO₃)₂ (0.1, 0.3, 0.6) and 1% W/W Ni (NO₃)₂/ SiO₂ were added to solution II.

C: Preparation of TiO₂/SiO₂/Ni nanocomposite: Solution II was added dropwise into solution I and vigorously stirred for 30 min at room temperature. The obtained transparent colloidal suspension was sonicated for 30 min. and aged for 48 h to form a gel. The sample was dried in an oven at 50°C and ultimately calcinated at 500°C for 4 hours.

All the above steps have been summarized in a chart in Fig. 1.

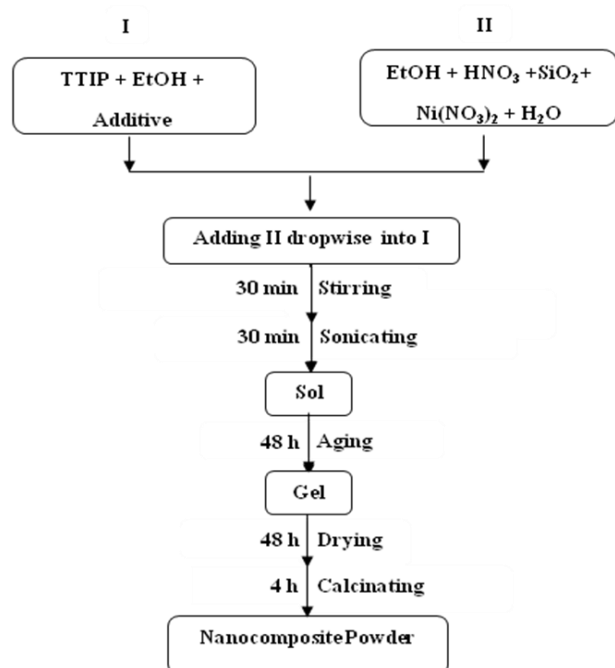


Fig. 1. Sample preparation chart

RESULTS AND DISCUSSION

FT-IR spectroscopy

Fig. 2 presents the FT-IR spectra of the samples investigated. According to these results, in all samples, wide absorption bands were observed around 3100-3700 cm⁻¹, which can be attributed to the OH stretching vibration of the surface hydroxyl group. Hydroxyl bands (3100-3700 cm⁻¹) appeared due to a great amount of propanol present during the hydrolysis of TTIP [15-20]. Moreover, because of the physically adsorbed water and hydroxyl group, absorption bands were observed around 1635 cm⁻¹ [19,20].

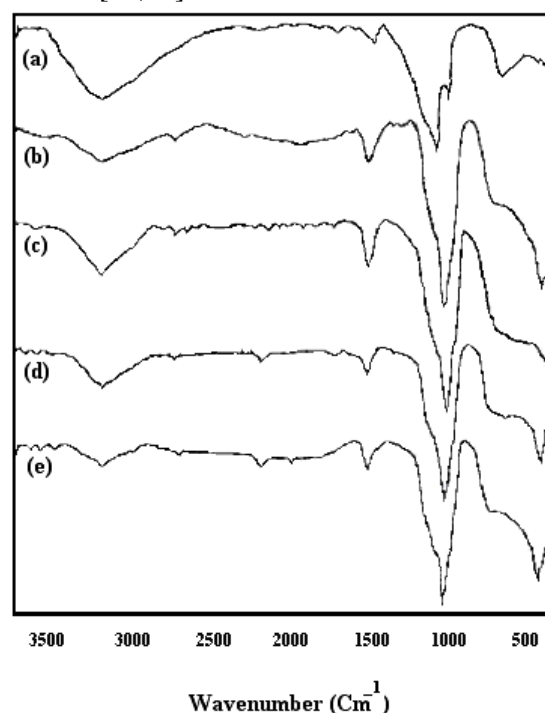


Fig. 2. FT-IR spectra of the sample sols. (a)Sample 1, (b)Sample 2, (c)Sample 3, (d)Sample 4 and (e) sample 5.

The bands at 1117 cm⁻¹ in the samples correspond to an asymmetric stretching vibration of the Ti-O bands [17-21] and the ones at 1073 cm⁻¹ are due to the symmetrical vibration of the Si-O-Si bands [20-22]. The FT-IR spectra show silicate absorptions at 789, 467 and 464 cm⁻¹, which can be assigned to Si-O-Si bending and stretching vibrations [22-24]. The peak at 602 cm⁻¹ can be assigned to a symmetric stretching vibration of the Ti-O-Ti group [22-25]. Furthermore, a band was observed at 2366 cm⁻¹, which can be assigned to Ni-TiO₂-SiO₂ [5, 7]. Exhibited broad peaks in the range of 400-1000 cm⁻¹ have contributions from the anatase phase [21-24].

XRD analysis

X-ray diffraction (XRD) analysis was employed to determine the crystallite phase and crystallinity of the samples and the results have been shown in Fig. 3.

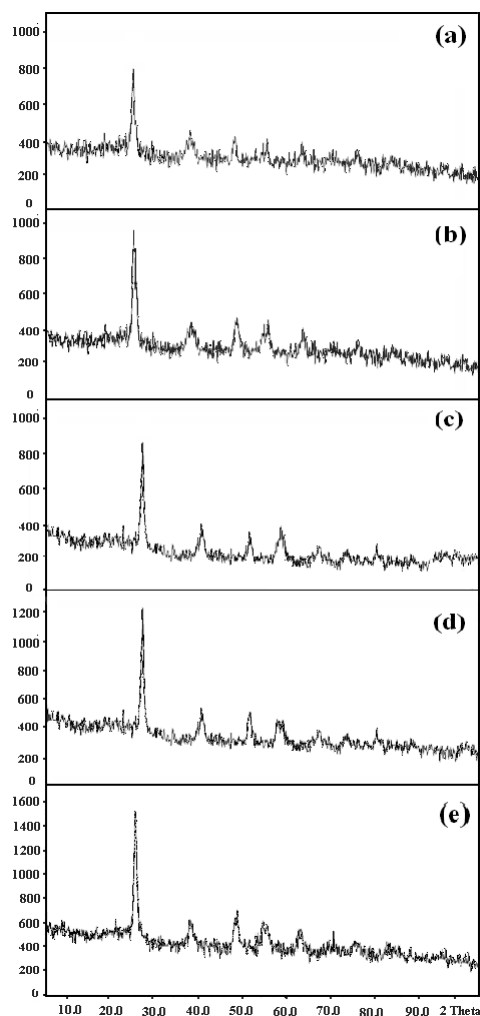


Fig. 3. XRD patterns of sol-gel synthesized TiO₂/SiO₂. (a) Sample 1, (b) Sample 2, (c) Sample 3, (d) Sample 4 and (e) Sample 5.

According to the XRD evaluation, the diffraction patterns of each sample are well in agreement with the anatase phase (the base peak in the range of $20 < 2\theta < 30$ is evidence of an anatase phase). Sample 1, without Nickel shows less of an anatase structure than other samples. The XRD results reveal that the samples show an anatase phase more than sample 1 after Ni doping and this leads one to conclude that metal doping is effective on anatase phase formation. Additionally, there is no notable shift of all diffraction peaks between the samples, confirming the successful doping of Ni into the lattice. However, the intensity of the diffraction peaks becomes higher with increasing Ni concentration.

Scanning Electron Microscopy (SEM) and EDAX analysis

All samples were identified by Scanning Electron Microscopy (SEM) analysis and their images are presented in Fig. 4. According to the images, in all samples, the nanoparticles are relatively uniform, global and slightly agglomerated. It is remarkable that the particle size decreases and becomes monotonous and particle distribution becomes narrow with the increase in Ni²⁺ doping concentration. This clearly reveals that the Nickel ion decreases the grain size. EDAX analysis has revealed that TiO₂, SiO₂ and Ni are present in all the samples.

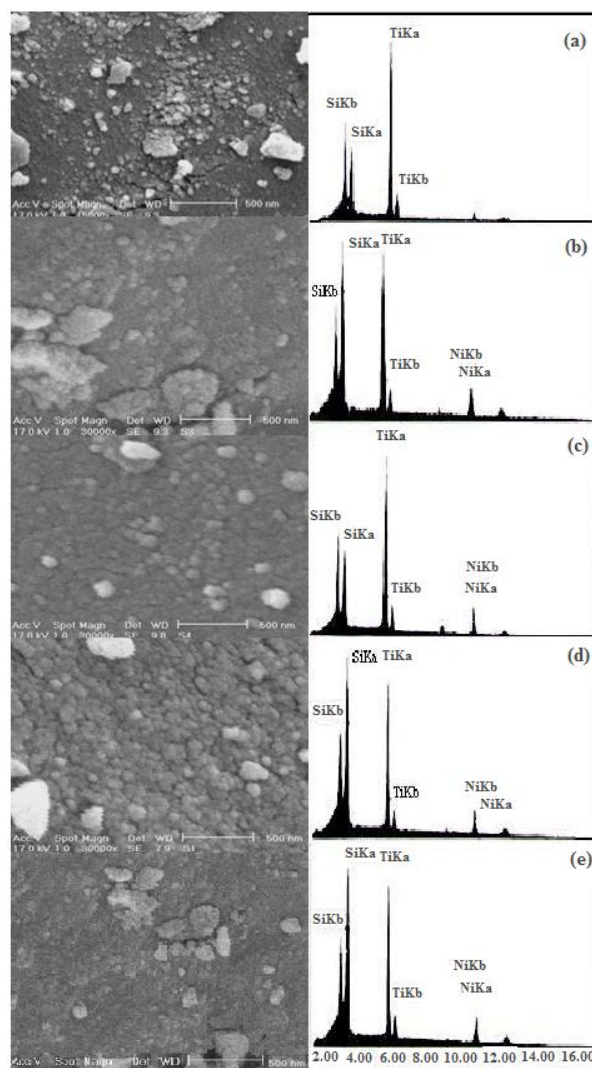


Fig. 4. SEM images for the sample powders. (a) Sample 1, (b) Sample 2, (c) Sample 3, (d) Sample 4 and (e) Sample 5.

UV-Visible spectra and Band gap calculation

UV-Vis diffuse reflectance spectroscopy was carried out to investigate the optical properties of the samples and the results are shown in Fig. 5. It

can be clearly seen that the maximum of the absorbance band shifts slightly toward a higher wavelength due to Ni doping and sample 5 shows huge absorption intensity in the higher wavelength region.

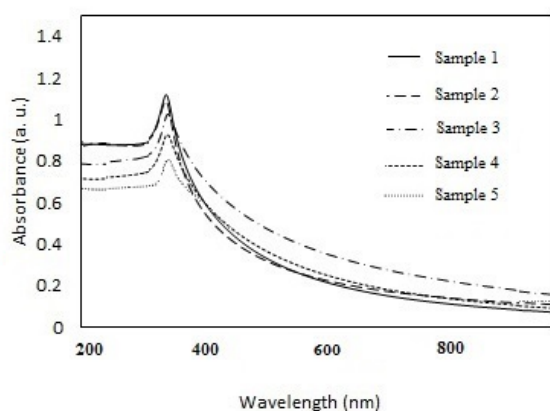


Fig. 5. Uv-vis spectra of the samples.

The absorption coefficients of the samples are analyzed utilizing a Tauc approach [26] and the direct band gap is calculated using the following equation:

$$\alpha = C (h\nu - E_g^{\text{bulk}})^2 / h\nu$$

Where α is the absorption coefficient, C is a constant, $h\nu$ is the photon energy and E_g^{bulk} is the band gap.

Table 1 shows the calculated band gap of the samples. According to these results, band gap decreases with doping Ni and increasing concentration of dopant. Fig. 6 shows the Tauc plots of the samples. Extrapolation of the linear region of the Tauc plot gives a band gap. From Fig. 6, it can be seen that, compared with sample 1, the band gap of the samples with a dopant decreases. It can be seen that the band gap slightly decreases with the increase in Ni concentration and these results are consistent with the Uv-Vis spectra.

Table 1. Calculated band gap of the samples

sample	Mole ratio ([dopant]/[TiO ₂])%	Band gap(eV)
1	-----	3.05
2	0.1	2.97
3	0.3	2.93
4	0.6	2.86
5	1	2.82

Evaluation of the photocatalytic activity of the samples

To investigate the photocatalytic activity of the samples and the effect of metal doping on the photocatalytic activity, several solutions of methyl orange (with a concentration of 5 mgL⁻¹) in

deionized water were selected as pollutant solutions for photodegradation. These solutions were set in the vicinity of a nano photocatalyst powder (0.5 g powder in 1L solution) and then placed in the dark for 24 h in order to eliminate the absorptive effect of the solution in the catalyst. Finally, the solutions were placed in the photoreactor and methyl orange concentration change was recorded by UV spectroscopy. This photoreactor system consisted of a cubic borosilicate glass reactor with an effective volume of 1000 mL, a cooling water jacket and a 15W UV lamp (Osram) with a quartz cover positioned inside the solution used as a UV light source. The reaction temperature was kept at 25 °C using cooling water.

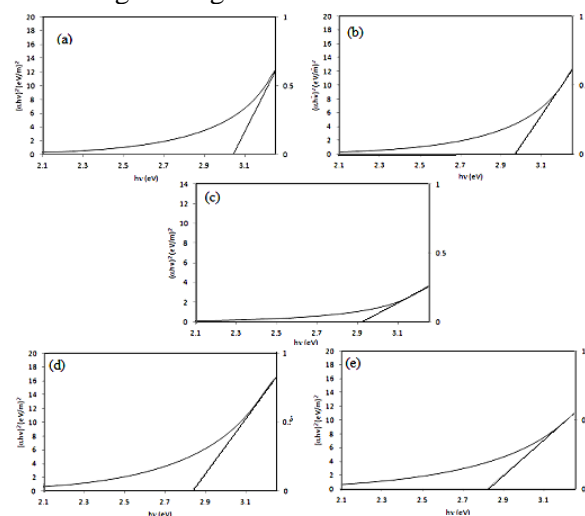


Fig. 6. The Tauc plots of samples. (a) Sample 1, (b) Sample 2, (c) Sample 3, (d) Sample 4 and (e) Sample 5.

The results are shown in Fig. 7.

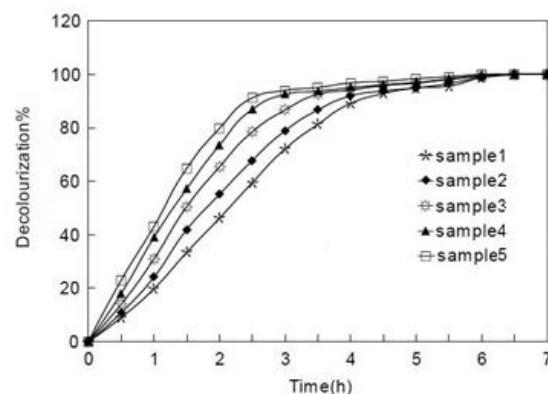


Fig. 7. Decolourization percentage of Methyl orange solution under UV radiation

According to these results, the photocatalytic activity increases with the application of metal doping. It seems that the better photocatalytic activity responses after Ni doping are due to the charge-transfer transition from the electron donor levels formed by the 3d orbital's of doped Ni²⁺ to

the conduction bands of the host materials [27]. Sample 5 (containing 1% Ni) has the highest activity in comparison with other samples. Therefore, the good photocatalytic ability of this sample can be attributed to the smaller particle size, porosity and less agglomerated nanostructure.

CONCLUSION

This research has verified that the photocatalytic activity of TiO₂/SiO₂ nanocomposite powder can be improved using metal doping. All samples have been prepared by the sol-gel method and HPC has been used as a modifier. SEM pictures have revealed that the particle size of the nanocomposite powder with 1% Ni was smaller than that of the other samples. Furthermore, the XRD pattern confirmed that the formation of the anatase structure in this sample is better than in other samples. UV-Vis diffuse reflectance spectroscopy showed a red shift with doping and 1% Ni was more effective than other concentrations. Moreover, the absorption coefficients of the samples were analyzed by the Tauc approach and the calculations confirmed that the application of dopands and dopant concentrations affect the band gap. The photocatalytic activity of the samples was examined for degradation of methyl orange in water under UV irradiation in a batch reactor. The results revealed that the photocatalytic activity of the nanocomposites increased in the presence of Nickel and according to other results; the sample with 1% Ni exhibited the best photocatalytic activity.

REFERENCES

1. C. Euvananont; C. Junin; K. Inpor; P. Limthongkul, C. Thanachayanont, *Ceram. Int.*, **34**, 1067 (2008).
2. S. Neatu; V.I. Parvulescu; G. Epure; N. Petera; V. Somoghi; G. Ricchiardi; S. Bordiga, A. Zecchina, *J. Appl. Catal. B.*, **91**, 546 (2009).
3. B. Braconnier; C.A. Paez; S. Lambert; C. Alie; C. Henrist; D. Poelman; J. Pirard; R. Cloots, B. Heinrichs, *Microporous Mesoporous Mater.*, **122**, 247 (2009).
4. Z. Liu; X. Zhang; T. Murakami, A. Fujishima, *Sol. Energy Mater. Sol. Cells.*, **92**, 1434 (2008).
5. T. A. Egerton, I. R. Tooley *J. Phys. Chem. B.*, **108**, 5066 (2004).
6. A. Fujishima; T. Rao, D. Tryk. *J. Photochem. Photobiol. C. Photochem. Rev.*, **1**, 1 (2000).
7. X. Fu; L. A. Clark; Q. Yang, M. A. Anderson, *J. Environ. Sci. Tech.*, **30**, 647 (1996).
8. X. Deng; Y. Yue, Z. Gao, *J. Appl. Catal. B.*, **39**, 135 (2002).
9. H. Hayashi, K. Torii, *J. Mater. Sci.*, **12**, 3671 (2002).
10. Y. Li; N. H. Lee; D. S. Lee; D. S. Hwang; J. S. Song; E. G. Lee, S. J. Kim, *J. Langmuir*, **20**, 10838 (2004).
11. R. Rodriguez; S. J. Sandoval; M. Estevez, S. Vargas, *J. Non-Cryst. Solids*, **351**, 167 (2005).
12. H. Imai, H. Hirashima, *J. Am. Ceram. Soc.*, **82**, 2301 (1999).
13. S. Liu; N. Jaffrezic, C. Guillard, *J. Appl. Surf. Sci.*, **255**, 2704 (2008).
14. M.M. Mohamed; T.M. Salama, T. Yamaguchi, *J. Colloids Surf.*, **207**, 25 (2002).
15. K. Guan, *J. Surf. Coat. Tech.*, **191**, 155 (2005).
16. M. Houmard; D. Riassetto; F. Roussel; A. Bourgeois; G. Berthome; J.C. Joud, M. Langlet, *J. Appl. Surf. Sci.*, **254**, 1405 (2007).
17. J. Ovenstone, *J. Mater. Sci.*, **36**, 1325 (2001).
18. M.P. Zheng; M. Gu; Y. Jin and G. Jin, *J. Mater. Sci. Eng. B.*, **77**, 55 (2000).
19. G. Zhao; Q. Tian; Q. Liu, G. Han, *J. Surf. Coat. Tech.*, **198**, 55 (2005).
20. K.M. Parida, N. Sahu, *J. Mol. Catal. A: Chem.*, **287**, 151 (2008).
21. M.P. Zheng; M.Y. Gu; Y.P. Jin; H.H. Wang; P.F. Zu; P. Tao, J.B. He, *J. Mater. Sci. Eng. B.*, **87**, 197 (2001).
22. J. Jiao; Q. Xu, L. Li, *J. Colloid Interface Sci.*, **316**, 596 (2007).
23. M. Houmard; D. Riassetto; F. Roussel; A. Bourgeois; G. Berthome; J.C. Joud, M. Langlet, *J. Surf. Sci.*, **602**, 3364 (2008).
24. P. Aberomand Azar; S. Moradi Dehaghi; S. Samadi; S. Kamyar, M. Saber Tehrani, *Asian J. Chem.*, **22**, 1619 (2010).
25. B. Khodadadi; M. Sabeti; S. Moradi; P. Aberomand Azar, S. Raies Farshid, *J. Appl. Chem. Res.*, **20**, 36 (2012).
26. H. Fu; C. Pan; W. Yao, Y. Zhu, *J. Phys. Chem., B*, **109**, 22432 (2005).
27. R. Niishiro; H. Kato, A. Kudo, *J. Phys. Chem. Chem. Phys.*, **7**, 2241 (2005).

ЕФЕКТ НА ДОТИРАНЕ С НИКЕЛ ВЪРХУ ФОТОКАТАЛИТИЧНАТА АКТИВНОСТ НА НАНОКОМПОЗИТИ ОТ $\text{TiO}_2/\text{SiO}_2$

Б. Хоодади

Департамент по химия, Университет в Кум, Кум, Иран

Постъпила на 24 януари, 2015 г.; коригирана на 31 юли, 2015 г.

(Резюме)

Пригответени са прахови наноконпозити от $\text{TiO}_2/\text{SiO}_2$ и $\text{TiO}_2/\text{SiO}_2/\text{Ni}$ по зол-гел метода. Освен това са добавени различни концентрации на примеси са да се изследва дотиращия ефект на металите. Структурите са установени с ИЧ-спектроскопия, сканираща електронна микроскопия (SEM), дисперсионна аналитична рентгенова дифракция (EDAX) и рентгенова дифракция (XRD). Абсорбционните коефициенти на пробите са анализирани по подхода на Таус и са изчислени директно забранените зони. Изследвана е фотокаталитичната активност на всички образци под ултравиолетово облъчване във водна среда. Резултатите показват, че дотирането с метали играе важна роля за намаляване размерите на частиците. Фотокаталитичният ефект се подобрява при дотиране.

Kinetic investigation of tetrahydrobenzo[b]pyran synthesis in the presence of fructose as a catalyst via a three-component reaction: an experimental study

H. Yaghoubian, S.M. Habibi-Khorassani*, A. Ebrahimi

Department of Chemistry, Faculty of Science, University of Sistan and Baluchestan, P. O. Box 98135-674, Zahedan, Iran

Received January 23, 2015, Revised October 13, 2015

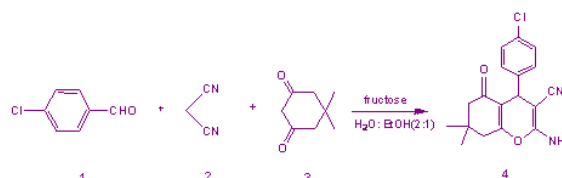
The synthesis reaction of tetrahydrobenzo[b]pyran from the reaction between 4-chlorobenzaldehyde, malononitrile with dimedone in the presence of fructose as a catalyst were subjected to a kinetic and mechanistic study by a UV spectrophotometric technique. The effects of various parameters such as the concentration, temperature, solvent composition and various catalysts on the reaction rate were examined. Experimental data fully matched the second order fits. The resultant rate constants obeyed the Arrhenius and Eyring equations. The relevant activation parameters (E_a , ΔH^\ddagger , ΔS^\ddagger and ΔG^\ddagger) were determined from these. In a solvent with a lower dielectric constant the rate of reaction decreased. In accordance with the experimental observations and steady state approximation, the first step of the proposed mechanism was recognized as a rate-determining step.

Keywords: Kinetics, Catalyst, Mechanism, Tetrahydrobenzo[b]pyran

INTRODUCTION

Benzopyrans and their derivatives, as a useful class of heterocyclic compounds, show biological and pharmacological properties, such as diuretic, anticancer, spasmolytic, anticoagulant and antianaphylactin activities [1]. They can also be employed as cognitive enhancers for the treatment of some neurodegenerative diseases, including Parkinson, Alzheimer, Huntington, AIDS associated dementia, Down's syndrome and also for the treatment of schizophrenia and myoclonus [2]. Furthermore, these compounds can be applied as potential biodegradable agrochemicals, pigments and photoactive materials [3-6]. In recent years, many studies on the synthesis of tetrahydrobenzo[b]pyrans have been reported [7-11]. Multi component reactions (MCRs) occur in one-pot and so these reactions are easier to perform than multistep syntheses reactions [12]. The considerable benefits due to MCRs are in low expenses, avoiding of time-consuming purification processes and complex synthetic pathways, shorter times of reaction, high yields and saving the energy [13]. Three-component reactions have appeared as a beneficial approach among the multi-component reactions since the combination of three compounds to obtain related products in a single step is quite economical [14-17]. Therefore, an effective and

suitable synthesis of tetrahydrobenzo[b]pyrans can usually be performed via a three-component reaction of an aromatic aldehyde, an acting methylene compound and dimedone in the presence of an appropriate catalyst [18]. In addition to synthesis, very valuable information about these compounds is the mechanism and rate of the reactions, the effect of various parameters can be obtained from the kinetic studies [19]. In previous works we have investigated the kinetics of the synthesis of new organics such as phosphorus ylides, phosphonate esters and others, both experimental and theoretical studies [20-24]. In this work we examine the experimental kinetics and mechanism of the reaction between 4-chlorobenzaldehyde 1, malononitrile 2, and dimedone 3 in the presence of fructose as a catalyst to attain tetrahydrobenzo[b]pyran 4 (Scheme 1). Fructose is a popular, commensurate, stable, cheap and clean catalyst, dissolvable in water synthesized by an environmentally desirable procedure.



Scheme 1. Synthesis reaction of tetrahydrobenzo[b]pyran, 4-chlorobenzaldehyde, malononitrile, and dimedone in the presence of fructose as a catalyst.

* To whom all correspondence should be sent:
E-mail: smhabibi@chem.usb.ac.ir

EXPERIMENTAL SECTION

4-chlorobenzaldehyde **1**, malononitrile **2**, dimedone **3**, fructose and ethanol were obtained from Merck (Darmstadt, Germany) and Fluka (Buchs, Switzerland), these were used without any purification. All of the experiments were accomplished by a carry UV-Vis spectrophotometer as follow:

General procedure

At first, 10^{-2} M solution of each compound (**1**, **2**, **3** and catalyst) was prepared in a mixture of 2:1 water: ethanol as a solvent. Then, the spectrum of each compound was recorded in the wavelength range 200-800 nm. In the second experiment, 0.2 mL of the solution of the catalyst and each reactant **2** and **3** were added into the cell, respectively (as there is no reaction between them). Then, 0.2 mL of reactant **1** was added to the mixture and the progress of the reaction was monitored at the ambient temperature (Fig.1).

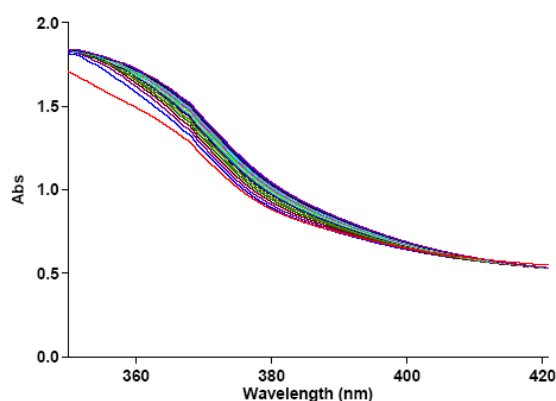


Fig. 1. The UV/Vis spectra of the reaction between 4-chlorobenzaldehyde **1** (10^{-2} M), malononitrile **2** (10^{-2} M) and dimedone **3** (10^{-2} M) in the presence of the fructose catalyst (10^{-2} M) and in a mixture of water: ethanol (2:1), the upward arrow showing the progress of the reaction

Thereupon, the suitable wavelength at which reactants **1**, **2**, **3** and the catalyst have relatively no absorbance was found to be 380 nm. The full kinetics and mechanism of the reaction can be investigated at this wavelength. Herein, in all the experiments, the UV-Vis spectrum of the product was measured over the concentration range (10^{-3} M < M product < 10^{-2} M) to corroborate a linear relation between the absorbance and concentrations values. In the third experiment under the same conditions just as the previous experiment, the absorbance curve was recorded versus the time at 40°C and 380 nm (Fig.2). Zero, first or second curve fittings can be drawn using the software associated with the UV-Vis instrument; also, the relevant rate constant can be calculated

automatically [25]. As can be seen in Fig. 2, the experimental absorbance data (dotted line) accurately fits the second order curve (solid line). Thus, the overall order of the reaction according to the rate law expressed in equation (1), can be written as: $\alpha+\beta+\gamma = 2$

$$\text{Rate} = k_{\text{ovr}} [\mathbf{1}]^{\alpha} [\mathbf{2}]^{\beta} [\mathbf{3}]^{\gamma} [\text{cat}], (1)$$

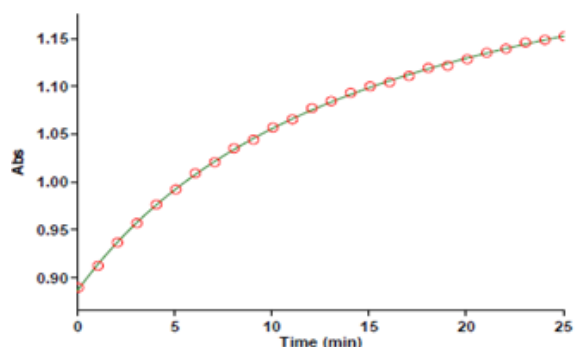


Fig. 2. Second order fit curve (solid line) accompanied by the original experimental curve (dotted line) for the reaction between compounds **1** (10^{-2} M), **2** (10^{-2} M) and **3** (10^{-2} M) in the presence of fructose (10^{-2} M) in a mixture of water: ethanol (2:1) at 380nm

RESULTS AND DISCUSSIONS

The Effect of Concentration

In order to determine the partial order with respect to each component three experiments were carried out in which the concentration of one of the components **1**, **2** or **3** was selected much less (5×10^{-3}) than the others (10^{-2}), separately. In other words, pseudo-order conditions were set for these reactions. The absorbance curves are shown in Figures (3-5).

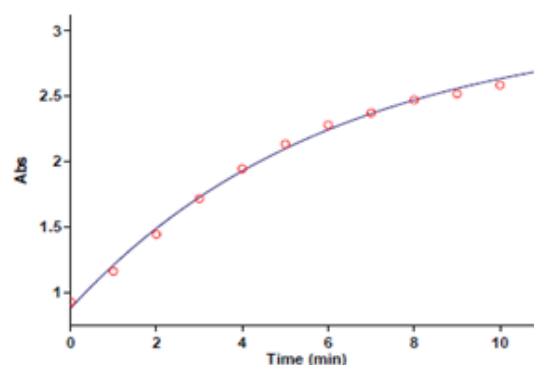


Fig. 3. The first pseudo order fit curve (solid line) along with the original experimental curve (dotted line) in relation to 4-chlorobenzaldehyde **1**, for the reaction between **1** (5×10^{-3} M), **2** (10^{-3} M) and **3** (10^{-3} M) in the presence of fructose and a mixture of water: ethanol (2:1) at 380nm

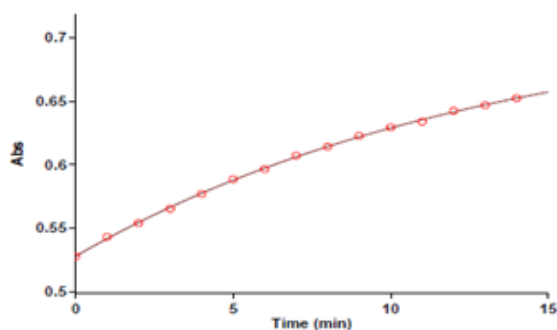


Fig. 4. First pseudo order fit curve (solid line) along with the original experimental curve (dotted line) in relation to malononitrile **1**, for the reaction between **1** (10^{-3} M), **2** (5×10^{-3} M) and **3** (10^{-3} M) in the presence of fructose and a mixture of water: ethanol (2:1) at 380nm

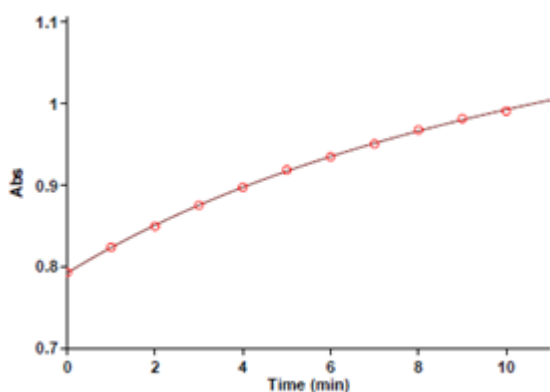


Fig. 5. Second pseudo order fit curve (solid line) accompanied by the original experimental curve (dotted line) for the reaction between compounds **1** (10^{-2} M), **2**

(10^{-2} M) and **3** (5×10^{-3} M) in the presence of fructose (10^{-2} M) in a mixture of water: ethanol (2:1) at 380nm

It is obvious that under pseudo-order conditions, the partial order of the reaction with respect to compounds **1** and **2** is one (Figs. 3, 4). In the other hands, $\alpha=\beta=1$. Also by matching the experimental data with a second order fit (Fig. 5) given the similarity of the calculated rate constants. From this plot of the rate constants calculated from the graph of Fig. 2, we thus say by changing the concentration of compound **3**, rate constants have not changed substantially. So we can rewrite equation 1 as follow:

$$\text{Rate} = k_{\text{ovr}}[1][2][\text{cat}], \quad k_{\text{obs}} = k_{\text{ovr}}[\text{cat}], \quad (2)$$

$$\text{Rate} = k_{\text{obs}}[1][2], \quad (3)$$

The Effect of Solvent and Temperature

Several experiments were performed for various temperatures and solvents under the same concentration of each component (10^{-2} M). The relevant rate constants obtained from the software are given in Table 1. The dependency of the rate constants ($\ln k$ and $\ln k/T$) on the reciprocal temperature showed adaptability with the Arrhenius and Eyring equations. Furthermore, the linearized form of the Eyring equations was investigated to compare these methods [13] (Figs. 6, 7). The activation parameters are given in Table2.

Table 1. Values of observed rate constants for the reaction between **1**, **2** and **3** in the presence of the fructose catalyst at 380nm and various temperatures.

λ (nm)	Solvent	$k_{\text{obs}}(\text{M} \cdot \text{min}^{-1})$						
		(a) 45.0 °C	(a) 40.0 °C	(a) 35.0 °C	(a) 30.0 °C	(a) 25.0 °C	(a) 20.0 °C	(b) 40.0°C
380	Water: ethanol (2:1)	8.18	6.12	4.33	3.33	2.40	1.75	6.18
380	ethanol	4.36	3.14	1.09	0.42	0.110	0.078	3.13

a: **1** (10^{-2} M), **2** (10^{-2} M), **3** (10^{-2} M), catalyst (10^{-2} M)

b: **1** (10^{-2} M), **2** (10^{-2} M), **3** (5×10^{-3} M), catalyst (10^{-2} M)

Table 2. Activation parameters for the reaction between 1, 2 and 3 in the presence of the fructose catalyst at 380nm.

solvent	$\Delta H^\ddagger(\text{kJ} \cdot \text{mol}^{-1})$	$\Delta S^\ddagger(\text{J} \cdot \text{mol}^{-1} \cdot \text{K}^{-1})$	$\Delta G^\ddagger(\text{kJ} \cdot \text{mol}^{-1})$	$E_a(\text{kJ} \cdot \text{mol}^{-1})$
Water: ethanol(2:1)	(a) 45.31	(a) -85.64	(a) 70.84	47.86
	(b) 45.54	(b) -84.80	(b) 70.82	

a: according to the Eyring equation,

b: according to the linearized form of the Eyring equation

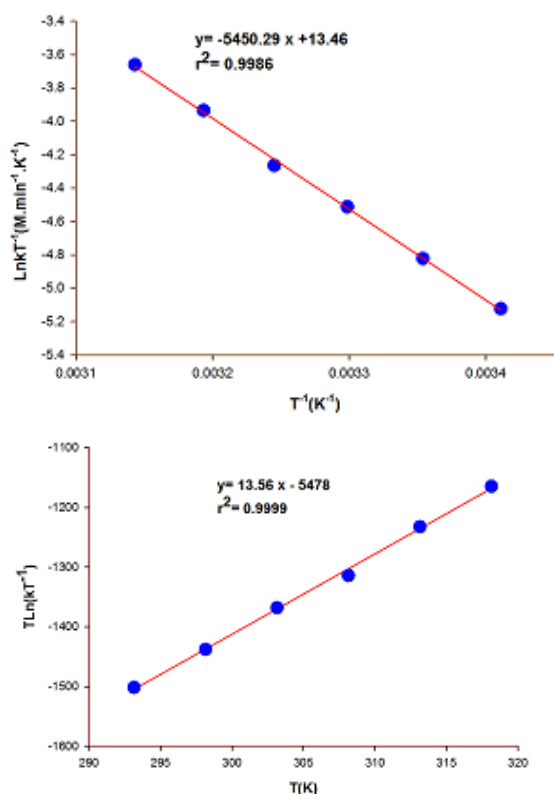


Fig. 6. Eyring plots for the reaction between 1, 2, 3 and fructose in a mixture of water: ethanol (2:1) at 380nm.

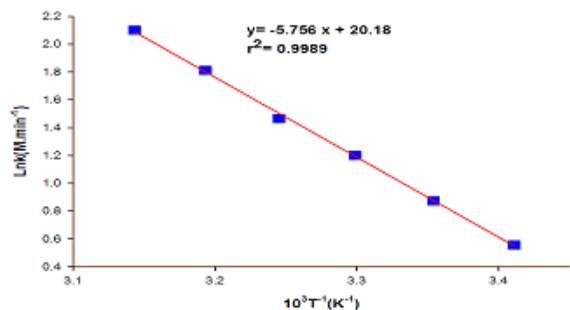


Fig. 7. An Arrhenius plot for the reaction between 1, 2, 3 and fructose in a mixture of water: ethanol (2:1) at 380nm.

According to the data in Table1, it can be seen that the reaction rate increases with increasing temperature. Moreover, in a solvent with a lower dielectric constant (ethanol) in comparison with a higher dielectric constant (mixture 2:1 water: ethanol) the reaction rate decreased. That can be attributed to the change in stability of the reactants and activated complexes in these environments. Furthermore, the positive value of ΔH^\ddagger (Table2) indicates that the reaction is needed to obtain a high value of the activation energy endothermic and a large negative value of ΔS^\ddagger determines a transition state that is more strongly ordered than the reactants.

Effect of the catalyst

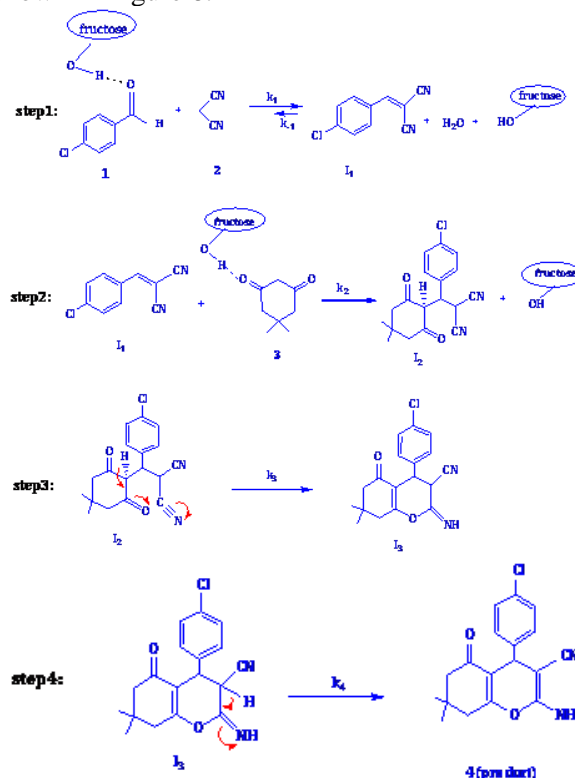
The reaction between 1, 2 and 3 was repeated in the presence of agar, sucrose and 1,4-diazabicyclo[2.2.2]octane(DABCO) as a catalyst in a mixture of water:ethanol (2:1). The reaction rate was increased in the presence of agar, sucrose and DABCO in comparison with the fructose (Table 3). Agar and DABCO have a poor interaction with a polar solvent compared to fructose, such that, it has more freedom to carry out its catalytic role. Also, due to sucrose it can establish hydrogen bonding with an oxygen atom in the 4-chlorobenzaldehyde more than fructose and was more active for the nucleophilic attack of the malononitrile compound.

Table 3. Effect of Various catalysts on the reaction between 1, 2 and 3 at 45°C and 380nm.

solvent	catalyst	$k_{obs}(M.min^{-1})$
Water: ethanol(2:1)	Fructose	8.18
	Agar	10.01
	Sucrose	8.84
	DABCO	9.36

Mechanism

By using the above results, the proposed reaction mechanism as a possible comment is shown in Figure 8:



Scheme 2. The proposed mechanism for the reaction between 1, 2 and 3 in the presence of fructose in a mixture of water: ethanol (2:1).

To determine which step of the proposed mechanism is the rate-determining step, the rate law was written for the final step of the reaction as:

$$\text{Rate} = k_4 [I_3], \quad (4)$$

By using the steady state approximation to obtain the concentration of all intermediates (I_1 , I_2 and I_3), the rate equation becomes:

$$\text{Rate} = \frac{k_1 k_2 [1][2][3][\text{cat}]}{k_{-1} [H_2O] + k_2 [3]}, \quad (5)$$

This equation is independent of the rate constants for the third and fourth steps. Thus, these steps have no chance to be rate determining steps; if $k_{-1} [H_2O] \ll k_2 [3]$; then, we can conclude:

$$\text{Rate} = k_1 [1][2][\text{cat}], \quad (6)$$

Hence, from the comparison between both equations (6) and (2) and the experimental data

$$\text{rate} = k_{\text{obs}} [1][2], \quad (7)$$

According to this equation, the order of the reaction with respect to compounds (**1**, **2** and **3**) is 1, 1 and zero, respectively and the overall order of the reaction is two, which was previously confirmed by the experimental data.

The presence of k_1 in the rate law (equation (6)) indicates that the first step is a rate-determining step and step 2 should be a fast step. In this case, the transition state (Scheme 2, step 1) carries a dispersed charge; hereupon, the solvent with a higher dielectric constant can be more effective on this dispersed charge in comparison with reactants **1** and **2**, that do not have any charge. Thus, the solvent stabilizes the species at the transition state more than the reactants. Therefore, E_a would be lower and accelerate the reaction rate.

CONCLUSION

The reaction rate was accelerated by the increase in temperature and was in compatibility with the Eyring and Arrhenius equations. It also followed the second-order kinetics and partial order with respect to compounds **1**, **2**, and **3** was 1, 1 and 0, respectively. The first step of the proposed mechanism was identified as a rate-determining step and this was affirmed by the steady-state approximation. Furthermore, in a solvent with a higher dielectric constant, the rate of the reaction increased. This pertains to different stabilizing effects of the solvent on the reactants and activated complex.

Acknowledgments: The authors sincerely thank the University of Sistan and Baluchestan for providing the financial support for this work.

REFERENCES

1. S. Balalaie, M. Sh.-Ahmadi, M. Bararjanian, *Catal. Commun.*, **8**, 1724 (2007).
2. D.-I. MaGee, P. Salehi, M. Dabiri, M. Bahramnejad, *Synth. Commun.*, **43**, 486 (2013).
3. L. Fotouhi, M. M. Heravi, A. Fatehi, Kh. Bakhtiari, *Tetrahedron Lett.*, **48**, 5379 (2007).
4. Zh. Yuan, F. Liang, *Curr. Org. Chem*, **18**, 2016 (2014).
5. D. Klostermeyer, L. Knops, T. Sindlinger, K. Polborn, W. Steglich, *Eur. J. Org. Chem.*, **2000**, 603 (2000).
6. A. A. Birkbeck, Z. Brkic, Robin-G.-F.-Giles, *Tetrahedron Lett.*, **45**, 6147 (2004).
7. S. Gurumurthi, V. Sundari, R. Valliappan, *E-J. Chem.*, **6**(S1), S466 (2009).
8. N. M. Abd El-Rahman, R. M. Borik, *World Appl. Sci. J.*, **31**(1), 01 (2014).
9. G. Sabitha, K. Arundhathi, K. Sudhakar, B. S. Sastry, J. S. Yadav. *Synth. Commun.*, **39**, 433 (2009)
10. P. P. Salvi, A. M. Mandhare, A. S. Sartape, D. K. Pawar, S. H. Han, S.S. Kolekar. *C. R. Chimie.*, **14**, 878 (2011).
11. A.-V. Borhade, B.-K. Uphade, D.R Tope, *J. Chem. Sci.*, **125**(3), 583 (2013).
12. I. Devi, P. J. Bhuyan. *Tetrahedron Lett.*, **45**, 8625 (2004).
13. N. Hazeri, M.T. Maghsoodlou, F. Mir, M. Kangani, H. Saravani, E. Molashahi, *Chin. J. Catal.*, **35**, 391 (2014).
14. M. Syamala. *Org. Prep. Proced. Int.*, **41**, 1 (2009).
15. J. S. J. McCahill, G. C. Welch, D. W. Stephan, *Angew. Chem. Int. Ed.*, **46**, 4968 (2007).
16. Z. Yuan, Gu.-Ch. Kuang, R. J. Clark, L. Zhu, *Org. Lett.*, **14**, 2590 (2012).
17. B. List, *J. Am. Chem. Soc.*, **122**, 9336 (2000).
18. Y.Lei Wang, Zh. Li, J. Luoa, Z.L. Liu., *J. Chin. Chem. Soc.*, **60**, 1431 (2013).
19. M. Dehdab, S. M. Habibi-Khorassani, M. Shahraki, *Catal. Lett.*, **144**, 1790 (2014).
20. M. Shahraki, S.M. Habibi-Khorassani, A. Ebrahimi, M.T. Maghsoodlou, A. Paknahad, *Prog. React. Kinet. Mech.*, **37**, 321 (2012).
21. S. Sh. Pourpanah, S.M. Habibi-Khorassani, M. Shahraki, *Chin. J. Catal.*, **36**, 757 (2015).
22. S.M. Habibi-Khorassani, M.T. Maghsoodlou, E. Aghdaei, M. Shahraki, *Prog. React. Kinet. Mech.*, **37**, 301 (2012).
23. M. Shahraki, S.M. Habibi-Khorassani, *J. Phys. Org. Chem.*, **28**(6), 396 (2015).
24. M. Shahraki, S.M. Habibi-Khorassani, M. Dehdab, *RSC Adv.*, **5**(65), 52508 (2015).
25. L.M. Schwartz, R. I. Gelb, *Anal. Che.*, **50**, 1592 (1978).

КИНЕТИЧНО ИЗСЛЕДВАНЕ НА СИНТЕЗАТА НА ТЕТРАХИДРОБЕНЗО[*b*]ПИРАН В
ПРИСЪСТВИЕ НА ФРУКТОЗА КАТО КАТАЛИЗАТОР ЧРЕЗ ТРИКОМПОНЕНТНА
РЕАКЦИЯ: ЕКСПЕРИМЕНТАЛНО ИЗСЛЕДВАНЕ

Х. Ягубиан, С.М. Хабиби-Хорасани*, А. Ебрахими

Департамент по химия, Научен факултет, Университет в Систан и Белучестан, П.К. 98135-674, Захедан,

Постъпила на 23 януари, 2015 г.; коригирана на 13 октомври, 2015 г.

(Резюме)

Синтезата на тетраhydrobenzo[*b*]пиран при реакцията между 4-хлоробензалдеhid, малонитрил и димедон в присъствие на фруктоза като катализатор. Извършено е кинетично и механистично изследване чрез ултравиолетова спектроскопия. Изследван е ефектът на различни параметри, като концентрации, температура, състав на разтворителя и различни катализатори върху скоростта на реакцията. Експерименталните данни напълно съответстват на реакции от втори порядък. Резултантните скоростни константи се подчиняват на уравненията на Arrhenius и Eyring. Съществените параметри за активацията (E_a , ΔH^\ddagger , ΔS^\ddagger и ΔG^\ddagger) са определени от тези уравнения. Скоростите на реакциите се понижават в разтворители с по-ниска диелектрична константа. В съответствие с експерименталните наблюдения и стационарно приближение е прието, че първият етап на предложения механизъм е скоростно-определящ за общата реакция.

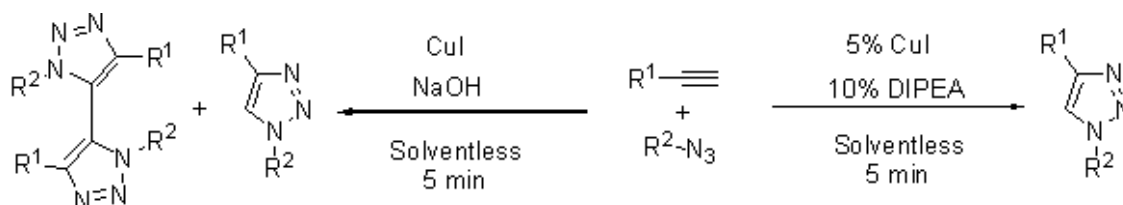
Solventless synthesis of triazoles and bistriazoles through Copper-catalyzed alkyne-azide cycloaddition

M. Pateraki,¹ G. K. Morales-Ortiz,¹ A. López-Guzmán,¹ A. Fuentes-Benites², E. Cuevas-Yañez^{1*}

¹Centro Conjunto de Investigación en Química Sustentable UAEM-UNAM. Carretera Toluca-Atzacomulco Km 14.5, Toluca, Estado de México, 50200, México.

²Departamento de Química Orgánica, Facultad de Química, Universidad Autónoma del Estado de México, Paseo Colón esq. Paseo Tollocan, Toluca, Estado de Mexico 50120, Mexico.

Received March 4, 2015, Revised October 6, 2015



A library of 1,2,3-triazoles, including a series of triazolyl styrenes which have a structural relationship with resveratrol, was synthesized through a novel solventless method that involves the straightforward treatment by grinding of several azides and alkynes in the presence of catalytic amounts of copper iodide and *N,N*-diisopropylethylamine. On the other hand, when sodium hydroxide was used as the base, a mixture of bistriazoles and triazoles was formed where 1,2,3-triazoles were the major products. This new solvent-free synthesis protocol is carried out under mild conditions for short times, affording the 1,4-regioisomers in high yields.

Keywords: Triazole, Bistriazole, Alkyne, Azide, Solventless.

INTRODUCTION

Copper-Catalyzed Alkyne-Azide Cycloaddition (CuAAC) is the best known example of an ideal reaction for Click Chemistry and one of the most important methods for molecular assembly [1], as well as a significant source of potentially active compounds [2-4]. Therefore, the development of new procedures for this reaction is highly desirable. Although several groups have thoroughly studied this reaction, designing catalysts and optimizing conditions, the research of this topic is far from complete.

One of the challenges of this reaction, sustainable by itself, is the exploration of the reaction conditions close to the principles of Green Chemistry, avoiding as far as possible, the generation of dangerous products. In this context, the development of solvent-free chemical processes is important and many examples of solventless chemical reactions are reported in the literature [5,6].

These reasons inspired us to start an

investigation with the aim of exploring the possibility to obtain 1,2,3-triazoles and bistriazoles in high yields through CuAAC using solvent free conditions. This work summarizes our recent successful efforts in this area.

EXPERIMENTAL

Instrument and chemical materials

The starting materials were purchased from Aldrich Chemical Co. and were used without further purification. The solvents were distilled before use. Silica plates of 0.20 mm thickness were used for thin layer chromatography. The melting points were determined with a Fisher-Johns melting point apparatus and they are not corrected. ¹H and ¹³C NMR spectra were recorded using a Bruker Advance 300; the chemical shifts (δ) are given in ppm relative to TMS as an internal standard (0.00). For analytical purposes the mass spectra were recorded on a Shimadzu GCMS-QP2010 Plus in the EI mode, 70 eV, 200 °C via a direct inlet probe. Only the molecular and parent ions (*m/z*) are reported. The IR spectra were recorded on a Bruker Tensor 27 equipment.

* To whom all correspondence should be sent:
E-mail: ecuevasy@uaemex.mx

Solventless copper-catalyzed cycloaddition of alkynes and azides.

Typical procedure. Successively added in a mortar were the corresponding alkyne (1 mmol), azide (1 mmol), DIPEA (0.01 mL, 0.1 mmol) and CuI (0.0095 g, 0.05 mmol). The mixture was homogenized in a mortar during 5 minutes using a pestle. The mixture was collected and the final product was purified by crystallization.

1-Benzyl-4-phenyl-1,2,3-triazole (3). White solid; mp 130°C (lit. 130-130.9°C) [7] ; IR (ATR): $\nu = 3128, 2927, 1461, 1269 \text{ cm}^{-1}$; $^1\text{H NMR}$ (CDCl₃, 300 MHz) δ 7.67-7.60 (m, 2H), 7.55 (dd, $J = 5.7, 3.3 \text{ Hz}$, 1H), 7.50 (s, 1H), 7.28-7.21 (m, 4H), 7.19-7.13 (m, 3H), 5.43 (s, 2H); $^{13}\text{C NMR}$ (CDCl₃, 75 MHz) δ 147.7 (C), 134.3 (C), 132.0 (C), 130.4 (CH), 130.1 (C), 128.7 (CH), 128.4 (CH), 127.7 (CH), 127.6 (CH), 125.3 (CH), 119.0 (CH), 53.8 (CH₂); MS [EI⁺] m/z (%) 235 [M]⁺ (20), 206 [M-HN₂]⁺ (50), 116 [M - C₆H₅N₃]⁺ (90), 91 [C₆H₅CH₂]⁺ (100).

1,4-diphenyl-1,2,3-triazole (4). Yellow solid; mp 65.0 °C; IR (ATR): $\nu = 2958, 1598, 1462, 1272$; $^1\text{H NMR}$ (CDCl₃, 300 MHz) δ 8.22 (s, 1H), 7.95-7.90 (m, 2H), 7.70 (dd, $J = 5.9, 3.8 \text{ Hz}$, 1H), 7.63-7.59 (m, 1H), 7.50-7.45 (m, 5H), 7.41-7.33 (m, 1H); $^{13}\text{C NMR}$ (CDCl₃, 75 MHz) δ 145.8 (CH), 130.6 (C), 128.9 (CH), 128.3 (CH), 127.9 (C), 126.7 (CH), 126.5 (CH), 126.1 (CH), 125.9 (CH), 119.7 (CH) ; MS [EI⁺] m/z (%) 221 [M]⁺ (35), 116 [M - C₆H₅N₂]⁺ (100), 104 [M - C₇H₅N₂]⁺ (50), 77 [C₆H₅]⁺ (90).

1-benzyl-4-[(4-bromophenoxy)methyl]-1,2,3-triazole (5). White solid; mp 111.0 °C; IR (ATR): $\nu = 3138, 2873, 1687, 1581, 1486$; $^1\text{H NMR}$ (CDCl₃, 300 MHz) δ 7.51 (s, 1H), 7.37 (dt, $J = 5.7, 2.9 \text{ Hz}$), 7.28 (d, $J = 3.3 \text{ Hz}$), 6.85 (d, $J = 8.9 \text{ Hz}$), 5.53 (s, 2H), 5.15 (s, 2H); $^{13}\text{C NMR}$ (CDCl₃, 75 MHz) δ 156.24 (C), 143.14 (C), 133.33 (C), 131.28 (CH), 128.11 (CH), 127.81 (CH), 127.06 (CH), 121.54 (CH), 115.61 (CH), 112.45 (C), 61.22 (CH₂), 53.23 (CH₂); MS [EI⁺] m/z (%) 343 [M]⁺ (35), 314 [M-HN₂]⁺ (3), 226 [M - C₈H₈N]⁺ (3), 184 [C₇H₆BrO]⁺ (4), 91 [C₆H₅CH₂]⁺ (100), 77 [C₆H₅]⁺ (35).

4-[(4-bromophenoxy)methyl]-1-phenyl-1,2,3-triazole (6). White solid; mp 60.0 °C; IR (ATR): $\nu = 3138, 2955, 1584, 1485$; $^1\text{H NMR}$ (CDCl₃, 300 MHz) δ 8.05 (s, 1H), 7.68-7.31 (m, 5H), 7.40 (d, $J = 8.9 \text{ Hz}$, 2H), 6.92 (d, $J = 8.9 \text{ Hz}$, 2H), 5.29 (s, 2H); $^{13}\text{C NMR}$ (CDCl₃, 75 MHz) δ 156.4 (C), 142.7 (C), 133.9 (C), 130.0 (CH), 129.9 (CH), 128.9 (CH), 127.7 (C), 127.1 (CH), 126.9 (CH), 119.7 (CH), 61.3 (CH₂); MS [EI⁺] m/z (%) 329 [M]⁺ (10), 164 [C₉H₉BrN₃O]⁺ (100). Elemental analysis calculated:

C, 54.56; H, 3.66; N, 12.73, found: C, 55.01; H, 3.75; N, 12.80.

4-[(4-bromophenoxy)methyl]-1-p-tolyl-1,2,3-triazole (7). White solid; mp 98.0 °C; IR (ATR): $\nu = 3139, 2958, 1589, 1518$; $^1\text{H NMR}$ (CDCl₃, 300 MHz) δ 8.00 (s, 1H), 7.60 (d, $J = 8.4 \text{ Hz}$, 2H), 7.40 (d, $J = 9.0 \text{ Hz}$, 2H), 7.32 (d, $J = 8.5 \text{ Hz}$, 2H), 6.91 (d, $J = 9.0, 2\text{H}$), 5.27 (s, 2H), 2.42 (s, 3H); $^{13}\text{C NMR}$ (CDCl₃, 75 MHz) δ 156.1 (C), 142.1 (C), 137.9 (C), 133.4 (C), 131.2 (CH), 129.0 (CH), 119.7 (CH), 119.3 (CH), 115.4 (CH), 112.3 (C), 61.0 (CH₂), 19.8 (CH₃); MS [EI⁺] m/z (%) 343 [M]⁺ (40), 314 [M-HN₂]⁺ (10), 211 [M - C₇H₇N₃]⁺ (100), 172 [M - C₆H₄BrO]⁺ (70). Elemental analysis calculated: C, 55.83; H, 4.10; N, 12.21, found: C, 56.13; H, 4.50; N, 12.30.

4-phenyl-1-p-tolyl-1H-1,2,3-triazole (8). White solid; mp 121.0 °C; IR (ATR): $\nu = 3124, 2956, 1605, 1482$; $^1\text{H NMR}$ (CDCl₃, 300 MHz) δ 8.16 (s, 1H), 7.67 (d, $J = 8.4 \text{ Hz}$, 2H), 7.60-7.42 (m, 5H), 7.34 (d, $J = 8.4 \text{ Hz}$, 2H), 2.44 (s, 3H); $^{13}\text{C NMR}$ (CDCl₃, 75 MHz) δ 148.1 (C), 138.9 (C), 134.6 (C), 132.4 (C), 130.85 (CH), 130.2 (CH), 128.9 (CH), 128.3 (CH), 125.9 (CH), 120.1 (CH), 22.6 (CH₃); MS [EI⁺] m/z (%) 235 [M]⁺ (20), 130 [M-C₇H₇N]⁺ (20), 91 [C₆H₅CH₂]⁺ (100).

[1-(4-methoxyphenoxy)-1,2,3-triazole-4-yl]methanol (9). Yellow solid; 80 °C; IR (ATR): $\nu = 2956, 2855, 1594, 1485$; $^1\text{H NMR}$ (CDCl₃, 300 MHz) δ 8.03 (s, 1H), 7.40 (d, $J = 9.0 \text{ Hz}$, 2H), 6.91 (d, $J = 8.9 \text{ Hz}$, 2H), 5.27 (s, 2H), 4.89 (s, 1H), 3.87 (s, 3H); $^{13}\text{C NMR}$ (CDCl₃, 75 MHz) δ 157.40 (C), 154.70 (C), 142.36 (C), 119.77 (CH), 118.11 (CH), 113.98 (CH), 54.30 (CH₃), 53.31 (CH₂); MS [EI⁺] m/z (%) 205 [M]⁺ (20), 149 [M - C₃H₄O]⁺ (95), 57 [M - C₈H₈N₂O]⁺ (100). Elemental analysis calculated: C, 53.35; H, 3.92; N, 11.67, found: C, 53.85; H, 4.10; N, 12.02.

4-[(4-bromophenoxy)methyl]-1-(4-methoxyphenyl)-1H-1,2,3-triazole (10). White solid; mp 109 °C; IR (ATR): $\nu = 2958, 2854, 1590, 1485$; $^1\text{H NMR}$ (CDCl₃, 300 MHz) δ 7.96 (s, 1H), 7.63 (d, $J = 9.0 \text{ Hz}$, 2H), 7.40 (d, $J = 9.0 \text{ Hz}$), 7.02 (d, $J = 9.0 \text{ Hz}$, 2H), 6.91 (d, $J = 9.0 \text{ Hz}$, 2H), 5.26 (s, 2H), 3.87 (s, 3H); $^{13}\text{C NMR}$ (CDCl₃, 75 MHz) δ 158.7 (C), 156.1 (C), 143.0 (C), 131.2 (CH), 129.1 (C), 121.0 (CH), 119.9 (CH), 115.4 (CH), 113.6 (CH), 112.3 (C), 61.0 (CH₂), 54.4 (CH₃); MS [EI⁺] m/z (%) 359 [M]⁺ (5), 280 [M - Br]⁺ (100).

4-[(4-bromophenoxy)methyl]-1p-tolyl-1,2,3-triazole (11). White solid; mp 155°C; IR (ATR): $\nu = 3123, 2921, 1608, 1460$; $^1\text{H NMR}$ (CDCl₃, 300 MHz) δ 8.11 (s, 1H), 7.94-7.86 (m, 2 H), 7.69 (d, $J = 9.0 \text{ Hz}$, 2H), 7.52-7.31 (m, 5H), 7.05 (d, $J = 9.0 \text{ Hz}$, 2 H), 3.89 (s, 3H); $^{13}\text{C NMR}$ (CDCl₃, 75 MHz)

δ157.40 (C), 154.70 (C), 142.36 (C), 119.58 (CH), 114.19 (CH), 54.39 (CH₃), 53.23 (CH₂); MS [EI⁺] m/z (%) 251 [M]⁺ (10), 149 [M - C₃H₆]⁺ (80), 116 [M - C₇H₇N₂O]⁺ (35), 102 [M - C₇H₇N₃O]⁺ (15), 77 [C₆H₅]⁺ (100).

[1-(4-methoxyphenyl)-1,2,3-triazole-4-yl]methyl butylcarbamate (12). White solid; mp 100 °C; IR (ATR): ν = 3153, 2928, 1580, 1484; ¹H NMR (CDCl₃, 300 MHz) δ7.99 (s, 1H), 7.62 (d, J = 8.9 Hz, 2H), 7.02 (d, J = 9.0 Hz, 2H), 5.26 (s, 2H), 3.87 (s, 3H), 3.19 (m, 2H), 1.53-1.43 (m, 2H), 1.37-1.29 (m, 2H), 0.91 (t, J = 7.1 Hz, 3H); ¹³C NMR (CDCl₃, 75 MHz) δ159.87 (C), 156.25 (C), 144.06 (C), 130.38 (C), 125.00 (C), 122.20 (CH), 114.76 (CH), 57.57 (CH₂), 55.61 (CH₃), 40.82 (CH₂), 31.94 (CH₂), 19.85 (CH₂), 13.68 (CH₃); MS [EI⁺] m/z (%) 304 [M]⁺ (20), 266 (100). Elemental analysis calculated: C, 59.20; H, 6.62; N, 18.41, found: C, 60.05; H, 6.87; N, 18.10.

4-[(4-bromophenoxy)methyl]-1-(4-bromophenyl)-1,2,3-triazole (13). White solid; mp 127 °C; IR (ATR): ν = 3123, 2921, 1516, 1460; ¹H NMR (CDCl₃, 300 MHz) δ8.02 (s, 1H), 7.71-7.60 (m, 4H), 7.40 (d, J = 8.9 Hz, 2H), 6.91 (d, J = 8.9 Hz), 5.27 (s, 2H); ¹³C NMR (CDCl₃, 75 MHz) δ157.0 (C), 144.7 (C), 135.73(C), 132.8 (CH), 132.3 (CH), 122.5 (C), 121.8 (CH), 120.6 (CH), 116.4 (CH), 113.5 (C), 61.9 (CH₂); MS [EI⁺] m/z (%) 406 [M]⁺ (10), 239 [M - C₆H₄BrN]⁺ (4), 211 [M - C₆H₄BrN₃]⁺ (100), 156 [C₆H₄Br]⁺ (40), 184 [C₇H₆BrO]⁺ (80). Elemental analysis calculated: C, 44.04; H, 2.71; N, 10.27, found: C, 43.90; H, 2.81; N, 10.90.

Ethyl 3-(4-chlorophenyl)-2-[4-phenyl-1,2,3-triazole-1-yl]acrylate (14). White solid; mp 127 °C; IR (ATR): ν = 3137, 2925, 1725, 1645; ¹H NMR (CDCl₃, 300 MHz) δ7.98 (s, 1H), 7.93-7.88 (m, 3H), 7.84 (s, 1H), 7.48-7.33 (m, 4H), 6.87-6.82 (m, 2H), 4.34 (q, J = 7.1 Hz, 2H), 1.32 (t, J = 7.1 Hz, 3H); ¹³C NMR (CDCl₃, 75 MHz) δ162.7 (C), 148.2 (C), 137.7 (C), 131.5 (CH), 130.8 (C), 130.0 (C), 129.4 (CH), 129.3 (C), 128.9 (CH), 128.8 (CH), 128.5 (CH), 125.8 (CH), 125.6 (C), 121.2 (CH), 62.5 (CH₂), 14.1 (CH₃); MS [EI⁺] m/z (%) 354 [M+1]⁺ (2), 324 [M - HN₂]⁺ (30), 251 [M - C₈H₆]⁺ (40), 102 [M - C₁₁H₁₀ClN₃O₂]⁺ (80). Elemental analysis calculated: C, 64.50; H, 4.56; N, 11.88, found: C, 64.00; H, 4.86; N, 10.90.

Ethyl (2-[4-((4-bromophenoxy)methyl)-1,2,3-triazole-1-yl]-3-(4-chlorophenyl) acrylate (15). White solid; mp 99 °C; IR (ATR): ν = 3144, 1722, 1644, 1590; ¹H NMR (CDCl₃, 300 MHz) δ7.94 (s, 1H), 7.64 (s, 1H), 7.39 (d, J = 9.0 Hz, 2H), 7.16 (d, J = 8.5 Hz, 2H), 6.88 (d, J = 8.9 Hz, 2H), 6.70 (d, J = 8.5 Hz, 2H), 5.30 (s, 2H), 4.30 (q, J = 7.1 Hz, 2H),

1.29 (t, J = 7.1 Hz, 3H); ¹³C NMR (CDCl₃, 75 MHz) δ162.6 (C), 157.0 (C), 144.4 (C), 139.2 (CH), 137.7 (C), 132.3 (CH), 131.3 (CH), 129.3 (CH), 129.1 (C), 125.4 (C), 124.6 (CH), 116.8 (CH), 113.6 (C), 62.5 (CH₂), 62.0 (CH₂), 14.1 (CH₃); MS [EI⁺] m/z (%) 461 [M]⁺ (5), 251 [M - C₁₁H₁₀ClO₂]⁺ (4), 154 [M - C₁₄H₁₃ClN₃O₃]⁺ (100). Elemental analysis calculated: C, 51.91; H, 3.70; N, 9.08, found: C, 52.19; H, 3.79; N, 9.90.

Ethyl 3-(4-chlorophenyl)-2-[4-((4-methoxyphenoxy)methyl)-1,2,3-triazole-1-yl] acrylate (16). Yellow oil; IR (ATR): ν = 2957, 2121, 1721, 823; ¹H NMR (CDCl₃, 300 MHz) δ7.94 (s, 1H), 7.63 (s, 1H), 7.16 (d, J = 8.5 Hz, 2H), 6.93 (d, J = 9.1 Hz, 2H), 6.83 (d, J = 9.2 Hz, 2H), 6.69 (d, J = 8.5 Hz, 2H), 5.28 (s, 2H), 4.31 (q, J = 7.1 Hz, 2H), 3.78 (s, 3H), 0.92 (t, J = 7.1 Hz, 2H); ¹³C NMR (CDCl₃, 75 MHz) δ162.7 (C), 154.3 (C), 151.9 (C), 145.2 (C), 139.1 (CH), 137.6 (C), 131.4 (CH), 130.8 (C), 129.3 (CH), 129.1 (C), 124.4 (CH), 116.1 (CH), 114.6 (CH), 62.6 (CH₂), 62.5 (CH₂), 55.8 (CH₃), 14.1 (CH₃); MS [EI⁺] m/z (%) 413 [M]⁺ (10), 123 [M - C₁₄H₁₃ClN₃O₂]⁺ (100). Elemental analysis calculated: C, 60.95; H, 4.87; N, 10.15, found: C, 60.98; H, 4.84; N, 10.80.

Ethyl 2-[4-(2-(butylcarbamoyloxy)ethyl)-1,2,3-triazole-1-yl]-3-(4-chlorophenyl] acrylate (17). Yellow solid; mp 129 °C; IR (ATR): ν = 3156, 1642, 1581, 1487, 1197; ¹H NMR (CDCl₃, 300 MHz) δ7.95 (s, 1H), 7.68 (s, 1H), 7.23 (d, J = 8.6 Hz, 2H), 6.75 (d, J = 8.5 Hz, 2H), 5.27 (s, 2H), 4.76 (s, 1H), 4.32 (q, J = 7.1 Hz, 2H), 3.17 (m, 2H), 1.37-1.21 (m, 6H), 0.91 (t, J = 7.1 Hz, 3H); ¹³C NMR (CDCl₃, 75 MHz) δ162.7 (C), 156.0 (C), 144.1 (C), 139.1 (CH), 137.6 (C), 135.2 (CH), 131.4 (CH), 130.8 (C), 129.3 (CH), 128.8 (C), 62.5 (CH₂), 57.6 (CH₂), 32.1 (CH₂), 26.3 (CH₂), 23.4 (CH₂), 14.1 (CH₃), 13.6 (CH₃); MS [EI⁺] m/z (%) 405 [M-1]⁺ (4), 363 [M - C₃H₇]⁺ (4), 349 [M - C₄H₉]⁺ (3), 250 [M - C₇H₁₁N₂O₂]⁺ (35), 154 [M - C₁₄H₁₃ClN₃O₃]⁺ (50), 57 [M - C₁₅H₁₄ClN₄O₄]⁺ (100). Elemental analysis calculated: C, 56.09; H, 5.70; N, 13.77, found: C, 56.80; H, 5.32; N, 14.01.

Solventless copper-catalyzed cycloaddition of alkynes and azides with NaOH.

Typical procedure. Successively added in a mortar were the corresponding alkyne (1 mmol), the azide (1 mmol), NaOH (0.40 g, 10.0 mmol) and CuI (0.0095 g, 0.05 mmol). The mixture was homogenized in a mortar for 5 minutes using a pestle. The mixture was collected and the final products were purified by column chromatography (SiO₂, hexane/AcOEt 8:2).

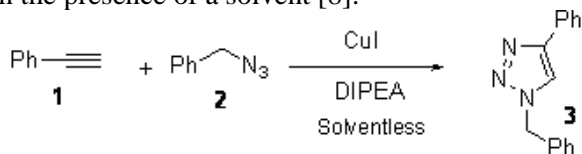
3,3'-dibenzyl-5, 5'-diphenyl -[4,4'] bi [(1,2,3)-triazolyl] (Table 4, Entry 1). White solid; mp 65 °C; IR (ATR): $\nu=$ 2953, 2852, 1602, 1456; ^1H NMR (CDCl₃, 300 MHz) δ 7.45 (m, 4H), 7.28-7.20 (m, 6H), 7.14 (m, 2H), 7.09 (m, 4H), 6.81 (d, 4H, J = 8.0 Hz), 5.57 (s, 2H), 5.26 (s, 2H); ^{13}C NMR (CDCl₃, 75 MHz) δ 147.52 (C), 132.57 (C), 128.93 (C), 128.66 (CH), 128.52 (CH), 128.47 (CH), 128.41 (CH), 127.87 (CH), 125.49 (CH), 119.59 (C), 52.37 (CH₂); MS [EI⁺] m/z (%) 468 [M]⁺ (40), 349 [M - C₇H₇N₂]⁺ (35), 321 [M - C₇H₇N₄]⁺ (35), 91 [C₆H₅CH₂]⁺ (100).

3,5,3',5'-tetraphenyl-[4,4']bi[(1,2,3)-triazolyl] (Table 4, Entry 2). White solid; mp 68 °C; IR (ATR): $\nu=$ 2957, 2855, 1514, 1461; ^1H NMR (CDCl₃, 300 MHz) δ 8.27 (d, J= 7.2 Hz, 3H), 7.76 (d, J=8.3 Hz, 4H), 7.55-7.42 (m, 11H), 2.47 (s, 6H); ^{13}C NMR (CDCl₃, 75 MHz) δ 139.12 (C), 133.73 (C), 131.01 (CH), 130.40 (C), 129.82 (CH), 129.34 (CH), 129.12 (CH), 128.25 (CH -35), 123.21 (CH), 121.14 (C), 20.56 (CH₃); MS [EI⁺] m/z (%) 468 [M]⁺ (40), 349 [M - C₇H₇N₂]⁺ (35), 321 [M - C₇H₇N₄]⁺ (35), 91 [C₆H₅CH₂]⁺ (100).

3,3'-dibenzyl-5,5'-bis[(4-bromophenoxy)methyl]-4,4'-bi[(1,2,3)-triazolyl] (Table 4, Entry 3). White solid; mp 179 °C; IR (ATR): $\nu=$ 3063, 2921, 1581, 1484; ^1H NMR (CDCl₃, 300 MHz) δ 7.23-7.33 (m, 10H), 6.87-6.89 (d, 4H), 6.44- 6.47 (d, 4H), 5.01 (s, 2H), 4.96 (s, 2H), 4.47 (s, 4H); ^{13}C NMR (CDCl₃, 75 MHz) δ 156.6, 145.5, 133.6, 132.3, 129.1, 129.0, 128.1, 122.1, 116.1, 113.7, 61.1, 52.6; MS [EI⁺] m/z (%) 686 [M]⁺ (2), 92 [C₆H₅CH₃]⁺ (100).

RESULTS AND DISCUSSION

The first studies were carried out using phenylacetylene (**1**) and benzyl azide (**2**) as starting materials (scheme 1). Among many plausible co-reactants to carry out CuAAC under solventless conditions, we decided to use CuI-DIPEA as a catalyst system which represents one of the simplest protocols when this reaction is performed in the presence of a solvent [8].



Scheme 1. Solventless cycloaddition between azide **2** and alkyne **1**.

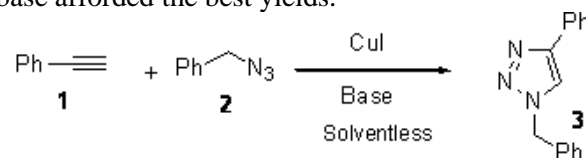
Moreover, we determined to place the alkyne, the azide, the copper salt and the base on a mortar and the resulting reaction mixture was homogenized by grinding with a pestle for a certain time. This procedure was essentially the same

during the course of the experiments in solvent-free conditions, and for this case, the direct reaction between alkyne **1** and azide **2** yielded 1-benzyl-4-phenyl-1,2,3-triazole (**3**) as the only reaction product. The effect of the concentration of both CuI and DIPEA was studied, and the results in table 1 show that the reaction is efficient with concentrations of 5 % mol CuI and 10% mol DIPEA.

Table 1. Effect of the concentration of CuI and DIPEA in the synthesis of triazole **3** under solventless conditions.

Entry	CuI (mmol/ mmol/ alkyne)	DIPEA (mmol/ mmol/ alkyne)	Reaction Time (min)	Yield (%)
1	0.1	1	2	95
2	0.05	1	2	95
3	0.025	1	2	88
4	0.0125	1	2	83
5	0.1	1	5	98
6	0.05	1	5	98
7	0.025	1	5	86
8	0.0125	1	5	82
9	0.1	0.1	5	98
10	0.05	0.1	5	98
11	0.025	0.1	5	85
12	0.0125	0.1	5	84

In addition, other bases were tested and the results are presented in table 2. Although triazole **3** was obtained in all cases, the use of DIPEA as a base afforded the best yields.



Scheme 2. Solventless cycloaddition between azide **2** and alkyne **1** in the presence of a base.

Table 2. Effect of the base in the synthesis of triazole **3** under solventless conditions.

Entry	Base	Yield (%)
1	DIPEA	98
2	Et ₃ N	88
3	Pyridine	70
4	K ₂ CO ₃	62
5	Na ₂ CO ₃	52
6	NaHCO ₃	53

In order to explore the reaction scope, we performed solventless CuAAC reactions with diverse alkynes and azides and the results in table 3 demonstrate that this procedure is broad in scope affording the corresponding 1,2,3-triazoles in high yields which were fully characterized by the conventional spectroscopic techniques.

Table 3. Synthesis of 1,2,3-triazoles under solventless conditions.

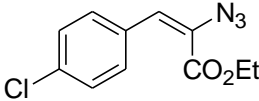
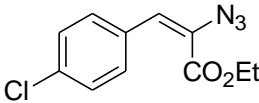
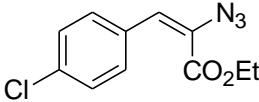
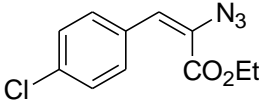
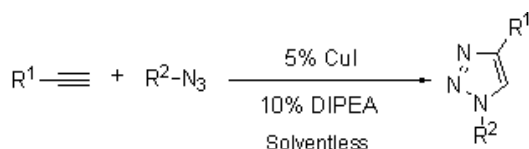
Compound	R ¹	R ²	Yield (%)
3	Ph	PhCH ₂	98
4	Ph	Ph	95
5	4-BrC ₆ H ₄ OCH ₂	PhCH ₂	57
6	4-BrC ₆ H ₄ OCH ₂	Ph	61
7	4-BrC ₆ H ₄ OCH ₂	4-CH ₃ C ₆ H ₄	75
8	Ph	4-CH ₃ C ₆ H ₄	92
9	CH ₂ OH	4-CH ₃ OC ₆ H ₄	87
10	4-BrC ₆ H ₄ OCH ₂	4-CH ₃ OC ₆ H ₄	71
11	Ph	4-CH ₃ OC ₆ H ₄	88
12	nBuNHCO ₂ CH ₂	4-CH ₃ OC ₆ H ₄	91
13	4-BrC ₆ H ₄ OCH ₂	4-BrC ₆ H ₄	72
14	Ph		87
15	4-BrC ₆ H ₄ OCH ₂		75
16	4-CH ₃ C ₆ H ₄ OCH ₂		82
17	nBuNHCO ₂ CH ₂		80

Table 4. Synthesis of triazoles and bistriazoles using solventless conditions.

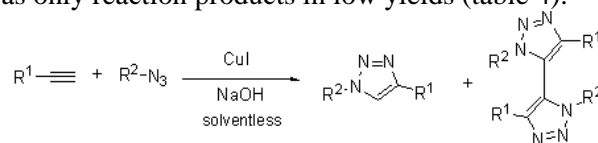
Entry	R ¹	R ²	% Triazole	% Bistriazole
1	Ph	PhCH ₂	30	15
2	Ph	4-CH ₃ C ₆ H ₄	35	20
3	4-BrC ₆ H ₄ OCH ₂	PhCH ₂	27	10

In these examples, triazoles **14-17** derived from ethyl 2-azido-3-(4-chlorophenyl)acrylate are similar to other heterocyclic analogs like resveratrol and have an important activity against lung and colon cancer cells.

**Scheme 3.** Synthesis of 1,2,3-triazoles under solventless conditions.

Other outstanding characteristic of the process is that the reaction times are short, and in the best of the cases these do not exceed 5 minutes. In addition, the purification of the final products is simple, in accordance with the essence of Click Chemistry.

On the other hand, we examined the use of sodium hydroxide in solventless CuAAC reactions. Previous reports described the formation of bistriazoles in the presence of inorganic bases [9], in particular, through the use of a high concentration of sodium hydroxide at low temperatures [10]. Thus, the solventless treatment of some alkynes and azides with excess sodium hydroxide and catalytic CuI yielded a mixture of triazoles and bistriazoles (scheme 4). In these processes, the yields of bistriazoles did not exceed 20% and in most cases the triazoles were obtained as only reaction products in low yields (table 4).

**Scheme 4.** Solventless synthesis of 1,2,3-triazoles and bistriazoles.

Despite these results, this method offers an alternative, direct and rapid protocol for the synthesis of these kinds of compounds with promising applications and the possibility of obtaining bistriazoles as major products of these processes that represent a great motivation to continue the studies in this area.

CONCLUSION

In summary, appropriately constituted alkynes and azides are easily converted to the corresponding 1,2,3-triazoles through a novel method that does not require the use of solvents in the presence of catalytic amounts of both CuI and DIPEA. This process combines short reaction times and high efficiency. In addition, when NaOH is used as the base, bistriazoles could be obtained through a solvent-free process. All the triazoles and bistriazoles described have biological potential activities and promise a broad application.

Acknowledgments: Financial support via the CONACYT (Project No. 135053) is gratefully acknowledged. The authors would like to thank Signa S.A. de C. V. and N. Zavala, A. Nuñez, L. Triana, for the technical support.

REFERENCES

1. M. Meldal, C.W. Tornøe, *Chem. Rev.*, **108**, 2952 (2008).
2. S.G. Agalave, S.R. Maujan, V.P. Pore, *Chem. Asian J.*, **6**, 2696 (2011).
3. H.C. Kolb, K.B. Sharpless, *Drug Discov. Today*, **8**, 1128 (2003).
4. Hein, C. D.; Liu, X. M.; Wang, D. *Pharm. Res.* **2008**, *25*, 2216.
5. H. Wang, K. Wen, L. Wang, Y.; Xiang, X. Xu, Y. Shen, Z. Sun, *Molecules*, **17**, 4533 (2012).
6. G.T. Tigineh, Y.S. Wen, L.K. Liu, *Tetrahedron*, **71**, 170 (2015).
7. H. Gallardo, G. Conte, F. Bryk, M.C.S. Lourenço, M.S. Costac, V.F. Ferreira, *J. Braz. Chem. Soc.*, **18**, 1285 (2007).
8. C.W. Tornøe, C. Christensen, M. Meldal, *J. Org. Chem.*, **67**, 3057 (2002).
9. Y. Angell, K. Burgess, *Angew. Chem. Int. Ed.*, **46**, 3649 (2007).
10. J. González, V. M. Pérez, D. O. Jiménez, G. Lopez-Valdez, D. Corona, E. Cuevas-Yañez, *Tetrahedron Lett.*, **52**, 3514 (2011).

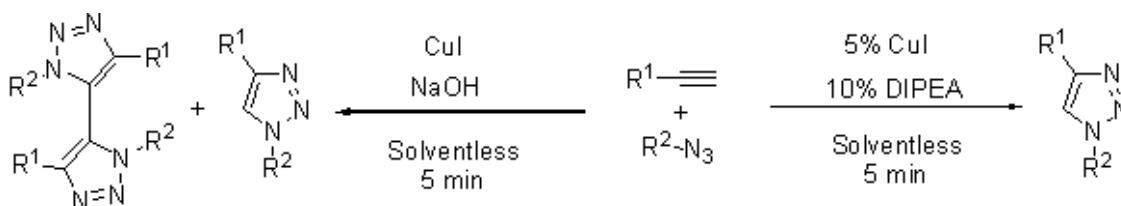
СИНТЕЗА БЕЗ РАЗТВОРИТЕЛ НА ТРИАЗОЛИ И БИС-ТРИАЗОЛИ ЧРЕЗ АЛКИН-АЗИД'ОВО ЦИКЛО-ПРИТЪКМЯВАНЕ, КАТАЛИЗИРАНО ОТ МЕД

М. Патераки¹, Г.К. Моралес-Ортиз¹, А. Лопес-Гусман¹, А. Фуентес-Бенитес², Е. Куевас-Янес^{1*}

¹Обединен изследователски център по устойчива химия UAEM-UNAM, Толука, Щат Мексико, 50200 Мексико и Автономен университет на щата Мексико, Толука, Щат Мексико, 50120 Мексико.

Постъпила на 4 март, 2015 г.; приета на 6 октомври, 2015 г.

(Резюме)



Синтезирани са 1,2,3-триазоли, включително серия от триазол-стирени, които имат структурна връзка с ресвератрол чрез нов метод без използване на разтворител. Методът включва пряко третиране чрез смилане на няколко азиди и алкини в присъствие на катализатор от меден йодид и *N,N*-ди-изопропил-етиламин. От друга страна, когато се използва натриева основа като алкален агент се получава смес от бис-триазоли и триазоли, при която 1,2,3-триазолите са главният продукт. Този нов протокол на синтезата се извършва при меки условия за кратко време, допускащ 1,4-позиционни изомери с високи добиви.

Effects of some hormone applications on germination and morphological characters of endangered plant species *Lilium artvinense* L. Onion scales

H. Sevik¹, M. Cetin^{2*}

¹Kastamonu University, Faculty of Engineering and Architecture, Environmental Engineering Department, Kuzeykent, Kastamonu/Turkey

^{2*}Kastamonu University, Faculty of Engineering and Architecture, Landscape Architecture Department, Kuzeykent, Kastamonu/Turkey

Received April 2, 2015, Revised September 18, 2015

Lilies are economically important plants because of their large and attractive flowers. Thus, many wild species of lilies have been cultivated to produce liliun bulbs or flowers. However, some non-cultivated species are still found in nature, picked and sold, which damages the natural populations of the species. The easiest and most effective way of preventing them from being nature picked is the identification of easy and cheap methods of producing them. This study attempts to determine the ways of producing *Lilium artvinense* by the use of bulb flakes. 4 hormones (Indole-3-acetic acid (IAA), Indole-3-butyric acid (IBA), Naphthaleneacetic acid (NAA), and Gibberellic acid (GA3) were used, and 12 hormone applications were made. 3 doses (1000 ppm, 3000 ppm, and 5000 ppm) were used from each hormone. In addition, a control group was used. Each application was made to the basal, middle, and apical parts of the bulb flakes. In this way, 39 applications were made in total. The applications to the bulb flakes were compared in terms of 6 characters (i.e. rooting percentage, the number of roots, root height, the number of scions, scion width and height). Hormone applications can increase the likelihood of success at least two-fold, thus the species can be produced easily and cheaply.

Keywords: Danger of extinction; Auxins; Gibberellins; Likelihood; Rooting; Sustainable plant.

INTRODUCTION

Lilium belongs to the group *Lilieae* of *Liliaceae* and contains about 120 species [1]. Lilies are economically important plants because of their large and attractive flowers [2]. Thus, many wild species of lilies have been cultivated to produce liliun bulbs or flowers. Almost all horticulturalists of lilies are used to flower cutting. Especially Asiatic and oriental hybrids receive a great deal of attention at the international market [3].

However, picking especially rare and endemic species from their natural habitats in some countries damage the populations of the species in their natural environment. The easiest and the most effective way of picking these species from their natural habitats is the identification of methods of producing the species in nursery conditions. If such methods are cheap and practical, they can be put into practice more effectively. Production with seeds is of vital importance so as not to damage the natural populations of endangered species.

“IUCN Red Data BOOK” and “National List of

European Threatened Plants List” contain 3 liliun species from Europe. *Lilium artvinense* is one of them [4]. Only found in a limited area, the *Lilium artvinense* draws attention with its yellow flowers. Its natural population is severely damaged when its bulbs are picked from their natural habitats. To protect the natural population of the species, easy and cheap means of producing this species should be taught to the locals, thereby preventing them from picking the species from their natural environment.

Previous research has mostly attempted to determine the microculture techniques of producing lilies. However, these techniques are difficult, expensive, and impractical for the locals. This study examines the production of *Lilium artvinense* by the use of bulb flakes.

MATERIALS AND METHODS

The bulbs belonging to *Lilium artvinense* used in the study were picked from Artvin. The bulbs picked on the 10th and 11th of July were kept by moistening them in a germination substrate. Applications were made on the bulbs brought to the laboratory on the 13th of July.

* To whom all correspondence should be sent:

E-mail: mehmet.cetin@temple.edu

Polyethylene tubes of 3x3x15 cm were prepared in the laboratory by filling 2/3 of them with a Klasmann sterile germination substrate. Then the bulb flakes were cut out of the basal parts via a sterile lancet. Each of the obtained nail-like bulbs was divided into 3 parts in such a way that the apical, middle and basal parts would be equal.

These 3 different parts taken from the nail-like flakes were separately subjected to the solutions of four different hormones Indole-3-acetic acid (IAA), Indole-3-butyric acid (IBA), Naphthalene acetic acid (NAA) and Gibberellic acid (GA3) in 3 different doses (1000 ppm, 3000 ppm, and 5000 ppm). In this way, 13 application groups ($3 \times 4 = 12 + 1$ [control] = 13) were formed in total. The applications were made by sinking the samples in the hormones for 3 to 5 seconds. The same application was made 3 times in such a way that each time included 15 samples (i.e. 15 apical samples, 15 basal samples, and 15 middle samples included). 15 parts were put in each one of the prepared tubes in a way that prevented them from touching one another, covered with a germination substrate of almost 2 cm and moistened immediately.

The prepared tubes were placed in perforated boxes that did not receive direct sunlight at a room temperature of 20 to 25°C. They were irrigated every other day for 120 days. The substrates reached the saturation point during irrigation. No water accumulation occurred in the tubes because both the tubes and the boxes in which they were placed were perforated, which made the excess water flow away. Measurements were carried out on the 10th of November (i.e. the 120th day). In the meanwhile, the substrates in the tubes were discharged onto the bench. The roots were cleaned carefully. The number of roots was determined first. Then the average root height was measured via a digital micro-compass. After that, each sample was cleaned with water; the number of scions was determined and scion heights and widths were measured. All measurements were conducted through a digital micro-compass with a precision of 0.01 mm. The obtained results were entered in the table. In this way, the effects of 13 applications on the rooting percentage (RP), root height (RH), the number of scions (CCN), scion height (CCH), and scion width (CW) were evaluated.

These data were subjected to analysis of variance via SPSS 17.0. Duncan's test was carried out for those characters and found to contain a statistical difference at the minimum 95% confidence level. In this way, homogenous groups were created.

The effects of the hormone application on the rooting percentage, the number of nascent, the scions, the number of roots, root length, scion height, scion width and root height were analyzed via SPSS. The average values, analysis of variance results, and Duncan's test results concerning the characters are given in Table 1.

The values in the table indicate that the hormone applications had effects on all characters at a 99.9% confidence level. The highest rooting percentage, the highest root, the biggest number of scions, the highest scion, and the widest scion were obtained from IAA hormone applications. The largest number of roots were obtained from IBA hormone applications. Each hormone dose application was treated as a separate application in order to determine the effects of the hormone x dose interaction on the rooting percentage and the morphological characters of nascent individuals. The obtained data were analyzed. The analysis results are given in Table 2.

As seen in table 2, no rooting occurred in the 1000 ppm GA3 application and no scion emerged in the 1000 ppm NAA application. Rooting took place in all other hormone applications and the control group. The statistical analysis results indicated significant differences at a 99.9% confidence level between the applications in terms of all characters. Table 2 demonstrates that the highest roots emerged at the 1000 ppm IBA application and the highest roots were obtained at the 3000 ppm GA3 application. The highest values were obtained for IAA applications. The highest rooting percentage (80.22%) was obtained from the 3000 ppm IAA application; the largest number of scions (0.92) were obtained from the 1000 ppm IAA application and the highest (6.55 mm) and widest (4.3 mm) scions were obtained from the 5000 ppm IAA application. The obtained values indicate that IAA hormone application can increase the rooting percentage two times more than the control group. In other morphological characters, hormone applications can yield 4 to 5 times higher values compared to the control group.

The apical, middle, and basal parts were taken from the bulb flakes through division of these nail-like flakes on the metamorphic underground stem into three equal parts in order to reveal the meristematic ability of these parts. These parts' rates of forming new individuals and the morphological characters of such individuals were determined. The average values of the obtained data, F value obtained through analysis of variance, and groups formed as a result of Duncan's test are given in Table 3.

The values in table 3 indicate that the apical, middle, and basal parts have statistically significant effects on all characters of the nascent individuals including rooting percentage at the 99.9% confidence level. Duncan's test yielded two homogenous groups in terms of the rooting percentage, scion height, scion width and three homogenous groups in terms of other characters. Individuals consisting of sections taken from the basal part of the teeth were included in the first homogenous group in terms of all characters. That shows that the basal parts obtained from the nail have quite high rooting percentages, and the individuals emerging in these parts are more developed than the individuals emerging in other parts in terms of morphological characters.

It was seen in the present study that each one of the apical, middle, or basal parts obtained through the division of the nail-like flakes on the stem into 3 equal parts has potential meristematic proliferation ability. Thus, it was found out that the potential ability of each liliun bulb to form a scion may correspond to at least 3-folds of the number of nail-like flakes in the bulb. The values in the table

show that while the sections obtained from the basal part have the highest values in all characters, those obtained from the apical section have the lowest values. That indicates that the meristematic proliferation ability decreases from the basal area to the apical area.

RESULTS AND DISCUSSIONS

Many studies have been conducted on the production of lilies so far. However, these studies focus on the production of lilies through microculture techniques. In these studies, IBA and NAA [5] have been used in *Lilium davidii* var. *unicolor* [6] and *Lilium longiflorum*; IAA, IBA, and NAA [7,8] have been used in *Lilium davidii* var. *unicolor* [9], *Lilium oriental*, and *Lilium longiflorum*; IAA and IBA [2] have been used in *Lilium longiflorum*; and BA and GA3 [10] have been used in *Lilium japonicum*. However, it is not reasonable to compare the results of these studies with those of the present study because of the use of different methods in them.

Table 1. The effects of the hormone applications on the rooting percentage and morphological characters.

Hormone	RP		RN		RH		CCN		CCH		CW	
IAA	70,45	d	1,84	b	73,92	D	0,87	c	5,44	c	3,43	d
IBA	54,78	c	2,20	b	69,67	C	0,66	bc	2,86	b	1,54	bc
GA3	17,44	a	1,00	a	53,95	Bc	0,53	b	3,26	b	2,09	c
NAA	51,82	c	1,79	b	50,51	A	0,26	a	1,12	a	0,60	A
Control	28,57	b	1,14	a	34,71	A	0,43	ab	1,53	a	0,97	Ab
F Value	40,627		9,076**		7,075**		15,800*		30,924**		35,532*	
	***		*		*		**		*		**	

Table 2. The effects of hormone x dose interaction on the rooting percentage and morphological characters.

HOR	DOSE	RP		RN		RH		CCN		CCH		CW	
IAA	5000	56,64	ef	2,36	e	84,16	fg	0,82	cd	6,55	f	4,3	G
IBA	5000	56,64	ef	2,18	de	85,2	fg	0,91	d	3,41	cde	2,08	cde
GA3	5000	27,47	c	1,29	bc	47,23	cd	0,57	bcd	4,06	de	2,76	ef
NAA	5000	36,36	cd	1,27	bc	78,77	efg	0,27	ab	1,94	bc	0,99	ab
IAA	3000	80,22	h	1,5	bcd	74,65	efg	0,86	cd	4,82	e	3,24	f
IBA	3000	64,1	fg	2	cde	64,69	def	0,56	bcd	2,68	bcd	1,38	bcd
GA3	3000	13,85	b	1,2	b	95,72	g	0,8	cd	4,1	de	2,4	def
NAA	3000	45,06	de	2,21	de	56,32	cde	0,5	bc	1,52	ab	0,86	ab
IAA	1000	71,6	gh	1,77	bcde	64,47	def	0,92	d	5,16	ef	2,89	ef
IBA	1000	39,1	cd	2,50	e	62,92	def	0,58	bcd	2,63	bcd	1,3	bc
GA3	1000	0	a	0	a	0	a	0	a	0	a	0	a
NAA	1000	72,19	gh	1,77	bcde	20,36	ab	0	a	0	a	0	a
Cont.	0	28,57	c	1,14	b	34,71	bc	0,43	b	1,53	ab	0,97	ab
F Value		25,564***		5,837***		9,265***		8,591***		13,512***		15,872***	

Table 3. Effect of the fraction position.

Position	RP		RN		RH		CCN		CCH		CW	
Apical	6,15	a	0,60	a	20,81	A	0,07	a	0,14	a	0,11	a
Medium	27,75	b	1,32	b	50,41	B	0,25	b	1,04	a	0,46	a
Basale	67,55	c	2,14	c	72,02	C	0,76	c	4,11	b	2,50	b
F Value	281,453***		40,790***		31,296***		45,892***		56,398***		58,096***	

Auxin group hormones including IAA, IBA and NAA are intensely used in rooting works. It is reported that the use of these hormones on many species including *Melissa officinalis* [11], *Robinia pseudoacacia* [12], *Pseudotsuga menziesii* [13], *Oryza sativa* [14] and *Pisum sativum* [15] can increase the rooting percentage. Gibberelins are the third most commonly used group among the plant growth regulators [16]. Although GA3 is mostly used for enhancing flower yield or plant growth [17], it also increases the rooting percentage [11,18].

CONCLUSIONS

Picking the endangered *Lilium* species from the nature and selling them damage the natural populations of these species badly. The most effective way of preventing them from being picked is the identification of methods of producing them in simple environments free of cost. The previous research has mostly aimed to determine the methods of producing lilia through microculture techniques. However, these methods are too difficult and costly to be implemented by villagers who pick them. Thus, they are ineffective for the solution of the problem.

This study made an attempt to identify the methods of producing lilies by use of bulb flakes in a simple, cheap, and effective way. It was found out that the hormones, which can be applied via very simple mechanisms, increase rooting success substantially and improve the morphological characters of the nascent individuals considerably. Especially IAA application can increase the rooting percentage minimum two-fold.

Since plants are vegetatively produced by the use of bulbs, the genetic structure is safeguard. Thus, the new plants to be produced will be genetically exactly the same as the rootstock plants. In this sense, when the individual characteristics desired have certain features (e.g. high flower yield, large flower formation, flowers in particular color tones, individuals resistant to stress conditions) are produced vegetatively, it is guaranteed that the desired features are maintained.

The present study showed that a minimum of 150-200 individuals can be produced out of a bulb of normal size. However, only the bulb flakes

outside the bulk should be taken without picking bulbs completely, and their internal parts should be left as they are so that these species do not disappear, and the natural existence of these populations is not damaged. At least 2-3 individuals can be produced out of one flake by cutting the collected bulb flake with a clean and sharp object.

In the present study, the greatest deal of rooting occurred for a 3000 ppm IAA application; the highest roots were formed for a 1000 ppm IBA application; the biggest number of scions were obtained for the 1000 ppm IAA application; and the highest and the widest scion formation took place for the 5000 ppm IAA application. Based on these results, the hormone application needed for the desired character to come to the forefront may be chosen. For instance, a 3000 ppm IAA application may be used for a high rooting percentage; a 1000 ppm IBA application may be used for high root formation; and a 5000 ppm IAA application may be used for bigger scion formation.

REFERENCES

1. Y.D. Gao, A.J. Harris, S.D. Zhou, X.J. He, *Mol Phylogenet Evol*, **68**, 443 (2013).
2. B.H. Han, H.J. Yu, B.W. Yae, K.Y. Paek, *Sci Hortic-Amsterdam*, **103**(1), 39 (2004).
3. M.L. Lian, D. Chakrabarty, K.Y. Paek, *Sci Hortic-Amsterdam*, **97**(1), 41 (2003).
4. A. Mitchell, *Sectional Species List. Lilies and Related Plants*, **2009-2010**, 100 (2009).
5. L. Bacchetta, P. C. Remotti, C. Bernardini, F. Saccardo, *Tiss Org* **74**: 37-44 (2003).
6. X. Lingfei, M. Fengwang, L. Dong, *Sci Hortic-Amsterdam* **119**(4): 458-461 (2009).
7. X.G. Chen Zhang, S. Ma, M. Zhong, Z.F. Guo, J. Ming, *Northern Horticulture*, **2010**,14 (2010).
8. F.Y. Yan, X.Y. Hu, X.H. Pei, D.S. Yin, *Agricultural Science*, **2008**, 06 (2008).
9. L. Jing, *Journal of Southern Agriculture*, **42**(8), 839 (2011).
10. M. Yamagishi, *J Jpn Soc Hortic Sci*, **64**(2), 367 (1995).
11. H. Sevik, K. Guney, *The Scientific World Journal Volume*, **2013**, Article ID 909507, (2013).
12. S. L. Swamy, S. Puri, A.K. Singhm, *New Forest*, **23**(2), 143 (2002).
13. M. Stefancic, F. Stampar, G. Osterc, *HortScience*, **40**(7), 2052 (2005).
14. T. Chhun, S. Taketa, S. Tsurumi, M. Ichii, *Plant Growth Regul*, **39**, 161 (2013).

15. A.C. Nordstrom, F.A. Jacobs, L. Eliasson, *Plant Physiol*, **96**, 856 (1991).
16. H. Sevik, K. Guney, *Soil-Water Journal*, **2**(2), 1647 (2013).
17. A.M. Kumlay, T. Eryigit, *Journal Science and Technology*, **1**(2), 47 (2011).
18. B. Cosge, B. Gurbuz, D. Soyler, N. Sekeroglu, *Journal of Crop Research*, **2**, 29 (2005).

ЕФЕКТИ НА НЯКОИ ХОРМОНИ ВЪРХУ ЗРЕЕНЕТО И МОРФОЛОГИЧНИТЕ ХАРАКТЕРИСТИКИ НА ЗАСТРАШЕНИЯ РАСТИТЕЛЕН ВИД *Lilium artvinense* L. ЛУКОВИЧНИ ЛЮСПИ

Х. Севик¹, М. Джетин^{2*}

¹Университет Кастамону, Факултет по инженерство и архитектура, Катедра по екологично инженерство, Кузейкент, Кастамону, Турция

²Университет Кастамону, Факултет по инженерство и архитектура, Катедра по ландшафтна архитектура, Кузейкент, Кастамону, Турция

Постъпила на 2 април, 2015 г.; приета на 15 септември, 2015 г.

(Резюме)

Лилиите са икономически важни растения поради техните големи и привлекателни цветове. При това много диви видове от лилиите се култивират за производството на луковичи и цветя. Но има и диво-растящи лилии, които се берат и продават, като с това се нарушават естествените им популации. Най-лесният и ефективен начин това да се предотврати е идентификацията на лесен и евтин начин за производството им. В тази работа се прави опит да се намери начин за производството на *Lilium artvinense* използвайки луковични люспи. Използвани са четири хормона (индол-3-оцетна киселина (IAA), индол-3-маслена киселина (IBA), нафтален-оцетна киселина (NAA) и гибелеринова киселина (GA3) и са приложени 12 пъти. Използвани са по три дози (1000 ppm, 3000 ppm, и 5000 ppm) от всеки хормон. Отделно е изпитана и контролна група. Всяко прилагане се прави на основната, средната и апикалната част на луковичните люспи. По този начин са направени общо 39 наблюдения. , In addition, a control group was used. Резултатите с луковични люспи са сравнени по шест показателя (процент на корени, брой на корените, височина на корените, брой на калемите, тяхната широчина и височина). Прилагането на хормони може да повиши успешните опити поне двойно, като при това растението се произвежда лесно и евтино.

BSA adsorption onto commercial activated carbon modified by microwave assisted chemical activation

M. B. Taşkın¹, S. Özbek², E. Demirhan^{1*}, B. Özbek¹

¹*Yıldız Technical University, Chemical Engineering Department, Davutpasa Campus, Esenler, Istanbul, Turkey*

²*Gedik University, Metallurgy and Materials Engineering Department, Kartal Campus, Kartal, Istanbul, Turkey*

Received April 15, 2015, Revised October 10, 2015

In the study, effects of pH and temperature on the equilibrium and the kinetics of bovine serum albumin (BSA) adsorption onto commercial and modified activated carbon were investigated. Activated carbon was modified firstly by treatment with Na₂CO₃, secondly thermally treated by microwave technique, and finally subjected to treatment with HCl. The modified activated carbon samples were characterized by Fourier Transform Infrared (FTIR) and BET analyses. The results indicated that it was possible to increase the surface area of the commercial activated carbon (CAC) after the modification process (MAC) with an enhancement percentage of 59%, compared to initial untreated CAC sample. The adsorption capacities decreased at pH values lower and higher than the isoelectric point value; and increased with increasing temperature for both activated carbon samples. Moreover, adsorption isotherm and kinetic data were well explained by the Langmuir isotherm and pseudo-second order kinetic models, respectively.

Keywords: Bovine serum albumin, activated carbon, microwave treatment, modification, adsorption, isotherm models, kinetics.

INTRODUCTION

The adsorption of proteins from solution onto solid surfaces is a vital and very active research field because of its application in protein purification, drug delivery systems, biosensors, design of food processing equipment and artificial implants. This process is complicated and involves various interactions. Most proteins are known as amphipathic molecules and this property makes them surface-active molecules. Hence, different results are obtained from the adsorption process because of the characteristic features of surfaces such as hydrophobicity and hydrophilicity. The adsorption process results in a change in physicochemical properties. The affinity of a protein for an interface is affected by the structural stability of the protein, the ionic strength and pH of the solution, and the surface properties of the sorbent [1-4].

Bovine serum albumin (BSA) is a globular blood plasma protein. It has a high conformational adaptability and is often used as a reference protein for adsorption experiments. Sustainability of the osmotic pressure and pH of blood, and transport of various compounds are the most important physiological functions of serum albumin. The

isoelectric point of BSA is about pH 4.5-5.0 [5-8].

Activated carbons (AC) are widely used as an effective adsorbent for the removal of organic pollutants such as dyes and heavy metals from aqueous solutions due to their large porous surface area, controllable pore structure, thermo stability and low acid/base reactivity. The physical and chemical properties of AC depend on their internal pore structure and surface functional groups. The commercial activated carbons are generally produced from wood and coconut shells. However, recently, other lignocellulosic materials, which are generally considered as a waste, have been used as precursors in the synthesis of this adsorbent for specific applications. The utilization of lignocellulosic biomass like rice hulls, bran, sawdust and fibers is very important for the economy, and simultaneously brings a solution to the waste problem [9-11].

In literature, the protein adsorption has been a subject of interest for various scientists and many studies have evaluated the adsorption of proteins on various adsorbents. In the present study, modified and non-modified activated carbons were used as adsorbents. For evaluation of the protein adsorption ability of the activated carbon samples, bovine serum albumin (BSA) was chosen as the target protein. The aims of this study were: i) to modify the surface properties of commercially available activated carbon; ii) to investigate the effect of pH and temperature on the adsorption of BSA from

* To whom all correspondence should be sent:
E-mail: elcindemirhan@gmail.com

aqueous solution; iii) to perform modelling studies to represent the adsorption isotherms and kinetics.

MATERIALS AND METHODS

Materials

Commercial activated carbon was obtained from Altek A.Ş., Istanbul. Bovine serum albumin and other chemicals of analytical grade were purchased from Sigma Aldrich.

Modification of activated carbon

Commercially available activated carbon Acticarbhone-CPW (produced from marine pine wood by chemical activation with phosphoric acid) was used in this study. Commercial activated carbon (CAC) was modified using the method described by Jiang et al. [10] with some modifications. Firstly, CAC was impregnated with a solution of 10% Na₂CO₃ at a ratio of 5:1 (weight of impregnation reagent/weight of activated carbon) and kept at room temperature for 24 h. Afterwards, the mixture was subjected to microwave treatment for 7 min at 540 W of microwave output power. The mixture was cooled to room temperature and then was boiled with 10% HCl solution for 30 min. After the boiling procedure, the mixture was washed several times with distilled water; and was dried at 100°C for 24 h. The modified activated carbon sample obtained from this treatment was named MAC.

Characterization of the modified activated carbon

In order to determine the physical and chemical changes of activated carbon after the modification treatment, the modified activated carbon (MAC) was characterized by Fourier Transform Infrared (FTIR) and BET analyses. Pore size distribution of CAC and MAC samples was analysed by the BJH desorption method. While FTIR was used to identify the chemical structure, surface structure was examined by BET analysis. FTIR spectra of the samples were collected using a Perkin Elmer Pyris1 FT-IR spectrometer. The KBr pellets were prepared containing 1/2 g of the activated carbon sample.

Protein adsorption studies

Adsorption experiments were carried out to evaluate the adsorption capacities and isotherms of activated carbon samples at different pH (4-7) and temperature (25-40°C) values. The experiment was initiated by the addition of adsorbent to 50 mL of BSA solution at the desired pH and temperature. Buffer solutions were used to keep the pH value steady. The mixture was shaken for 60 min at 100

rpm in a shaking incubator. During the processing time of 60 min, the samples were taken from the mixture at timed intervals and centrifuged to remove the particles. The protein concentration in the supernatant was determined by the Lowry method [12]. The amount of protein adsorbed on the adsorbent was calculated by the mass balance before and after adsorption. For each sample, the assay was carried out in triplicate and the average was taken. In this study, all experiments were carried out at least in duplicate and the reproducibility between trials was within ±5%. Adsorption capacities were calculated by using the following equation:

$$q_e = \frac{(C_0 - C_e) \cdot V}{m}$$

where q_e is the equilibrium adsorbed concentration (mg/g), C_0 and C_e are the initial and equilibrium protein concentrations (mg/L), respectively. V is the volume of the solutions and m is the weight of adsorbent (g).

Adsorption isotherm models

Langmuir, Freundlich and Temkin isotherm models were used to evaluate the data obtained from the BSA adsorption experiments:

Langmuir model:

$$\frac{1}{q_e} = \frac{1}{Q \cdot b \cdot C_e} + \frac{1}{Q}$$

where q_e is the equilibrium adsorbed concentration (mg g⁻¹), C_e is the equilibrium protein concentration (mg L⁻¹), Q is the maximum sorption capacity (mg g⁻¹) and b is the adsorption equilibrium constant.

Freundlich model:

$$\ln q_e = \ln K_F + \frac{1}{n} \ln C_e$$

where K_F is the Freundlich affinity coefficient, n is the Freundlich exponential coefficient.

Temkin model:

$$q_e = \frac{RT}{b_T} \ln A_T + \frac{RT}{b_T} \ln C_e$$

where A_T and b_T are the Temkin coefficients.

Adsorption kinetics of protein

Several methods are available to study the adsorption mechanism. In this study, in order to determine the adsorption kinetics, the data obtained from the BSA adsorption process were analysed with the pseudo-first order, pseudo-second order, Elovich and intra particle diffusion models.

Pseudo-first order model:

$$\log \frac{q_e - q_t}{q_e} = \frac{k_1 t}{2.303}$$

where q_e is the adsorbed amount at equilibrium (mg g^{-1}); q_t is the adsorbed amount at time t (mg/g); k_1 is the pseudo-first order adsorption kinetic parameter (min^{-1})

Pseudo-second order model:

$$\frac{t}{q_t} = \frac{1}{k_2 q_e^2} + \frac{t}{q_e}$$

where k_2 is the pseudo-second order adsorption kinetic parameter ($\text{g mg}^{-1} \text{min}^{-1}$).

Elovich model:

The Elovich equation is valid for chemisorption kinetics and systems in which the surface is heterogenous.

$$q_t = \frac{1}{\beta} \ln(\alpha\beta) + \frac{1}{\beta} \ln t$$

where α is the initial adsorption rate ($\text{mg g}^{-1} \text{min}$); β is a constant related to the extent of surface coverage and activation energy consumption (g mg^{-1})

Intra particle diffusion model:

$$q_t = k_i t^{0.5} + C_i$$

where k_i is the intra particle diffusion kinetic parameter ($\text{mg g}^{-1} \text{min}^{-2}$); C_i is a constant related to layer thickness (mg g^{-1}).

RESULTS AND DISCUSSION

Characterization of the modified activated carbon

The FTIR results of CAC and MAC are shown in Fig. 1 (a-b). As can be seen from these figures, there is no significant difference between the FTIR spectra of these two activated carbon samples. This could be explained with the neutralizing effect between Na_2CO_3 and HCl used for modification of the activated carbon. According to literature, the peaks observed around 3400 cm^{-1} were stretches arisen from $-\text{OH}$ groups [11, 13-15]. When two spectra of activated carbon were compared, it was observed that the $-\text{OH}$ stretching intensity of MAC sample slightly decreased due to the treatment with Na_2CO_3 .

Table 1 BET surface analysis results of CAC and MAC samples

Sample	S_{BET} (m^2/g)	S_{mes} (m^2/g)	V_{tot} (cm^3/g)	V_{mic} (cm^3/g)	V_{mes} (cm^3/g)	R_{avg} (nm)
CAC	1572	1014	1.608	0.256	1551	2.026
MAC	2492	1653	2.427	0.402	2296	1.948

On the other hand, in both spectra, peaks were present around 1155 cm^{-1} , which pointed to C-O stretching [15]. Moreover, it was considered that the observed peaks around 1565 cm^{-1} contained multi groups and these groups were referred to as C=C and $-\text{COOH}$ groups, as stated in the literature [11, 15-17].

The results of surface structure analyses of CAC and MAC are given in Table 1. Pore size distribution of CAC and MAC samples analysed by the BJH desorption method is presented in Figure 2 (a,b). Generally, the surface areas of these two activated carbon samples were high because of numerous micropores on the surface structure. The findings showed that the surface area of modified AC increased up to $2492 \text{ m}^2/\text{g}$ compared to the initial untreated AC sample surface area of $1572 \text{ m}^2/\text{g}$. On the other hand, it was found that the mesoporous surface area increased from 1014 to $1653 \text{ m}^2/\text{g}$ with an enhancement rate of 1.63.

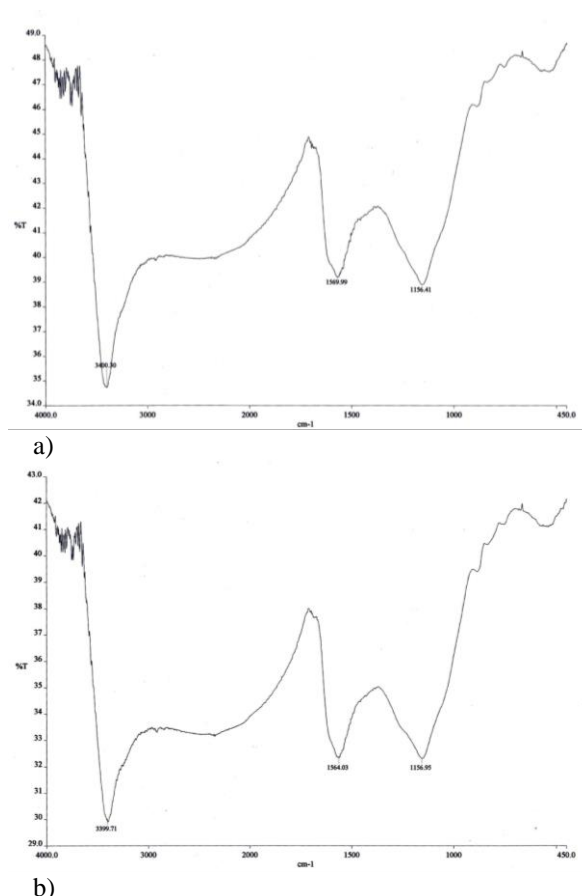
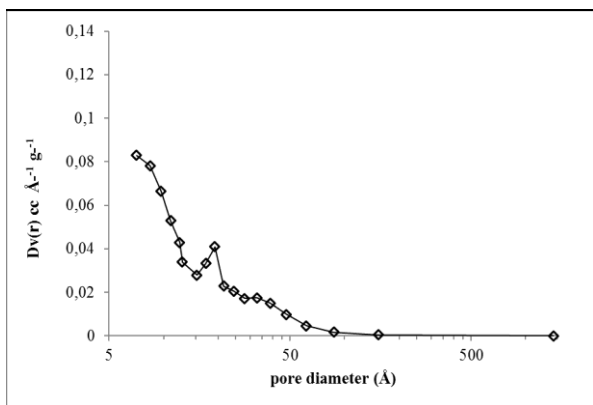
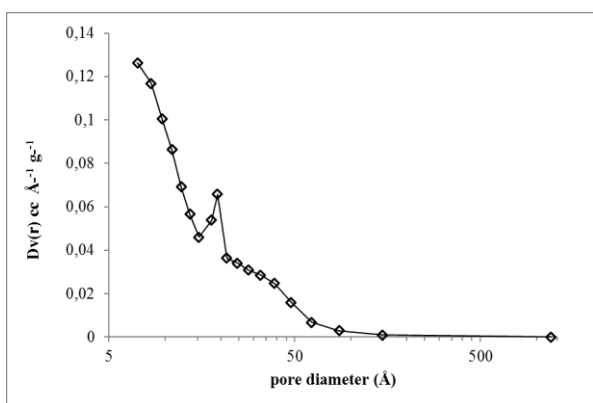


Fig. 1. FT-IR spectra of a) CAC b) MAC.



a)



b)

Fig. 2. Pore size distribution in a) CAC b) MAC.

Moreover, as a result of micropore intensity increase in the MAC sample, it was observed that the average pore diameter decreased from 2.026 nm to 1.948 nm. According to the literature, pores with a diameter of $2 < r < 50$ nm are defined as mesopores. The increase in the average pore diameter of MAC samples (mesopores) was similar to that of CAC samples. This obviously showed that although diameters of mesopores were $r > 2$ nm, these values were very small to increase the pore diameter. In other words, the diameter of the obtained mesopores was similar to that of micropores.

Adsorption of BSA on the commercial (CAC) and modified (MAC) activated carbon

Effect of pH on BSA adsorption

pH is one of the critical and most important parameters for determining the adsorbent's surface characteristics and the adsorption equilibrium in the adsorption process. It affects the chemical speciation of ions and the ionization of active functional sites on the sorbent surface. The effect of pH on the adsorption of BSA onto commercial (CAC) and modified (MAC) activated carbon samples was assessed in the pH range from 4 to 7 and the pH dependence of BSA adsorption is

presented in Figure 3. As can be seen from this figure, maximum adsorption capacities are observed at pH 5 for both activated carbon samples, which is near to the isoelectric point of BSA. The adsorbed amount of BSA decreased at pH values lower and higher than the isoelectric point value. This decrease could be explained by the bilateral electrostatic repulsion of protein molecules since they are with the same electric charge. Protein molecules at the pI are natural, and the repulsion force between BSA molecules becomes almost zero [2,18,19]. Therefore, according to these results, the optimum pH value was found as 5.0 for BSA adsorption.

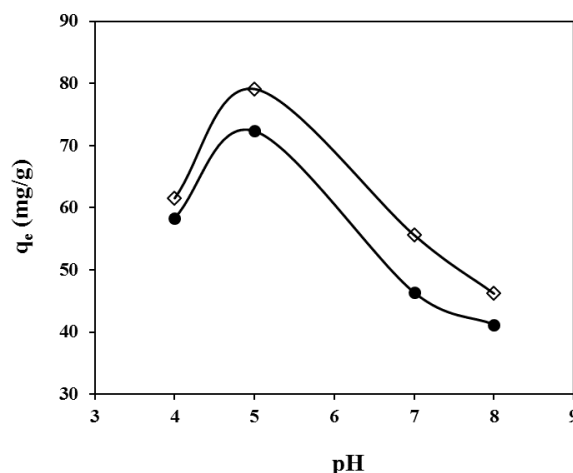


Fig. 3. Effect of pH on the BSA adsorption capacity of activated carbon samples (● CAC; ◇ MAC).

Effect of temperature on BSA adsorption

In order to investigate the effect of temperature on the adsorption of BSA onto CAC and MAC samples, the experiments were performed in the temperature range from 25 to 40°C. The BSA adsorption capacity of CAC and MAC in respect to temperature is presented in Fig. 4. The results showed that the temperature of solution extremely influenced the BSA adsorption. The adsorption capacity of all samples increased with increasing temperature. This increase might be due to the increase of the diffusion on adsorbent surfaces with increasing protein activity. The same result was stated in the studies of BSA adsorption on TiO₂ [5], BSA adsorption on SBA-15 [20] and BSA adsorption on monodispersed hollow silica nanospheres [18].

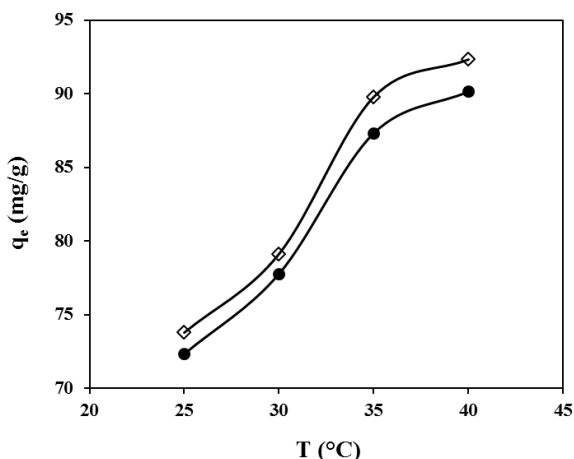


Fig. 4. Effect of temperature on the BSA adsorption capacity of activated carbon samples (● CAC; ◇ MAC)

Adsorption isotherm modelling

Three classic adsorption models (Langmuir, Freundlich and Temkin isotherm models) were used to describe the equilibrium adsorption data of the BSA onto activated carbon samples. Among these isotherm models, Langmuir isotherm model was determined as the most appropriate one for the BSA adsorption data with high values of the correlation coefficient (R^2) and low values of the standard error (σ). This result indicates that BSA adsorption occurs as a monolayer onto the homogenous adsorbent surface. The estimated parameters of these models are presented in Table 2.

As can be seen in Table 2, the maximum adsorption capacity of CAC and MAC for BSA

adsorption was found as 134.77 mg/g and 136 mg/g, respectively, at 40°C and pH 5. It was observed that the adsorption capacity decreased at pH 7 and pH 8. This showed that the maximum adsorption occurred at pH 5 near its isoelectric point, where it is neutral. This could be explained with the hydrophobic interactions between BSA and activated carbon. Furthermore, it was known that BSA was negatively charged at pH 7.5. So, above this pH value, the adsorption was limited because of the electrostatic repulsions between the negatively charged activated carbon and BSA molecules [21].

On the other hand, the maximum adsorption capacity values of MAC were slightly higher than those of the CAC samples. This slight increase was explained with the large molecular size of BSA to enter the micropores. As explained in the previous section, the mesopore diameter of the MAC sample was similar to that of the micropores. So, these mesopores were not sufficient to increase the adsorption capacity of the MAC sample. The same behaviour was observed in the adsorption of BSA onto materials with different pore size in the literature [22-23].

Additionally, the mineral residue remaining on the surface of the activated carbon increased the hydrophilicity of the MAC sample, which could prevent the increase of the adsorption capacity [24].

Table 2. Estimated parameters and statistical values of isotherm models for BSA adsorption onto CAC and MAC samples (pH= 5.0, T= 40°C).

CAC Sample			
Langmuir Isotherm			
Q (mg/g)	b (L/mg)	σ	R^2
134.77	0.02703	0.00077	0.9359
Freundlich Isotherm			
K_F (mg ^{1-1/n} L ^{1/n} g ⁻¹)	n	σ	R^2
41.99	5.7060	0.07896	0.9172
Temkin Isotherm			
A_T (L/g)	b_T (J/mol)	σ	R^2
1.1737	131.9671	10.8043	0.8842
MAC Sample			
Langmuir Isotherm			
Q (mg/g)	b (L/mg)	σ	R^2
136.00	0.01884	0.00057	0.9433
Freundlich Isotherm			
K_F (mg ^{1-1/n} L ^{1/n} g ⁻¹)	n	σ	R^2
36.50	5.1647	0.06207	0.9437
Temkin Isotherm			
A_T (L/g)	b_T (J/mol)	σ	R^2
0.6562	123.2266	8.1491	0.9213

Adsorption kinetics modelling

Evaluation of the adsorption kinetics and adsorption equilibrium is very important to plan and control the adsorption process. In order to describe the adsorption kinetics, the pseudo-first order, the pseudo-second order, Elovich and the intra particle diffusion models were used for the evaluation of kinetic data obtained from the adsorption experiments. The adsorption kinetics experiments were carried out at different temperature and pH values. The estimated parameters and statistical data of these models are presented in Tables 3 and 4.

As can be seen from the tables, among these models, the second order kinetic model was found as the most appropriate one for all experimental data with high values of the coefficient of determination and low standard error values. Therefore, because of the fact that the pseudo-

second order kinetic model suggests that the adsorption process incorporates chemisorption mechanism, it may be concluded that adsorption of BSA molecules onto activated carbon samples consists of chemical adsorption. The result obtained was in agreement with the studies published in the literature, and several authors have stated that the pseudo-second order kinetic model was better for BSA adsorption onto monodispersed hollow silica nanospheres [18] and Fe₃O₄ magnetic nanoparticles [19].

A summary of the BSA adsorption capacity of several adsorbents studied by several authors is given in Table 5. The adsorption capacities of CAC and MAC were higher than the results proposed in the literature for BSA adsorption except for silica gel, sepiolite and activated carbon.

Table 3. Statistical values of adsorption models for BSA adsorption onto CAC and MAC samples for various temperature values (pH= 5.0).

CAC Sample								
T (°C)	Pseudo-first order		Pseudo-second order		Elovich		Intraparticle	
	R ²	σ	R ²	σ	R ²	σ	R ²	σ
25	0.9662	5.9986	0.9937	0.0287	0.9280	8.6661	0.8432	12.3238
30	0.9716	5.0766	0.9927	0.0318	0.9215	8.3377	0.8887	9.8437
35	0.9856	4.1337	0.9978	0.0150	0.9749	5.4351	0.8450	13.0579
40	0.9837	4.5692	0.9976	0.0148	0.9621	6.9312	0.8732	12.3885
MAC Sample								
T (°C)	Pseudo-first order		Pseudo-second order		Elovich		Intraparticle	
	R ²	σ	R ²	σ	R ²	σ	R ²	σ
25	0.9757	4.5804	0.9975	0.0186	0.9638	5.5739	0.8685	10.3576
30	0.9739	4.9770	0.9941	0.0278	0.9373	7.6453	0.8769	10.5424
35	0.9797	5.0747	0.9974	0.0157	0.9542	7.5709	0.8794	12.0425
40	0.9810	5.0075	0.9980	0.0135	0.9653	6.7349	0.8737	12.5541

Table 4. Statistical values of adsorption models for BSA adsorption onto CAC and MAC samples for various pH values (T= 40°C).

CAC Sample								
pH	Pseudo-first order		Pseudo-second order		Elovich		Intraparticle	
	R ²	σ	R ²	σ	R ²	σ	R ²	σ
4	0.9522	5.5917	0.9787	0.0684	0.8556	9.4456	0.8976	8.0669
5	0.9837	4.5692	0.9976	0.0148	0.9621	6.9312	0.8732	12.3885
7	0.9378	4.8705	0.9671	0.1236	0.8562	7.2486	0.8067	8.2916
8	0.9357	3.9330	0.9829	0.0929	0.9071	4.6951	0.8939	4.9982
MAC Sample								
pH	Pseudo-first order		Pseudo-second order		Elovich		Intraparticle	
	R ²	σ	R ²	σ	R ²	σ	R ²	σ
4	0.9861	2.7174	0.9973	0.0254	0.9767	3.5281	0.8132	9.5382
5	0.9810	5.0075	0.9980	0.0135	0.9653	6.7349	0.8737	12.5541
7	0.8638	8.6977	0.9409	0.1297	0.7757	10.8938	0.8233	9.7983
8	0.9410	3.0856	0.9836	0.1190	0.9073	3.8342	0.8512	4.7872

Table 5. Adsorption capacities of various adsorbents compared with the present study.

Adsorbents	Experimental Conditions		Adsorption capacity (mg/g)	Ref.
	pH	Temp. (°C)		
Sepiolite	7.0	25	219.4	[1]
Kaolinite	7.0	25	29.1	[1]
Expanded perlite	7.0	25	2.3	[1]
Unexpanded perlite	7.0	25	1.1	[1]
Activated carbon	7.0	23	13.4	[9]
Silica coated MnFe ₂ O ₄	3.8	25	100	[14]
Activated carbon	7.0	40	3.2	[26]
Activated carbon	5.7	25	312	[27]
Activated carbon	5.3	25	27.3	[28]
Silk fibroin microspheres	7.4	37	16	[29]
TiO ₂	5.0	40	82	[30]
Silica gel	7.0	25	228	[31]
Hydroxyapatite	6.8	30	49	[32]
Commercial activated carbon	5.0	40	134.8	Present study
Modified activated carbon	5.0	40	136	Present study

CONCLUSIONS

Commercially available AC powder was modified by treating with chemical activation agents such as Na₂CO₃ and HCl, followed by heat treatment applying microwave technique. After the modification process, the surface area of the modified AC increased up to 2492 m²/g compared to the initial untreated AC sample surface area of 1572 m²/g.

Adsorption experiments were carried out using adsorption equilibrium and kinetics to investigate the adsorption ability of the commercial and modified activated carbon samples.

The maximum adsorption capacities for CAC and MAC samples were obtained at pH 5, near to pI of the protein where the repulsion force between adsorbed proteins is minimal. The amount of adsorbed BSA increased with increasing temperature for CAC and MAC samples, which indicates that the adsorption of BSA on activated carbon samples is an endothermic process. The isotherm data for BSA adsorption on activated carbon fitted well the Langmuir isotherm model. The maximum adsorption capacity of CAC and MAC for BSA adsorption was found as 134.77 mg/g and 136 mg/g, respectively, at 40°C and pH 5. Furthermore, kinetic data fitted the pseudo-second order kinetic model. Hence, it can be concluded that activated carbon samples can be employed as effective adsorbents for adsorption of proteins.

Acknowledgements: This research has been supported by Yıldız Technical University Scientific Research Projects Coordination Department. Project Number: 2011-07-01-KAP02.

REFERENCES

1. M. Alkan, Ö. Demirbas, M. Doğan, O. Arslan, *Micropor. Mesopor. Mat.*, **96**, 331 (2006).
2. W. Li, S. Li, *Colloid Surface A.*, **294**, 159 (2007).
3. L. Song, K. Yang, W. Jiang, P. Du, B. Xing, *Colloid Surface. B.*, **94**, 341 (2012).
4. K. Nakanishi, T. Sakiyama, K. Imamura, *J. Biosci. Bioeng.*, **91(3)**, 233 (2001).
5. T. Kopac, K. Bozgeyik, J. Yener, *Colloid Surface A.*, **322**, 19 (2008).
6. F. Sezões, L.R. Carrott, P.A. Mourão, P.J. Carrot, *Adsorpt. Sci. Technol.*, **28**, 777 (2010).
7. E. Mavropoulos, M.L.F.M. Kede, N.C.C. da Rocha, A. Machado Costa, A. Tosi, M.H. Prado da Silva, A.M. Rossi, *Bioceramic Develop. Appl.*, **1**, D101115, (2011).
8. E. Edri, O. Regev, *Anal. Chem.*, **80**, 4049 (2008).
9. N. Dizge, B. Tansel, *J. Hazard. Mater.*, **185**, 996 (2011).
10. L. Jiang, F. Ma, G. Liang, *Adv. Manage. Sci.*, **3**, 320 (2010).
11. Z. Liu, L. Li, L. Tang, R. Shi, Q. Gu, X. Liang, X. Yao, *J. Environ. Chem. Eng.*, **1**, 131 (2013).
12. O.H. Lowry, J.N. Rosebrough, A.L. Farr, R.J. Randall, *J. Biol. Chem.*, **193**, 265 (1951).
13. F.J. Lopez-Garzon, M. Domingo-Garcia, M. Perez-Mendoza, P.M. Alvarez, V. Gomez-Serrano, *Langmuir*, **19**, 2838 (2003).

14. H.F. Liang, Z.C. Wang, *Mater. Chem. Phys.*, **124**, 964 (2010).
15. P. Ramachandran, R. Vairamuthu, S. Ponnusamy, *J. Eng. Appl. Sci.*, **6(11)**, 15 (2011).
16. A.M. Puziy, O.I. Poddubnaya, A. Martinez-Alonso, F. Suarez-Garcia and J.M.D Tascon, *Carbon*, **40**, 1493 (2002).
17. Y. Guo and R.M. Bustin, *Int. J. Coal Geol.*, **37**, 29 (1998).
18. M.J. Hwang, O.H. Kim, W.G. Shim, H. Moon, *Micropor. Mesopor. Mat.*, **182**, 81 (2013).
19. S. Kamran, M. Asadi, G. Absalan, *Microchim. Acta*, **180**, 41 (2013).
20. T.P.B. Nguyen, J.W. Lee, W.G. Shim, H. Moon, *Micropor. Mesopor. Mat.*, **110**, 560 (2008).
21. W. Shen, Z. Li, Y. Liu, *Recent Pat. Chem. Eng.*, **1**, 27 (2008).
22. F. Sezões, L.R. Carrott, P.A. Mourão, P.J. Carrot, *Adsorp. Sci. Technol.*, **28**, 777 (2010).
23. D.P. Xu, S.H. Yoon, I. Mochida, W.M. Qiao, Y.G. Wang, L.C. Ling, *Micropor. Mesopor. Mat.*, **115**, 461 (2008).
24. H. Marsh, F. Rodriguez-Reinoso, *Activated Carbon*. Elsevier (2005).
25. S.Z. Qiao, H. Zhang, X. Zhou, S. Budihartono, G.Q. Lu, *Stud. Surf. Sci. Catal.*, **165**, 425 (2007).
26. G. Sekaran, M. Mariappan, K.V. Raghavan, *Bioprocess Eng.*, **15**, 165 (1996).
27. V.L. Sigal, P.V. Osadchii, *Pharm. Chem. J.*, **21**, 647 (1987).
28. R.Y.A. Wu, PhD Thesis, Purdue University, West Lafayette, 1982.
29. Y. Srisuwan, P. Srihanam, Y. Baimark, *J. Macromol. Sci.*, **46**, 521 (2009).
30. C.E. Giacomelli, M.J. Avena, C.P. De Puli, *J. Colloid Interface Sci.*, **188**, 387 (1997).
31. C.E. Giacomelli, W. Norde, *J. Colloid Interface Sci.*, **233**, 234 (2001).
32. G. Yin, Z. Liu, J. Zhan, F. Ding, N. Yuan, *Chem. Eng. J.*, **87**, 181 (2002).

АДСОРБЦИЯ НА АЛБУМИН ОТ ГОВЕЖДИ СЕРУМ (BSA) ВЪРХУ ТЪРГОВСКИ АКТИВЕН ВЪГЛЕН И МОДИФИЦИРАН С ХИМИЧНО АКТИВИРАНЕ С МИКРОВЪЛНОВО ВЪЗДЕЙСТВИЕ

М.В. Ташкын¹, С. Йозбек², Е. Демирхан^{1*}, Б. Йозбек¹

¹Технически университет Йълдъз, Департамент по химично инженерство, Есенлер, Истанбул, Турция

²Университет Гедик, Департамент по металургия и материалознание, Картал, Истанбул, Турция

Постъпила на 15 април, 2015 г., приета на 10 октомври, 2015 г.

(Резюме)

В настоящата работа са изследвани ефектите на рН и температурата върху равновесието и кинетиката на адсорбция на албумин от говежди серум (BSA) върху търговски и модифициран активен въглен. Активният въглен беше модифициран с микровълнова техника със следващо третиране със солна киселина. Модифицираният активен въглен беше охарактеризиран с Фуриерова ИЧ-спектроскопия (FTIR) и BET анализи. Резултатите показват, че по този начин е възможно да се повиши повърхността на търговския активен въглен (САС) след модификацията до (МАС) с 59%, в сравнение с контролната проба (САС). Адсорбционният капацитет намалява при ниски рН, но е по-висок отколкото в изо-електричната точка. Той нараства с температурата са двата изследвани въглена. Освен това, адсорбционната изотерма и кинетичните данни се обясняват добре с изотермата на Langmuir и кинетично уравнение от псевдо-втори порядък.

EPR study of gamma - irradiated homeopathic medicines

K. I. Aleksieva*, N. D. Yordanov

Molecular catalysis with centre of EPR spectroscopy, Institute of Catalysis, Bulgarian Academy of Sciences, 1113, Sofia, Bulgaria

Received April 22, 2015, Revised October 26, 2015

The EPR studies of homeopathic medicines from plant (aconite, arnica, belladonna, bryony, dulcamara, symphytum and eupatorium) and animal (cuttle) origin before and after gamma-irradiation are reported. Before irradiation all samples are EPR silent. After gamma-sterilization however they all exhibit a specific “sugar-like” EPR spectrum due most probably to sucrose used as an excipient. These stable free radicals can be used to identify radiation processing a long time after irradiation.

Keywords: homeopathic pills; gamma – irradiation; EPR.

INTRODUCTION

Gamma rays have been intensively used to sterilize drugs, medical devices and foodstuffs [1]. One of the main advantages of the process is the opportunity for sterilization of the products even in their final packages [2]. This process however must be under control. Electron Paramagnetic Resonance (EPR) spectroscopy is an unambiguous technique for determining the origin and stability of the radiation induced free radicals in the solid state. Thus, it has been accepted by the European Union as a standard procedure for identification of irradiated foods [3; 4; 5]. As for foodstuffs, it could be interesting to be able to prove whether or not a drug has been irradiated [6]. In view of this a wide variety of gamma-irradiated antibiotics were studied by EPR [7]. The character and stability of radicals in drugs following ionizing radiation varies depending on their structure and the propensity of the solid matrix to free radical trapping. The decay rates of gamma-induced free radicals in drugs that have a wide application in anticancer [8] and anti-asthmatic therapy [9] have been investigated. The EPR spectroscopic properties were determined and suggestions concerning the possible structure of gamma induced radicals for anti-emetic [10] and antipyretic drugs [11] have been made. In these samples however there is only one substance – an active pharmaceutical ingredient (API). Most of the other pills are a mixture of an API which varies from 2 -10% of the weight of the pill and the remaining 98 – 90% are excipients [12]. This case is similar to the homeopathic pill case in which the

API is extremely low and thus the identification of the radiation sterilization is possible only from the EPR spectra of the excipients. Therefore, previous research [12, 13] on the stability of the induced radicals by irradiation and mechanical treatment in some excipients will be very useful.

In the present communication we report the EPR spectra obtained before and after gamma irradiation of some homeopathic medicines in order to prove the samples have been irradiated or not. Also, the stability of the radiation induced free radicals is determined.

EXPERIMENTAL

Materials

Homeopathic pills from different plant (aconite, arnica, belladonna, bryony, dulcamara, symphytum and eupatorium) and animal origin (cuttle) were purchased from a local pharmacy and were divided in two portions. The first batch was passed for irradiation, the second was separated as control samples. After gamma-irradiation the samples were kept under normal environmental conditions (temperature 19–22 °C, humidity 70–80%), available in the laboratory.

Irradiation

Homeopathic pills were simultaneously gamma-irradiated by the “Gamma 1300” irradiator with a single dose of 10 kGy. The irradiation was performed at room temperature and in the air. All further manipulations of the irradiated samples were performed at least 72 h after irradiation in order to avoid any interference by the radiation induced short living paramagnetic species.

* To whom all correspondence should be sent:
E-mail: kati@ic.bas.bg

Instrumentation

EPR measurements were performed at room temperature on a JEOL JES-FA 100 spectrometer operated in the X-band. Standard cylindrical cavity operating in the TE₀₁₁ mode was used. All samples were accommodated in quartz EPR sample tubes (i.d./o.d. 4/5 mm). The parameters used to record a single scan EPR spectrum of each sample were: microwave power 1 mW; modulation frequency 100 kHz and amplitude 0,25 mT; sweep width 10 mT, sweep time 2 min. and time constant 1 sec.

RESULTS AND DISCUSSION

EPR spectra

Before irradiation all studied pills do not show EPR spectra.

After irradiation all homeopathic medicines exhibit a typical EPR spectrum (Figure 1). It is worth to note that the same EPR spectrum was recorded from sucrose, white and brown sugar [14]. This feature, as well as its independence of the origin of the sugar [15] is very important from a dosimetric point of view because EPR can be used also for emergency radiation monitoring. The previous ENDOR [16] and high-frequency EPR studies [17] of irradiated sucrose show that the spectrum shown in Figure 1 is complex. At least three separate EPR spectra due to different paramagnetic species are superimposed on it [17]. In homeopathic pills sucrose is most probably used as an excipient. This is in accordance with the well-known fact that to reach the homeopathic concentrations, a preparation selected starting substance or compound is serially diluted in water or ethyl alcohol. Thus we cannot record any EPR spectrum from an active ingredient.



Fig. 1. EPR spectrum of homeopathic medicines after gamma-irradiation.

Study of the stability of radiation induced free radicals

The fading kinetics of the radiation induced EPR signal is an important characteristic of the materials because after irradiation it limits the time interval in which the identification of radiation processing is unambiguous. Since typically, for the given excipient this period strongly depends on the structure of the material under study, its storage conditions before and after irradiation, the humidity, exposure to air, light and temperature. In order to find the stability of radiation-induced EPR signals in homeopathic pills their kinetics were studied for a period of 200 days after irradiation. The studies show that radiation induced radicals in sucrose remain stable (Figure 2). Each point of Figure 2 is an average of at least three measurements. This result is imported in direction of emergency purpose because it is known that sucrose is found to be a very promising radiation sensitive material for gamma-irradiation with respect to both retrospective and reference solid state EPR dosimetry [18].

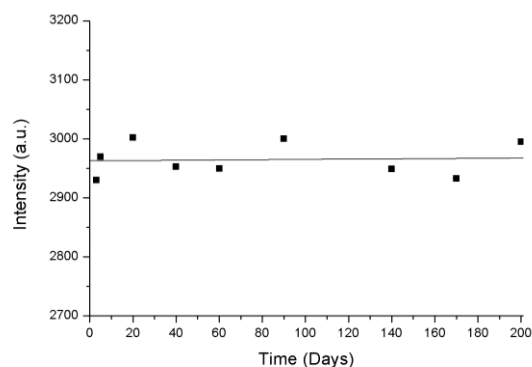


Fig. 2. Kinetics of the stability of a radiation induced signal in homeopathic medicines.

CONCLUSION

The results of EPR studies on homeopathic pills from: aconite, arnica, belladonna, bryony, dulcamara, symphytum, eupatorium and cuttle show that gamma-irradiation induce free radicals of sucrose, which is used as an excipient. No EPR spectra from active substances were record most probably due to their low concentration. Thus, the gamma-induced free radicals in sucrose present as excipient can be used for identification of radiation processing a long time after irradiation.

REFERENCES

1. D. Petrisor, G. Damian, S. Simon, *Radiat. Phys. Chem.*, **77**, 463 (2008)
2. H. Delincee, *Food Sci. Techn.*, **9**, 73 (1998).
3. EN 1786, *European Committee for Standardization, Brussels* (1996).
4. EN 1787, *European Committee for Standardization, Brussels* (2000).
5. EN 13708, *European Committee for Standardization, Brussels* (2001).
6. J. Raffi, S. Gelly, P. Picerelle, P. Prinderre, A.P. Chamayou, M. Baron, *Radiat. Phys. Chem.*, **63**, 705 (2002).
7. M. Gibella, A-S. Crucq, B. Tilquin, P. Stocker, G. Lesgards, J. Raffi, *Radiat. Phys. Chem.*, **58**, 69 (2000).
8. H. B. Ambroz, E. M. Kornacka, B. Marciniec, G. Przybytniak, *J. Radioanal. Nucl. Chem.*, **254**, 293 (2002).
9. J. P. Basly, J. L. Duroux, M. Bernard, *Int. J. Pharmac.* **142**, 125 (1996).
10. G. Damian, *Talanta*, **60**, 923 (2003).
11. M. Polat, M. Korkmaz, *Radiat. Eff. Def. Solids*, **161**, 51 (2006).
12. K. Aleksieva, N. D. Yordanov, *Radiat. Eff. Def. Solids*, **167**, 685 (2012).
13. J. Raffi, S. Gelly, L. Barral, F. Burger, P. Picerelle, P. Prinderre, M. Baron, A. Chamayou, *Spectrochim. Acta* **58**, 1313 (2002).
14. N. D. Yordanov, V. Gancheva, E. Georgieva, *Radiat. Phys. Chem.*, **65**, 269 (2002).
15. T. Nakajima, T. Otsuki, *Appl. Radiat. Isot.* **41**, 359 (1990).
16. G. Vanhaelewyn, J. Sadlo, F. Callens, W. Mondelaers, D. DeFrenne, P. A Matthys, *Appl. Radiat. Isot.* **52**, 1221 (2000).
17. E. Georgieva, L. Pardi, G. Jeschke, X. Gatteschki, L. Sorace, N. D. Yordanov, *Free Radical Res.*, **40**, 553 (2006).
18. Y. Karakirova, E. Lund, N. D. Yordanov, *Radiat. Meas.*, **43**, 1337 (2008).

ЕПР ИЗСЛЕДВАНЕ НА ГАМА-ОБЛЪЧЕНИ ХОМЕОПАТИЧНИ ЛЕКАРСТВА

К. И. Алексиева*, Н. Д. Йорданов

Молекулен катализ с център по ЕПР спектроскопия, Институт по катализ, Българска академия на науките, ул. „Акад. Г. Бончев“ бл. 11, София 1113, България

Постъпила на 22 април 2015 г., приета на 26 октомври 2015 г.

(Резюме)

Представени са резултати от ЕПР изследване на хомеопатични лекарства от растителен (самакитка, арника, беладона, дива тиква, червено кучешко грозде, черен оман и еупаториум) и животински произход (сепия) преди и след гама-облъчване. Преди облъчване не се регистрира ЕПР спектър. След гама-стерилизация при всички проби се детектира специфичният т. нар. „захароподобен“ ЕПР спектър, който най-вероятно се дължи на захароза, използвана като пълнител. Тези стабилни радикали може да се използват за идентифициране на радиационната обработка дълго време след облъчването.

Anticancer evaluation of novel quinazolines carrying a biologically active pyrimidine, triazine, benzo[*d*][1,3]dioxol, morpholinophenyl, quinoline, sulfonamide moieties

M. M. Ghorab^{1,2*}, M. S. Alsaïd¹

¹ Department of Pharmacognosy, College of Pharmacy, King Saud University, P.O. Box 2457, Riyadh 11451, Saudi Arabia

² Department of Drug Radiation Research, National Center for Radiation Research and Technology, Atomic Energy Authority, Nasr City, Cairo, Egypt

Received April 25, 2015, Revised June 5, 2015

A novel series of quinazolines incorporating a biologically active 4, 6-dimethylpyrimidine, 1, 2, 4-triazine, benzo[*d*][1,3]dioxol, morpholinophenyl, quinoline, sulfonamide and thioureamoieties **9-14**, **15,16,19**, **20** and 2-hydrazinylquinazoline derivative **22** were designed and synthesized using methyl 2-isothiocyanato derivative **2** as strategic starting material. The structure of the newly synthesized compounds was confirmed by elemental analyses and spectral data. All the prepared compounds were evaluated for their *invitro* anticancer activity against breast cancer cell lines. It was found that quinazoline carrying free amino group at 3-position with sulfa-phenazole group at 2-position **20** and thioureido derivative bearing sulfa-phenazole **16** with IC₅₀ values (2.64 and 4.60 µg/mL) showed better activity than doxorubicin as positive control. In addition compounds **14**, **12** and **15** are nearly as active as doxorubicin as reference drug, while compounds **9**, **13**, **11** and **19** exhibited a moderate activity. On the other hand, compounds **10** and **22** showed no activity.

Keywords: Synthesis, Dihydroquinazoline Derivatives, Anti-breast Cancer Activity.

INTRODUCTION

Natural and synthetic quinazolinone derivatives constitute an important class of fused heterocycles, which influence numerous cellular processes. These scaffolds as a core unit have been extensively studied in a number of biologically active compounds because of their broad range of biological medicinal, physiological and pharmacological applications [1-8]. In recent years, quinazolines, as an important pharmacophore, have emerged as a versatile template for inhibition of a diverse range of receptor tyrosine kinases [9-13]. The most widely studied of these is the epidermal growth factor receptor (EGFR), with the small-molecule inhibitor gefitinib being the first agent from this class to be approved for the treatment of Non-Small Cell Lung Cancer [14-18]. Subsequent research aimed at further exploration of the SAR of this novel template has led to the discovery of highly selective compounds that target EGFR such as Erlotinib, Lapatinib and Vandetanib [19-21] (**Fig. 1**). These compounds act via competing with ATP for binding at the catalytic domain of tyrosine kinase. Later on, a great structural variety of compounds of structurally diverse classes have proved to be highly potent and selective ATP-competitive inhibitors [22-25].

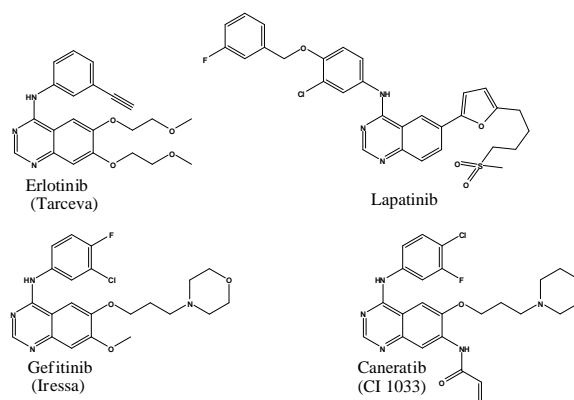


Fig. 1. EGFR-tyrosine kinase inhibitors.

Based on the good performance of quinazoline derivatives in anticancer application, the development of novel quinazoline derivatives as anticancer drugs is a promising field. Varied biological activities have been attributed to sulfonamide compounds, including carbonic anhydrase inhibition, antitumoral, antimalarial and antimicrobial activities [26-28]. In the design of new drugs, the development of hybrid molecules through the combination of different pharmacophores may lead to compounds with interesting biological profiles [29]. In view of the above mentioned knowledge based facts of different pharmacophores and in continuation of

our research programme [30-40], we have synthesized quinazoline carrying a biologically active 4, 6-dimethylpyrimidine, 1, 2, 4-triazine, benzo[d][1,3]dioxol, morpholino-phenyl, quinoline, sulfonamide moieties to evaluate their anti-breast cancer activity.

MATERIALS AND METHODS

Melting points (uncorrected) were determined in open capillary on a Gallen Kamp melting point apparatus (Sanyo Gallen Kamp, UK). Precoated silica gel plates (*Kieselgel* 0.25 mm, 60 F254, Merck, Germany) were used for thin layer chromatography. A developing solvent system of chloroform/methanol (8:2) was used and the spots were detected by ultraviolet light. IR spectra (KBr disc) were recorded using an FT-IR spectrophotometer (Perkin Elmer, USA). ¹H-NMR spectra were scanned on a NMR spectrophotometer (Bruker AXS Inc., Switzerland), operating at 500 MHz for ¹H- and 125.76 MHz for ¹³C. Chemical shifts are expressed in δ-values (ppm) relative to TMS as an internal standard, using DMSO-*d*₆ as a solvent. Elemental analyses were done on a model 2400 CHNSO analyser (Perkin Elmer, USA). All the values were within ± 0.4 % of the theoretical values. All reagents used were of AR grads.

CHEMISTRY

Synthesis of quinazoline derivatives 9-14.

General procedure

A mixture of methyl-2-isothiocyanatobenzoate **2** (1.93g, 0.01mol) and aromatic amines (0.012mol) in dry dimethylformamide (10mL) containing 3 drops of triethylamine was refluxed for 12h., then left to cool. The solid product formed upon pouring onto ice/water was collected by filtration and recrystallized from dioxane to give **9-14**, respectively.

4-(2-Phenylquinazolin-4-ylamino)benzenesulfonamide (9)

Yield, 84%; m.p. 172.5 °C. IR: 3381 (NH), 3081 (arom.), 2971, 2828 (aliph.), 1691 (CO), 1610 (CN), 1281 (CS). ¹H-NMR: 2.2 [s, 6H, 2CH₃], 6.5 [s, 1H, CH pyrimidine], 7.0-8.2 [m, 4H, Ar-H], 8.6 [s, 1H, NH]. ¹³C-NMR: 26.7 (2), 112.6, 114.6, 118.7, 122.8, 125.4, 130.6, 136.9, 161.2, 164.8 (2), 167.1, 173.6. Anal. Calcd. For C₁₄H₁₂N₄OS (284.34): C, 59.14; H, 4.25; N, 19.70. Found: C, 59.46; H, 4.55; N, 19.39.

3-(5, 6-Dimethyl-1,2,4-triazin-3-yl)-2-thioxo-2,3-dihydroquinazolin-4(1H)-one (10)

Yield, 88%; m.p. 95.9 °C. IR: 3411 (NH), 3056 (arom.), 2917, 2837 (aliph.), 1686 (CO), 1621 (CN), 1272 (CS). ¹H-NMR: 2.4, 2.8 [2s, 6H, 2CH₃], 6.9-8.2 [m, 4H, Ar-H], 8.5 [s, 1H, NH]. ¹³C-NMR: 16.3, 18.7, 113.6, 118.0, 125.4, 126.1, 130.8, 140.3, 146.2, 161.3, 162.6, 168.5, 175.7. Anal. Calcd. For C₁₃H₁₁N₅OS (285.32): C, 54.72; H, 3.89; N, 24.55. Found: C, 54.98; H, 4.13; N, 24.22.

3-(Benzo[d][1,3]dioxol-5-ylmethyl)-2-thioxo-2,3-dihydroquinazolin-4(1H)-one(11)

Method A:

A mixture of **2** (1.93g, 0.01 mole) and benzo[d][1,3]dioxol-5-ylmethanamine (1.51g, 0.01 mole) in dry dimethylformamide (15 mL) containing 3 drops of triethylamine was refluxed for 3 h. The obtained solid while hot was separated and recrystallized from dioxane to give **11**.

Method B:

A mixture of **2** (1.93g, 0.01 mole) and benzo[d][1,3]dioxol-5-ylmethanamine (1.51g, 0.01 mole) in dry dimethylformamide (15 mL) was stirred at room temperature for 2 h. The obtained material recrystallized from dioxane to give **11** (m.p and mixed m.p).

Yield, 79%; m.p. 281.5 °C. IR: 3261 (NH), 3100 (arom.), 2928, 2844 (aliph.), 1691 (CO), 1263 (CS). ¹H-NMR: 5.5 [s, 2H, CH₂], 5.9 [s, 2H, CH₂ pipronyl], 6.8-7.9 [m, 7H, Ar-H], 12.9 [s, 1H, NH]. ¹³C-NMR: 48.3, 100.8, 107.9, 108.2, 115.6, 120.9, 124.5 (2), 127.2, 130.3, 135.5, 139.0, 146.1, 146.9, 159.3, 175.7. Anal. Calcd. For C₁₆H₁₂N₂O₃S (312.34): C, 61.53; H, 3.87; N, 8.97. Found: C, 61.81; H, 4.09; N, 8.62.

3-(4-Morpholinophenyl)-2-thioxo-2,3-dihydroquinazolin-4(1H)-one(12)

Yield, 93%; m.p. 392.4 °C. IR: 3261 (NH), 3081 (arom.), 2966, 2881 (aliph.), 1679 (CO), 1260 (CS). ¹H-NMR: 2.7- 3.3 [m, 8H, 4CH₂], 6.8-7.8 [m, 8H, Ar-H], 8.0 [s, 1H, NH]. ¹³C-NMR: 51.2 (2), 62.6 (2), 112.6 (2), 116.7, 120.1, 121.7, 123.8 (2), 125.1, 128.2, 133.0, 141.2, 144.3, 162.2, 173.6. Anal. Calcd. For C₁₈H₁₇N₃O₂S (339.41): C, 63.70; H, 5.05; N, 12.38. Found: C, 63.40; H, 5.31; N, 12.05.

3-(Quinolin-3-yl)-2-thioxo-2,3-dihydroquinazolin-4(1H)-one(13)

Yield, 72%; m.p. 341.8 °C. IR: 3167 (NH), 3062 (arom.), 1699 (CO), 1620 (CN), 1265 (CS). ¹H-NMR: 7.0- 8.1 [m, 10H, Ar-H], 8.3 [s, 1H, NH]. ¹³C-NMR: 114.6, 117.0, 126.7 (2), 127.3, 127.4, 127.8, 128.4, 128.7, 130.3, 135.5, 137.4, 139.0, 141.8,

163.6, 176.3. Anal.Calcd. For $C_{17}H_{11}N_3OS$ (305.35): C, 66.87; H, 3.63; N, 13.76. Found: C, 66.52; H, 3.95; N, 13.47.

N-(5, 6-Dimethoxy-pyrimidin-4-yl)-4-(4-oxo-2-thioxo-1, 2-dihydroquinazolin-3(4*H*)-yl)benzenesulfonamide(14)

Yield, 77%; m.p. 178.4^oC. IR: 3246 (NH), 3100 (arom.), 2943, 2861 (aliph.), 1670 (CO), 1618 (CN), 1338, 1199 (SO₂). ¹H-NMR: 3.8, 3.9 [2s, 6H, 2OCH₃], 7.0-8.3 [m, 9H, Ar-H], 8.7 [s, 1H, NH], 11.0 [s, 1H, SO₂NH]. ¹³C-NMR: 54.1, 55.6, 113.2, 118.7, 119.6, 120.1, 121.3, 125.8, 127.3 (2), 129.1, 130.3, 133.4, 134.1, 140.8, 152.6, 153.1, 162.3, 164.6, 174.8. Anal.Calcd. For $C_{20}H_{17}N_5O_5S_2$ (471.51): C, 50.95; H, 3.63; N, 14.85. Found: C, 51.19; H, 3.37; N, 14.58.

*Methyl-2-(3-(4-morpholinophenyl)thioureido)benzoate (15) and methyl-2-(3-(4-(N-(1-phenyl-1*H*-pyrazol-5-yl)-sulfonyl)phenyl)thioureido)benzoate(16)*

A mixture of compound **2** (1.93g, 0.01 mole) and 4-morpholinoaniline and/ or sulfa-phenazole (0.01 mole) in dry dimethylformamide (15 mL) was stirred at room temperature for 2 h. The obtained solid upon pouring into ice water recrystallized from ethanol to give compounds **15** and **16**, respectively.

15: Yield, 69%; m.p. 381.3 ^oC. IR: 3261, 3189 (NH), 3057 (arom.), 2981, 2861 (aliph.), 1678(CO), 1246 (CS). ¹H-NMR: 2.7-3.7 [m, 8H, 4CH₂], 4.1 [s, 3H, OCH₃], 6.8-8.0 [m, 8H, Ar-H], 13.0 [s, 2H, 2NH]. ¹³C-NMR: 48.4 (2), 52.3, 66.0 (2), 114.9 (2), 121.2, 123.6, 125.5, 126.7 (2), 130.0, 132.6 (2), 141.0, 144.6, 162.2, 173.2. Anal.Calcd.For $C_{19}H_{21}N_3O_3S$ (371.45): C, 61.44; H, 5.70; N, 11.31. Found: C, 61.14; H, 5.44; N, 11.65.

16: Yield, 82%; m.p. 187.3^oC. IR: 3312, 3277 (NH), 3086 (arom.), 2976, 2831 (aliph.), 1682 (CO), 1618 (CN), 1371, 1156 (CS). ¹H-NMR: 3.7 [s, 3H, OCH₃], 6.6-8.2 [m, 15H, Ar-H], 11.0 [s, 1H, SO₂NH], 11.9 [s, 2H, 2NH]. ¹³C-NMR: 52.6, 103.7, 118.1, 120.7 (2), 122.0 (2), 124.4, 124.8, 125.1, 127.6 (2), 128.1 (2), 129.3, 130.8, 133.6, 134.7, 138.1, 139.5, 140.2, 142.9, 166.0, 176.3. Anal.Calcd. For $C_{24}H_{21}N_5O_4S_2$ (507.58): C, 56.79; H, 4.17; N, 13.80. Found: C, 56.48; H, 4.50; N, 14.07.

*3-Amino-2-(4-morpholinophenylamino) quinazolin-4(3*H*)-one(19) and 4-(3-amino-4-oxo-3, 4-dihydroquinazolin-2-ylamino)-N-(1-phenyl-1*H*-phenyl-1*H*-pyrazol-5-yl) benzenesulfonamide(20)*

A mixture of compounds **15** or **16** (0.01 mole) and hydrazine hydrate (0.012 mole) in absolute ethanol (20 mL) was refluxed for 15 h (after

evolution of all H₂S). The reaction mixture was poured on to ice water and the obtained solid recrystallized from dioxane to give compounds **19** and **20**, respectively.

19: Yield, 86%; m.p. 184.6^oC. IR: 3408, 3366, 3219 (NH, NH₂), 3088 (arom.), 2937, 2843 (aliph.), 1688 (CO), 1622 (CN). ¹H-NMR: 3.1- 3.7 [m, 8H, 4CH₂], 5.6 [s, 2H, NH], 6.2-8.3 [m, 8H, Ar-H], 9.1[s, 1H, NH]. ¹³C-NMR: 48.8 (2), 66.2 (2), 116.4 (2), 117.5 (2), 121.5, 124.8, 126.8, 127.2, 130.6, 133.9, 134.0, 148.5, 160.9, 161.0. Anal.Calcd. For $C_{18}H_{19}N_5O_2$ (337.37): C, 64.08; H, 5.68; N, 20.76. Found: C, 64.33; H, 5.39; N, 20.48.

20: Yield, 85%; m.p. 331.3^oC. IR: 3448, 3275, 3205 (NH, NH₂), 3100 (arom.), 1666 (CO), 1620 (CN), 1346, 1172 (SO₂). ¹H-NMR: 5.8 [s, 2H, NH₂], 6.2-8.4 [m, 15H, Ar-H], 9.2 [s, 1H, NH], 11.2 [s, 1H, SO₂NH]. ¹³C-NMR: 103.6, 112.0 (2), 117.6, 120.8 (2), 124.1, 124.8, 125.2, 126.3, 128.6 (2), 129.0, 129.6 (2), 131.4, 134.0, 137.1, 140.7, 145.9, 146.0, 161.2, 167.1. Anal.Calcd. For $C_{23}H_{19}N_7O_3S$ (473.51): C, 58.34; H, 4.04; N, 20.71. Found: C, 58.05; H, 4.30; N, 20.98.

*3-(Benzo[d][1,3]dioxol-5-ylmethyl)-2-hydrazinylquinazolin-4(3*H*)-one(22)*

A mixture of compound **11** (3.12g, 0.01 mole) and hydrazine hydrate (1g, 0.02 mole) was refluxed for 24 h (lead acetate paper). The obtained solid while hot was recrystallized from ethanol-dimethylformamide to give compound **22**.

Yield, 89%; m.p. 154.6^oC. IR: 3376, 3261 (NH, NH₂), 3059 (arom.), 2951, 2873 (aliph.), 1688 (CO), 1617 (CN). ¹H-NMR: 5.1 [s, 2H, N-CH₂], 5.9 [s, 2H, O-CH₂-O], 6.8-8.0 [m, 7H, Ar-H], 8.9 [s, 1H, NH], 9.5 [s, 1H, NH₂]. ¹³C-NMR: 42.3, 101.0, 107.8, 108.5, 120.6, 121.7, 124.4, 127.0, 127.1, 133.6, 134.2, 147.7, 148.6, 151.7, 161.3, 162.0. Anal.Calcd.For $C_{16}H_{14}N_4O_3$ (310.30): C, 61.93; H, 4.55; N, 18.06. Found: C, 61.64; H, 4.23; N, 17.88.

IN-VITRO ANTICANCER EVALUATION

The cytotoxic activity was measured *in vitro* for the newly synthesized compounds using the SulfoRhodamine-B stain (SRB) assay [41]. The *in vitro* anticancer screening was done at the Pharmacology Unit, the National Cancer Institute, Cairo University. Cells were plated in 96- multi-well plates (10⁴ cells per well) for 24 h before treatment with the compound, to allow attachment of cells to the wall of the plate. Test compounds were dissolved in DMSO and diluted with saline to the appropriate concentration. Different concentrations of the compound under test (10, 25, 50 and 100 µg/ml) were added to the cell

monolayer. Triplicate wells were prepared for each individual dose. Monolayer cells were incubated with the compound(s) for 48 h at 37 °C and in an atmosphere of 5% CO₂. After 48h cells were fixed, washed, and stained for 30 min with 0.4% (*m/V*) with SRB dissolved in 1 % acetic acid. Excess unbound dye was removed by four washes with 1 % of acetic acid and attached stain was recovered with a Tris-EDTA buffer. Color intensity was measured in an enzyme-linked immunosorbent assay ELISA reader. The relation between the surviving fraction and drug concentration is plotted to get the survival curve for the breast tumor cell line after the specified time. The molar concentration required for 50 % inhibition of cell viability (IC₅₀) was calculated and the results are given in (Table 1).

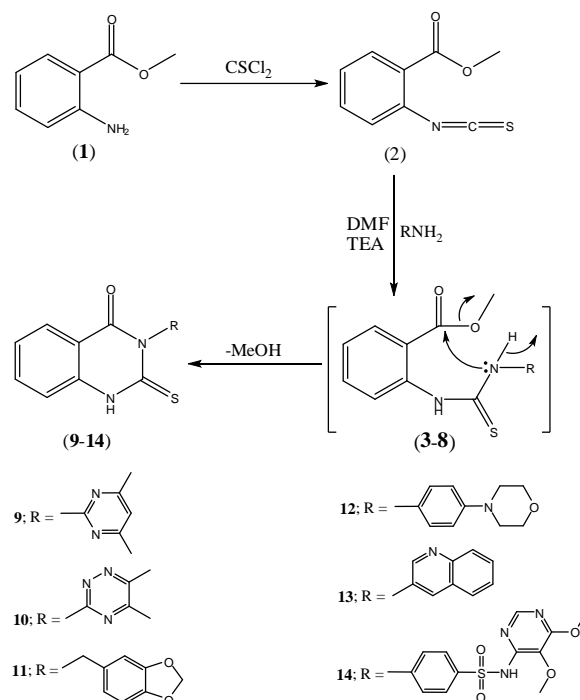
RESULTS AND DISCUSSION

Chemistry

The aim of this work was to design and synthesize novel quinazoline incorporating a biologically active 4, 6-dimethylpyrimidine **9**, 5,6-dimethyl-1,2,4-triazine **10**, benzo[*d*][1,3]dioxol-5-ylmethan **11**, 4-morpholinophenyl **12**, quinolone **13** and benzenesulfonamide **14**, thioureido derivatives **15** and **16**, 3-aminoquinazoline derivatives **19**, **20** and 2-hydrazinylquinazoline derivative **22** to evaluate their anti-breast cancer activity. Thus, interaction of methyl-2-isothiocyanatobenzoate **2** with 2-amino-4, 6-dimethylpyrimidine, 2-amino-5,6-dimethyl-1,2,4-triazine, benzo[*d*][1,3]dioxol-5-ylmethanamine, 4-morpholinoaniline, 3-aminoquinoline and sulfadoxinein dry *N,N*-dimethylformamide containing triethylamine as catalyst afforded the corresponding quinazoline derivatives is presented in **9-14** (Scheme 1).

The IR of compound **15** showed the absence of a N=C=S group and the presence of the characteristic bands at 3261, 3189 cm⁻¹ (NH), 3057 cm⁻¹ (aromatic) 1678 cm⁻¹ (CO), 1246 cm⁻¹ (CS). The ¹H-NMR of compound **15** exhibited signals at 4.1 ppm assigned to the OCH₃ group, 13.0 ppm due to 2NH groups. The IR of compound **16** revealed the absence of the N=C=S group and the presence of characteristic bands at 3312, 3277cm⁻¹ (NH), 1682 cm⁻¹ (CO), 1618cm⁻¹ (CN), 1371, 1156 cm⁻¹ (SO₂), 1256 cm⁻¹ (CS). The ¹H-NMR of compound **16** revealed signals at 3.7 ppm attributed to the OCH₃ group, 11.0 ppm assigned to the SO₂NH group, 11.9 ppm corresponding to 2NH groups. In addition the interaction of compound **15** and **16** with hydrazine hydrate in refluxing ethanol furnished the corresponding 3-aminoquinazoline derivatives **19**

and **20**. Compounds **19** and **20** were obtained through the formation of the intermediated **17** and **18**.



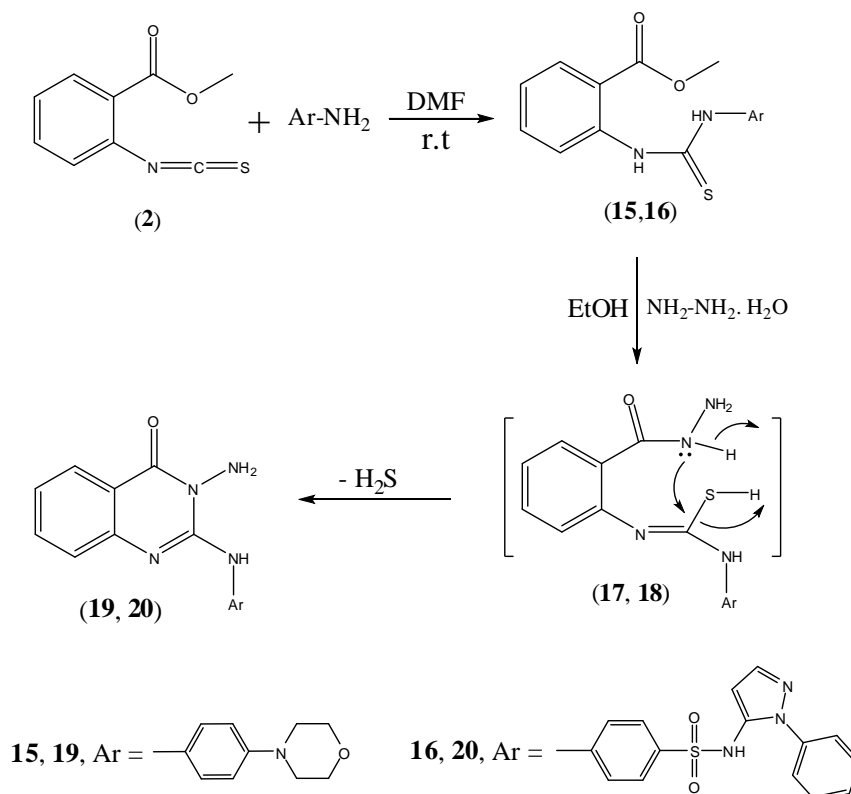
Scheme 1: Formation of quinazoline derivatives **9-14**

The structures of the obtained compounds were established on the basis of elemental analyses and spectral data. The IR spectra of compounds **9-14** showed the absence of N=C=S group and the presence of absorption bands for (NH), (aromatic), (aliphatic), (CO), (CN), (CS) and (SO₂) in compound **14**. ¹H - NMR exhibited singlets assigned to the NH group which were exchanged upon deuteration. Also, the interaction of compound **2** with 4-morpholinoaniline and/or sulfaphenazolein dimethylformamide at room temperature furnished the corresponding thioureido derivatives **15** and **16**, respectively. The structure of compounds **15** and **16** was elucidated on the basis of microanalysis, IR, ¹H-NMR and ¹³C-NMR (Scheme 2).

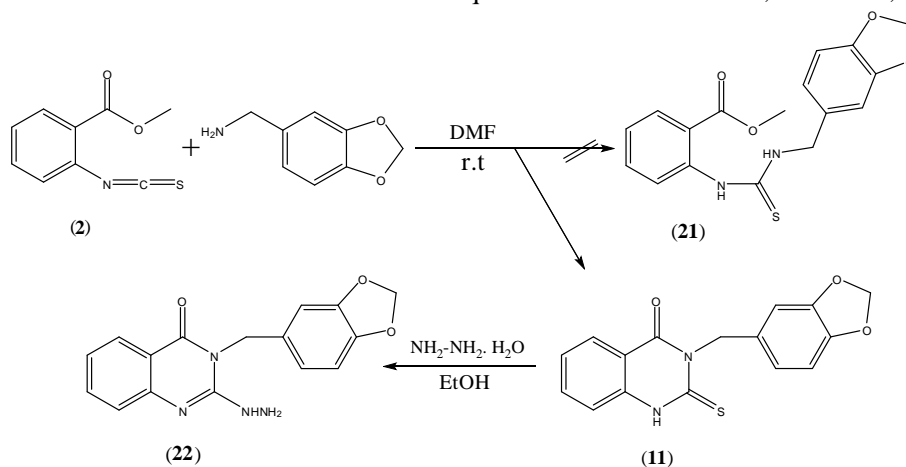
The reaction was proceeding via the elimination of 1 mole of H₂S. The structure of compound **19** and **20** was confirmed on the basis of elemental analyses, IR, ¹H-NMR, and ¹³C-NMR. The IR of compound **19** revealed the absence of a OCH₃ group and the presence of the characteristic bands at 3408, 3366, 3219 cm⁻¹(NH, NH₂), 1688cm⁻¹ (CO), 1622 cm⁻¹ (CN). The ¹H-NMR of compound **19** exhibited signals at 5.6 ppm assigned to the NH₂ group, 9.1 ppm attributed to the NH group. The IR of **20** showed characteristic bands at 3448, 3275, 3205 cm⁻¹ (NH, NH₂), 1666 cm⁻¹(CO), 1620cm⁻¹ (CN), 1346,1172cm⁻¹(SO₂). ¹H-NMR of **20**

revealed signals at 5.8 ppm due to the NH₂ group, 9.2 ppm corresponding to the NH group, 11.2 ppm attributed to the SO₂NH group. When compound **2** reacted with benzo[d][1,3]dioxol-5-ylmethanamine in absolute ethanol at room temperature the unexpected cyclic 3-aminoquinazolin **11** was obtained instead of the expected thiourea derivative **21** (Scheme 3). The corresponding 2-hydrazinylquinazoline **22** was obtained in good yield via the reaction of compound **11** with hydrazine hydrate in refluxing ethanol. This

reaction was proceeding through the elimination of one molecule of H₂S (lead acetate paper). The structure of compound **22** was proved on the basis of elemental analysis, IR, ¹H-NMR and ¹³C-NMR. The IR of **22** revealed the absence of the CS group and presence of characteristic bands at 3376, 3261cm⁻¹(NH, NH₂), 1688cm⁻¹(CO), 1617cm⁻¹(CN). ¹H-NMR of **22** exhibited signals at 5.1 ppm attributed to the N-CH₂ group, 5.9 ppm assigned to the O-CH₂-O group, 8.8 ppm due to the NH group, 9.5 ppm corresponding to the NH₂ group.



Scheme 2: Formation of thiourea and quinazoline derivatives **15, 16** and **19, 20**



Scheme 3: Formation of 2-hydrazinylquinazoline derivative **22**

IN-VITRO ANTICANCER EVALUATION

The newly synthesized compounds were evaluated for their *in vitro* anticancer activity versus the human breast cancer cell line (MCF7). Doxorubicin was used as the reference drug in this study. Table 1 shows the *in vitro* cytotoxic activity of the newly synthesized compounds. Some of the tested compounds exhibited significant activity compared to doxorubicin. It was found that quinazoline carrying the free amino group at the 3-position with a biologically active sulfa-phenazole at 2-position **20** and thioureido having a biologically sulfa-phenazole **16** (with IC₅₀ values of 2.64, 4.60 µg/ml) exhibited higher anti-breast cancer activity than the reference drug (with IC₅₀ value of 5.40 µg/ml). Further, quinazoline bearing the biologically active sulfa-doxine at the 3-position with the thione group at 2-position **14**, quinazoline incorporating morpholinophenyl at 3-position with the thione group at 2-position **12** and thioureido carrying morpholinophenyl moiety **15** (with IC₅₀ values 5.68, 8.62, and 9.66 µg/ml) are nearly as active as doxorubicin. On the other hand, compounds **9**, **11**, **13** and **19** revealed slightly lower activity than that of doxorubicin. It is clear from the present data that the comparison of the cytotoxicity of the quinazoline derivatives against the breast cancer cell line (MCF7) (**Table 1**) has showed that the cell killing potency follows the order **20**>**16**>Doxorubicin >**14**>**12**>**15**>**9**>**13**>**1**>**19** with IC₅₀ values (2.64, 4.64, 5.40, 5.68, 8.62, 9.66, 16.63, 19.06, 24.20, 24.31 µg/ml). The biological screening of the tested compounds could offer an encouraging framework in this field which may lead to the discovery of potent anti-breast cancer agents.

Table 1. *In vitro* anti-breast cancer (MCF-7) activity of newly synthesized compounds

Compound. No.	IC ₅₀ (µg / mL) ^a MCF-7
Doxorubicin	5.40
9	16.63
10	NA
11	24.20
12	8.62
13	19.06
14	5.68
15	9.66
16	4.60
19	24.31
20	2.64
22	NA

^aIC₅₀ value: Concentration causing 50% inhibition of cell viability.

NA: No activity.

CONCLUSION

In this work, novel quinazolines having a biologically active 2,3-dihydroquinazoline, 1,2-dihydroquinazoline, quinazoline-4(3*H*)-one and 3,4-dihydroquinazoline derivatives were synthesized and their *in-vitro* anti-breast cancer activity was evaluated among the tested compounds, two candidates (**20** and **16**) showed effectiveness on the breast cancer cell line, the active compounds could be considered as useful templates for further development to obtain more potent anti-breast cancer agent(s). Also, compounds **14**, **12** and **15** are nearly as active as doxorubicin as a reference drug. In addition, compounds **9**, **11**, **13** and **19** exhibited a moderate activity. Compounds **10** and **22** showed no activity.

Acknowledgment: The authors would like to extend their sincere appreciation to the Deanship of Scientific Research at King Saud University for its funding of this research through the Research Group Project no. **RGP- 302**.

REFERENCES

- G. Bonola, E. Sianesi, *J. Med. Chem.*, **13**, 329 (1970).
- R. J. Alaimo, H. E. Russell, *J. Med. Chem.*, **15**, 335 (1972).
- E. M. Bermanand, L. M. Werbel, *J. Med. Chem.*, **34**, 479 (1991).
- O. I. El-Sabbagh, S.M. Ibrahim, M. M. Baraka, H. Kothayer, *Arch. Pharm.*, **343**, 274 (2010).
- J. I. Levin, P. S. ChanBailey, A. S. Katocs, A. M. Venkatesan, *Bioorg. Med. Chem. Lett.*, **4**, 1141 (1994).
- R. P. Maskey, M. Shaaban, I. Grun-Wollny, H. Laatsch, *J. Nat. Prod.*, **67**, 1131 (2004).
- D. J. Connolly, D. Cusack, T. P. O'Sullivan, P. J. Guiry, *Tetrahedron*, **61**, 10153 (2005).
- Y. S. Sadanandam, K. R. M. Reddy, A. BhaskarRao, *Eur. J. Med. Chem.*, **22**, 169 (1987).
- S.K. Srivastava, V. Kumar, S.K. Agarwal, R. Mukherjee, A.C. Burman, *Anticancer Agents Med Chem.*, **9**, 246 (2009).
- O. Cruz-López, A. Conejo-García, M.C. Núñez, M. Kimatrai, M.E. García-Rubiño, F. Morales, V. Gómez-Pérez, J.M. Campos, *Curr. Med. Chem.*, **18**, 943 (2011).
- A. Garofalo, L. Goossens, P. Six, A. Lemoine, S. Ravez, A. Farce, P. Depreux, *Bioorg. Med. Chem. Lett.*, **21**, 2106 (2011).
- B.Lüth, W. Löwe, *Eur. J. Med. Chem.*, **43**, 1478 (2008).
- Y.S. Lee, S.H. Seo, B.S. Yang, J.Y. Lee, *Arch. Pharm. (Weinheim)*, **338**, 502 (2005).
- G. Cui, M. Cui, Y. Li, Y. Liang, W. Li, H. Guo, S. Zha, *Med. Oncol.*, **32**, 570 (2015).
- M.P. Mathew, E. Tan, C.T. Saeui, P. Bovonratwet, L. Liu, R. Bhattacharya, K.J. Yarema, *Bioorg. Med. Chem. Lett.*, **25**, 1223 (2015).

16. A. Bellizzi, M.R. Greco, R. Rubino, A. Paradiso, S. Forciniti, K. Zeeberg, R.A. Cardone, S.J. Reshkin, *Int. J. Oncol.*, **46**, 1214 (2015).
17. D.M. Jackman, L.A. Cioffredi, L. Sharmeen, L.K. Morse, J. Lucca, S.R. Plotkin, P.J. Marcoux, M.S. Rabin, T.J. Lynch, B.E. Johnson, S. Kesari, *Oncotarget.*, **6**, 4527 (2015).
18. M. Nakao, H. Muramatsu, K. Sone, S. Aoki, H. Akiko, Y. Kagawa, H. Sato, T. Kunieda, *Mol. Clin. Oncol.*, **3**, 403 (2015).
19. T. Koizumi, S. Sasaki, A. Sakamoto, T. Kobayashi, *Ann. Palliat. Med.*, **2**, 111 (2013).
20. M. Nolting, T. Schneider-Merck, M. Trepel, *Cancer Res.*, **201**, 125 (2014).
21. M. Brassard, G. Rondeau, *Biologics.*, **6**, 59 (2012).
22. A. Levitzki, *Eur. J. Cancer.*, **38**, 511 (2002).
23. S. Harakeh, M.D. Assef, M. El-Sabban, M. Haddadin, H.G. Muhatasib, *Chemico-Biol. Interactions.*, **148**, 101 (2004).
24. A. Levitzki, *Pharmacol. Ther.*, **82**, 231 (1999).
25. M.A. Bogoyevitch, D.P. Fairlie, *Drug. Discovery. Today.*, **12**, 622 (2007).
26. J. Drews, *Science.*, **287**, 1960 (2000).
27. C.T. Supuran, A. Casini, A. Mastrolorenzo and A. Scozzafava, *Mini-Rev. Med. Chem.*, **4**, 625 (2004).
28. F. Abbate, A. Casini, T. Owa, A. Scozzafava, C.T. Supuran, *Bioorg. Med. Chem. Lett.*, **14**, 217 (2004).
29. V.R. Solomon, C. Hu, H. Lee, *Bioorg. Med. Chem.*, **17**, 7585 (2009).
30. M. M. Ghorab, F.A. Ragab, H.I. Heiba, M.G. El-Gazzar, S.S. Zahran, Synthesis, anticancer and radiosensitizing evaluation of some novel sulfonamide derivatives. *Eur. J. Med. Chem.*, **92**, 682, (2015).
31. M.M. Ghorab, M.S. Alsaïd, M. Ceruso, Y.M. Nissan, C.T. Supuran, *Bioorg. Med. Chem.*, **14**, 3684 (2014).
32. M. M. Ghorab, M. Ceruso, M. S. Alsaïd, Y. M. Nissan, R. K. Arafa, C. T. Supuran, *Eur. J. Med. Chem.*, **87**, 186 (2014).
33. M.S. Al-Dosari, M.M. Ghorab, M.S. Alsaïd, Y.M. Nissan, A.B. Ahmed, *Eur. J. Med. Chem.*, **69**, 373 (2013).
34. M.M. Ghorab, F.A. Ragab, H.I. Heiba, R.M. El-Hazek, *Eur. J. Med. Chem.*, **46**, 5120 (2011).
35. M.S. Alsaïd, M.M. Ghorab, M.S. Al-Dosari, M.M. Hamed, *Eur. J. Med. Chem.*, **46**, 201 (2011).
36. M.M. Ghorab, F.A. Ragab, H.I. Heiba, H.A. Youssef, M.G. El-Gazzar, *Bioorg. Med. Chem. Lett.*, **20**, 6316 (2010).
37. M.S. Alsaïd, M.M. Ghorab, S.I. Alqasoumi, E.M. El-Hossary, E. Noaman, *Eur. J. Med. Chem.*, **45**, 3011 (2011).
38. S.I. Alqasoumi, A.M. Al-Taweel, A.M. Alafeefy, M.M. Ghorab, E. Noaman, *Eur. J. Med. Chem.*, **45**, 1849 (2010).
39. S.I. Alqasoumi, A.M. Al-Taweel, A.M. Alafeefy, E. Noaman, M.M. Ghorab, *Eur. J. Med. Chem.*, **45**, 738 (2010).
40. M.M. Ghorab, F.A. Ragab, M.M. Hamed, *Eur. J. Med. Chem.*, **44**, 4211 (2009).
41. P. Skehan, R. Storeng, D. Scudiero, A. Monks, J. McMahon, D. Vistica, J.T. Warren, H. Bokesch, S. Kenney, M.R. Boyd, *J. Nat. Cancer Inst.*, **82**, 1107 (1990).

ОЦЕНКА НА ПРОТИВОТУМОРНАТА АКТИВНОСТ НА НОВИ ХИНАЗОЛИНИ, СЪДЪРЖАЩИ БИОЛОГИЧНО АКТИВНИ ПИРИМИДИН, ТРИАЗИН, БЕНЗО [d][1,3] ДИОКСОЛ, МОРФОЛИНОФЕНИЛ, ХИНОЛИН И СУЛФОНАМИДИ

М.М. Гораб^{1,2*}, М.С. Алсаид¹

¹ Департамент по фармакогнозия, Колеж по фармация, Университет „Крал Сауд“, Риад 11451, Саудитска Арабия

² Департамент по радиологични изследвания на лекарствата, Национален център за радиологични изследвания и технологии, Служба по атомна енергетика, Наср Сити, Кайро, Египет

Получена на 25 април, 2015 г., Коригирана на 5 юни, 2015 г.

(Резюме)

Нова серия хиनाзолини, включващи биологично активни 4,6-диметилпиридин, 1,2,4-триазин, бензо[d][1,3]диоксол, морфолинофенил, хинолин, сулфонамид и тиокарбамидни съставки **9-14**, **15,16,19**, **20** и 2-хидразинил-хиназолиново производно **22** са конструирани с използването на метил 2-изоцианато- производно **2** като стратегически основно вещество. Структурата на ново-синтезираните съединения бе потвърдена с елементарен анализ и спектрални данни. Всички приготвени съединения са оценени за тяхната *in vitro* противоракова активност срещу клетъчни линии за рак на гърдата. Намерено е, че хиназолинът със свободна аминогрупа на 3-то място с сулфа-феназолова група на 2-ро място (**20**) и тиокарбамидовите производни, носещи сулфа-феназол **16** с IC₅₀ - стойности (2.64 и 4.60 µg/mL) показват по-добра активност от доксорубицина като положителен контрол. Допълнително съединенията **14**, **12** и **15** са близки по активност до доксорубицина като сравнително лекарство, докато съединенията **9**, **13**, **11** и **19** показват умерена активност. От друга страна съединенията **10** и **22** не показват активност.

Comparison of the components of the volatile oils from leaves of *Ziziphus jujuba* extracted by changing the solvent system and the separation methods

Z. Aghajani*, A.A. Engashte-Vahed

Department of Chemistry, Qom Branch, Islamic Azad University, Qom, Iran

Received April 12, 2015, Revised November 3, 2015

Quantity and quality of the components of volatile oils are highly dependent on the conditions of extraction. In this study, the volatile components of the leaves of *Ziziphus jujuba* in the flowering period were investigated by changing the extraction solvent and the method of extraction. At first, the volatile components were extracted by changing the type of the extraction solvent in the simultaneous distillation-extraction (SDE) method. Then, the effects of the extraction method on the quality and quantity of the extracted compounds were studied using the hexane solvent via two methods of SDE and percolation. The extracted volatile oils were separated and identified using GC/MS and GC/FID. The extraction method itself, proved to have the most effect on the number and type of the compounds of the volatile oils. Also the mean of molecular weight and solubility of the compounds of the extracted volatile oils in water, were so different from one another.

Keywords: *Ziziphus jujuba*; Separation method; Volatile oil; Simultaneous distillation-extraction; Cold percolation method

INTRODUCTION

Aromatic plants have been known for a very long time and the use of them in the food and perfume industries have a long history [1].

Ziziphus is a genus of the family Rhamnaceae which consists of about 40 species and is a small spiny shrub, distributed in warm-temperate zones and subtropical regions throughout the world [2].

In Iran, *Ziziphus* is mostly found in the central regions and Khorasan and Golestan provinces.

The drupe and the flesh of *Ziziphus* contain its most medicinal properties, also the leaves have shown healing properties. The infusion of the leaves is usually gargled to treat sore throat, bleeding gums and joint pain [3-5].

Kurihara *et al.* [6] extracted the saponin, ziziphin, from the dried leaves of *Z. jujuba*. Leaves of *Z. jujuba* due to the existence of the active substance of ziziphin, can suppress the sweet taste sensation in flies (*Pharma regina*), rats and hamsters [6].

In a study conducted by Shirdel and Mirbadalzadeh [7] it was determined that the ethanolic extract of leaves of *Z. jujuba* has a hypoglycemic effect in diabetes mellitus patients and its effect is similar to that of glibenclamide [7].

The anti-allergic activity of the water extract of leaves of *Z. jujuba* was studied by measuring its

inhibitory effect on the activation of hyaluronidase (bovine testes) *in vitro*; and *Z. jujuba* proved to have strong anti-allergic activity [7].

El Husseiny and El Kholy [8] evaluated insecticidal properties of different extracts of the leaves of *Z. jujuba*. They showed that Petroleum ether extract of the leaves of *Z. jujuba* is able to reduce the population dynamics of *Culex pipiens*; either directly through larval kill, or indirectly through its latent effects expressed in reduction of egg hatchability, inhibition of adult emergence, interruption of life stages and the effect that it has on sex ratio [8].

Due to the fact that plant extracts usually are a combination of various types of bioactive compounds, their separation, identification and characterization of those bioactive compounds still remain a big challenge in the way of the processes [9].

In the traditional methods of extracting natural compounds from plants such as water or steam distillation and extraction with organic solvents such as soaking, there are some disadvantages such as loss of volatile components, degradation of compounds and remaining toxic solvents [10, 11]. Due to the increasing usage of natural compounds in the recent years, the effects of different extraction methods and types of solvent on the quality and quantity of volatile compounds, extracted from the leaves of *Z. jujuba* during the flowering season were studied.

* To whom all correspondence should be sent:

E-mail: haj_aghajani@yahoo.com

MATERIALS AND METHODS

Materials

Leaves of *Z. jujuba* were collected from one of the central provinces of Iran (Qom province) during the flowering period in 2014. The plant materials were authenticated by the Department of Botany of Islamic Azad University, Qom Branch.

Samples were dried and subsequently ground in a blender to obtain fine powder. All reagents and chemicals used in this study were from Merck or Sigma Companies.

Extraction methods

Extraction by SDE method

The volatile oils of *Z. jujuba* were extracted from dried leaves samples via hydro-distillation, using the simultaneous distillation-extraction (SDE) method [12]. Also the organic solvents of n-hexane and ethyl acetate were used in the extraction process. The extraction process took 2 h. Then the solvent was removed and the solution was dried over anhydrous sodium sulfate. The extracted oils were stored at 4°C in a sealed vial until analyzed.

Extraction by cold percolation method

The plant extracts were prepared by the cold percolation method. Ten grams of dried powder were added to 300 ml of solvent in a conical flask and the mixture was kept for 48 hours with intermittent shaking. After that, the extract was filtered through Whatman No. 1 filter paper; then the solvent was removed using a rotary evaporator and subsequently dried, until a constant weight of each extract was obtained. The residues were stored at 4°C for further use [13].

Gas chromatography analysis

Analytical gas chromatography of the volatile oils was carried out using a Hewlett-Packard 5975B series gas chromatograph with Agilent HP-5 capillary column (30 m×0.25 mm, f.t 0.25 µm); carrier gas He; split ratio 1:10 and using a flame ionization detector. The column temperature was adjusted at 50°C which was unchanging for 10 min and was programmed to rise up to 240°C at a rate of 4°C/min and then stay constant at that temperature for 15 min. GC/MS was performed on an HP 5975B with a Hewlett-Packard 5973 quadrupole detector, on capillary column HP-5 (30 m×0.25 mm; f.t 0.25 µm).

The MS was operated at 70 eV ionization energy. Retention indices were calculated using retention times of n-alkanes that were injected after

the volatile oil at the same chromatographic conditions. Quantitative data were obtained from the electronic integration of the FID peak areas.

The components of the oils were identified by comparing their mass spectra and Kovats indexes with Wiley library and published books, data bases available and credible websites [14].

RESULTS AND DISCUSSION

In this study, qualitative and quantitative characteristics of the components of the volatile oil of the leaves of *Z. jujuba* in the flowering season were evaluated after changing certain parameters such as the extraction solvent and the extraction method.

At first the components of the volatile oils were extracted by changing the type of extraction solvent in the SDE method. Ethyl acetate and hexane as the polar and aprotic solvents, with different dipole moments were used ($D_{\text{Hexane}} = 0.08$, $D_{\text{Ethyl acetate}} = 1.88$).

In the second segment, by using the hexane solvent but changing the extraction method from

SDE to cold percolation, the effects of the extraction method on the quality and quantity of the extracted compounds were studied.

Other important matters to take into consideration are the type and number of the extracted compounds. The compounds separated using the hexane solvent and the SDE method have a noticeable difference compared to the compounds separated by the percolation method; that is to say Eugenol, trans-β-Ionone, α-Farnesene and 2-Hexenal are some of the main compounds in the SDE method which were not separated in the percolation method. Likewise α-Pinene, Linoleic acid and Diisooctyl adipate were some of the separated constituents of the percolation method which were not obtained in the SDE method.

Some compounds such as palmitic acid and phytol, exist in both of the separation methods but their percentages are different. From the SDE method while using the hexane solvent, 34 compounds were obtained; but this number for the ethyl acetate solvent with the same method is 30 (Tables 1 & 2). When the SDE method and the hexane solvent were used, 34 volatile compounds were extracted while only 11 volatile compounds were obtained from the percolation method with the same solvent. As it can be seen, in separation of compounds by the SDE method, there is only a little difference in the number of extracted compounds after changing the solvent but, when the separation method is changed, this difference is much greater.

It was previously reported that volatile oil content of medicinal plants is influenced by the extraction method. Gavahian and his colleague demonstrated that essential oils obtained by hydrodistillation and steam distillation, were almost similar in their physical properties and chemical compositions [15] but Xie et al. showed that among the three extraction methods, the solvent extraction method could extract compounds with low volatility and high molecular weight. They proved that both of the methods of headspace

solid-phase microextraction and steam distillation, could extract volatile components [16].

In order to study the extracted compounds, parameters such as solubility in water and the boiling point were used. According to the results demonstrated in Table 3, the mean of solubility values of the extracted compounds in water (in 20°C) by the SDE method when using the ethyl acetate solvent, was 2414.01 ppm; while this value for the hexane solvent was 882.22 ppm.

Table 1. Chemical composition of the volatile oils of the leaves of *Z. jujuba* extracted by the SDE method

No	Components	extracted solvent: Ethyl acetate ^a (%)	extracted solvent: Hexane ^b (%)	RI ^c
1	Octane	-	9.10	≤ 800
2	n-Hexanal	2.45	-	800
3	(E)-2-Hexenal	26.31	11.26	852
4	Xylene	1.38	-	870
5	6-Methyl-5-hepten-2-one	-	1.80	991
6	α-Toluenol	0.96	-	1044
7	cis-Linalool oxide	-	1.04	1092
8	trans-Linalool oxide	0.67	-	1093
9	Terpinolene	-	2.26	1104
10	(3E)-6-Methyl-3,5-heptadien-2-one	-	0.61	1110
11	Naphthalene	14.21	-	1191
12	Fenchol	-	0.95	1197
13	α-Terpineol	1.40	-	1198
14	Dodecane	1.70	-	1200
15	Tridecane	1.34	-	1300
16	Eugenol	-	9.58	1367
17	Cyclohexane	-	5.00	1396
18	Tetradecane	2.01	-	1401
19	Dihydropseudoionone	-	1.67	1456
20	trans-β-Ionone	2.83	5.55	1493
21	Pentadecane	2.26	-	1501
22	α-Farnesene	-	6.13	1511
23	δ-Cadinene	-	6.31	1528
24	Dihydroactinolide	1.88	1.27	1540
25	E-Nerolidol	1.27	2.85	1569
26	(E)-3-Eicosene	1.05	-	1593
27	Hexadecane	2.17	-	1601
28	Benzophenone	1.86	-	1639
29	Benzyl benzoate	3.60	-	1776
30	Hexahydrofarnesyl acetone	1.33	-	1849
31	1-Butyl 2-isobutyl phthalate	-	0.56	1968
32	Diisobutyl phthalate	2.20	0.92	1877
33	Dibutyl phthalate	2.74	-	1972
34	Palmitic acid	3.28	2.55	1980
35	Phytol	9.57	16.63	2118
36	Diisooctyl adipate	1.23	-	2400
Total		89.70	86.04	

^aCompounds extracted with hexane by the SDE method; ^bCompounds extracted with hexane by the percolation method

^cRI: Relative retention indices to C8–C24 n-alkanes on HP-5 MS column

Table 2. Chemical composition of the hexane extract of the volatile oils of the leaves of *Z. jujuba* extracted by the SDE and Percolation methods

No	Components	SDE method ^a (%)	Percolation method ^b (%)	RI ^c
1	Octane	9.10	-	≤ 800
2	(E)-2-Hexenal	11.26	-	852
3	6-Methyl-5-hepten-2-one	1.80	-	991
4	cis-Linalool oxide	1.04	-	1092
5	Terpinolene	2.26	-	1104
6	(3E)-6-Methyl-3,5-heptadien-2-one	0.61	-	1110
7	Fenchol	0.95	-	1197
8	Eugenol	9.58	-	1367
9	Cyclohexane	5.00	-	1396
10	Dihydropseudoionone	1.67	-	1456
11	trans-β-Ionone	5.55	-	1493
12	α-Farnesene	6.13	-	1511
13	δ-Cadinene	6.31	-	1528
14	Dihydroactinolide	1.27	2.08	1540
15	E-Nerolidol	2.85	-	1569
16	α-Pinene	-	7.90	1841
17	Z-11-Tetradecenoic acid	-	1.47	1848
18	1-Butyl 2-isobutyl phthalate	0.56	-	1968
19	Diisobutyl phthalate	0.92	-	1877
20	Dibutyl phthalate	-	3.63	1972
21	Palmitic acid	2.55	18.42	1980
22	Phytol	16.63	31.70	2118
23	Linoleic acid	-	13.54	2154
24	Diisooctyl adipate	-	8.03	2400
25	Pentacosane	-	3.68	2495
Total		86.04	90.45	

^aCompounds extracted with hexane by the SDE method; ^bCompounds extracted with hexane by the percolation method; ^cRI: Relative retention indices to C8–C24 n-alkanes on HP-5 MS column

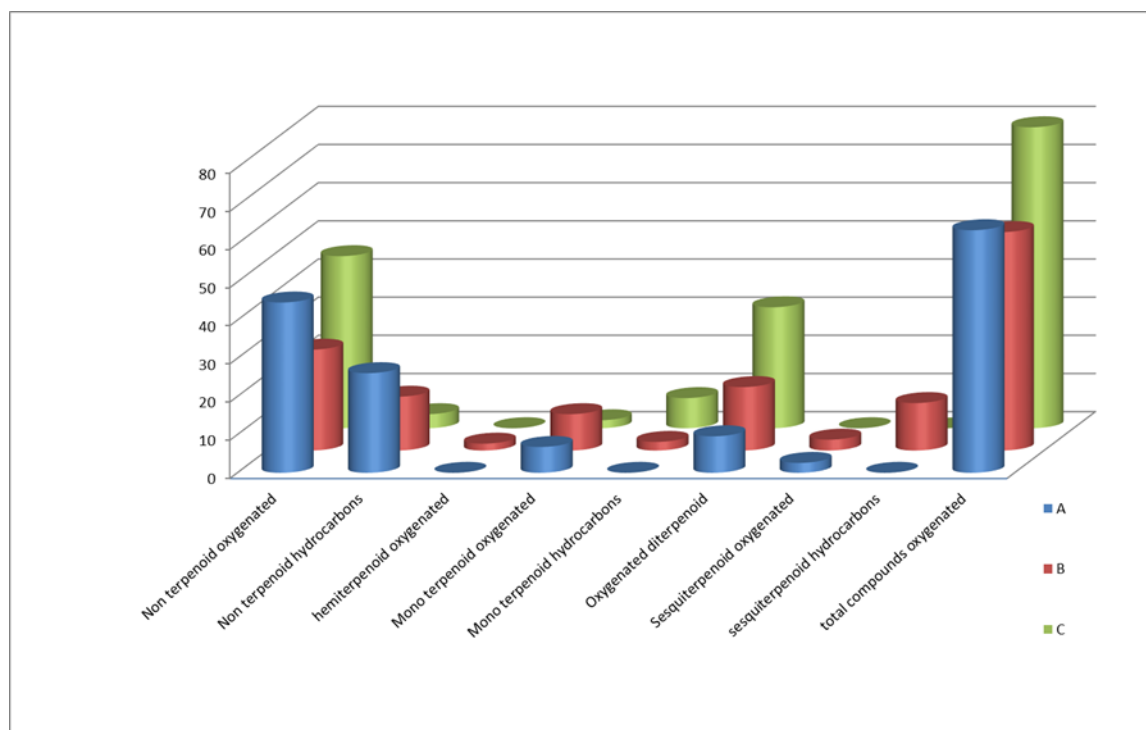


Fig. 1. The category of the compounds extracted from the volatile oils of the leaves of *Z. jujuba* by the SDE and Percolation methods

A: Compounds extracted with Ethyl acetate by SDE method

B: Compounds extracted with Hexane by SDE method

C: Volatile compounds extracted with Hexane by percolation method

Table 3. Comparison of the compounds extracted from the volatile oils from the leaves of *Z. jujuba* by the SDE and percolation methods using three measured parameters

Parameter measured	A	B	C
Average molecular weight	203.15	188.61	265.94
Average solubility in water (In 25 °C , ppm)	2414.01	882.22	68.63
Average boiling point (In 760 mm Hg)	260.86	237.23	284.11

A: Compounds extracted with ethyl acetate by SDE method;
 B: Compounds extracted with hexane by SDE method;
 C: Volatile compounds extracted with hexane by percolation method.

The mean of the boiling points of the extracted compounds for the ethyl acetate was 260.86°C and the mean of the boiling points of the extracted compounds for the hexane solvent was 237.23°C.

The results showed that the boiling point and solubility of the extracted molecules in water have a direct relationship with the dipole moment of the extraction solvent. It can be concluded that the ethyl acetate solvent in comparison with the hexane solvent, has extracted compounds with higher dipole moment values. This result is compatible with the existing difference between the numbers of extracted oxygenated compounds (Figure 1).

The second segment of this study investigated the extraction methods by which the volatile components were extracted by the hexane solvent using the two methods of SDE and percolation and then, the results of these methods were compared to each other.

According to Table 3, the mean solubility of the extracted compounds in water (in 20°C) using the percolation method was 68.63 ppm; while this value for the SDE method was 882.22 ppm. Also, the mean molecular weight of the compounds extracted by the percolation method was 265.94 u and for the SDE method it was 188.61 u. These results clearly confirm the ability of the SDE method in separating compounds with higher dipole moments and lesser molecular weight compared to the percolation method.

CONCLUSIONS

Due to the fact that volatile oils are used in different industries, finding the best extraction methods in order to improve their quality and also, to obtain the most suitable chemical compounds for

any particular application is crucial. According to the changes in quality and quantity of the volatile oils that can be observed in tables 1-3 and figure 1, it can be concluded that the SDE method can separate compounds with higher dipole moment but lesser molecular weight in comparison with the percolation method. Also as it was expected, these results reveal this fact that the compounds separated by the ethyl acetate solvent are more polar than the compounds separated by the hexane solvent.

Acknowledgements: Authors acknowledge the kind financial supports of the Research Council of Qom Branch, Islamic Azad University, Qom, Iran"

REFERENCES:

1. N. Mezzomo, B.R. Mileo, M.T. Friedrich, J. Martinez, S.R. Ferreira, *Bioresour. Technol.* **101** (14), 5622 (2010).
2. N. Kathleen, E. D. Brenzel, Sunset Western Garden Book. Sunset Publishing Corporation. 1995, p. 606.
3. G.R. Amin, Traditional medicinal plants of Iran. Research Deputy Publications of Hygiene Ministry. Islamic Republic of Iran, [in Persian] 1997, p. 230.
4. R. Omid Beigi, Approach the Production and Processing Plants. Tarahan Publisher, Tehran, Iran, 1997, p. 109.
5. G. Usher, A dictionary of plants used by man. CBS Publishers and distributors, Delhi, India, 1974.
6. Y. Kurihara, K. Oohubo, H. Tasaki, H. Kodama, Y. Akiyama, A. Yagi, B. Halperm, *Tetrahedron*, **44**: 61 (1988).
7. Z. Shirdel, R. Mirbadalzadeh, *Elixir Hor. & Sig.* **31**: 1957 (2011).
8. I.M. El Husseiny, S.E. El Kholy *J. Adv. Biol.* **6**(2): 1066 (2015).
9. G. Brusottia, I. Cesari, A. Dentamaro, G. Caccialanza, G. Massolinia. *J. Pharm. Biomed. Anal.* **87**: 218 (2014).
10. A. Ruiz-Rodriguez, G. Reglero, E. Ibanez, *J. Pharm. Biomed. Anal.* **51**, 305 (2010).
11. I.T. Agar, C. Sarmiento, R. Garces, N. Kaska, S. Kafkas, B.E. Ak, *Acta Horti*, **419**: 405 (1995).
12. H. Ebrahimabadi, A. Mazoochi, F. Jookar Kashi, Z. jafari-Bidgoli, H. Batooli, *Food Chem. Toxicol.*, **48**: 1371 (2010).
13. S.D. Sarker, L. Nahar, *Methods Mol Biol.* **864**: 301 (2012).
14. R.P. Adams, *J. Chromatogr. A.* **985**: 137 (1995).
15. M. Gavahian, R. Farhoosh, A. Farahnaky, K. Javidnia, F. Shahidi. *Int. Food Res. J.* **22** (1): 277 (2015).
16. Z.S. Xie, X.J. Xu, C.Y. Xie, J.Y. Huang, M. Yang, D.P. Yang. *J. Pharm. Anal.* **3**(3): 215 (2013).

СРАВНЯВАНЕ НА КОМПОНЕНТИТЕ НА ЛЕТЛИВИ МАСЛА ОТ ЛИСТАТА НА *Ziziphus jujuba* ЧРЕЗ ПРОМЯНА НА РАЗТВОРИТЕЛЯ И МЕТОДА НА РАЗДЕЛЯНЕ

З. Агаяни *, А. А. Енгаще-Вахед

Департамент по химия, Ислямски университет „Азад“, Клон в Кум, Кум, Иран

Постъпила на 12 април, 2015 г., Коригирана на 3 ноември, 2015 г.

(Резюме)

Количествата и качествата на компонентите на летливите масла силно зависят от условията на екстракция. В настоящата работа ние изследвахме летливите компоненти в листата на *Ziziphus jujuba* в периода на цъфтеж, променяйки екстрагента и метода на екстракция. Най-напред, ние екстрахирахме летливите компоненти чрез промяна на разтворителя чрез едновременна дестилация и екстракция (SDE); във втората част, използвайки хексан като разтворител по два метода (SDE и перколация), ние изследвахме ефекта на метода на екстракция върху количеството и качеството на екстрахираните съединения. Екстрахираните масла бяха разделени и идентифицирани чрез GC/MS и GC/FID. Най-голяма разлика се наблюдава, когато методът на екстракция бе променен по начин, при който броят и типът на съединенията драстично се променя. Също така средната молекулна маса и средната разтворимост на компонентите на екстрахираните летливи масла са различни.

Physicochemical and electrochemical study of lead acid battery positive active mass (PAM) modified by the addition of bismuth

N.Chahmana*¹, M.Matrakova², L.Zerroual¹

¹Laboratoire d'Energétique et Electrochimie du Solide (LEES), Université Sétif, Sétif, Algeria.

²Institute of Electrochemistry and Energy Systems "Akad.Evgeni Budevski" - Bulgarian Academy of Sciences, Sofia, Bulgaria.

Received May 15, 2015, Revised October 8, 2015

This study attempts to discuss the influence of Bi alone and its combination with Sb and Sn on the electrochemical performance of the PAM of lead acid batteries. The different additives were added in the electrolyte as cations. PAMs were prepared by electro formation of cured battery plates in the presence and absence of a dopant (non-doped sample ND). The results from different analyses showed that bismuth alone gives a remarkable improvement of the capacity. The highest performance of PAM is obtained when bismuth is mixed with tin together as dopants. The incorporation of bismuth and tin cations leads to an increase of the quantity of structural water in PAM. This increases the hydrated and amorphous zones within the PbO₂ particles and leads to an improvement of the electrochemical capacity.

Key words: Lead acid battery, Positive active mass, Bismuth, Tin, Antimony, Capacity.

INTRODUCTION

The active mass of the positive plate of the lead-acid battery is a gel-crystal system that conducts electricity by electrons and protons in hydrated areas of the gel zones [1]. The properties of the active material were modified by the introduction of dopants, but few reports in the literature deal with these investigations [2-7]. The effect of the addition of ions of the elements of group V (Arsenic, Antimony and Bismuth) introduced in the spin alloy or in the solution during the rebuilding process of the active material structure and the PbO₂ powder density were investigated. The results showed that these dopants decrease the value of the critical density [8]. H.Y. Chen *et al.* [9] found that bismuth improves the capacity and cycle life. In our previous works, we studied the effect of the doping of lead dioxide with some metallic ions on the composition of PAM gel zones and its relationship to battery performance. The results showed that the quantity of water present in the gel zones and PAM discharge capacity are mainly dependent on the nature of the dopant [10, 11].

The aim of this work is the study of the physicochemical properties of the lead acid battery positive active mass, modified by adding Bi alone and combined with Sb and Sn at different concentrations and their electrochemical

performances. The study was based on chemical analysis, X-ray diffraction (XRD), thermogravimetry (TG) and scanning electronic microscopy (SEM). The capacity of the different PAMs is determined by galvanostatic discharge.

EXPERIMENTAL

Plate preparation

In order to investigate the effect of bismuth on the positive active mass, four kinds of positive electrodes were prepared. Lead dioxide was prepared by electroformation of industrial cured battery plates (with grids cast from a Pb-5wt. % Sb alloy) in acidic solution according to the method described by Voss and Freundlich [12]. The cured plates were soaked in 1.40s.g. H₂SO₄ solution for 18h and then formed in 1.05s.g. H₂SO₄ solution. The dopants were dissolved in the electrolyte as Bi₂O₃, Sb₂O₃ and SnCl₂. Table 1 shows the concentrations of dopants.

Table 1. Concentrations of the different dopants added to the PAM.

Dopant	Concentration, ppm
Bi	25
Bi-Sb	25-50
Bi-Sn	25-100

The formed plates were washed in running water for several hours to remove the excess of sulfuric acid. Then they were dried overnight at 110°C. Part of the active mass was removed from the grids,

* To whom all correspondence should be sent:
E-mail: nchahmana@yahoo.fr

washed with a hot saturated acetate ammonium solution to remove the PbSO₄ traces, dried and ground to a powder.

The positive active materials were characterized by XRD analysis using an APD-15 Philips 2134 diffractometer. The changes in relative intensity of the X-ray characteristic diffraction lines for the different phases in PAM were adopted as a measure of the phase changes in the PAM with the effect of additives.

The thermal analysis tests were performed using an instrument supplied by MettlerToledo: TGA/SDTA 851e. All measurements were carried out in a nitrogen atmosphere at a gas flow-rate of 50cm³min⁻¹ and at a constant heating rate of 10Kmin⁻¹.

The SEM observations were performed by a scanning and transmission electron microscope JEOL 200 CX (Japan).

Electrochemical tests were performed with a classical three electrode cell. The working electrode is a PAM powder hand pressed on a conductive graphite collector. A platinum sheet was used as a counter-electrode. The non-doped and doped electrodes were discharged at a constant cathodic current of 1mA and the potential versus capacity curves were recorded using a Hg/Hg₂SO₄/saturated K₂SO₄ reference electrode. All the experiments were carried out at room temperature in 1.28 s.g. H₂SO₄ solution.

RESULTS AND DISCUSSION:

Chemical analysis

Table 2 summarizes the chemical composition of the PAM samples formed in solutions with different additives. The data show that traces of bismuth, tin and antimony are present in the active mass. The highest percentage of Bi is obtained for the solution containing Bi and Sn. Small quantities of unconverted PbSO₄ were found in the majority of the samples.

Table 2. Results from chemical and ICP-AES analyses of doped and non-doped PAMs.

Samples	PbO ₂ %	PbSO ₄	PbO	Sn.10 ³ %	Bi.10 ³ %	Sb10 ³ %
ND	89.50	3.24	5.19	0	0	0
Bi	86.07	1.25	5.89	0	4.0	0
Bi-Sb	86.37	2.58	6.55	0	5.6	5.0
Bi-Sn	85.90	1.87	8.80	4.0	9.7	0

XRD analysis

All detected peaks in Fig.1 were identified to be β-PbO₂. No differences in the spectra were observed, but changes in peak intensity were

clearly detected between the modified PAMs and unmodified one.

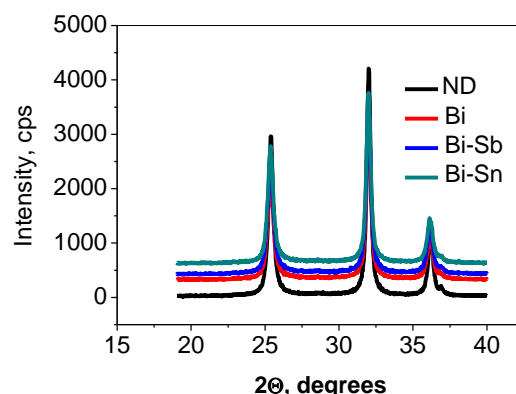


Fig 1. XRD patterns of doped and non-doped PAMs.

The average crystallite size was calculated from the full width at the half maximum (FWHM) of [110] diffraction lines using the Sherrer equation. The crystallite size values showed that more amorphous particles of PbO₂ were obtained in solutions containing the different additives. As a consequence we can deduce that Bi, Sn and Sb tend to diminish the crystallinity of the PAM particles. The crystallite sizes calculated for the different PAMs are reported in Table 3.

Table 3. Average crystallite sizes calculated for doped and non-doped PAMs.

Samples	Size (nm)
ND	21.9
Bi	18.2
Bi-Sb	18.2
Bi-Sn	18.4

Thermal analysis

The changes in water content in the PAMs are measured by thermal analysis. The thermo gravimetric (TG) curves are shown in Fig. 2. The values for the structural water are reported in Table 4. It is clear that the additives increase the water content in the PAMs. The highest amount of structural water is obtained for sample containing Bi-Sn mixture.

Table 4. Values of structural water in PAMs.

Samples	Structural water (%)
ND	0.58
Bi	1.39
Bi-Sb	2.13
Bi-Sn	2.41

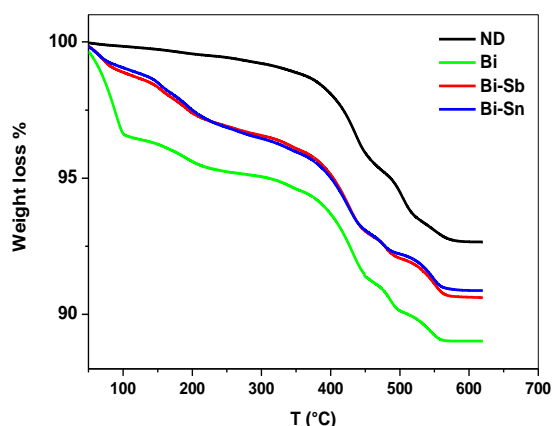


Fig 2. TG curves of doped and non-doped PAMs.

Fig.3 presents the obtained DTG curves - the first derivative of the TG curves normalized toward the mass of the samples. The DTG curves for all samples have characteristic peaks in the range from 50 to 300°C that are related to the evaporation of water in different parts of the PAM. The peaks at a temperature higher than 300°C are related to the degradation of PbO_2 to PbO . The DTG curve for the non-doped sample features two characteristic peaks in the range from 50 to 300°C. The first one at 100°C is related to the evaporation of the physisorbed water and the second one is related to the evaporation of the structural water from the gel zone of the positive active mass. In the temperature range from 100 to 300°C the two additional peaks appear for doped PAMs. These peaks are indicative of different types of bounded water in the PAMs gel zones and confirm that the dehydration of PAMs occurs in three stages. We can deduce from the thermal analysis that the addition of Sn increases the quantity of the structural water as described earlier [11].

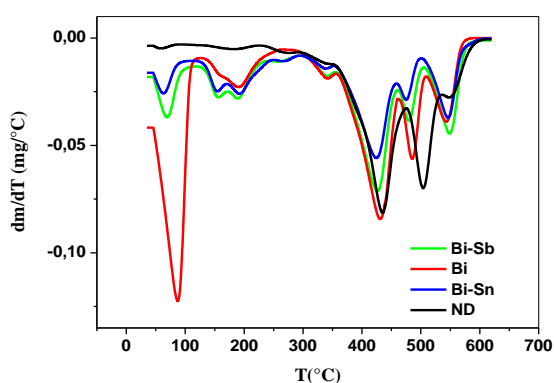


Fig 3. DTG curves of doped and non-doped PAMs.

SEM morphology

Fig.4 presents the scanning electron micrographs of different PAMs. The micrographs show that the morphology of the positive active

material is not affected by the bismuth incorporation.

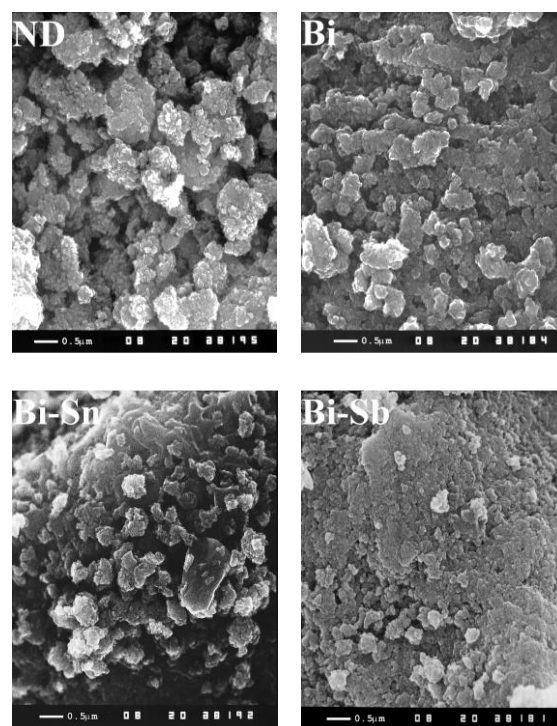


Fig 4. SEM micrographs of the PAMs with dopants.

Electrochemical properties

Fig.5 shows the discharge curves of modified PAMs compared to the positive active mass without additives (ND). Bismuth incorporated in the PbO_2 gel zones improves its electrochemical activity. It is clear that the capacity of PAM with bismuth alone is considerably better than a non-doped one. In order to see the effect of the synergy of bismuth, tin and antimony which have proved their positive influence on PAM in earlier studies, we have introduced mixtures of Bi-Sb and Bi-Sn in the PAM. The best capacity is obtained for PAM formed in H_2SO_4 containing the mixture of Bi-Sn(100-25 ppm). Fig.6 presents the variation of the PAM's capacity versus the amount of structural water in the samples. The data show that the highest capacity is obtained for the PAM doped by a Bi-Sn mixture, which contains the greatest amount of structural water and the higher percentage of Pb^{IV} .

The doping of PAM leads to the incorporation of bismuth, antimony and tin cations which increase the quantity of the structural water in PbO_2 . This obviously leads to PAMs with more hydrated and amorphous zones, consequently the capacity increases. The improvement in the percentage of the capacity of PAM is mentioned in Table 5.

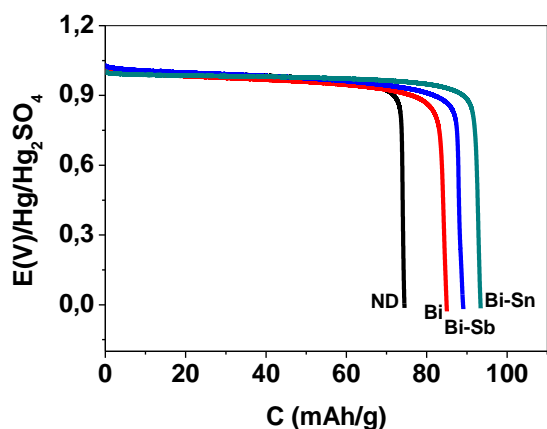


Fig 5. Comparison of the electrochemical behavior of non-doped PAM (ND) and ones with Bi alone and mixtures of Bi-Sb and Bi-Sn.

Table 5. Capacity (%) of different PAMs.

	Bi	Bi - Sb	Bi - Sn
Capacity (%)	14.16	19.46	25.57

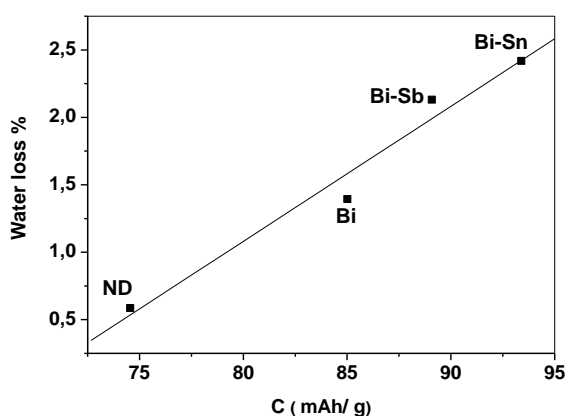


Fig 6. Evolution of the discharge capacity of different PAMs with the loss of structural water.

CONCLUSIONS

The objective of this work was the development of a battery with improved properties. The different results have shown that bismuth yields a remarkable increase in capacity. Better

performance for PAM is obtained when Bi and Sn are added together in the electrolyte. This can be explained by the fact that a mixture of Bi and Sn modifies the hydrated and the gel parts of PAM leading to more amorphous and small sized hydrated particles. Hence the capacity increases and a synergy is obtained when the positive active mass is doped by a mixture of Bi and Sn. The incorporation of the different metallic cations leads to an increase in the quantity of a structural water which improves the electrochemical activity of PAM. These results should be applied in the process of lead acid battery technology.

REFERENCES

1. D. Pavlov, E. Bashtavelova, V. Manev, A. Nasalevska, *Journal of Power Sources*, **19**, 15 (1987).
2. A. Boggio, M. Maja, N. Pennazi, *Journal of Power Sources*, **9**, 221 (1983).
3. I.H. Yao, D.C. Johnson, *J. Electrochem. Soc.*, **134**, 1973 (1987).
4. S. Hattori, M. Yamaura, M. Kino, M. Yamane, H. Nakashima, J. Yamashita, J. Nakayama, *ILZRO Project No. LE-276, Rep. No. 5*, International Lead Zinc Research Organization, Riverside, CA, USA, 1980.
5. M.T. Frost, J.A. Hamilton, K. Harowfield, R.J. Hill, J.F. Moresby, D.A.J. Rand, *ILZRO Project No. LE 290, Prog. Rep. No. 3*, International Lead Zinc Research Organization, Riverside, CA, USA, 1980.
6. T. G. Chang, J. A. Brown, Evaluation of battery oxides, *ILZRO Project No. LE 272*, International Lead Zinc Research Organization, Riverside, CA, USA., 1979.
7. D. Pavlov, A. Dakhouché, T. Rogachev, *Journal of Power Sources*, **30**, 117 (1990).
8. D. Pavlov, *Journal of Power Sources*, **33**, 221 (1991).
9. H.Y. Chen, L. Wu, C. Rena, Q.Z. Luo, Z. H. Xie, X. Jiang, S.P. Zhu, Y.K. Xia, Y.R. Luo, *Journal of Power Sources*, **95**, 108 (2001).
10. N. Chahmana, L. Zerroual, M. Matrakova, *Journal of Power Sources*, **191**, 144 (2009).
11. N. Chahmana, M. Matrakova, L. Zerroual, D. Pavlov, *Journal of Power Sources*, **191**, 51 (2009).
12. E. Voss, J. Freundlich, D.H. Collins (ed.), *Batteries*, **287**, 73 (1963).

ФИЗИКОХИМИЧНО И ЕЛЕКТРОХИМИЧНО ИЗСЛЕДВАНЕ НА ПОЛОЖИТЕЛНАТА АКТИВНА МАСА В ОЛОВЕН АКУМУЛАТОР, МОДИФИЦИРАН ЧРЕЗ ДОБАВЯНЕ НА БИСМУТ

Н. Чахмана*¹, М. Матракова², Л. Зеруал¹

¹Лаборатория по енергетика и електрохимия на твърдото тяло, Университет в Сетиф, Сетиф, Алжир
²Институт по електрохимия и енергийни системи „Акад. Евгени Будевски, Българска академия на науките, София, България.

(Резюме)

Изследва се влиянието на бисмут, както и неговите комбинации с антимон и калай, върху електрохимичните свойства на положителната активна маса в оловния акумулатор. Различните добавки са направени в електролита и са под формата на катйони. Положителните активни маси са получени след формиране на зрели плочи в присъствие или отсъствие на добавки. Резултатите от различни анализи показват, че бисмутът като самостоятелна добавка значително увеличава капацитета на клетката. Характеристиките на положителната активна маса са най-добри, когато добавката е комбинация от бисмут и калай.

Присъствието на йоните на Bi и Sn спомага за повишаване количеството на структурна вода в положителната активна маса. Така се увеличават зоните с хидратираните аморфни частици PbO₂, което води до увеличаване на капацитета.

Kinetic studies on the NaBH₄/H₂O hydrogen storage system with CoCl₂ as a catalyst

A. Kaur*, D. Gangacharyulu, P.K. Bajpai

Department of Chemical Engineering, Thapar University, Patiala, India

Received April 28, 2015, Revised September 26, 2015

Hydrogen energy is considered at worldwide scale as a substitute to replace fossil fuels and to establish clean and secure energy future. Hydride based hydrogen storage, for instance sodium borohydride (NaBH₄), has acknowledged substantial concern as a potential hydrogen source for portable fuel cell applications. The present paper highlights the kinetic studies of the NaBH₄/CoCl₂/H₂O system and the factors affecting the hydrogen generation rate (HGR) - NaBH₄ concentration, NaOH concentration and temperature. It also reports the results on addition of alumina nanoparticles to the NaBH₄/CoCl₂/H₂O system, for accelerating the hydrogen generation rate, owing to better reactivity of the nanoparticles. Cobalt chloride is extensively used as a catalyst, being a reactive and cost-effective non-noble metal that expedites NaBH₄ hydrolysis reaction. Kinetic studies show that the hydrolysis reaction of NaBH₄ is of first order. The rate increases with respect to sodium borohydride and decreases with respect to sodium hydroxide. It is also observed that the rate increases with the increase in temperature. Characterization of residue is performed by SEM, EDS and XRD analysis that confirmed that the particles agglomerate together. Boron, sodium, cobalt, chlorine and oxygen are present with weight percentages of 78.46%, 3.41%, 0.05%, 0.07% and 18.01%, respectively. The diffraction peak at $2\theta = 45^\circ$ predicted from XRD analysis shows the presence of Co₂B in the residue.

Keywords: Hydrogen energy; Sodium borohydride; Cobalt chloride; Alumina, Nanoparticles

INTRODUCTION

Inquisitiveness in hydrogen as a fuel has grown and numerous advances in hydrogen production and utilization have been made. Technologies for hydrogen storage ought to be significantly advanced if a hydrogen based energy system, particularly in the transportation sector, is to be acknowledged [1]. Storing hydrogen is relatively difficult because of its low density and critical temperature. Presently, there are three ways to store hydrogen: (a) as a compressed gas, (b) as cryogenic liquid hydrogen (LH₂) and (c) solid-state hydrogen storage [2, 3]. The main drawback of compressed gas and cryogenic liquid hydrogen storage is the low volumetric density of the system. Solid-state hydrogen storage involves storage of hydrogen in complex chemical hydrides. These hydrides have high hydrogen content and hydrogen can be released through several chemical pathways. Hydrolysis of chemical hydrides takes place at comparatively low temperatures and gives promising theoretical hydrogen storage efficiencies [4, 5].

Among diverse chemical hydrides, sodium borohydride (NaBH₄) has been considered as the most attractive hydrogen storage material. It is a safe practical means of producing hydrogen and has

high hydrogen content (10.7 wt %) [6, 7]. Hydrolysis of sodium borohydride is a heat releasing reaction. No side reactions or volatile byproducts are formed and the generated hydrogen is of high purity (no traces of CO and S) and humidified (heat generates some water vapor). Additionally, sodium borohydride is the least expensive metal hydride commercially available. Furthermore, it is safe to use, handle and store. Eqn. 1 gives the hydrolysis reaction of NaBH₄.



Rate kinetics of the above reaction is slow without a catalyst that affects the hydrogen release. Therefore, for the fast kinetics of the hydrolysis reaction of NaBH₄, a highly reactive catalyst is obligatory. Many catalysts like RuCl₃, RhCl₃, CoCl₂, H₂PtCl₂, FeCl₂, and PdCl₂ are used for NaBH₄ hydrolysis. In terms of reactivity and cost, CoCl₂ is the most favored one [8]. As compared with other non-noble metal catalysts like nickel, maximum hydrogen generation is reported with cobalt based catalysts [9]. Catalytic potential of cobalt (II) and (III) salts has been studied in the literature and CoCl₂ showed the preminent performance as a catalyst for hydrolysis reaction of NaBH₄ [10-13]. It is also found that the catalytic active phase of CoCl₂ as a catalyst in NaBH₄ hydrolysis is cobalt boride that could be formed as Co_xY or Co_xB_y [14]. Heat of hydrolysis of sodium borohydride is lower when compared with other chemical hydrides as shown in Table 1 [15].

* To whom all correspondence should be sent:
E-mail: er.arsh87@gmail.com

Hydrogen storage as high pressurized gas or liquid cannot fulfill future storage goals. Chemically or physically combined storage of hydrogen in other materials has various advantages over other storage methods. Intensive kinetic studies have been done on complex hydrides for progression of hydrogen generation (HG) properties [4].

Efficiency of hydride based hydrogen storage systems can be improved if the particle size is reduced to the low nanometer range. Hydrogen desorption rate increases due to the high surface-to-volume ratio of the nanoparticles, which further reduces the external energy required for hydrogen desorption [16]. Studies are also carried out on hydrogen generation with a combination of nanoparticles of alumina with NaBH_4 due to a mutual promoting mechanism that exists between hydrolysis of NaBH_4 and $\text{Al}_2\text{O}_3/\text{H}_2\text{O}$ reactions [17, 18]. The constituted dual fuel system exhibited complementary attributes, such as eminent hydrogen density, reduced material cost and adequate controllability of the reactions at moderate temperatures, making it promising for mobile and portable hydrogen source applications [17].

The present kinetic study reports on the reactivity of the $\text{NaBH}_4\text{-CoCl}_2$ system and the effect of Al_2O_3 nanoparticles on the hydrogen generation rate for the $\text{NaBH}_4\text{-CoCl}_2$ system.

MATERIALS AND METHODS

The chemicals used in the investigation were sodium borohydride powder (purity 97%), cobalt chloride salt powder in hexa-hydrate form (purity of 98%) procured from Loba Chemie Ltd., and sodium hydroxide pellets (purity 97%) procured from CDH Laboratory and Al_2O_3 nanoparticles (20 nm, 99% purity) from Sigma Aldrich.

The schematic experimental setup used for the study is shown in Fig.1. It consists mainly of a

three-port reactor, the left-hand port of which is equipped with a thermowell for placing a thermometer; the middle port is connected to a dropping funnel and the right-hand port guides the generated hydrogen gas to a water-replacement system. The water-replacement system consists of a measuring cylinder filled with water and a water container to submerge the cylinder. The volume of the hydrogen generated is measured using the measuring cylinder. To adjust the reaction temperature in the reactor, thermostatically controlled water bath is used.

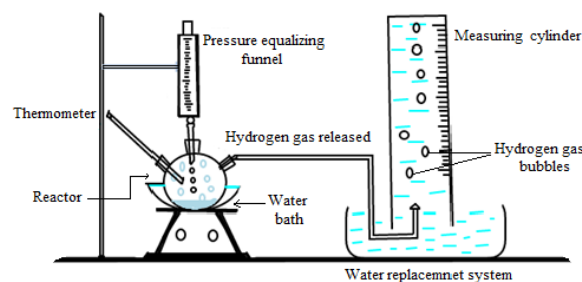


Fig.1. Schematic diagram of the experimental setup.

Dried NaBH_4 and CoCl_2 are put in the reaction flask. Then 10 mL solution of NaOH and water is added with a pressure-equalizing funnel and guided to the reactor. Hydrogen gas is collected in the measuring cylinder by downward displacement of water and the volume of hydrogen produced is monitored with time.

The residue left after hydrolysis reaction of NaBH_4 is kept in an incubator at 60-70°C overnight for drying. The black solid obtained after drying is characterized by SEM (scanning electron microscopy), EDS (energy dispersive X-ray spectroscopy) and XRD (X-ray diffraction) analysis.

Table 1. Comparison of chemical hydrides with heat of hydrolysis reaction [5]

Sample		Hydride		Heat of hydrolysis reaction (kJ/mole H_2)
No.	Name	% H_2 by weight	% H_2 in stoichiometric mixture	
1.	LiBH_4	18	8.5	-90
2.	LiH	13	8	-145
3.	NaBH_4	10.5	7.5	-80
4.	LiAlH_4	10.5	7.5	-150
5.	AlH_3	10	7	-158
6.	MgH_2	7.5	6.4	-161
7.	NaAlH_2	7.2	6	-140
8.	CaH_2	4.9	5.1	-140
9.	NaH	4.9	4	-150

The morphology of the residue was observed on a scanning electron microscope (JEOL JSM-6510 LV) equipped with an integrated silicon drift detector (SDD) technology to carry EDS analysis. The specimens were coated with 50 μm thick gold film in an automatic sputter coater (Polaron) to avoid charging under an electron beam prior to SEM.

Structural characterization of the residue was carried out by recording its X-ray diffraction patterns using PANalytical X'Pert Pro Diffractometer operated at 45 kV and 40 mA with monochromatic Cu-Kα radiation (λ=1.5406 Å), in the 2θ range of 20 - 80°.

ANALYSIS

Qualitative analysis of hydrogen gas is done by pop test and the presence of hydrogen gas is confirmed by a squeaky pop sound. Quantitative analysis test is conducted by gas chromatography on AIMIL-NUCON gas chromatograph. The analysis confirmed the presence of hydrogen gas with a purity of 85%, the rest being nitrogen from air as per recovery basis from the sample. The rate eqns. describing the relation between the rate of hydrogen generation and the concentration of sodium borohydride are given below.

$$r_{H_2} \approx C_{NaBH_4}^\alpha \quad (2)$$

Here r_{H_2} is the rate of hydrogen generation in moles/L.sec, C_{NaBH_4} is the concentration of NaBH₄ in moles/L, and α is the reaction order. Hydrogen generation rate (HGR) linearly decreases with the increase in NaOH concentration at a fixed NaBH₄ concentration and temperature. As a result,

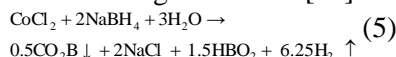
$$r_{H_2} = \frac{1}{(1 + k_1 C_{NaOH})} \quad (3)$$

where, C_{NaOH} is the concentration of NaOH in moles/L and k_1 is a proportionality constant. Combining eqns. (2) and (3), the rate of hydrogen generation is obtained assuming k to be another proportionality constant [19].

$$r_{H_2} = \frac{kC_{NaBH_4}^\alpha}{1 + k_1 C_{NaOH}} \quad (4)$$

RESULTS AND DISCUSSION

In the present study, the factors affecting the rate of sodium borohydride hydrolysis reaction: sodium borohydride concentration, sodium hydroxide concentration and temperature were observed. The hydrolysis reaction is given below [20].



Effect of NaBH₄ concentration on the rate

In a series of experiments by varying the initial concentration of NaBH₄ and keeping the NaOH (0.25 moles/L) and CoCl₂ (0.02 moles/L) concentrations constant, the effect of NaBH₄ on HGR was determined. On increasing the concentration of sodium borohydride, the number of collisions between the molecules increases, consequently increasing the rate of the reaction. According to Fig. 2, the HGR increases with increase in NaBH₄ concentration at constant NaOH and CoCl₂ concentrations. The solution becomes more viscous at higher concentrations of NaBH₄ due to the conversion of NaBH₄ to sodium metaborate [21].

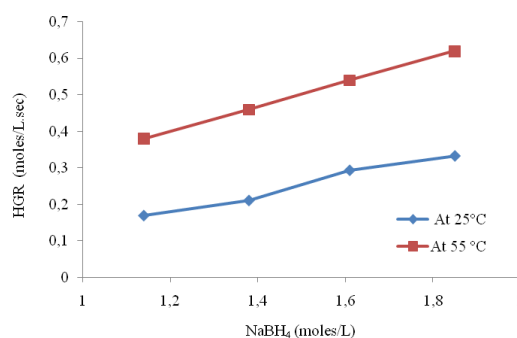


Fig. 2. Effect of NaBH₄ concentration on HGR.

Effect of temperature on the rate

The temperature is a measure of the kinetic energy of a system. Higher temperature implies higher average kinetic energy of molecules and more collisions occurring per unit time. Acceleration of H⁺, OH⁻, BH⁴⁻ and Cl²⁺ ions is directly related to the temperature of hydrolysis reaction [22]. The reaction rate increases with the increase in temperature as indicated by the slope of the line shown in Fig. 3.

Readings are taken at NaBH₄ equal to 1.38 moles/L and CoCl₂ 0.02 moles/L. Activation energy calculated for NaBH₄/CoCl₂/H₂O system from the Arrhenius equation is $E = 37.931$ kJ/mol and $A = 12.54 \times 10^8$ sec⁻¹.

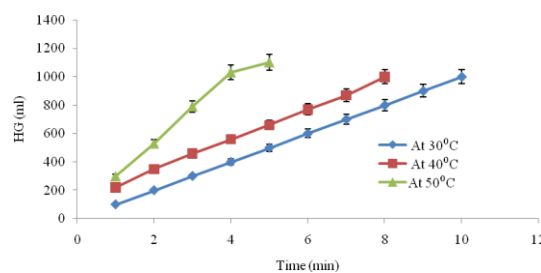


Fig. 3. Hydrogen generation with time at different temperatures

Effect of sodium hydroxide (NaOH) concentration on the rate

To increase the shelf life of NaBH₄ solutions and to suppress its self-hydrolysis, NaBH₄ solutions were maintained at alkaline conditions by adding NaOH. According to Fig. 4 (a, b), HGR initially increases with the increase in NaOH but decreases beyond 0.25 moles/L. These experiments were conducted at 1.14 and 1.38 moles/L NaBH₄ and constant CoCl₂ (0.02 moles/L) concentration at 45°C.

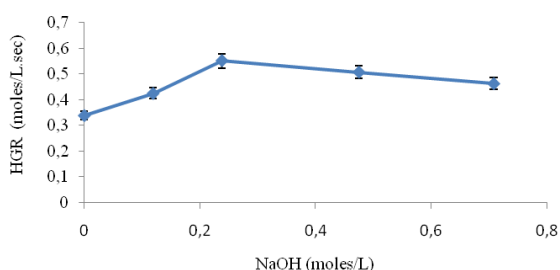


Fig. 4(a). Variation of HGR with NaOH concentration at 1.14 moles/L NaBH₄.

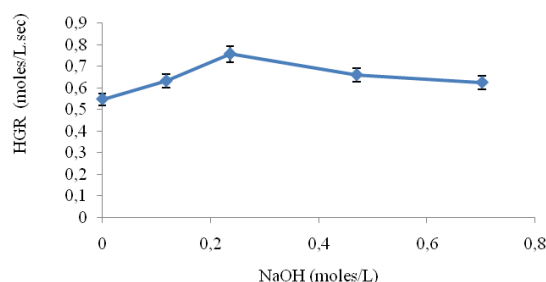


Fig. 4(b). Variation of HGR with NaOH concentration at 1.38 moles/L NaBH₄.

These observations were made at relatively low concentrations of NaOH and it was observed that at higher concentrations of NaOH, HGR decreases due to high alkalinity of the solution.

REGRESSION ANALYSIS

It is assumed that the maximum hydrogen generation rate is the initial value of hydrogen generation. The parameters ($k/(1 + k_1C_{NaOH})$) and α in Eqn. (4) can then be determined by regression analysis and are given in Table 2. To determine the rate constants k and k_1 , Eqn. (4) was modified to Eqn. (6).

$$\frac{1}{r_{H_2}} = \frac{1}{k} C_{NaBH_4} + \frac{k_1}{k} \frac{C_{NaOH}}{C_{NaBH_4}}, \quad (6)$$

Table 2. Kinetic parameters at different temperatures.

Sample No.	Temperature (°C)	NaOH (moles/L)	$k/(1 + k_1C_{NaOH})$ (mL ² /mol.sec)	α
1.	25	0	0.165	1.28
2.	35	0	0.270	1
3.	45	0	0.324	1.3
4.	25	0.25	0.246	1.03
5.	35	0.25	0.343	1.17
6.	45	0.25	0.527	1.04
7.	25	0.70	0.29	1.3
8.	35	0.70	0.3	1.27
9.	45	0.70	0.479	1.2

The order of the reaction with respect to NaBH₄ concentration α equals to 1 with an experimental error of ± 0.2 (Table 2). Plot of inverse of hydrogen generation rate ($1/r_{H_2}$) versus the ratio of NaOH and sodium borohydride concentration (C_{NaOH}/C_{NaBH_4}) gives a straight line, as shown in Fig. 5. The intercept on the y axis gives ($1/kC_{NaBH_4}$) and the slope gives (k_1/k), from which both k and k_1 may be determined as shown in Table 3.

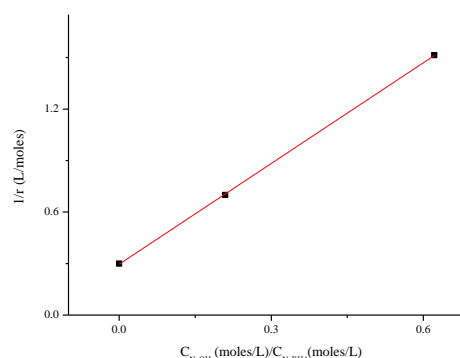


Fig. 5. Effect of NaOH/ NaBH₄ ratio on the rate.

Table 3. Rate constants k and k_1

Sample No.	NaBH ₄ (moles/L)	Temperature (°C)	k	k_1
1.	1.14	25	0.604	3.03
2.	1.14	45	2.009	5.843
3.	1.14	65	3.02	5.88
4.	1.38	25	0.875	2.85
5.	1.38	45	2.09	3.76
6.	1.38	65	3.81	8.11
7.	1.61	25	0.76	1.13
8.	1.61	45	1.94	2.96
9.	1.61	65	4.31	6.20

CHARACTERIZATION OF THE RESIDUAL SUBSTANCE

The morphology of the black colored solid residue formed after hydrolysis reaction of NaBH_4 in presence of CoCl_2 catalyst was analyzed by SEM and the images are shown in Fig. 6 (a, b, c and d). The particles are observed to agglomerate together and the rough surface indicates the presence of cobalt [10].

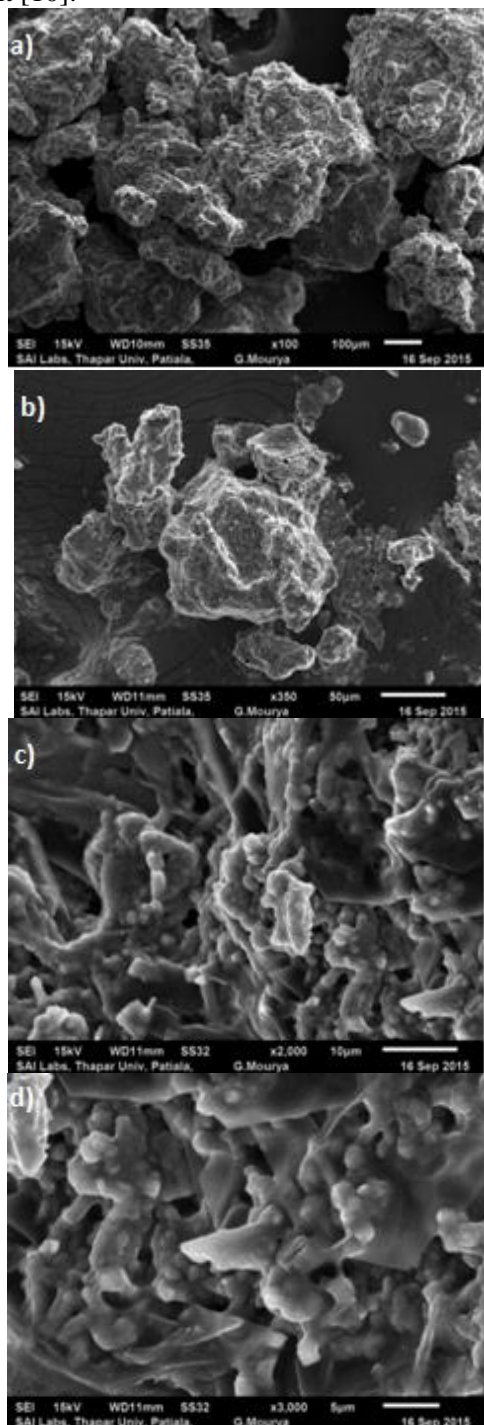


Fig. 6. (a, b, c and d) SEM images of the residual material.

EDS analysis of residual material's surface (Fig.7) provides quantitative information about its elemental composition. Elemental percentages of byproducts of NaBH_4 hydrolysis are given in Table 4.

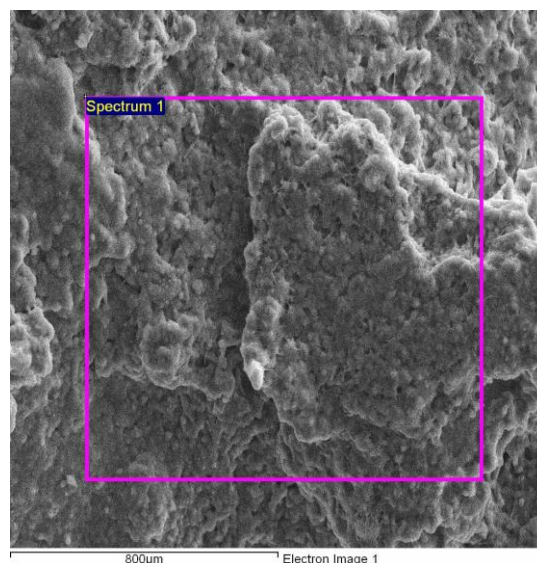


Fig.7. Sectioned area of residual material for EDS analysis

It is observed that boron (78.46 wt%) is present in maximum percentage in the residue followed by oxygen (18.01 wt%), sodium (3.41 wt%), chlorine (0.07 wt%) and cobalt (0.05 wt%)

Table 4. Elemental percentages of NaBH_4 hydrolysis byproducts.

Element	Weight (%)	Atomic (%)
B	78.46	85.04
O	18.01	13.19
Na	3.41	1.74
Cl	0.07	0.02
Co	0.05	0.01

According to literature, cobalt boride (Co_2B , Co_3B) and other Co-B compounds with different degrees of oxidation are expected to be present in the residue obtained after hydrolysis of NaBH_4 in presence of CoCl_2 catalyst. These compounds are reported to be an amorphous mixture of Co-B based catalysts having varying cobalt, boron and oxygen contents [23]. The diffraction peak around 2θ range between 40° and 50° is assigned to cobalt borides (Co_xB) or metallic Co^0 phases [8, 24]. Similar results are observed by XRD analysis (Fig. 8) of the residual material. Diffraction peaks around $2\theta = 45^\circ$ confirm the presence of Co_2B (Ref. Code 01-089-1994) [14]. Another Co-B based compound like cobalt borate $\text{Co}_2\text{B}_2\text{O}_5$ (Ref. Code 01-073-1772 and Na based byproducts like sodium borate hydrate ($\text{Na}_2\text{B}_4\text{O}_7 \cdot 10\text{H}_2\text{O}$, Ref Code 01-088-1411 and sodium boride ($\text{Na}_3\text{B}_2\text{O}$, Ref. Code 00-012-0) are also present in the residue.

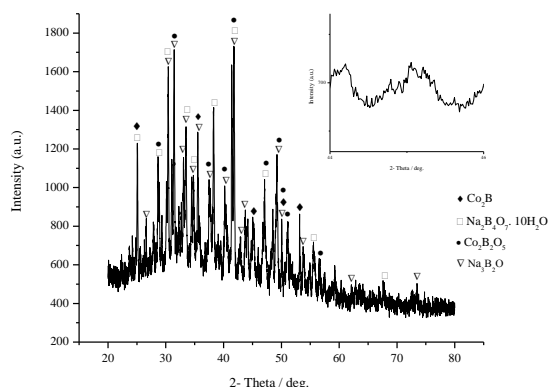


Fig.8. XRD analysis of the residual material

Hydrogen generation rate (HGR) studies using Al_2O_3 (nanoparticles) in the $\text{NaBH}_4/\text{CoCl}_2/\text{H}_2\text{O}$ system

Experiments were performed to study the effect on HGR of the addition of Al_2O_3 (nanoparticles) to the $\text{NaBH}_4/\text{CoCl}_2$ system. As shown in Fig. 9, HGR increases with NaBH_4 concentration at all concentrations of Al_2O_3 . Readings are taken for 1.008, 1.26, 1.49 and 1.73 moles/L NaBH_4 at 0.046, 0.065 and 0.083 moles/L Al_2O_3 for constant CoCl_2 (0.02 moles/L) concentration. The addition of Al_2O_3 nanoparticles is found to improve the kinetics of NaBH_4 hydrolysis [22].

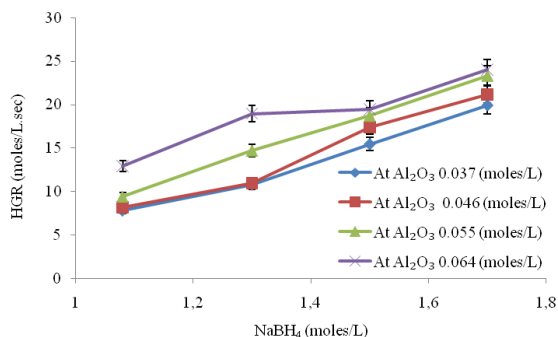


Fig. 9. Effect of NaBH_4 concentration on HGR.

The addition of alumina nanoparticles to the $\text{NaBH}_4/\text{CoCl}_2/\text{H}_2\text{O}$ system results in high HGR thus improving the system storage density. Due to the supporting mechanism existing between NaBH_4 hydrolysis reaction and $\text{Al}_2\text{O}_3/\text{H}_2\text{O}$ reaction, hydrogen generation performance is increased [17]. Studies are still in progress to understand the actual role of alumina nanoparticles for the increased performance characteristics of the examined system.

CONCLUSIONS

Hydrolysis reaction of sodium borohydride with cobalt chloride as a catalyst is a first-order reaction.

Hydrogen generation rate increases with the increase in temperature, sodium borohydride (NaBH_4) concentration and decreases with sodium hydroxide (NaOH) concentration.

The rate constant 'k' with respect to sodium borohydride and the rate constant 'k₁' with respect to sodium hydroxide increase significantly when the temperature is increased from 45 to 65°C.

The gas chromatography analysis indicates that the hydrogen gas has a purity of 85%, the rest being nitrogen.

The residue of the NaBH_4 hydrolysis reaction is characterized by SEM, EDS and XRD.

According to SEM and EDS analysis, the particles agglomerate together with maximum percentage of boron in the residue. XRD analysis shows the presence of Co-B and Na based compounds in the residue.

The hydrogen generation rates are found to be higher for the hydrolysis in the $\text{Al}_2\text{O}_3/\text{NaBH}_4/\text{CoCl}_2/\text{H}_2\text{O}$ system compared to the $\text{NaBH}_4/\text{CoCl}_2/\text{H}_2\text{O}$ system.

Acknowledgements: The authors gratefully acknowledge the support provided by the management of Thapar University, Patiala for providing the necessary facilities to carry out this research work and the financial help from Rajiv Gandhi Fellowship to A. Kaur by UGC.

REFERENCES

1. A. E. Y. Marrero, A. M. Beard, A. D. Thomas, M. A. Matthews, *Industrial & Engineering Chemistry Research*, **48**, 3703 (2009).
2. G. Moussa, R. Moury, U. B. Demirci, T. Sener, P. Miele, *International Journal of Energy Research*, **37**, 825 (2013).
3. U. Eberle, M. Felderhoff, T. Schuth, *Angewandte Chemie International Edition*, **48**, 6608 (2009).
4. B. Sakintuna, F. L. Darkrim, *International Journal of Hydrogen Energy*, **32**, 1121 (2007).
5. U. B. Demirci, P. Miele, *Energy and Environmental Science*, **2**, 627 (2009).
6. R. Retnamma, A. Q. Novais, C. M. Rangel, *International Journal of Hydrogen Energy*, **36**, 9772 (2011).
7. Y. Shang, R. Chen (2006). *Energy and Fuels*, **20**, 2142 (2006).
8. P. A. M. Boss, C. A. Becker, G. W. Anderson, B. J. Wiedemeier, *Industrial and Engineering Chemical Research*, **54**, 7714(2015).
9. P. Brack, S. E. Dann, K. G. U. Wijayantha, *Energy Science & Engineering*, **3**, 188(2015).
10. O. Akdim, U. B. Demirci, P. Mieli, *International Journal of Hydrogen Energy*, **36**, 13669 (2011).
11. U. B. Demirci, O. Akdim, J. Hannauer, R. Chamoun, P. Miele, *Science China*, **53**, 1870 (2010).

12. J. C. Walter, A. Zurawski, D. Montgomery, M. Thornburg, M. Revankar, *Journal of Power Sources*, **179**, 335 (2008).
13. O. Akdim, U. B. Demirci, D. Muller, P. Miele, *International Journal of Hydrogen Energy*, **34**, 2631 (2009).
14. U. B. Demirci, P. Miele, *Physical Chemistry Chemical Physics*, **16**, 6885 (2014).
15. Y. Wu, Presentation at the GCEP-Stanford University, (2003)
16. G. D. Snow US Patent 6 589 312 (2003).
17. H. B. Dai, G. L. Ma, H. J. Xia, P. Wang, *Fuel Cells*, **11**, 424 (2011).
18. D. W. Zhuanga, Q. Kang, S.S Muir, X. Yaoc, H. B. Dai, G. L. Maa, P. Wang, *Journal of Power Sources*, **224**, 304 (2013).
19. H. S. Fogler, Elements of Chemical Reaction Engineering, 3rd edition. Englewood Cliffs, NJ: Prentice Hall, 2000.
20. S. U. Jeong, R. K. Kim, E. A. Cho, H. J. Kim, H. M. Nam, *Journal of Power Sources*, **44**, 129 (2005).
21. O. Metin, S. Ozkar, *Energy and Fuels*, **23**, 3517 (2009).
22. Y. Wang, L. T. Zhou, H. Yuan, W. H. Shen, R. Tang, M. Q. Fan, K. Y. Shu, *International Journal of Electrochemical Science*, **8**, 9764 (2013).
23. G. M. Arzac, T. C. Rojas, A. Fernandez, *ChemCatChem*, **3**, 1313 (2011).
24. G. N. Glavee, K. J. Klabunde, C. M. Sorensen, G. C. Hadjapanayis, *Langmuir*, **8**, 773 (1992).

КИНЕТИЧНИ ИЗСЛЕДВАНИЯ ВЪРХУ СИСТЕМАТА ЗА СЪХРАНЕНИЕ НА ВОДОРОД $\text{NaBH}_4/\text{H}_2\text{O}$ С CoCl_2 КАТО КАТАЛИЗАТОР

А. Каур*, Д. Гангачарюлу, П.К. Баджпаи

Департамент по химично инженерство, Университет Тапар, Патинала, Индия

Получена на 28 април, 2015 г., коригирана на 26 септември, 2015 г.

(Резюме)

Водородът се приема в световен мащаб като заместител на изкопаемите горива и да установи чисто и сигурно енергийно бъдеще. Съхранението на водорода като хидриди (например натриев борохидрид (NaBH_4)) е срещнало сериозна загриженост като потенциален източник на водород за портативни устройства. Настоящата работа засяга кинетични изследвания върху системата $\text{NaBH}_4/\text{CoCl}_2/\text{H}_2\text{O}$ и факторите, влияещи на скоростта на генериране на водород (HGR): концентрацията на NaBH_4 , на NaOH и температурата. В нея също се съобщава за резултатите за добавянето на нано-частици от диалуминиев триоксид към системата $\text{NaBH}_4/\text{CoCl}_2/\text{H}_2\text{O}$, за ускоряването на скоростта на генериране на водород, дължащи се на по-добрата реактивоспособност на нано-частиците. Кобалтовият хлорид е широко използван като изгоден катализатор с неблагороден метал, който ускорява хидролизата на NaBH_4 . Кинетичните изследвания показват, че хидролизата на NaBH_4 се описва от уравнение от първи порядък. Скоростта нараства с натриевия борохидрид и намалява с натриевата основа. Освен това е наблюдавано че скоростта на реакцията нараства с температурата. Охарактеризирането на остатъка е извършено чрез SEM, EDS и XRD, при което се установява, че частиците се агломерират. В остатъка се съдържат бор, натрий, кобалт, хлор и кислород в тегловни проценти съответно 78.46%, 3.41%, 0.05%, 0.07% и 18.01%. Дифракционният пик при $2\theta = 45^\circ$, установен от рентгеноструктурния анализ показва наличието на Co_2B в остатъка.

Studying the effect of doping metal ions onto a crystalline hematite-based humidity sensor for environmental control

A. S. Afify^{1*}, M. Ataalla², A. Hussain¹, M. Hassan¹, A. Mohammed³, M. Milanova⁴, J.M. Tulliani¹

¹ Politecnico di Torino, Department of Applied Science and Technology, 10129 Torino, Italy

² University of Chemical Technology and Metallurgy, Department of Materials Science, 1756 Sofia, Bulgaria

³ Chemistry Department, Deanery of Academic Services, Taibah University, Al-Madinah Al-Munawwarah, Saudi Arabia. On vacation from the Higher Institute of Optics Technology, Heliopolis, Cairo, Egypt

⁴ Institute of General and Inorganic Chemistry, BAS, Acad. G. Bonchev Str. bld. 11, 1113 Sofia, Bulgaria

Received March 24, 2015, Revised October 26, 2015

Humidity sensors have several applications in both industrial processing and environmental control. Pure and doped hematite has proved to exhibit remarkable humidity sensing properties. The aim of this investigation is to study the effect of doping of some metal ions (Li^+ , Mg^{+2} , Ba^{+2} , Sr^{+2} , and Na^+) onto the crystalline hematite and to determine their sensitivity towards relative humidity (RH). The obtained crystalline samples were characterized by X-Ray Diffraction (XRD) combined with Field Emission Scanning Electron Microscopy (FESEM). The doped sodium metal ions (Na^+) hematite sample showed a significant response towards relative humidity at room temperature.

Keywords: Doping, Hematite, Humidity sensors.

INTRODUCTION

Measurements and/or control of humidity are important not only for human comfort but also for a broad spectrum of industries and technologies. Humidity sensors have several applications in industrial processing, domestic applications and environmental control [1-4].

Adding metal ions to humidity sensing materials have been widely reported in literature due to their abundance in nature hence, efforts were made to denote their effects [5]. Doping of metal ions affects the microstructure and creates surface defects or oxygen vacancies of the sensing material [6-8].

Ferric oxide has a wide range of applications as a magnetic material [9]. In addition it is very sensitive to humidity and can be used as a humidity sensor [10]. $\alpha\text{-Fe}_2\text{O}_3$ is an n-type semiconductor, it is the most stable iron oxide under ambient conditions, nontoxic, corrosion-resistant, low cost and abundant. These features render it suitable for numerous promising applications, such as catalysts/photocatalysts [11-13], contrast reagents/drug delivery [14] and gas sensors [15].

Nanocomposite materials containing $\alpha\text{-Fe}_2\text{O}_3$ doped with noble metals (e.g., Pd, Pt, and Au) can lead to a synergetic effect depending on the preparation conditions, chemical composition, sintering temperature, sintering time and doping

with various additives [16]. Different techniques were used for producing hematite films on the solid substrate like sputtering [17], laser ablation [18], electrodeposition [19], spray pyrolysis (SP) [20, 21], ion beam induced chemical vapor deposition (IBICVD) [22], plasma enhanced chemical vapor deposition (PECVD) [23] and aerosol-assisted chemical vapor deposition (AACVD) [24]. The aim of this study is to investigate the doping effect of some metal ions (Mg^{+2} , Ba^{+2} , Sr^{+2} , Li^+ , and Na^+) onto a crystalline hematite and to determine their sensitivity to humidity. The sensors studied were prepared by a screen printing technique.

EXPERIMENTAL

Powder synthesis

All reagents were ACS grade from Sigma-Aldrich. 1 mole of $\alpha\text{-Fe}_2\text{O}_3$ powder (Aldrich >99%, particle size distribution lower than 2 μm) was dispersed in distilled water, then a dispersing agent was added (Daraven 2 wt% of the used powder). The solution was then ultrasonicated for 2 h. The prepared dispersed solution was mixed stepwise with 1.0 L aqueous solution of the salts (for precipitation of metal hydroxide as the pH was adjusted with NaOH): Li_2CO_3 , MgCO_3 , $\text{Ba}(\text{NO}_3)_2$, $\text{Sr}(\text{NO}_3)_2$ and Na_2CO_3 .

The dispersed solution was ultrasonicated again for 1 h, the solid content in solution was diluted to 4 wt% by adding distilled water. Finally, the dispersion was dried at 115°C overnight.

* To whom all correspondence should be sent:
E-mail: Ahmed.Afify@polito.it

The dried powder was treated at 800°C for 1 h with a heating ramp of 2°C/min. The powders were then manually grounded by means of an agate mortar and an agate pestle before the screen printing process.

Powder characterization

Particle size distribution was determined after powder calcination by means of a laser granulometer (Malvern 3600D) and after dispersion in ethanol and sonication for 10 min. X-ray diffraction patterns were collected on powders by means of an X'Pert High Score Philips Analytical Diffractometer, equipped with a Cu anticathode (λ Cu K α anticathode= 0.154056 nm). Samples were scanned at a rate of 0.02°/s in the range from 5° to 70° in 2 θ after calcinations of the prepared powder. Finally, samples were chromium sputtered for FESEM (Field Emission Scanning Electron Microscopy, Zeiss Merlin) investigations.

Humidity sensor preparation and testing

The sensors were screen printed onto α - alumina substrates with platinum electrodes fired at 980°C for 20 min. (with a heating ramp of 2°C/min.) [25, 26]. Screen printing inks were made of the doped α -Fe₂O₃ powders and an organic vehicle (Terpenol), which acts as a temporary binder for the unfired film and confers the appropriate rheological properties to the paste.

After deposition the samples were dried in air at room temperature prior to being heat treated at 800°C, (with a heating ramp of 2°C/min.) for 1h. The humidity sensors were tested in a laboratory apparatus made of a thermostated chamber, operated at 25°C, in which the relative humidity (RH) could be varied between 0 and 96% [27].

The laboratory apparatus for testing the sensors was calibrated to ensure a constant air flow during the electrical measurements and RH was varied by steps, each one of 3 min. An external alternating voltage ($V = 3.6$ V at 1 kHz) was applied on each tested sensor, acting as a variable resistance of the electrical circuit described above. A 2000 series Keithley digital multimeter was used to measure the tension V_{DC} at the output of the circuit.

The sensor resistance was determined by a calibration curve drawn substituting the sensors, in the circuit, by known resistances. The sensor response (SR), expressed in %, was defined as the relative variation of the starting resistance, compared with the resistance measured under gas exposure (eq. 1):

$$SR(\%) = 100 \frac{|R_0 - R_g|}{R_0} \quad (\text{eq. 1})$$

Where R_0 and R_g are the starting (in the absence of the test gas) and the gas exposed measured resistances of the sensors, respectively.

RESULTS AND DISCUSSION

Materials characterization

Particle size distribution

Commercial α -Fe₂O₃ has a particle size distribution lower than 2 μ m. Generally, doped metal ion-hematite samples thermally treated at 800°C for 1 h present a larger particle size distribution as shown in Table 1. This could be attributed to particle's agglomeration during the drying process. Moreover, the variation in size is due to their atomic radius.

The cumulative weight below 50% of the hematite doped metal ions particle size is less than 40 μ m, means it could be passed through the opening of the screen-printing mesh. Sieving was performed for Sodium and Barium doped hematite to obtain a size less than 40 μ m as shown in Fig.1.

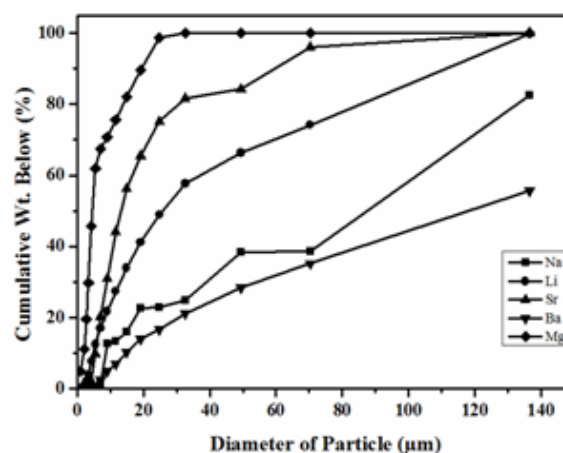


Fig. 1. Particle size distribution of metal ions doped onto hematite powders.

XRD measurements

For the sake of comparison with the metal-ions doped hematite, the XRD pattern of a commercial α -Fe₂O₃ (JCPDS card n°33-664) is shown in Fig. 2a. XRD patterns of the different doped α -Fe₂O₃ powders presented in Fig.2b, 2c, 3a, 3b showed well crystallized phases.

Sodium doped hematite was crystallized in NaFeO₂ form according to (JCPDS card n°1-74-1351), the structure of NaFeO₂ is a layer ordered rock salt type structure [27].

Table 1. Diameter of the doped metal ions hematite powders (μm)

Cumulative wt%	Na^+ ($\alpha\text{-Fe}_2\text{O}_3$) [μm]	Li^+ ($\alpha\text{-Fe}_2\text{O}_3$) [μm]	Sr^{2+} ($\alpha\text{-Fe}_2\text{O}_3$) [μm]	Ba^{2+} ($\alpha\text{-Fe}_2\text{O}_3$) [μm]	Mg^{2+} ($\alpha\text{-Fe}_2\text{O}_3$) [μm]
10%	7.03	5.58	5.61	14.55	1.92
50%	91.13	25.36	13.19	122.62	4.7
90%	149.2	85.33	65.88	220.72	19.19

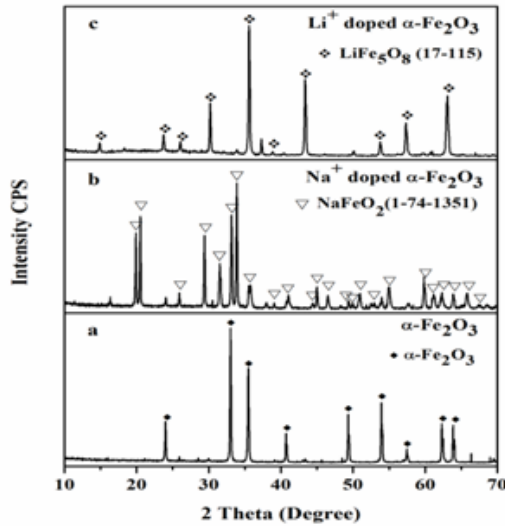


Fig. 2. XRD pattern of a) $\alpha\text{-Fe}_2\text{O}_3$, b) sodium-doped hematite and c) lithium-doped hematite

LiFe_5O_8 (JCPDS card n°17-115) with a cubic spinel structure derived from lithium-doped hematite [28].

The $\text{Sr}_4\text{Fe}_6\text{O}_{13}$ phase obtained according to (JCPDS card n° 1-78-2403) from a strontium doped hematite sample, the phase formed when the powder calcined above 775°C which matches the thermally treated powder at 800°C [29].

$\text{Ba}_{10}\text{Fe}_{10}\text{O}_{28}$ (JCPDS cards n°54-966) and $\text{Fe}_{1.9}\text{Mg}_{0.16}\text{O}_3$ (JCPDS cards n°1-70-2674) are detected in barium and magnesium doped hematite, respectively.

FE-SEM observation and microanalysis

FESEM micrographs of unfired, fired at 800°C commercial hematite as well as Na^+ doped hematite heat treated at 800° are shown in Figs.4a, 4b and 4c respectively in order to distinguish the morphological difference between all of them.

According to the FESEM analysis, unfired hematite appears denser with less porosity than fired hematite (see Figs 4a, and 4b). Fired Na^+ doped hematite powder has the biggest grains size in comparison with the particles size of the fired and unfired hematite (see Figs 4a, 4b and 4c). This could be attributed to the diffusion of sodium ions into the crystalline hematite.

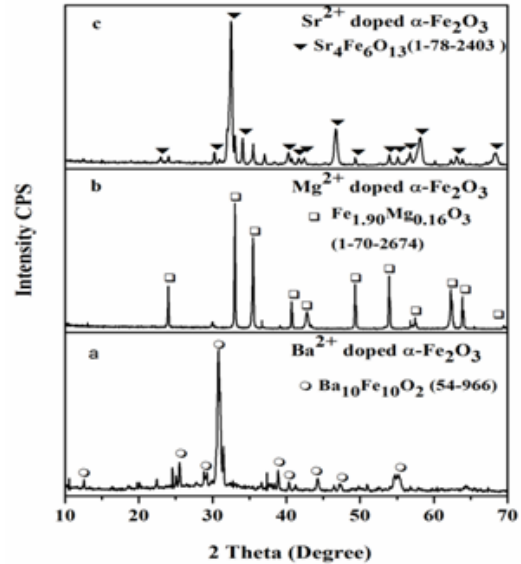


Fig.3. XRD pattern of a) barium-doped hematite, b) magnesium-doped hematite and c) strontium-doped hematite

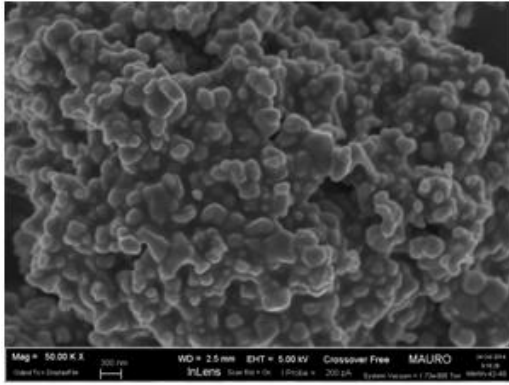
FESEM data also showed that the fired sodium doped hematite film is characterized by well distributed porosity, which makes this material appropriate as a gas sensor. Energy dispersive x-ray (EDX) analysis of sodium doped hematite showed that Na^+ and Fe^{2+} were well distributed in all the samples (see Table 2. and Fig. 5) which is in a good agreement with the XRD data for the NaFeO_2 phase.

Table 2. EDX of the fired Na-doped hematite sample at 800°C .

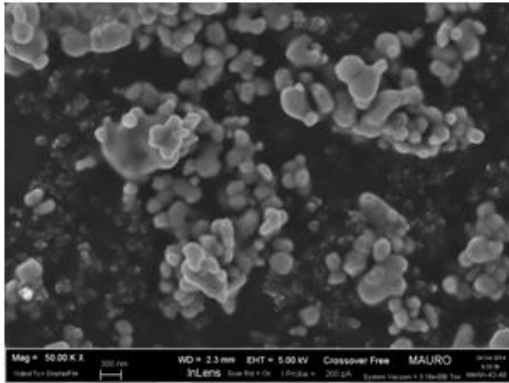
Metals	At%	Wt%
Na	8.42 ± 1.2	3.65
Fe	91.58 ± 3.2	96.35

Sensitivity towards relative humidity

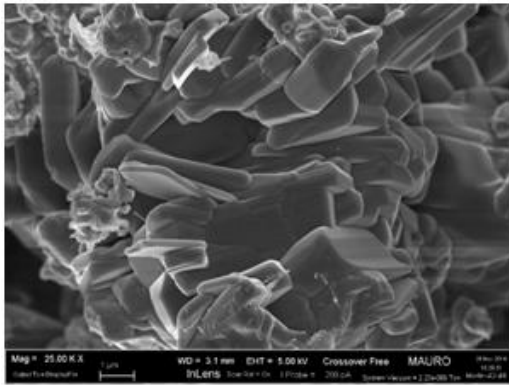
Fig. 6 illustrates the sensors' response to RH. Among the different investigated samples, Na^+ doped hematite showed a significant response to RH at room temperature starting from 32% RH.



(a)



(b)



(c)

Fig. 4. FESEM micrographs of a) unfired hematite powder, b) hematite powder heat treated at 800°C for 1 h and c) Na⁺ doped hematite heat treated at 800°C for 1 h.

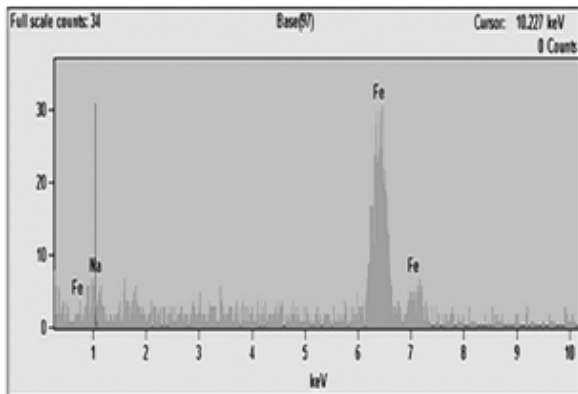


Fig. 5. EDX maps of fired sodium -doped hematite at 800°C

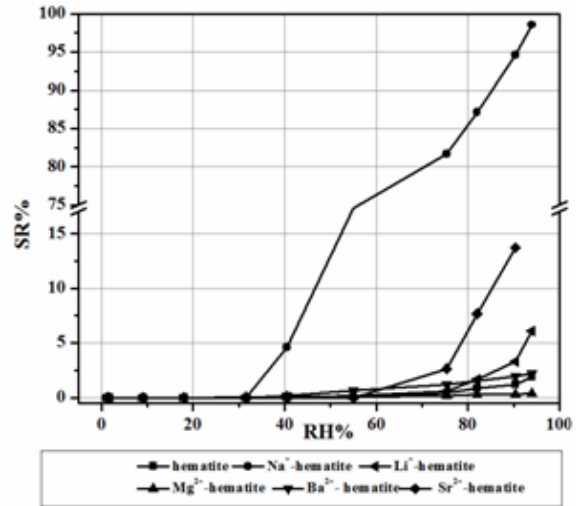


Fig. 6. Sensors response to relative humidity changes.

While the other metal ions doped hematite samples show a poor sensitivity to RH. Fig.7 shows the change in V_{DC} as a function of time for Na⁺ doped hematite sensors. The response times (the time taken by a sensor to achieve 90% of the total resistance change in the case of gas adsorption) and the recovery times (the time necessary to reach 90% of the total resistance changes in the case of gas desorption) are reported in Table 3. These response and recovery times are quite fast.

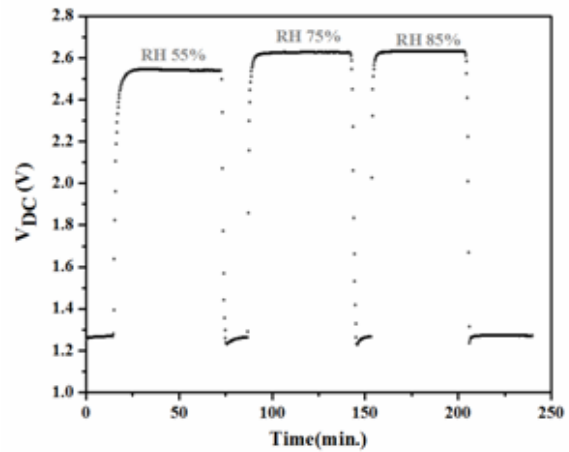


Fig. 7. Changes in V_{DC} as a function of RH changes at room temperature for Na⁺ doped hematite sensor.

Table 3. Response and recovery time of the Na⁺ doped hematite based sensor

Humidity change	0-55% RH	0-75% RH	0-85% RH
Response time (min.)	2.5	2.1	1.2
Humidity change	55-0% RH	75-0% RH	85-0% RH
Recovery time (min.)	1.0	2.5	2.5

CONCLUSION

A simple and low cost chemical method was used to synthesize hematite doped with different alkali and alkaline-earth metals. The screen printing technique was applied to realize humidity sensors from the prepared powders.

Doping of hematite with metal ions can create surface defects or oxygen vacancies that possess a high local charge density which increases the adsorption sites for water vapor. The investigated Li^+ , Mg^{+2} , Ba^{+2} , and Sr^{+2} doped hematite based sensors exhibit a low sensitivity to RH.

While, Na^+ doped hematite based sensors show a significant response towards RH and their response and recovery time were quite fast. Further work should be devoted to improve the sensitivity of the sodium doped hematite in order to obtain novel RH sensors and to examine its sensitivity to other gases such as NO_x and H_2 .

Acknowledgment: This work was supported by the Erasmus-Mundus program (EMECW) through grants attributed to A. Afify (Action 2 WELCOME Project, Coordination Office: Politecnico di Torino, Turin, Italy) and M. Ataalla (Medastar Project, Coordination Office: Ovideo University, Madrid, Spain).

REFERENCES

1. Q. Hao, L. Li, X. Yin, S. Liu, Q. Li, T. Wang, *Mat. Sci. Eng. B*, **176**, 600 (2011).
2. R. E. Newnham, *Br. Ceram. Trans.*, **98**, 251 (1999).
3. J. M. Tulliani, C. Baroni, L. Zavattaro, C. Grignani, *Sensors*, **13**, 12070 (2013).
4. K. Carr-Brion, *Moisture Sensors in Process Control*; Elsevier Applied Science Publishers: London, UK, 1986.
5. E. Traversa, *Sens. Actuators B*, **23**, 135 (1995).
6. T. Y. Kim, D. H. Lee, Y. C. Shim, J.U. Bu, S. T. Kim, *Sens. Actuators, B*, **9**, 221 (1992).
7. Y.C. Yek, T.Y. Tseng, *IEEE Trans. Compon. Hybrids Manufact. Technol.*, **12**, 259 (1989).
8. B. M. Kulwicki, *J. Am. Ceram. Soc.*, **74**, 697 (1991).
9. S. S. Nair, M. Mathews, P. A. Joy, S. D. Kulkarni, M. R. Anantharaman, *J. Mag. Mag. Mater.*, **283**, 344 (2004).
10. C. L. Zhu, Y. J. Chen, R. X. Wang, L. J. Wang, M. S. Cao, X. L. Shi, *Sens. Actuators B*, **140**, 185 (2009).
11. W. Weiss, D. Zscherpel, R. Schlögl, *Catal. Lett.*, **52**, 215 (1998).
12. B. C. Faust, M. R. Hoffmann, D.W. Bahnemann, *J. Phys. Chem.*, **93**, 6371(1989).
13. T. Ohmori, H. Takahashi, H. Mametsuka, E. Suzuki, *Phys. Chem. Chem. Phys.*, **2**, 3519 (2000).
14. A. K. Gupta, M. Gupta, *Biomaterials*, **26**, 3995 (2005).
15. E. Comini, V. Guidi, C. Frigeri, I. Riccò, G. Sberveglieri, *Sens. Actuators B*, **77**,16 (2001).
16. A. Y. Lipare, P. N. Vasambekar, A. S. Vaingankar, *J. Magn. Magn Mater*, **279**, 160 (2004).
17. E. L. Miller, D. Paluselli, B. Marsen, R. E. Rocheleau, *Thin Solid Films*, **466**, 307 (2004).
18. F. Zhou, S. Kotru, R. K. Pandey, *Thin Solid Films*, **408**, 33 (2002).
19. Y. S. Hu, A. Kleiman-Shwarsstein, A. J. Forman, D. Hazen, J. N. Park, E. W. McFarland, *Chem. Mater.*, **20**, 3803 (2008).
20. A. Duret, M. Grätzel, *J. Phys. Chem. B.*, **109**, 17184 (2005).
21. F. Le Formal, M. M. Grätzel, K. Sivula, *Adv. Funct. Mater.*, **20**, 1099 (2010).
22. L. Yuberto, M. Ocaña, A. Justo, L. Contreras, A. R. González-Elipe, *J. Vac. Sci. Technol. A*, **18**, 2244 (2000).
23. B. J. Kim, E. T. Lee, G. E. Jang, *Thin Solid Films*, **341**, 79 (1999).
24. A. A. Tahir, K. G. Upul Wijayantha, S. Saremi-Yarahamadi, M. Mazhar, V. McKee, *Chem. Mater.*, **21**, 3763 (2009).
25. J. Savage, *Handbook of Thick Film Technology*, P. J. Holmes, R.G. Loasby Eds., Electrochemical Publications Ltd., Scotland, 1976, p. 51.
26. W. Qu, *Solid State Ionics*, **83**, 257 (1996).
27. M. Viret, D. Rubi, D. Colson, D. Lebeugle, A. Forget, P. Bonville, G. Dhalenne, R. Saint-Martin, G. Andre', F. Ott, *Mater. Res. Bull.*, **47**, 2294 (2012).
28. F. O. Ernst, H. K. Kammler, A. Roessler, S. E. Pratsinis, W. J. Stark, J. Ufheil, P. Nova'k, *Mater. Chem. Phys.*, **101**, 372 (2007).
29. A. Fossdal, M.-A. Einarsrud, T. Grande, *J. Solid State Chem.*, **177**, 2933 (2004).

ИЗСЛЕДВАНЕ НА ЕФЕКТА НА ДОТИРАНЕ С МЕТАЛНИ ЙОНИ НА КРИСТАЛНИ ВЛАГОВИ СЕНЗОРИ НА ОСНОВАТА НА ХЕМАТИТ

А. Афифи¹, М. Атаалла², А. Хюсейн¹, М. Хасан¹, А. Мохамед³, М. Миланова⁴, Ж.М. Тюлиани¹

¹ *Политехнически университет, Факултет по наука и технологии, 10129 Торино, Италия*

² *Химикотехнологичен и металургичен университет, Факултет по материалознание 1758 София, България*

³ *Институт по оптични технологии, Хелиополис, Кайро, Египет*

⁴ *Институт по обща и неорганична химия, БАН*

Постъпила на 24 март, 2015 г. коригирана на 26 октомври, 2015 г.

(Резюме)

Влаговите сензори намират широко приложение, както в индустриалното производство, така и за контрол на околната среда. Доказано е, че хематитът ($\alpha\text{-Fe}_2\text{O}_3$), както недотиран, така и дотиран с различни метални йони показва забележителни свойства като влагов сензор. Целта на настоящето изследване е да се изучи ефекта на дотиране с метални йони (Li^+ , Mg^{+2} , Ba^{+2} , Sr^{+2} и Na^+) на кристални влагови сензори на основата на хематит. Получените материали са охарактеризирани чрез рентенофазов анализ и сканираща електронна микроскопия. Установено е, че Na^+ -дотиран хематит показва висока чувствителност спрямо относителната влажност на въздуха при стайна температура.

Anti-influenza A activity of C-geranyl flavonoids isolated from *Paulownia tomentosa* and *Maclura pomifera*

H. I. Moon^{1,*}, Y. B. Kim², S. K. Kim³

¹Department of Medicinal Biotechnology, Dong-A University, Busan 604-714, Republic of Korea.

²Department of Bioindustrial Technologies, Konkuk University, Seoul 143-701, Republic of Korea

³Department of Animal Science and Technology, Konkuk University, Seoul 143-701, Republic of Korea

Received September 16, 2015, Revised December 16, 2015

C-Geranyl flavonoids have received considerable attention as a simple flavanone with antioxidant, anti-carcinogenic, and anti-inflammatory effects. Influenza virus infection causes thousands of deaths and millions of hospitalizations worldwide every year and the emergence of resistance to anti-influenza drugs has prompted scientists to seek for new natural antiviral materials. In this study, we screened six natural flavonoids from different sources to identify the most potent antiviral flavonoid A/PR/8/34 (H1N1) against human influenza. The two methoxy group flavonoids including 3'-O-methyl-5'-O-methyldiplacone showed potent anti-influenza activity. Therefore, 3'-O-methyl-5'-O-methyldiplacone may be of value as a virus-protector to healthy tissue surrounding influenza A during chemotherapy to obtain better antiviral control with a significant dose.

Key words: C-Geranyl flavonoids, anti-influenza, influenza A, virus-protector.

INTRODUCTION

Influenza viruses affiliated to the *Orthomyxoviridae* family have caused significant morbidity and mortality in humans through epidemic or pandemic diseases [1]. Influenza virus infection remains an important health problem, particularly for babies, young and elderly people, and imposes significant social-economic costs [2]. The main strategies for dealing with influenza involve vaccination and antiviral drugs. Even though annual vaccination is the core preventive strategy for influenza infections, natural antiviral drugs development is necessary to provide additional preventive and therapeutic benefits [3]. *Paulownia tomentosa* (Thunb.) Siebold&Zucc. ex Steud. belongs to the family *Scrophulariaceae* in deciduous trees distributed throughout Korea, China, and Japan. Previous publications have reported polyphenolic compounds, such as iridoids, phenolic glycosides, flavonoids, and phenylethanoids in the MeOH and EtOH extracts of *P. tomentosa*. Iridoids, lignans and flavonoids have been reported as bioactive compounds of *P. tomentosa* [4,5]. Among them, geranylated flavonoids are known as the main bioactive constituents. In fact, most of the substances that have been isolated so far are polar, usually glycosides [6]. Diplacone (6-C-geranyl-eriodictyol), is a prenylated flavonoid, a simple flavanone, among four geranyl flavonoids that have

been known for inhibitory effects on inflammations and/or cancer. Furthermore, we reported that the hydroxylation patterns of the flavonoid B ring play a critical role in the cellular function of the C-geranyl flavonoids group [7]. *Maclura pomifera* commonly called osage orange in deciduous trees including *Cudrania* and other genera of *Moraceae* and flavonoids has been reported as a bioactive compound of *Maclura pomifera*. Among them, prenylated isoflavones are known as the main bioactive constituents. Previous publications have reported polyphenolic compounds, such as osajin and pomiferin in the MeOH and EtOH extracts of *Maclura pomifera* [8]. In this study, we tested the efficacy of the flavonoid B ring of C-geranyl flavonoids against the influenza A virus.

EXPERIMENTS AND EQUIPMENT

Preparation of the C-geranyl flavonoids

Diplacone analogues (PT1~PT4) were kindly provided by Professor Karel Šmejkal of the University of Veterinary and Pharmaceutical Sciences Brno as standards for isolation from *Paulownia tomentosa* [6]. Osajin (PT5) and pomiferin (PT6) were recrystallized from the methanolic solution after preconcentration under vacuum from *Maclura pomifera* [9]. PT1~PT6 were diplacone, 3'-O-methyl-5'-hydroxydiplacone, 3'-O-methyl-5'-O-methyldiplacone, 3'-O-methyl diplacol, osajin and pomiferin. A 50 mM stock solution of PT1~PT6 was made in absolute ethanol, and working dilutions were prepared directly with

* To whom all correspondence should be sent:

E-mail: himun68@dau.ac.kr

dimethyl sulfoxide (DMSO; Sigma-Aldrich). Tamiflu (oseltamivir) was kindly provided by the Immunogenetics Laboratory, Department of Animal Biotechnology, Konkuk University. The control vehicle was culture media containing amounts of DMSO equivalent to those present in PT1~PT6.

Virus, cells, and reagents

Influenza virus A/Puerto Rico/8/34 (A/PR/8/34) was kindly provided by the Immunogenetics Laboratory, Department of Animal Biotechnology, Konkuk University. Madin-Darby canine kidney (MDCK) cells were obtained from the American Type Culture Collection (ATCC CCL-3) and maintained in minimum essential media (MEM; Gibco, USA) supplemented with 10% fetal bovine serum (FBS; HyClone, USA) and 100 U/ml penicillin/streptomycin (Gibco). Before virus infection, MDCK cells were washed with PBS and cultured in virus growth medium (MEM without FBS) supplemented with 10% bovine serum albumin (Sigma-Aldrich, USA), 100 U/ml penicillin/ streptomycin, and 2 µg/ml trypsin TPCK (Gibco).

Cell viability and antiviral assays

MDCK cells were seeded in a 96-well plate at 2×10^4 cells/well for the determination of cell viability. When the cells reached confluency 24 h after seeding, they were washed twice with PBS and treated with the indicated concentrations of flavonoid. After incubation at 37°C for 48 h in a 5% CO₂ incubator, cell viability was determined using an MTT assay kit (Sigma-Aldrich) and an xMark™ spectrophotometer (Bio-Rad, USA) to measure absorbance at 490 nm. For the antiviral assay, cells were infected with A/PR/8/34 virus at 100 TCID₅₀ when they reached 80–90% confluence. Two hours post-infection, the virus-containing medium was replaced with virus-free growth medium containing flavonoids. Cell viability was determined 48 h post-infection by a MTT assay using a spectrophotometer to measure absorbance at 490 nm.

Statistical analysis

The results were expressed as the mean ± SE. Each value represents the mean of at least three independent experiments in each group. The statistical significance of the difference between two cell populations was determined using the two-tailed Student's t-test (Origin software; OriginLab). P values equal to or less than 0.05 and 0.01 were

considered significant. A difference was considered to be significant at $P < 0.05$.

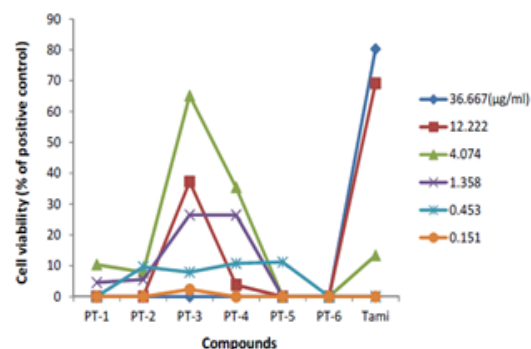


Fig. 1. Screening for antiviral flavonoids with antiviral assays. Structure of the two methoxy group flavonoids showing the positions of the free hydroxyl groups located on the B ring on the PT-3.MDCK cells infected with A/PR/8/34 virus at 100TCID₅₀. Two hours post-infection, the medium was replaced with virus-free growth medium containing C-geranyl flavonoids. The MTT assay was performed 48 h after infection (* $P < 0.05$).

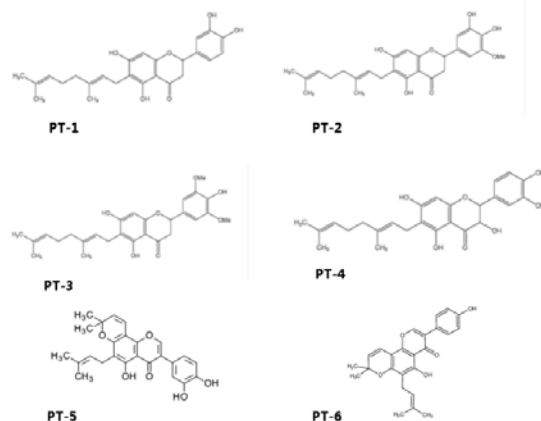


Fig.2. Structures of the PT 1~6

RESULTS AND DISCUSSION

Antiviral effect of the C-geranyl flavonoids. To screen for antiviral flavonoids, we first assessed cell viability after treating cells with the six flavonoids listed in Fig.1. The C-geranyl flavonoids (diplacone, 3'-O-methyl-5'-hydroxydiplacone, 3'-O-methyl-5'-O-methyldiplacone, 3'-O-methyldiplacol, osajin and pomiferin) and Tamiflu increased the viability of MDCK cells (Fig. 1). We then tested the antiviral effect of the six flavonoids, which have free hydroxyl groups positioned at different locations on the B ring (Fig. 2). The 3'-O-methyl-5'-O-methyldiplacone (PT-3) exhibited a more potent antiviral effect than the other C-geranyl group flavonoids (Fig. 1). The antiviral effect of the two methoxy group flavonoids was quantified using the selectivity index (SI), which was calculated using the 50% cytotoxic concentration (CC₅₀) (Fig

1). The results indicate that the two methoxy group 3'-O-methyl-5'-O-methyl-diplacone, PT-3 may be an effective natural antiviral compound.

Acknowledgments: This work was carried out with the support of "Cooperative Research Program for Agriculture Science & Technology Development (Project title: Construction of safety establishment techniques on supplementary feed probiotics and fermented feeds, Project No. PJ010906)" Rural Development Administration, Republic of Korea.

REFERENCES

1. P. Palese, *Nature Med.*, **10**, S82 (2004).
2. G. K. Neumann, Y. Fujii, Kino, Y. Kawaoka, *Proc. Natl. Acad. Sci. U S A*, **102**, 16825 (2005).
3. F. G. Hayden, *Curr. Opin. Infect. Dis.*, **19**, 169 (2006).
4. S. Damtoft, S. R. Jensen, *Phytochemistry*, **35**, 1187 (1994).
5. A.M. Toshihiro, S. Toshihiro, K. Akihito, F. Takashi, T. Makoto, S. Harukuni, K. Yumiko, *Chemistry & Biodiversity*, **9**, 318 (2012).
6. Š.G. Karel, M. Lenka, L. Radek, J. Filip, F. Dagmar, V. Ján, S Hana, *J. Nat. Prod.*, **70**, 1244 (2007).
7. E.R. Lee, G.H. Kang, S.G. Cho, *Recent Pat. Biotechnol.*, **1**, 139 (2007).
8. R.H. Yang, J. Hanwell, R. Zhang, K.A. Meckling, *J Agric. Food Chem.*, **59**, 13328 (2011).
9. D. Giuliano, R.S. Monache, V. Alberto, B. Bruno, M. Barbara, P. Gabriella, P. Cleofe, C. Enrico, *Phytochemistry*, **37**, 893 (1994).

АНТИ-ГРИПНА А-АКТИВНОСТ НА С-ГЕРАНИЛОВИ ФЛАВОНОИДИ, ИЗОЛИРАНИ ОТ *Paulownia tomentosa* И *Maclura pomifera*

Х. И. Мун^{1*}, И. Б. Ким², С. К. Ким³

¹Департамент по медицинска биотехнология, Университет Донг-А, Бусан 604-714, Република Корея

²Департамент по биопромишлени технологии, Университет Конкук, Сеул 143-701, Република Корея

³Департамент по зоология и технология, Университет Конкук, Сеул 143-701, Република Корея

Получена на 16 септември, 2015 г., коригирана на 16 декември, 2015 г.

(Резюме)

С-геранил-флавоноидите са заслужили значително внимание като прости флаванони с антиоксидантна, анти-карциногенна и противовъзпалително действие. Грипните вирусни инфекции причиняват всяка година хиляди смъртни случаи и милиони хоспитализации по света. Необходимостта от противогрипни лекарства е накарала учените на търсят нови природни противовирусни вещества. В тази работа ние подбрахме шест естествени флавоноиди от различни източници и идентифицирахме най-мощния антивирусен флавоноид А/PR/8/34 (H1N1) срещу грипа при хора. Два флавоноида с метокси-групи в молекулите си, включително 3'-О-метил-5'-О-метилдиплакон показва висока анти-грипна активност. Затова 3'-О-метил-5'-О-метилдиплаконът може да бъде полезен като вирус-протектор на здравите тъкани срещу вирусите от грип А по време на хемотерапията за по-добър противовирусен контрол при значителна доза.

Antioxidant activity of polysaccharides from fermented *Meconopsis* Vig. endophytic fungi

L. Yang, D. Hua, W. J. Wang, A. M. Yang, M. Y. Fu

College of Life Science and Engineering, Lanzhou University of Technology, Lanzhou, 730050, China
The Key Lab of Screening, Evaluation and Advanced Processing of TCM and Tibetan Medicine, Gansu Educational Department

Received September 16, 2015, Revised October 17, 2015

Abstract: 24 endophytic fungi were isolated from four kinds of plants of the *Meconopsis* genus: *M. chelidonifolia*, *M. punicea*, *M. henrici* and *M. integrifolia*. Intracellular and extracellular polysaccharides were extracted from the 24 fungi after fermentation. Hydroxyl radical scavenging, DPPH test and reducing power assays were used to screen the antioxidant activity of the polysaccharide samples. The results showed that 8 strains of extracellular polysaccharides produced by fermentation were in amounts higher than 100 mg per 500 ml fermented liquid; the 48 kinds of polysaccharide samples possess low antioxidant activity.

Key words: *Meconopsis*, Endophytic fungi, Polysaccharides, Antioxidant.

INTRODUCTION

Meconopsis is a genus of flowering plants of the family *Papaveraceae*. There are about 40 species grown in China. *Meconopsis integrifolia* and *Meconopsis nepaulensis* are important herbal plants, which have been used in traditional folk medicine for the treatment of cough, detoxication, etc. So far, its endophytic fungi antioxidant activity has not been investigated [1-3]. We isolated 24 fungus strains from four kinds of the *Meconopsis* plant. In order to obtain strains of strong antioxidant activity, we subjected the fungi to liquid fermentation, extracted the polysaccharides and compared their antioxidant activity.

MATERIALS AND METHODS

24 strains of fungi were isolated from *Meconopsis chelidonifolia*, *Meconopsis punicea*, *Meconopsis henrici* Bur. et Franch and *Meconopsis integrifolia* (Maxim.) Franch.

Extraction of polysaccharides

The fungi liquid and thallus was separated and was fermented in 500 ml PD medium, vacuum spin steaming the liquid from 500 to 60 ml. Three volumes of 95% ethanol were added. After the keeping the mixture in a refrigerator at 5-10°C for 12 h, the active polysaccharide fully precipitated. The polysaccharide was washed 2 times with

anhydrous ethanol, acetone and ether, respectively and was dried at 60°C for 2 h. The dry thallus was grinded and passed through a 60 mesh sieve. A 20 fold volume of water was added to extract intracellular polysaccharide at 98°C for 2 h. The procedure was repeated twice and the extracts were merged. Impurities in the protein were removed by the Sevag method.

Analysis of the content of polysaccharides

Add 0.1 mL, 0.2 mL, 0.4 mL, 0.6 mL, 0.8 mL and 1. mL, respectively, of a glucose solution (0.1mg/mL) into tubes, and fill with water until 1 mL. Use 1 mL water as a blank. Add 1 mL phenol solution (5%) and 5 mL concentrated sulfuric acid to each tube. Heat in a boiling water bath for 15 min, then cool to room temperature. Measure the OD value of each tube at 490 nm. In this way the standard curve was prepared (Figure 1). Each sample was analyzed in triple. Polysaccharide content (PD)= $x50\text{mL}/5\text{mg}\times 100\%$

$$y=8.538x-0.027$$

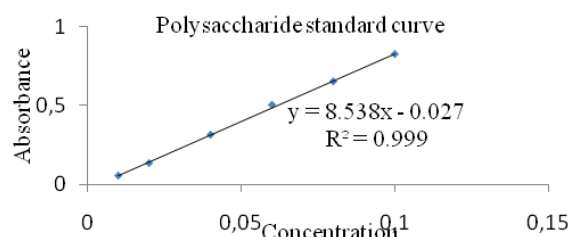


Fig. 1. Polysaccharide standard curve.

* To whom all correspondence should be sent:
E-mail: yanglin-401@163.com

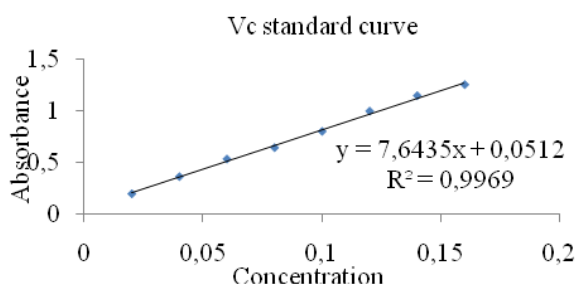


Fig. 2. Vc standard curve.

Screening for antioxidant activity.

Determination of hydroxyl radical scavenging activity

To a polysaccharide sample (1 mg/L) in a test tube add 1 mL FeSO₄ solution (6mmol/L), 1 mL salicylic acid-ethanol solution (6mmol/L), 1 mL sample solution, 1mL 0.1% H₂O₂ and 4 mL

distilled water, shake well in a 37°C water bath for 30 min. Cool to room temperature and measure the absorbance value of each tube at 51 nm.

$$\text{Clearance (\%)} = [1 - (A_{\text{sample}} - A_{\text{contrast}}) / A_{\text{blank}}] \times 100\%$$

DPPH (1,1-diphenyl-2-picrylhydrazyl) free radical scavenging activity

To a polysaccharide sample (1mg/L), in a test tube add 2 ml of 0.025 mg/L ethanol solution of DPPH, shake well at room temperature for 30 min. Measure the absorbance value of each tube at 517 nm [4].

$$\text{Inhibition of DPPH radical (\%)} = [1 - (A_{\text{sample}} - A_{\text{contrast}}) / A_{\text{blank}}] \times 100\%$$

Table 1. Results of endophytic fungi polysaccharide content determination

Sample	QMP(mg)	\bar{A}	PC(%)	QP(mg)	Sample	QMP(mg)	\bar{A}	PC(%)	QP(mg)
YL101	96.6	0.82	99.99	96.6	QL204	121.3	0.38	47.80	58.0
YL101 I	12.0	0.82	99.56	12.0	QL204	4.2	0.57	70.10	2.9
YL201	347.2	0.78	95.34	331.0	QL205	136.2	0.81	98.28	133.9
YL201 I	10.7	0.78	95.35	10.2	QL205	0.010.6	0.08	12.90	0.0014
YL202	390.5	0.13	18.75	73.2	QS102	0.296.4	0.70	86.21	0.26
YL202 I	12.3	0.12	18.28	2.2	QS102 I	0.103.6	0.68	83.05	0.086
YL203	436.5	0.19	25.66	112.0	BS101	423.2	0.25	33.39	141.3
YL203 I	13.7	0.78	95.35	13.1	BS101 I	15.9	0.11	16.88	2.7
YL204	16.5	0.19	25.78	4.3	BS102	54.5	0.41	52.13	28.4
YL204 I	25.4	0.61	75.67	19.2	BS102 I	18.0	0.22	29.88	5.4
YL205	35.1	0.03	7.74	2.7	RL201	196.7	0.53	65.60	129.0
YL205 I	27.1	0.11	16.88	4.6	RL201 I	16.7	0.43	54.06	9.0
YL1 E	36.1	0.25	33.04	11.9	RL202	29.4	0.45	56.58	16.6
YL1 I	7.0	0.14	19.81	1.4	RL202 I	16.6	0.42	52.72	8.8
YL2 E	34.7	0.42	53.07	18.4	RL203	30.8	0.82	99.99	30.8
YL2 I	26.0	0.30	39.36	10.2	RL203 I	28.4	0.82	99.80	28.4
YS101 E	887.4	0.82	99.80	885.6	RL204	574.6	0.12	17.81	102.3
YS101 I	12.2	0.79	96.40	11.8	RL204 I	15.7	0.03	7.51	1.2
YR202	44.5	0.13	18.40	8.2	RS202	55.4	0.62	76.14	42.3
YR202I	31.1	0.09	14.41	4.5	RS202 I	13.4	0.41	51.83	6.9
QL201	212.9	0.16	22.38	47.6	RS203	14.7	0.69	84.22	12.4
QL201 I	26.0	0.05	9.85	2.6	RS203 I	16.5	0.72	87.85	14.5
QL202	68.4	0.33	41.94	28.7	RS302	2302	0.40	50.37	116.0
QL202 I	17.6	0.19	26.25	4.6	RS302 I	34.3	0.68	83.29	28.6

Notes: I intracellular polysaccharide, E extracellular polysaccharide; MP quantity of mixture polysaccharide; PC polysaccharide concentration; QP quantity of polysaccharide; \bar{A} average absorbance of three parallel sets.

Table 2. Results of the determination of hydroxyl radical scavenging activity.

Sample	A _{sample}	A _{contrast}	A _{blank}	Clearance(%)	Sample	A _{sample}	A _{contrast}	A _{blank}	Clearance(%)
YL101 E	0.431	0.001		30.86	QL204 E	0.1213	0.381		20.58
YL101 I	0.564	0.023		13.02	QL204 I	0.0042	0.571		19.29
YL201 E	0.578	0.000		7.07	QL205 E	0.1362	0.812		19.29
YL201 I	0.570	0.012		10.13	QL205 I	0.0106	0.083		7.56
YL202 E	0.538	0.001		13.67	QS102 E	0.2964	0.709		19.13
YL202 I	0.600	0.009		4.98	QS102 I	0.1036	0.682		6.59
YL203 E	0.597	0.004		4.66	BS101 E	0.4232	0.258		11.25
YL203 I	0.534	0.023		17.85	BS101 I	0.0159	0.117		12.22
YL204 E	0.307	0.013		52.73	BS102 E	0.0545	0.418		36.82
YL204 I	0.555	0.016		13.34	BS102 I	0.0180	0.228		14.31
YL205 E	0.433	0.017		33.12	RL201 E	0.1967	0.533		11.58
YL205 I	0.512	0.004		18.33	RL201 I	0.0167	0.434	0.622	3.54
YL1 E	0.543	0.006	0.622	13.17	RL202 E	0.0294	0.456		30.55
YL1 I	0.527	0.016		17.88	RL202 I	0.0166	0.423		8.68
YL2 E	0.547	0.007		22.19	RL203 E	0.0308	0.826		46.30
YL2 I	0.534	0.022		8.20	RL203 I	0.0284	0.825		9.81
YS101 E	0.455	0.007		27.97	RL204 E	0.5746	0.125		7.88
YS101 I	0.575	0.021		10.93	RL204 I	0.0157	0.037		-
YR202 E	0.506	0.012		20.58	RS202 E	0.0554	0.623		-
YR202I	0.520	0.000		16.40	RS202 I	0.0134	0.415		-
QL201 E	0.447	0.013		30.23	RS203 E	0.0147	0.692		7.23
QL201 I	0.530	0.019		17.85	RS203 I	0.0165	0.723		-
QL202 E	0.354	0.004		43.73	RS302 E	0.2302	0.403		26.37
QL202 I	0.568	0.013		10.77	RS302 I	0.0343	0.684		10.61

Note:- no hydroxyl radical scavenging activity

Reducing power assay

Different extracts and a standard (1 mg/mL) in 1 mL of distilled water were mixed with phosphate buffer (2.5 mL, 0.2 mol/L, pH 6.6) and potassium ferricyanide (2.5 mL, 1% w/v) was added to the mixture, which was then centrifuged for 10 min at 3000 r/min. The upper layer of the solution (2.5 mL) was mixed with distilled water (2.5 mL) and FeCl₃ (0.5 mL, 0.1% w/v) and the absorbance was measured at 700 nm on a spectrophotometer [5]. High absorbance value of the reaction mixture indicates a high reductive potential. Draw the standards of different concentration of vitamin C curve. (Figure 2.)

RESULTS AND DISCUSSION

10 kinds of polysaccharide contents are below 20% of the samples. The polysaccharide samples still contain a lot of impurities which should be removed before application. Polysaccharide contents are shown in Table1.

The experimental results showed that the polysaccharide from the fermented liquid of YL204 has the highest activity of hydroxyl radical scavenging (52.73%). Thallus polysaccharide in RL204,RS202 and RS203 has no activity of hydroxyl radical scavenging. Results are shown in Table 2.

The results showed that thallus polysaccharide and polysaccharide from fermented liquid in YL202 have higher DPPH (1,1-diphenyl-2-picrylhydrazyl) free radical scavenging activity (45.50% and 42.78%, respectively). 12 samples displayed no activity (Table 3).

The results showed that all 48 samples have ability of reducing power. YL202 and YL2 have stronger ability equivalent V_c (0.0210 mg/ml and 0.0216 mg/ml, respectively). Results are shown in Table 4.

Table 3. Results of DPPH (1,1-diphenyl-2-picrylhydrazyl) free radical scavenging activity

Sample	A _{sample}	A _{contrast}	A _{blank}	Clearance(%)	Sample	A _{sample}	A _{contrast}	A _{blank}	Clearance(%)
YL101 E	0.315	0.017		18.80	QL204 E	0.308	0.062		32.97
YL101 I	0.473	0.084		-	QL204 I	0.370	0.019		4.36
YL201 E	0.356	0.037		13.08	QL205 E	0.304	0.016		21.53
YL201 I	0.288	0.018		26.43	QL205 I	0.701	0.285		-
YL202 E	0.208	0.008		45.50	QS102 E	0.397	0.103		19.89
YL202 I	0.306	0.096		42.78	QS102 I	0.489	0.113		-
YL203 E	0.292	0.005		21.80	BS101 E	0.302	0.002		18.26
YL203 I	0.287	0.049		35.15	BS101 I	0.449	0.160		21.25
YL204 E	0.458	0.025		-	BS102 E	0.284	0.017		27.25
YL204 I	0.381	0.031		4.63	BS102 I	0.257	0.025		36.78
YL205 E	0.480	0.052		-	RL201 E	0.280	0.010		26.43
YL205 I	0.350	0.017	0.367	9.26	RL201 I	0.380	0.015	0.367	0.54
YL1 E	0.299	0.029		26.43	RL202 E	0.433	0.160		25.61
YL1 I	0.352	0.026		11.17	RL202 I	0.367	0.017		4.63
YL2 E	0.417	0.067		4.63	RL203 E	0.286	0.006		23.71
YL2 I	0.496	0.103		-	RL203 I	0.346	0.022		11.72
YS101 E	0.631	0.152		-	RL204 E	0.303	0.006		19.07
YS101 I	0.366	0.042		11.71	RL204 I	0.401	0.027		-
YR202 E	0.531	0.051		-	RS202 E	0.554	0.177		-
YR202I	0.431	0.038		-	RS202 I	0.664	0.241		-
QL201 E	0.336	0.019		13.62	RS203 E	0.342	0.010		9.54
QL201 I	0.331	0.037		19.89	RS203 I	0.330	0.011		13.08
QL202 E	0.346	0.049		19.07	RS302 E	0.483	0.197		22.71
QL202 I	0.278	0.014		28.07	RS302 I	0.296	0.040		30.25

Notes: - no DPPH free radical scavenging activity

Table 4. Results of reducing power assay.

Sample	A _{sample}	Equivalent V _c (mg/ml)	Samples	A _{sample}	Equivalent V _c (mg/ml)	Sample	A _{sample}	Equivalent V _c (mg/ml)
YL101 E	0.158	0.0140	YS101 E	0.139	0.0115	BS102 E	0.150	0.0129
YL101 I	0.147	0.0125	YS101 I	0.130	0.0103	BS102 I	0.175	0.0162
YL201 E	0.114	0.0082	YR202E	0.142	0.0119	RL201 E	0.191	0.0183
YL201 I	0.129	0.0102	YR202I	0.117	0.0086	RL201 I	0.158	0.0139
YL202 E	0.125	0.0097	QL201 E	0.180	0.0169	RL202 E	0.184	0.0174
YL202 I	0.212	0.0210	QL201 I	0.149	0.0128	RL202 I	0.151	0.0131
YL203 E	0.172	0.0158	QL202 E	0.177	0.0165	RL203 E	0.153	0.0133
YL203 I	0.148	0.0126	QL202 I	0.133	0.0107	RL203 I	0.149	0.0128
YL204 E	0.165	0.0149	QL204 E	0.157	0.0138	RL204 E	0.156	0.0137
YL204 I	0.140	0.0116	QL204 I	0.133	0.0107	RL204 I	0.140	0.0116
YL205 E	0.173	0.0159	QL205 E	0.149	0.0128	RS202 E	0.125	0.0096
YL205 I	0.172	0.0158	QL205 I	0.141	0.0117	RS202 I	0.129	0.0102
YL1 E	0.144	0.0121	QS102 E	0.165	0.0148	RS203 E	0.174	0.0161
YL1 I	0.132	0.0106	QS102 I	0.158	0.0139	RS203 I	0.162	0.0145
YL2 E	0.216	0.0216	BS101 E	0.137	0.0112	RS302 E	0.185	0.0175
YL2 I	0.135	0.0110	BS101 I	0.131	0.0104	RS302 I	0.143	0.0120

From the three different assays used, we got some previous information of endophytic fungi in the *Meconopsis* plant. Especially the endophytic fungi in *Meconopsis chelidonifolia* displayed high quality of polysaccharides and excellent antioxidant potential. Intracellular and extracellular polysaccharides in YL202 fungus possess the highest antioxidant capacity in DPPH free radical scavenging activity. This method is considered as the most accurate method used to assess the antioxidant activity of samples and the widely used assay. Different samples showed inconformable antioxidant capacity in the different assays. Besides, we found that samples' hydroxyl radical scavenging activity is due to more than 30% to extracellular polysaccharide. The results of this study showed that *Meconopsis* endophytic fungi

may become a potential source of natural antioxidants. This first report study provides information and basic work on the bioactivity and compounds of *Meconopsis* endophytes.

REFERENCES

1. Z.Q. Guo, Q. Guo, S.Y. Zhang, C. Li, X.Y. Chai, P.F. Tu, *Biochemical Systematics and Ecology*, **55**, 329 (2014).
2. J. Liu, H. Wu, F. Zheng, W. Liu, F. Feng, N. Xie, *J. Sep. Sci.*, **37**, 2513 (2014).
3. J.S. He, B. Huang, *Journal of Ethnopharmacology*, **141**, 104 (2012).
4. A. Gao, B. Zhao, *China Journal of Chinese Materia Medica*, **38**, 284 (2013).
5. M. Yadav, A. Yadav, J.P. Yadav, *Asian Pac. J. Trop. Med.*, **7**, 256 (2014).

АНТИОКСИДАНТНА АКТИВНОСТ НА ПОЛИЗАХАРИДИ ОТ ФЕРМЕНТИРАНИ *Meconopsis* Vig. ЕНДОФИТНИ ФУНГИ

Л. Янг, Д. Хуа, У. Дж. Уанг, А. М. Янг, М. И. Фу

Колеж за науки за живота и инженерство, Технологичен университет в Ланжоу, Ланжоу 730050, Китай
Ключова лаборатория по скрийнинг, оценка и нови процеси по ТСМ и тибетска медицина, Департамент по образование Гансу

Получена на 16 септември, 2015 г., коригирана на 17 октомври, 2015 г.

(Резюме)

Двадесет и четири ендофитни гъбички (фунги) бяха изолирани от 4 вида растения от рода *Meconopsis*: *M. chelidonifolia*, *M. punicea*, *M. henrici* и *M. integrifolia*. От гъбичките са извлечени вътре-клетъчни и извънклетъчни полизахариди след 24-часова ферментация. Анализи по отстраняване на хидроксилните радикали, DPPH-тест и намалена мощност са използвани за скрийнинг на антиоксидантната активност на образците от полизахаридите. Резултатите показват, че при 8 щамове екстрацелуларните полизахариди, получени при ферментация са повече от 100 mg за 500 ml ферментационна среда; 48 вида полизахариди притежават ниска антиоксидантна активност.

CdSe nanomaterials: kinetics, thermodynamics, antioxidant activity and application to Denim fabric

Ö. Altun*, N. Becenen

Trakya University, Department of Chemistry, 22030 Edirne/TURKEY

Received August 8, 2015, Revised September 10, 2015

For the first time in this study, the kinetics and thermodynamics of the CdSe nanomaterials were determined by spectral measurements. In addition, as a contribution to the literature, antioxidant activity, application to denim fabric and testing of finished fabric for antimicrobial activities of CdSe nanomaterials were investigated. According to absorbance measurements, the activation energy (E_a) and other activation thermodynamic parameters (ΔS , ΔH and ΔG) were determined. The study showed that the process was endothermic and was a nonspontaneous process during activation. The presence of nanoparticles on denim fabric surfaces was confirmed by Scanning Electron Microscope (SEM). The nano CdSe impregnated denim fabric (100% cotton) showed excellent antibacterial activity against *Staphylococcus aureus* and *Escherichia coli*. Additionally, the CdSe nanomaterials demonstrated significant antioxidant activity.

Keywords: CdSe Nanomaterials, Kinetics, Thermodynamics, Antioxidant Activity, Antibacterial Activity

INTRODUCTION

Nanotechnology is regarded as a key technology which will not only influence technological development in the near future, but will also have economic, social and ecological implications. The technology can be used in engineering desired textile attributes, such as fabric softness, durability, breathability, water repellency, fire retardancy and antimicrobial resistance [1]. With the advent of nanotechnology, a new area has developed in the realm of textile finishing. Nano coating on the surface of textiles and clothing enhances the UV blocking, antimicrobial and self cleaning properties of the material [2].

The inherent properties of textile fibers provide room for the growth of micro-organisms. Besides, the substrate structures and chemical processes may induce growth of bacteria. Infestation by bacteria causes cross infection by pathogens and development of odor where the fabric is worn next to skin. With the use of nano sized particles, the number of particles per unit area is increased, and thus antibacterial effects can be maximized [3].

Nanomaterials are tiny particles with particle size mainly below 20 nm, as the optimum size quantity can be attained below this range. It is reported that optimum size variation in CdSe nanocrystals due to quantum confinement is from 1 to 11 nm, which means it contain 10-10.000 atoms.

As the size decreases, number of atoms on the surface may result in loss of optical properties and shift in absorption frequency to the red region of the visible spectrum due to increase in particles [4-6].

CdSe has attracted great interest due to its high photosensitivity, its attractive application to photo conducting cells and the dependence of its properties on size [7]. Traditionally, CdSe nanomaterials have been prepared through a solid-state reaction between elemental cadmium and selenium at relatively high temperatures [8, 9]. Various chemical methods have been introduced to synthesize CdSe nanomaterials, such as solvothermal synthesis [10], laser ablation [11] and hard template [12].

In the previous studies, the effect of CdSe nanomaterials on humans are reported, such as cytotoxic [13], toxic [14], genotoxic [15]. For example, in the study by Young and colleagues [15], the genotoxic effect of CdSe/ZnS nanomaterials is measured in human cancer cells by comet and micronucleus assays. Treatment with CdSe/ZnS nanomaterials resulted in the most severe extent of cell death.

The main of this research study is kinetics, antioxidant activity, application to denim fabric and testing of finished fabric for antimicrobial activities of CdSe nanomaterials. In addition, as a contribution to the literature, for the first time in this study, the kinetics and thermodynamics of the CdSe nanomaterials are determined by spectral measurements.

* To whom all correspondence should be sent:
E-mail: ozlenaltun@yahoo.com, nbeceneni@yahoo.com

EXPERIMENTAL

Material and measurements

All reagents were purchased from commercial sources and used as supplied. UV/Vis spectra were measured with a Shimadzu UV-1700 Pharma spectrophotometer in the 200-800 nm range. Bruker X Flash XRD-6110 and Shimadzu XRD-6000 were employed for the XRD analyses. For the SEM analysis, nano finished samples were mounted on a specimen stub with double sided adhesive tape coated with gold in a sputter coater and examined with a Scanning Electron Microscope (SEM) model ZEIS LEVO LS 10.

Synthesis of the CdSe nanomaterials [16]

30 mg Se and 5 mL of 1-octadecene were mixed and 0.4 mL of trioctylphosphine was added. The solution was stirred. It was warmed as necessary to speed up the dissolution of Se. The stock solution was stored at room temperature. Then, 17.4 mg cadmium acetate and 0.6 mL oleic acid were added in 10 mL octadecene and heated. When the temperature reached 225 °C, 1 mL of selenium solution at the room temperature was transferred into the cadmium solution. The orange-red-brown reaction mixture was cooled to room temperature followed by addition of 10 mL of toluene and was stirred at room temperature for half an hour. The reaction mixture was then centrifuged and washed with the same solvent to obtain orange or brown powder.

Yield (%): 88, UV-Vis (λ /nm): 431 and 458, IR (cm^{-1} /KBr): 2923(sym $-\text{CH}_2$), 2854 (asym $-\text{CH}_2$), 1450 ($\delta_{\text{as}}-\text{CH}_3$), 1600 ($=\text{CH}$), 1700-1720 (C=O), TGA (°C, a rate of 10 °C / min under nitrogen atmosphere): 250-330 (organic capping), 800 (CdSe), XRD (2θ): 23.89473, 25.39343, 41.98555, 45.80425 and 49.67800.

Kinetics and thermodynamics procedure

There is no paper in the literature on the kinetics of the synthesis reaction of CdSe nanomaterials [17-21]. Rate formulas are derived from the experimental data. The rate formula is [22],

$$\ln C / C_0 = -k t, (1)$$

where t is the time, C is the concentration at the time t , C_0 is the concentration $t = 0$, and k is the rate constant.

According to the Beer-Lambert law [23], because absorbance is proportional to the concentration, equation 1 can be rearranged as follows,

$$\ln A / A_0 = -k t \cdot (2)$$

where A is the absorbance at time t , A_0 is the absorbance at $t = 0$.

The activation energy can be determined by the Arrhenius equation [22]:

$$k = A e^{-E_a/RT}, (3)$$

where k is rate constant, A is the frequency factor or the Arrhenius Arrhenius constant, E_a is the activation energy, R is the universal gas constant ($8.314 \text{ JK}^{-1}\text{mol}^{-1}$) and T is absolute temperature.

According to transition state theory, thermodynamic parameters are assigned an activated complex as follows [24]:

$$A = RT / N h e^{\Delta S / R}, (4)$$

$$\Delta H = E_a - RT, (5)$$

$$\Delta G = \Delta H - T\Delta S, (6)$$

where N is the Avogadro constant ($6.022 \times 10^{23} \text{ mol}^{-1}$), h is the Planck constant ($6.626 \times 10^{-34} \text{ Js}$), ΔS is the activation entropy, ΔH is the activation enthalpy, and ΔG is the activation energy or the Gibbs energy of activation.

Antioxidant activity procedure

The antioxidant activity [25-28] of the CdSe nanomaterials was determined in vitro as described with slight modifications as follows: The compounds were serially diluted in DMSO to obtain a concentration range of 1.25–20 mM on a 96 well plate. The reaction mixture consisted of 100 μL of 0.5 mM 2,2-diphenyl-1-picrylhydrazyl radical (DPPH), and 100 μL of each concentration of the test compounds using DMSO as the solvent. For positive control, 2,6-di-tert-butyl-4-methylphenol (BHT) was used at a concentration range of 0.0625–2 mM in methanol. The solvents, DMSO and methanol, were used as blanks. Duplicate experiments were performed. The plates were covered with aluminum foil and kept in the dark for 20 minutes after which the absorbance was read on a Tecan-PC infinite M 200 Pro Plate reader at the absorbance wavelength of 517 nm. The percent antioxidant activity was calculated as follows:

$$\text{Antioxidant (\%)} : 100 \times (A_0 - A_1 / A_0), (7)$$

where A_0 is the absorbance of the blank and A_1 is the absorbance in the presence of the sample or positive control.

General procedure for application to denim fabric

The denim fabric used in the experiments was 100 % cotton, weight was 247 g/m^2 , the warp was dyed blue and the weft yarn wasn't dyed. CdSe nanomaterials were sprayed on denim fabric by using a spray gun [29, 30].

Nanomaterials were applied on the face side of the fabric with concentration 1%, material to liquor ratio 1:20, and acrylic binder 1%. The 100 % cotton denim fabric was cut to a size of 30 x 30 cm. This fabric was coated with CdSe nanomaterials by using a spray gun. The hand spray gun was filled with a dispersion of nanomaterials. The fabric substrate was fixed on a vertical board. The nanomaterials solution was evenly sprayed over the fabric by maintaining a constant distance between the fabric and spray gun nozzle. The excess solution was squeezed using a padding mangle. After padding, the fabric was dried naturally.

Antibacterial activity procedure

To investigate the in vitro antibacterial activity, denim fabric impregnation was done with CdSe nanomaterials separately. Antibacterial test AATCC-100 [31-33] was carried out against *Staphylococcus aureus* (Gram positive bacteria) and *Escherichia coli* (Gram negative bacteria). The percentage reduction of bacteria by the 100 % cotton denim fabric is reported as R,

$$R (\%) = 100 \times (A-B / A), \quad (8)$$

where R is % reduction, A is the number of bacteria on the untreated fabric after 24 hours and B is the number of bacteria on the antibacterial treated fabric after 24 hours.

RESULTS AND DISCUSSION

Kinetics and thermodynamics results

During the measurements of the absorbance, The orange- red-brown reaction mixture was cooled to room temperature followed by addition of 10 mL of toluene and was stirred at room temperature for half an hour. Then, all kinetic experiments were carried out at temperatures of 60, 70, 80 and 90 °C. The absorbance values determined are tabulated in Table 1. Decreasing absorbance values show that the the particle growth is a logarithmic function of time and temperature. At first, the particles grow fast, but then, the growth rate slows down.

Table 1. Absorbance values of CdSe nanomaterials at different temperatures

t (min)	Absorbance(nm)			
	T = 60 (°C)	T = 70 (°C)	T = 80 (°C)	T = 90 (°C)
0	2.383	2.383	2.383	2.383
15	2.207	2.201	2.196	2.191
30	2.137	2.130	2.123	2.116
45	2.086	2.077	2.068	2.060
60	2.043	2.033	2.024	2.014
75	2.007	1.996	1.985	1.975
90	1.974	1.962	1.951	1.939
105	1.944	1.932	1.919	1.908
120	1.917	1.904	1.891	1.879

Rate formulas are derived from the experimental data. If $\ln A$ vs. t is plotted according to equation (2), the slope gives k (Fig. 1). The values of the rate constant k in equation (2) are as follows [t (°C), k (min^{-2})] : 60 °C, 5.11×10^{-3} , 70 °C, 5.29×10^{-3} , 80 °C, 5.45×10^{-3} , and 90 °C, 5.60×10^{-3} . According to Fig. 1., reaction is first order.

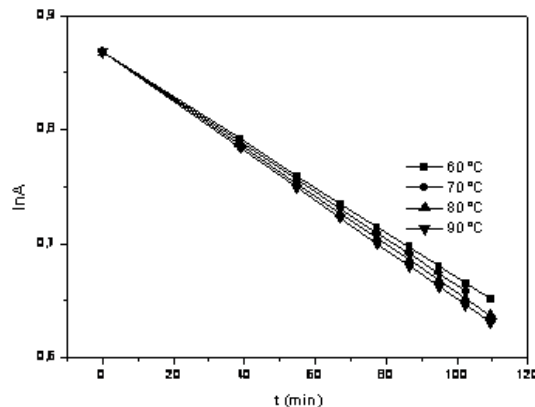


Fig. 1. The plot of $\ln A$ vs, t for the CdSe nanomaterials.

Where $\ln k$ is plotted against the reciprocal of the temperature ($1/T$), $-E_a/R$ represents the slope, and the intercept gives $\ln A$ (Fig. 2). The values of E_a and A were calculated as 3289 J and $1.676 \times 10^{-2} \text{ min}^{-1} = 2.79 \times 10^{-4} \text{ s}^{-1}$, respectively.

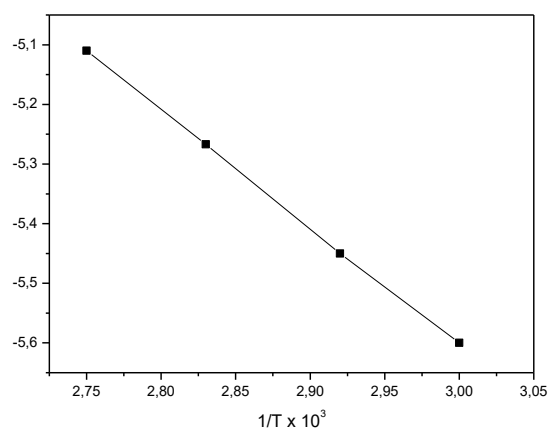


Fig. 2. The plot of $\ln k$ vs, $1/T$ for the CdSe nanomaterials.

Thermodynamic parameters at 60, 70, 80 and 90 °C were calculated by means of equations (4), (5), and (6). These values are given in Table 2.

Table 2. The thermodynamic parameters for the CdSe nanomaterials.

T (°K)	ΔH (J mol ⁻¹)	ΔS (J mol ⁻¹ K ⁻¹)	ΔG (J mol ⁻¹)
333	520.818	-148.022	49812.144
343	437.678	-147.775	51124.503
353	354.538	-147.540	52436.158
363	271.398	-147.307	53743.839

The positive value of ΔH shows that the process is endothermic and a certain amount of energy is received during activation. The negative value of ΔS and the positive value of ΔG show that the process is a nonspontaneous process from a physicochemical respect. The enthalpy and entropy values decrease with increasing temperature while Gibbs free energy values increase, as can be seen from Table 2.

Antioxidant Activity

The antioxidant results of the CdSe nanomaterials are given in Fig.3. According to Fig. 3, the antioxidant activity increased significantly. As reported, the increased antioxidant activity is a result of the electron withdrawing effect of the metal ion which facilitates the release of hydrogen to reduce the DPPH radical. CdSe nanomaterials also show significant free radical scavenging ability when tested against DPPH.

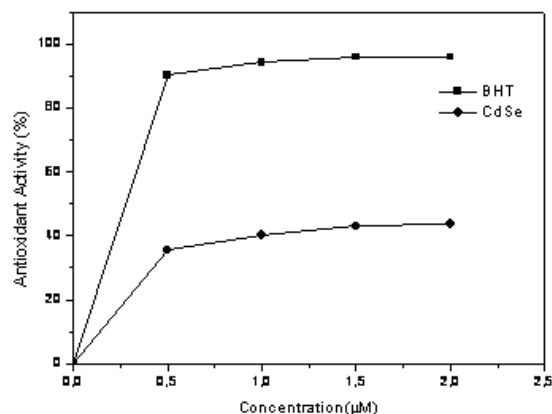


Fig. 3. Percent antioxidant activity of CdSe nanomaterials.

Analysis of the finished denim fabric with CdSe nanomaterials using SEM

The surfaces of the treated fabric were observed by SEM microscopy. Fig. 4 and Fig. 5 the SEM micrographs show SEM image of the untreated 100 % cotton denim fabric and the nano scaled CdSe nanomaterials on 100 % cotton denim fabric samples, respectively. In Fig. 5, the nanoparticles

are well dispersed on the fabric surfaces, although some aggregated CdSe nanomaterials are still visible. The particles size plays a primary role in determining their adhesion to the fabric. It is reasonable to expect that the largest particle agglomerates will be easily removed from the fabric surface, while the smaller particles will penetrate deeper and adhere strongly into the fabric matrix.

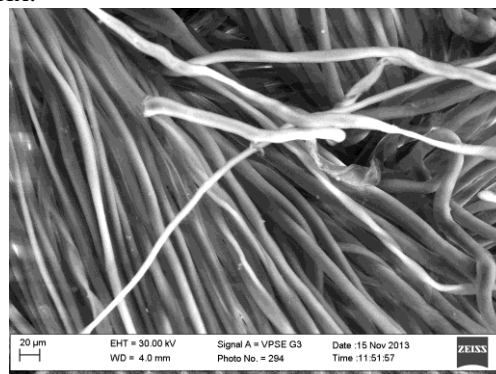


Fig. 4. SEM image of the untreated 100 % cotton denim fabric.

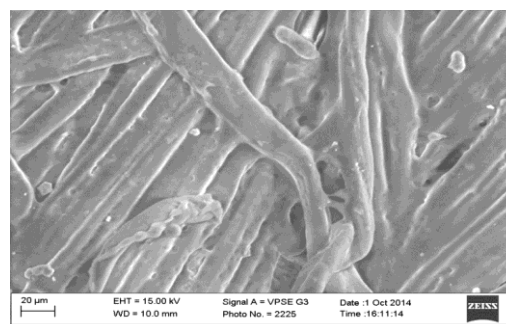


Fig. 5. SEM image of 100 % cotton denim fabric treated with CdSe nanomaterials.

Also in Fig. 6 and Fig. 7 SEM micrographs show that the presence of Cd and Se metals on the denim fabric. Red and green points demonstrate that the presence of Cd metal and Se metal, respectively.

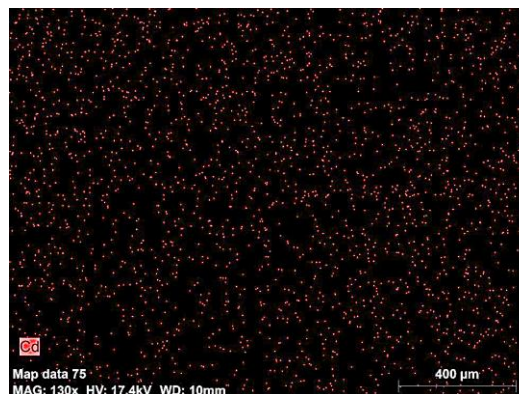


Fig. 6. Colorful SEM image of 100 % cotton denim fabric treated with CdSe nanomaterials. Red points demonstrate that the presence of Cd metal.

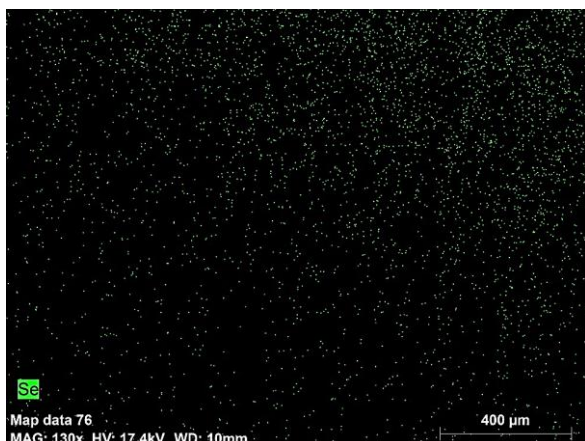


Fig. 7. Colorful SEM image of 100 % cotton denim fabric treated with CdSe nanomaterials. Green points demonstrate that the presence of Se metal

Antibacterial Activity

The results for the AATCC-100 susceptibility tests recorded in Table 2 show that the CdSe nanoparticles have significant antibacterial activity against *Staphylococcus aureus* and show moderate activity against *Escherichia coli*. As a result, CdSe nanomaterials are preferable to other inorganic forms of cadmium because of its higher efficiency in preventing infection.

Table 3. Antibacterial activity of CdSe nanomaterials treated denim fabric.

Fabric sample	<i>Staphylococcus aureus</i>	<i>Escherichia coli</i>
Untreated Denim fabric	No reduction 80.20 %	No reduction 20 %

CONCLUSION

In the present study, the kinetic and thermodynamic parameters such as the activation energy (E_a), the activation entropy (ΔS), the activation enthalpy (ΔH), and the Gibbs energy (ΔG) of CdSe nanomaterials was determined by spectral measurements. The activation energy is found to be approximately 3289 J. The rate constant does not depend on temperature due to the lower activation energy. That is, lower activation energy signifies that the rate constant does not change rapidly with temperature. Finally, the reaction is entropy controlled and the enthalpy contribution changes slightly with change in temperature.

It was shown that the nano-CdSe impregnated on denim fabric showed excellent antibacterial activity against two representative bacteria *Staphylococcus aureus* and *Escherichia coli*. This work provides a simple method for CdSe nano composites and their application onto denim fabric

to impart antibacterial function. Additionally, the nano CdSe demonstrates significant antioxidant activity.

Acknowledgement: We thank to the Trakya University TUBAP-2010/43 for the financial support and dietician Figen ESEN from Osman Gazi University, Faculty of Medicine, Eskişehir/TURKEY for her help.

REFERENCES

1. Y.W.H.C. Wong, W.M. Yuen, M.Y.S. Leung, S.K.A. Ku, *AUTEX Res.J.*, **6**, 1(2006).
2. J. L.Hoon, *Text. Res. J.*, **75**(7), 551 (2005).
3. J.L. Xin, S.Y. Yeo, H.J. Lee, S.H. Jeong, *J. Mater. Sci.*, **38**(10), 2143 (2003).
4. B.K.H. Yen, N.E. Stott, K.F. Jensen, M.G. Bawendi, *Adv. Mater.*, **15**, 1858 (2003).
5. S.J. Rosenthal, J. McBride, S.J. Pennycook, L.C. Feldman, *Surf. Sci. Rep.*, **62**, 111 (2007).
6. V.L. Colvin, M.C. Schlamp, A.V. Alivisatos, *Nature*, **370**, 354 (1994).
7. P. Alivisatos, *Science*, **271**, 933 (1996).
8. C.B. Murray, D.J. Norris, M.G. Bawendi, *J. Am. Chem. Soc. (ACS)*, **124**, 8706 (1993).
9. Z.A. Peng, X.G. Peng, *J. Am. Chem. Soc. (ACS)*, **124**, 3343 (2002).
10. Y. Xie, W.Z. Wang, Y.T. Qian, X.M. Liu, *J. Solid State Chem.*, **147**, 82 (1999).
11. C.M. Rouleau, D.H. Lowndes, *App. Surf. Sci.*, **418**, 127 (1998).
12. Q. Yang, K. Tang, C. Wong, Y. Qian, *Mater. Lett.*, **57**, 3508 (2003).
13. C. Kirchner, T. Liedl, S. Kudera, T. Pellegrino, A.M. Javier, H.E. Gaub, S. Stoilzle, N. Fertig, W.J. Parak, *Nano Lett.*, **5**(2), 332 (2005).
14. L. Wang, D.K. Nagesha, S. Selvarasah, M.R. Dokmeci, R.L. Carrier, *J. Nanobiotechnol.*, **6**, 11 (2008).
15. Y.J. Choi, Y.J. Kim, J.W. Lee, Y. Lee, Y. Lim, H.W. Chung, *J. Nanosci Nanotechnol.*, **12** (3), 2160 (2012).
16. E.M. Boatman, G.C. Lisensky, *J. Chem. Edu.*, **82**(11), 1697 (2005).
17. K.B. Gavazov, M. Türkyılmaz, Ö. Altun, *Bulg. Chem. Commun.*, **40**(1), 65 (2008).
18. O. Altun, E. Dolen, M. Pekin, H. Aboul-Enein, *Ins. Sci. Technol.*, **31**(1), 15 (2003).
19. O. Altun, H. Akbaş, E. Dolen, *Spectrochim. Acta Part A*, **66**(2), 499 (2007).
20. O. Altun, S. Bilcen, *Spectrochim. Acta Part A*, **75**(2), 789 (2010).
21. O. Altun, C. Küçüktepe, O. Yörüük, A.F. eyizoğlu, *Synt React. Inorg.Metal-Org. Nano-Metal Chem.*, **43**(3), 221 (2013).
22. K.J. Laidler, *Chemical Kinetics*, Harper & Row Publishers, New York, 1987.
23. H.W. Dudley, I. Fleming, *Spectroscopic Methods in Organic Chemistry*, Mc Graw-Hill Book Co Ltd, London, 1987.

24. J.W. Moore, R.G. Pearson, Kinetic and Mechanism, John Wiley&Sons, New York, 1981.
25. H. Lignert, K. Vallentin, C.Eriksson, *J. Food Process. Preserv.*, **3**, 87 (1979).
26. K. Shimada, K. Fujikawa, K. Yahara, T. Nakaura, *J. Agric. Food Chem.*, **40**, 945 (1992).
27. B. Tanti, A.K. Buragohain, L. Guring, D. Kakati, A.K. Das, S.P. Borad, *IJNPR*, **1**(1), 17 (2010).
28. A. Choudhary, R. Sharma, M. Nagar, M. Mohsin, H.S. Meena, *J. Chil. Chem. Soc.*, **56**(4), 911 (2011).
29. K.L. Edwards, *Mater. Des.*, **19**(1), 1 (1998).
30. N. Gokarneshan, P.P. Gopalakrishnan, B. Jeyanthi, *Int. J. Basic Appl. Chem. Sci.*, **2**(2), 8 (2012).
31. D.T.W. Chun, G.R. Gamble, *J. Cotton Sci.*, **11**, 154 (2007).
32. R. Rajendran, C. Balakumar, J. Kalaivani, R. Sivakumar, *J. Text. Apparel Technol. Manage*, **7**(2), 1 (2011).
33. S. Agnihotri, S. Mukherji, *RSC Adv.*, **4**, 3974 (2014).

НАНОМАТЕРИАЛИ ОТ CdSe: КИНЕТИКА, ТЕРМОДИНАМИКА, АНТИОКСИДАНТНА АКТИВНОСТ И ПРИЛОЖЕНИЕ В DENIM-ТЪКАНИТЕ

Й. Алтун*, Н. Бедженен

Тракийски университет, Департамент по химия, 22030 Одрин, Турция

Постъпила на 8 август, 2015 г.; коригирана на 10 септември, 2015г.

(Резюме)

За пръв път са изследвани кинетиката и термодинамиката на наноматериали от CdSe с помощта на спектрални методи. Допълнително са изследвани антиоксидантната и антимикуробната активност на CdSe – наноматериалите нанесени върху denim-текстил. Определени са активиращата енергия (E_a) и други термодинамични параметри (ΔS , ΔH и ΔG) с помощта на измервания на абсорбционни спектри. Изследванията показват, че процесът е ендотермичен и не е спонтанен по време на активирането. Наличието на наночастици върху denim-тъканите е потвърдено със сканираща електронна микроскопия (SEM). Импрегнираните с наночастици от CdSe denim-тъкани (100% памук) показват отлична антибактериална активност спрямо бактериите *Staphylococcus*.

Effect of 6-hydroxy-7,4'-dimethoxyflavone on antidiabetic effects in normal and streptozotocin-induced diabetic rats

H. I. Moon^{1,*}, D. W. Kim², S. K. Kim³, S. H. Seo¹

¹Department of Medicinal Biotechnology, Dong-A University, Busan 604-714, Republic of Korea.

²National Institute of Animal Science, RDA, Wanjugun 565-851, Republic of Korea

³Department of Animal Science and Technology, Konkuk University, Seoul 143-701, Republic of Korea

Received September 4, 2015; Revised October 25, 2015

Kaempferia parviflora is a famous endemic Thailand species of the family *Zingiberaceae*. MeOH extract of *Kaempferia parviflora* was consecutively partitioned with organic solvents such as CHCl₃, EtOAc and BuOH. CHCl₃ fractions were diluted with distilled water and extracted with n-hexane and CH₂Cl₂. Five methoxyflavone compounds were isolated from the CH₂Cl₂ fractions with column chromatography. The structures of the isolated compounds were identified as 3,5,7,3',4'-pentamethoxyflavone (KP1), 5,7-dimethoxyflavone (KP2), 5,7,4'-trimethoxyflavone (KP3), 3,5-dihydroxy-3'-methoxyflavone (KP4) and 6-hydroxy-7,4'-dimethoxyflavone (KP5) by ¹D H-NMR spectral analysis and comparison of spectral data with literature values. KP5 showed significant hypoglycemic activity in streptozotocin-induced diabetic rats for 28 days. It significantly decreased the serum glucose and triglycerides while it increased the serum insulin in diabetic rats but not in normal rats (p < 0.05; at doses of 50, 100 and 150mg/kg for 28 days). It had no effect on C-peptide (ECLIA). Further structure-activity relationships of position 6 in the aromatic ring B will be reported in due course.

Keywords: *Kaempferia parviflora*, α -glucosidase inhibitory activity, streptozotocin-induced diabetic rats, methoxyflavone

INTRODUCTION

Kaempferia parviflora (KP) is a species of the genus *Kaempferia* which involves 35 species and belongs to the family of *Zingiberaceae*. There are indigenes in Thailand which are spread in Loei, Pitsanulok and Phetchabun. They are called kra-chai-dum or Thai black ginger [1]. KP is a plant that grows relatively low to the ground. It is a understory plant which has short fleshy rhizomes dark purple in colour, tuberous roots, straight and curved leaf ends and white with violet small blooms under the leaves [2]. KP extracts in ethanol or methanol are effective to visceral fat accumulation, hyperinsulinemia, glucose intolerance, hypertension, diabetes, antiobesity, peripheral neuropathy, anti-gastric ulcer and Alzheimer's disease [3]. 5,7,4'-Trimethoxyflavone and 5,7,3'4'-tetramethoxyflavone display antiplasmodial activity; 3,5,7,4'-methoxyflavone has antifungal and low-level antimycobacterial activity [4]; 5,7-dimethoxyflavone affects multidrug resistance associated proteins (MRP) - mediated transport in A549 cells [5]. Among the structures, the 5,7-methoxy groups lead to significant inhibitory activity while the 5-hydroxy

group decreases the inhibitory activity. Non-insulin-dependent diabetes mellitus (NIDDM) is one of the main adult diseases [6]. Type 1 leads to destruction of the pancreatic langerhans β -cells producing insulin. Type 2 is a secretory decrease in insulin from pancreatic langerhans β -cells or lowering of insulin resistance due to excess glucose absorption [7]. Hyperglycemia and hyperlipidemia are involved in the development of microvascular and macrovascular complications of diabetes, which are the major causes of morbidity and mortality due to diabetes [8]. The current study describes the isolation of five methoxyflavones from *Kaempferia parviflora*. In the context of our natural product chemistry program dealing with the development of new potent antidiabetic agents, we examined the 6-hydroxy-7,4'-dimethoxyflavone as a lead for novel antidiabetic agents.

MATERIALS AND METHODS

General experimental procedures

¹H NMR spectra were recorded with an Agilent MR 400 DD2 400MHz spectrometer in CDCl₃ and DMSO-*d*₆ solution and chemical shifts (δ) are reported as parts per million (ppm). Coupling constant (J) is reported in hertz (Hz). Melting points were measured using a Fisher-Johns melting point

* To whom all correspondence should be sent:
E-mail: himun68@dau.ac.kr

apparatus and are uncorrected. Column chromatography was conducted using silica gel 60 (40-63 and 63-200 μm particle size, Merck) and RP-18 (40-63 μm particle size, Merck)

Plant Material

Kaempferia parviflora rhizomes were kindly provided by Professor Kim Soo-Ki from the Animal Sciences Department of Konkuk University. The rhizomes of *Kaempferia parviflora* were identified by Prof. Hyung-In Moon. A voucher specimen (No.2012-0405) has been deposited in the Herbarium of the Dong-A University (Busan, South Korea).

Extraction and fractionation

The rhizomes of *Kaempferia parviflora* (5 kg) were sliced. Reflux extraction was performed with 9 L of MeOH, three times at 5°C. The MeOH extracts (198 g) were combined and concentrated *in vacuo* at 40°C. The MeOH extract was diluted with distilled water (0.9 L) and then partitioned with CHCl_3 (0.6 L \times 3). CHCl_3 -soluble part was evaporated (84.3 g) and diluted with distilled water (1L). CHCl_3 -soluble part, diluted with distilled water, was partitioned with n-hexane (0.9 L \times 3), CH_2Cl_2 (0.7 L \times 3), EtOAc (0.8 L \times 3) and BuOH (0.8 L). The CH_2Cl_2 extract (49 g) was separated by silica gel column chromatography. A mobile gradient (from 30:1 to 0:1 v/v) was used and 12 fractions were obtained (K1-K12). The mobile phase for K1 to K8 was CHCl_3 :MeOH (30:1 v/v). For K9 CHCl_3 :MeOH (10:1 v/v) was used. For K10 and K11 CHCl_3 :MeOH (5:1 v/v) was used. For K12 CHCl_3 :MeOH (1:1 v/v) was used. All fractions were recrystallized at -20°C from MeOH. Each recrystallized fraction was separated by filtering. The recrystallized compounds were dried at room temperature and the MeOH-soluble fractions were evaporated at 40°C. KP1 (5.6 g) was recrystallized from the K5 fraction. KP2 (3 g) was recrystallized from the K6 fraction. KP3 (2.7g) was recrystallized from the K4 fraction. K2 crystal fraction was separated by silica gel column chromatography. KP4 (2.16 g) was isolated from the K2 crystal fraction (6 g) with silica gel column chromatography using CHCl_3 as mobile phase. K8 crystal fraction (288 mg) was separated by Sephadex-LH20 column chromatography using 100% MeOH as mobile phase. KP5 was obtained from the K8 crystal fraction.

KP1: Bright yellow powder, $^1\text{H-NMR}$ (CDCl_3 , 300MHz) δ : 7.82 (1H, d, 5'-H), 6.99(1H, d, 6'-H),

6.62 (1H, s, 2'-H), 6.56 (1H, s, 6-H), 6.37 (1H, s, 8-H), 3.95 (3H, s, OCH_3), 3.91 (3H, s, OCH_3), 3.88 (3H, s, OCH_3), 3.77 (3H, s, OCH_3), 3.49 (3H, s, OCH_3)

KP2: Bright yellow powder, $^1\text{H-NMR}$ (CDCl_3 , 300MHz) δ : 7.84 (2H, d, 2' and 6'-H), 7.51 (2H, t, 4'-H), 7.00 (2H, t, 3' and 5'-H), 6.70 (H, s, 3-H), 6.57 (H, s, 6-H), 6.39 (H, s, 8-H), 3.96 (3H, s, OCH_3), 3.92 (3H, s, OCH_3)

KP3: Bright yellow powder, $^1\text{H-NMR}$ (CDCl_3 , 300MHz) δ : 7.71 (2H, d, 2' and 6'-H), 6.98 (2H, d, 3' and 5'-H), 6.77 (1H, s, 3-H), 6.51 (1H, s, 6-H), 6.35 (1H, s, 8-H), 3.96 (3H, s, OCH_3), 3.91 (3H, s, OCH_3), 3.88 (3H, s, OCH_3)

KP4: Yellow powder, $^1\text{H-NMR}$ (CDCl_3 , 300MHz) δ : 12.75 (1H, s, OH), 12.60 (1H, s, OH), 8.09 (1H, t, 5'-H) 7.92, (1H, d, 6'-H), 7.57 (1H, s, 2'-H), 7.54 (1H, d, 4'-H), 6.53 (1H, d, 8-H), 6.48 (1H, d, 6-H), 6.40 (1H, t, 7-H), 3.90(3H, s, OCH_3)

KP5: Yellow powder, $^1\text{H-NMR}$ (CDCl_3 , 300MHz) δ : 10.20 (1H, s, OH), 7.88 (2H, d, 2' and 6'-H), 6.90 (2H, d, 3' and 5'-H), 6.83 (1H, s, 3-H), 6.58 (1H, s, 5-H), 6.50 (1H, s, 8-H), 3.89 (3H, s, OCH_3), 3.82 (3H, s, OCH_3)

α -Glucosidase inhibitory activity assay

The α -glucosidase inhibitory activity of compounds KP 1~5 was measured. The inhibitory assay was done by the chromogenic method with a slight modification. α -Glucosidase from *saccharomyces cerevisiae* (10 $\mu\text{g/ml}$, 14 U/mg, sigma) was dissolved in 100 mM phosphate buffer (PB, pH 7.0) containing 0.2% BSA and 0.02% NaN_3 and was used as an enzyme solution. 4-Nitrophenyl- α -D-glucopyranoside (Sigma, 5 mM) in the same buffer (pH 7.0) was used as a substrate solution. The enzyme solution (90 μl) contained concentrations of 0, 20, 40, 80, 100 μM of KP compounds, respectively, (18 μl) of the tested materials was mixed in a well of a microtiter plate and measured for titer (415 nm) at zero min with a microplate reader. After incubation for 5 min, the substrate solution (90 μl) was added and the reaction was carried out at room temperature for 5 min. The increase in absorbance from zero time was measured.

Animals

Adult male Wistar rats with body weights of 200-250 g were purchased from the Korea SAMTAKO CO., LTD (Kyunggido, South Korea), housed in specific pathogen-free facilities and provided with autoclaved water and standard food. The animals were housed at a controlled temperature (20-22°C) and relative humidity (55%-

59%), with a normal 12-hour light-and-dark cycle. All experiments conducted on mice were in accordance with the guidelines for the care and use of laboratory animals approved by Dong-A University.

Experimental induction of diabetes in rats

Male adult Wistar rats were injected with streptozotocin (STZ). Streptozotocin was dissolved in saline immediately before use and injected intraperitoneally (i.p.) in a single dose of 250 mg/kg. Five days after injection, rats with fasting blood glucose higher than 180 mg/dL were used for the experiments. Ten rats were used in each experiment. Each animal was used once. The food was removed from the cages 12 hours before testing. Streptozotocin (purity 99%) was purchased from Sigma Co. The volume of the above three doses was kept constant at 1 mL.

Drug administration

KP1~5 were suspended in acacia gum with saline and administered orally through orogastric tubes at doses of 50, 100 and 150 mg/kg body wt. The volume of the above three doses was kept constant at 1 mL.

Experimental design

In the experiment, a total of 60 rats (50 diabetic rats, 10 normal rats) were used. Diabetes was induced in rats 5 days before starting the treatment. The rats were divided into nine groups, each group involving six rats.

Group I: Normal control rats administered i.p. 1 mL acacia gum with saline daily, for 28 days using an intragastric tube.

Group II: Control drug rats administered i.p. 1 mL acacia gum with Metformin (250 mg/kg) daily, for 28 days using an intragastric tube.

Group III: Diabetic control rats administered i.p. 1 mL acacia gum with STZ (250 mg/kg), for 28 days using an intragastric tube.

Group IV: Diabetic control rats administered i.p. KP5 (50 mg/kg bw) in 1 mL acacia gum with saline daily, for 28 days using an intragastric tube.

Group V: Diabetic rats administered i.p. KP5 (100 mg mg/kg bw) in 1 mL acacia gum with saline daily, for 28 days using an intragastric tube.

Group VI: Diabetic rats administered i.p. KP5 (150 mg mg/kg bw) in 1 mL acacia gum with saline daily, for 28 days using an intragastric tube.

Biochemical assays

Biochemical assays of male adult Wistar rats were performed using a modified method of Eidi

[9]. After 28 days of treatment, blood samples were drawn from the heart. Serum glucose, insulin, triglycerides and C-peptide levels were determined. The serum insulin was estimated by using a radioimmunoassay kit (Diasorin, Italy) and the triglycerides by the method of Rifai [10].

Statistical analysis

All data were expressed as mean \pm SEM. Statistical analysis was carried out using one way ANOVA followed by the Tukey post hoc test. The criterion for statistical significance was $p < 0.05$.

RESULTS AND DISCUSSION

The current study describes the isolation of five methoxyflavones from *Kaempferia parviflora*. Molecular structures were determined through a combination of spectroscopic analyses, including ^1H nuclear magnetic resonance (NMR), mass spectrometry (MS) data, and literature data. The effects of the isolated compounds (0-100 μM) on the inhibition of the α -glucosidase based assay are reported here. Compound KP1 was obtained as a bright yellowish amorphous powder. It was detected as a bright yellow color on TLC when visualized with 5% sulfuric acid spray reagent. In the ^1H NMR (CDCl_3) spectra of KP1, typical aromatic ring signals were observed, as well as five methoxy singlet signals of the 3,5,7,3',4' position methoxy groups. The five singlet signals at δ 3.49 to δ 3.95 indicated methoxy groups. Compound KP2 was obtained as a yellow amorphous powder. It was detected as a bright yellow color on TLC when visualized with 5% sulfuric acid spray reagent. In the ^1H NMR (CDCl_3) spectra of KP2 aromatic ring signals and two methoxy signals were observed. Two methoxy signals were indicated at δ 3.92 and δ 3.96. Compound KP3 was obtained as a yellow-white amorphous powder. It was detected as a bright yellow color on TLC when visualized with 5% sulfuric acid spray reagent. ^1H NMR (CDCl_3) spectra of KP3 indicated the presence of 5,7,4' substituted methoxy group protons at δ 3.88, δ 3.91 and δ 3.96 signals and typical aromatic ring signals were observed at δ 8.1 to δ 6.3. Compound KP4 was obtained as a bright yellow amorphous powder. It was detected as a yellow color on TLC when visualized with 5% sulfuric acid spray reagent. ^1H NMR (CDCl_3) spectra of KP4 indicated aromatic ring signals, two hydroxyl and one methoxy signal. Two hydroxy signals and one methoxy signal were indicated at δ 12.60, δ 12.75 and δ 3.90. Two hydroxy groups were indicated at 3,5 position and one methoxy group at 3' position. Compound KP5 was obtained as a white amorphous powder. It was

detected as a bright yellow color on TLC when visualized with 5% sulfuric acid spray reagent. In the ^1H NMR (CDCl_3) spectra of KP5, typical aromatic ring signals, as well as two methoxy singlet signals at the 7,4' position and one hydroxyl singlet signal at the 6 position were observed. Two methoxy singlet signals and one hydroxyl singlet signal were indicated at δ 3.82, δ 3.89 and δ 10.20. KP1~5 compounds were dissolved in DMSO and the total volume was 196 μl for all concentrations (Fig. 1).

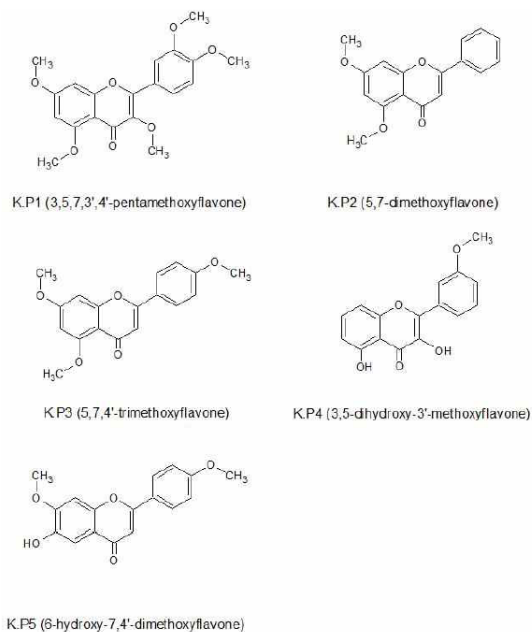


Fig. 1. Structures of KP1~5.

KP2~5 were confirmed to cause a dose dependent increase in α -glucosidase inhibitory activity. KP1 did not cause a dose dependent increase in α -glucosidase inhibitory activity. KP2 and KP3 showed lower dose inhibitory activity from 30 to 40% at 100 μM concentration, KP4 and KP5 showed a high inhibitory activity to 55% and 78%, respectively. KP5 inhibitory activity was confirmed to rapidly increase from 80 μM concentration, and the inhibitory activity of KP4 was highest (57%) at the 80 μM concentration (Fig. 2).

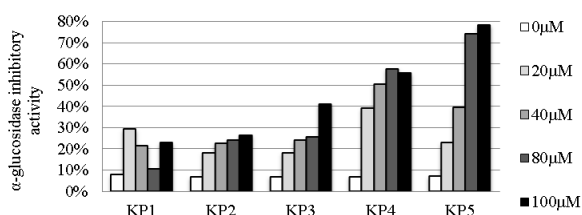


Fig. 2. α -Glucosidase inhibitory activity of KP1~5 with the inhibitory assay done by the chromogenic

method with a slight modification. The increase in absorbance from zero time was measured.

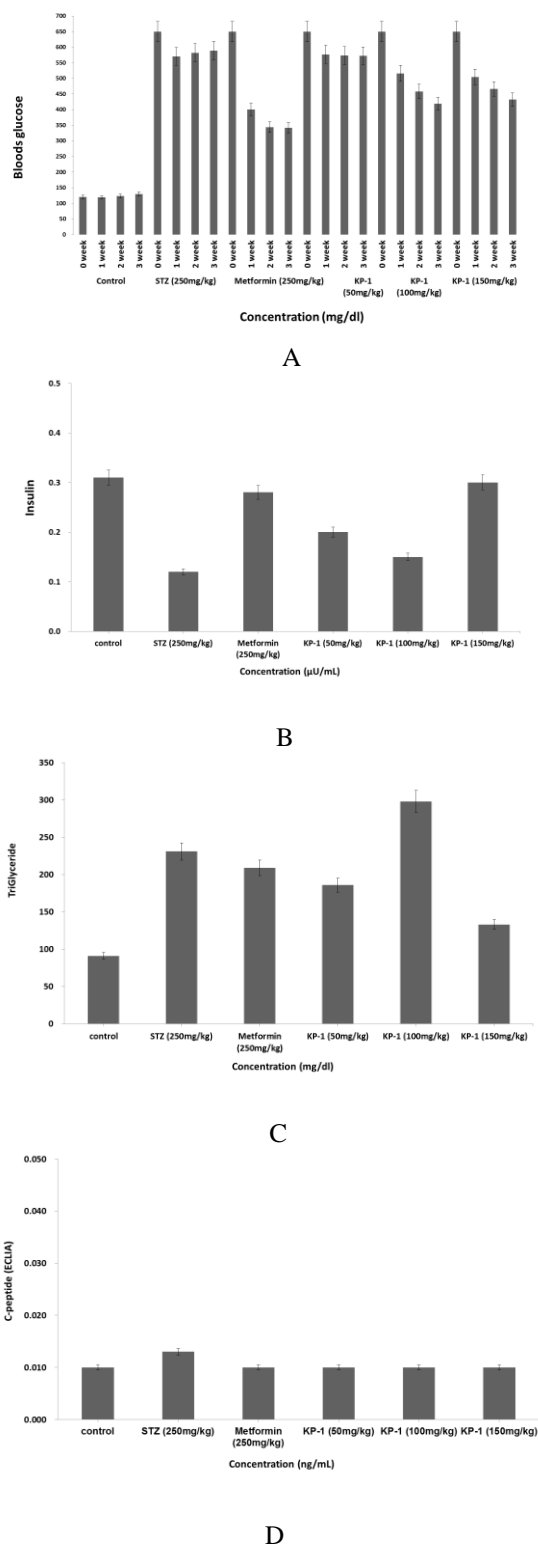


Fig. 3. Effect of 6-hydroxy-7,4'-dimethoxyflavone (KP-5) on the mean values of serum glucose (A), insulin (B), triglycerides (C) and C-peptide (D) after 28 days of treatment (50, 100, 150 mg/kg bw/day, i.p.). *The criterion for statistical significance was $p < 0.05$.

The 6-hydroxyl group of baicalein (5,6,7-trihydroxyflavone) was important to α -glucosidase inhibitory activity; flavones which lack a hydroxyl group on any of positions 5, 6, or 7, showed no activity [11]. KP4 and KP5 seem to be depending on the presence of the hydroxyl position in the flavone structure. We have found that the MeOH extract of *Kaempferia parviflora* has α -glucosidase inhibitory activity. KP5 significantly inhibited the α -glucosidase inhibitory activity in a dose-dependent manner. Figure 3 shows the effects of KP5 on serum glucose, insulin, triglycerides and C-peptide in diabetic rats.

The results showed that serum glucose and triglycerides of diabetic rats increased while serum insulin decreased, when compared with normal rats. The administration of KP5 at doses of 50, 100 and 150 mg/kg body wt tended to bring serum glucose ($p < 0.05$), insulin ($p < 0.05$), triglycerides ($p < 0.05$) and C-peptide ($p < 0.05$) significantly toward normal values, while normal rats did not exhibit any significant alterations in these parameters during the experiment. The 150 mg/kg bw treatment groups were found to be more effective than the 50 and 100 mg/kg bw. The administration of KP5 did not change C-peptide levels in normal and diabetic rats. The results indicated that KP-5 (150 mg/kg bw) treatment significantly decreased serum glucose and triglycerides while it increased the serum insulin levels in treated diabetic rats compared with the control diabetic rats. The results also showed that KP-5 (150 mg/kg bw) treatment caused a significant decrease in the level of serum in diabetic rats. This may be due to a metabolic disturbance in diabetes reflected in the high activities of xanthine oxidase, lipid peroxidation and increased triglycerides. As a result, KP-5 (150 mg/kg bw) is a potential antidiabetic agent for the tested streptozotocin-induced diabetes.

CONCLUSION

We have found that KP-5 (150 mg/kg bw) showed decreasing antidiabetic potency *in vivo*. Further study on the mode of action of position 6 on ring B is under progress. Taken together, our findings provide important information on the

structural features that influence the functional activities of this class of compounds and offer new possibilities for further explorations to improve potency from damage of STZ-induced diabetic rats. It is shown that KP-5 may be of use as an anti-diabetic agent.

Acknowledgments: This work was carried out with the support of "Cooperative Research Program for Agriculture Science & Technology Development (Project title: Construction of safety establishment techniques on supplementary feed probiotics and fermented feeds, Project No. PJ010906)" Rural Development Administration, Republic of Korea.

REFERENCES

1. T. Supinya, S. Sanan, K. Sopa, *J Ethnopharmacol.*, **116**, 191 (2008).
2. P. Denpong, N. Junya, Y. Ryoko, M. Teruo, S. Khaetthareeya, O.R. Bung, Y. Chavi, T. Mikihisu, *J Pharm Sci.*, **96**, 223 (2007).
3. C. Rujjanawate, D. Kanjanapothi, D. Amornlerdpison, S. Pojanagaroon, *J Ethnopharmacol.*, **102**, 120 (2005).
4. Y. Chavi., P. Khanchara, D. Supawadee, W. Varima, K. Prasat, *Fitoterapia*, **75**, 89 (2003).
5. P. Denpong, N. Junya, M. Chie., F. Kyoko, S. Khaetthareeya, S. Bung-orn, Y. Ryoko, T. Mikihisu, *Eur. J. Pharmacol.*, **566**, 67 (2007).
6. M. Toshiro, U. Tetsuya, O. Tomoyuki, S. Koichi, T. Norihiko, M. Kiyoshi. *J. Agric. Food Chem.*, **49**, 1948 (2001).
7. W. Jun, K. Jun, K. Hideyuki, N. Ryoya, *Biosci. Biotechnol. Biochem.*, **61**, 177 (1997).
8. H. Hans-Peter, W. Hans, E.R.I Egon, B.M. Beatrice, U. AndreQa, S. Giorgio, *The J. Biol. Chem.*, **257**, 4522 (1982).
9. A. Eidi, M. Eidi, R. Darzi, *Phytotherapy Res.*, **23**, 347 (2009).
10. N. Rifai., P.S. Bachorik, J.J. Albers, in: Burtis CA, Ashwood ER (eds) Tietz Textbook of clinical chemistry. 3rd ed. Philadelphia: WB Saunders, 1999, p. 809.
11. G.A.O. Hong, N. Tetsuo, K. Jun, K. Takanori, *Biosci. Biotechnol. Biochem.*, **68**, 369 (2004).

ЕФЕКТ НА 6-ХИДРОКСИ-7,4'-ДИМЕТОКСИФЛАВОН ВЪРХУ АНТИДИАБЕТИЧНИТЕ ПРОЯВИ ПРИ НОРМАЛНИ ПЛЪХОВЕ И ТАКИВА С СТРЕПТОЗОТОЦИН-ИНДУЦИРАН ДИАБЕТ

Х. И. Мун^{1*}, Д. В. Ким², С. К. Ким³, С. Х. Сео¹

¹ Департамент по медицинска биотехнология, Университет Донг-А, Бусан 604-714, Република Корея

² Национален институт по зоологически науки, Ванджугун 565-851, Република Корея

³ Департамент по животновъдни науки и технологии, Университет Конкук, Сеул 143-701, Република Корея

Получена на 4 септември, 2015 г.; коригирана на 25 октомври, 2015 г.

(Резюме)

Caempferia parviflora е известно ендемично тайландско растение от семейство *Zingiberaceae*. Неговите метанолови екстракти последователно се разделят с органични разтворители, като CHCl_3 , EtOAc и BuOH. Хлороформните фракции се разреждат с дестилирана вода и се екстрахират с n-хексан и метиленхлорид. От фракцията с метилен хлорид са изолирани пет метоксифлавонови съединения с помощта на колонна хроматография. Структурите на изолираните съединения са идентифицирани като 3,5,7,3',4'-пентаметоксифлавоон (КР1), 5,7-диметоксифлавоон (КР2), 5,7,4'-триметоксифлавоон (КР3), 3,5-дихидрокси-3'-метоксифлавоон (КР4) и 6-хидроксиу-7,4'-диметоксифлавоон (КР5) чрез ¹D Н-ЯМР спектрален анализ и сравнение с литературни данни.

КР5 проявява значителна хипогликемична активност при плъхове със стрептозотоцин-индуциран диабет в продължение на 28 дни. Той намалява значително серумната глюкоза и триглицеридите, докато повишава серумния инсулин при диабетичните плъхове, но не и при нормалните плъхове ($p < 0.05$, при дози от 50, 100 и 150mg/kg за 28 дни). Препаратът няма ефект върху С-пептидите (ECLIA). Следващата зависимост между структура и активност на позиция 6 в ароматния пръстен В ще бъде съобщен в близко време.

Fluorocarbon nanostructures (PFOB-NEP) as camel milk lactoferrin and its anti-cancer effects on human breast cancer cell line MCF7

H. R. I. Keykanlu¹, S. Zibaei^{2*}, M. Ardjmand³, A. A. Safekordi⁴

¹Department of Chemical Engineering, Science and Research Branch, Islamic Azad University, Tehran, Iran

²Razi Institute, Ministry of Jihad-e-Keshavarzi, Mashhad, Iran

³Department of Chemical Engineering, South Tehran Branch, Islamic Azad University, Tehran, Iran

⁴Department of Chemical Engineering, Sharif University of Technology, Tehran, Iran

Received January 5, 2016, Accepted January 14, 2016

Given the prevalence of cancer in the world, it is important to find new drugs for its treatment. Despite great advances in cancer treatment, a significant tendency for new anticancer agents due to the increased resistance of cancer cells to anticancer drugs is currently being expanded.

In this research the biological properties of lactoferrin (LF) from camel milk were studied and attempt was made to provide a way for preserving the three-dimensional structure of LF and increasing LF life resulting in preventing its denaturation by proteolysis *via* loading it on perfluorooctyl bromide nanoemulsion particles (PFOB-NEP). LF was extracted from camel milk by ion-exchange chromatography (carboxymethyl Sephadex C-50 resin) and its purity was confirmed by SDS-PAGE. Due to the biologically inert, chemically stable, non-biodegradable, nontoxic and nonvolatile properties of perfluorocarbon, PFOB-NEP was prepared using an oil-in-water emulsion method (O/W). LF was loaded onto the NEPs, then its characteristics and anti-cancer effects on human breast cancer cell line MCF7 were evaluated. According to the results, LF accession to NEPs was proved by circular dichroism and tryptophan fluorescence spectroscopy methods. The entrapment efficiency of LF into NEPs was about 91%. The mean diameter of the NEPs did not change after accession of LF (~ 100 nm) and the zeta potential of the NEPs was increased from -18.43 mV (without LF) to 21.61 mV (110.68µg/mL LF).

Keywords: Lactoferrin, Perfluorooctyl bromide (PFOB), Nanoemulsion Particles (NEP), Oil-in-water Emulsion, Camel Milk, Circular Dichroism (CD).

INTRODUCTION

Camel milk and cow milk are different in chemical composition, but in general camel milk contains all essential micronutrients that are found in cow milk including whey proteins such as LF and immunoglobulin [1]. Camel milk generally has white and opaque color, it has a sweet and sharp taste, but sometimes, depending on the eaten plant in the desert by the camel, it may be prone to salinity [2]. Because of the higher salt and lactose content of camel milk, its freezing point is lower than that of cow milk (between -0.57°C and -0.61°C). Camel milk is slightly higher in lactose content than cow milk. However, levels of potassium, magnesium, iron, copper, manganese, sodium and zinc are higher than in cow milk. Camel milk has anti-cancer, anti-diabetic, antimicrobial and hypoallergic properties for which LF, immunoglobulins, lysozyme or vitamin C play a major role among its compounds [3]. LF, also named lactotransferrin, is a glycoprotein of the

transferrin family with a molecular weight of about 80 kDa [4]; the molecular weight of LF purified from camel milk was determined as 79.5 kDa and 75.3 kDa.

The concentration of camel milk LF (0.22 mg/mL) is about 2.44 times that of cow milk LF, and the concentration of camel milk colostrum LF was reported about 5.1 mg/mL on the second day after parturition, while its content in cow milk colostrum is about 0.5 mg/mL [4].

Camel milk LF concentration in the first week after parturition varied from 1.422 to 0.586 mg/mL [5,6].

This protein consists of a single polypeptide chain containing 703 amino acids that are folded into two globular lobes. These lobes, also called C – (carboxy) and N – (amino) terminal regions, are connected with an α -helix. Each lobe consists of two domains known as C1, C2, N1, and N2. The domains create one iron binding site on each lobe (Fig. 1) [7,8]. LF has the ability to combat bacteria (Gram+ and Gram-), yeast, fungi, viruses, and parasites [9]. Due to the wide distribution of LF in various tissues and the positive charge on its

* To whom all correspondence should be sent:
E-mail: s.zibae@mrzi.ac.ir

network, this protein is a multi-functional protein [10,11].

LF has been identified in blood, tears, saliva, vaginal fluids, semen, nasal and bronchial secretions, bile, gastrointestinal fluids, urine, mucous secretions, secretions from exocrine glands and in specific granules of neutrophils [7,12,13]. A high amount of LF is present in milk and colostrum (7 g/L) [14,15]. LF is also found in fish and egg yolks [16].

LF is used in feed, food and pharmaceuticals. It exhibits anti-inflammatory and anticarcinogenic activities and has several enzymatic functions [17,18]. At higher concentrations of LF, it was found to act as a pro-oxidant [18].

Antibacterial activity [19] of LF is effected by two mechanisms: (1) LF at the site of infection keeps out of reach iron which is a nutrient for the organism, thus LF shows a bacteriostatic effect; (2) direct interaction of LF with infectious microorganisms [20]. The peptide lactoferricin (LFcin) released from LF by pepsin proteolysis under acidic conditions exhibits higher antimicrobial activity than LF [21]. LFcinB displays *in vitro* cytotoxic activity *versus* various types of mouse and human cancer cell lines, including leukemia cells, fibrosarcoma cells, various carcinomas, and neuroblastoma cells [22,23]. LF is the only transferrin, which is able to maintain iron in a wide range of pH even if pH is too acidic. It is also resistant to proteolysis [17]. LF is able to stop the growth of cancer cells through the inhibition of cell proliferation by altering the expression or activity of regulatory proteins, and through activation of natural killer cells. It inhibits tumor growth through the activation of apoptosis (programmed cell death) [7,24]. LF can be used to increase the anti-cancer effect of anti-cancer drugs such as apotransferrin. Kishore Golla et al. evaluated the effect of doxorubicin loaded apotransferrin and LF nanoparticles (apodoxonano or lactodoxonano) in the drug orally for hepatocellular carcinoma treatment (HCC) in rats. Apodoxonano and lactodoxonano in comparison to doxo showed improved efficacy, bioavailability and safety [25]. LF is an iron-binding glycoprotein with antihypertensive properties [26]. It is available as a commercial extract from bovine milk and offers potential as a therapeutic intervention for preterm infants modulating infections and intestinal pathologies [27].

According to the research done about the effect of human, bovine, sheep and camel milk LF on the C hepatitis virus it was found that camel milk LF had the highest effect [28].

LF extracted from milk can be marketed as a food supplement. In addition, it has a great potential in the field of biomedicine. The structure of this protein as of other proteins is fragile, so a small change in the structure may reduce its activity. Lipid-based carriers which are produced by self-assembly have become favorite for a broad scientific and commercial usage as carriers for the delivery of peptides and proteins during the past few years [10,29]. A way to avoid denaturation by proteolysis and dilution effect is to trap proteins or peptides in nanopores (or coating) until this action causes a reduction in water activity and thus helps to their stability in storage [30]. Nanoliposomes may be fit for oral administration of LF and could be a useful approach for LF availability to tumor cells [31]. Its three-dimensional structure has been attempted *via* nanoencapsulation within lipid nanovesicles, integrating a multiple water-in-oil-in-water emulsion [10]. The production of biocompatible nanoemulsions can also help to it. Since perfluorocarbons (PFCs) are biologically inert, chemically stable, nonbiodegradable, nontoxic and nonvolatile, they can produce biocompatible nanoemulsions. Specifically, perfluorooctyl bromide (PFOB) is mostly used due to its low vapor pressure helping to reduce pulmonary emphysema [32-34]. PFOB is used as an ultrasound contrast agent [35]. The biological half-lives were estimated to be 12 days (PFOB) [36]. *In vivo* sensitivity for inflammation imaging was assessed using the ear clip injury model. The result of this test for PFOB provided 37%. In the present study, perfluorocarbon NEPs were formulated for LF loading, and the optimum nanostructure characteristics were found. The nanostructure particle size was analyzed and the particle size distribution, charge, as well as the surface morphology were determined. The obtained results showed the proper incorporation of LF into NEP.

MATERIALS AND METHOD

Bioactive protein: camel milk was obtained from Torkaman Sahra located in the northeast parts of Iran and stored at -20°C until needed. The bioactive LF (purity: >85%) from bovine whey was purchased from Sigma-Aldrich (USA). Chemicals and biochemicals: perfluorooctyl bromide (PFOB) 99%, carboxymethyl Sephadex C-50 resin, soybean phosphatidylcholine (lecithin), dipalmitoyl-sn-glycero-3-phosphoethanolamine (DPPE, assay: >99%) were purchased from Sigma-Aldrich (USA). Other chemicals and biochemicals including protein marker 26612 were purchased from Thermo

Scientific (USA). HCl (37%), NaCl, monosodium phosphate, acrylamide, bisacrylamide, Tris, TEMED, ammonium persulfate (APS), sodium dodecyl sulfate (SDS), ethanol, methanol tetramethylbenzidine (TMB), acetic acid, silver nitrate, sodium thiosulfate, formaldehyde, sodium carbonate, sulfuric acid, hydrogen peroxide, dimethyl sulfoxide (DMSO), citric acid, bovine serum albumin (BSA), coomassie brilliant blue (C.Blue) G250 were purchased from Merck (Germany). Analytical equipment: all spectrophotometric readings were carried out using quartz cuvettes on an UV-VIS spectrophotometer, Shimadzu (Kyoto, Japan). Upper speed vacuum centrifuge (Ultracentrifuge) model VS-30000i of VISION SCIENTIFIC CO. LTD was used. Micro-spin/ FUGE/ VOTEX KIAGEN (Molecular Biology Company), magnetic stirrer (yellow MAGHS7), pH meter of Metrohm, Switzerland (827 pH lab) were used. Eppendorf centrifuge tubes (5415D) and sodium dodecyl sulfate polyacrylamide gel electrophoresis (SDS-PAGE) of Sigma PS 2000-2 (USA) were used. Cation exchange chromatography column (10×3 cm) was used. Orbital shaker (FINEPCR SH30t) was used. The zeta potential and particle size of the nanoemulsion particles were determined on a ZetaCompact (CAD Instruments, France) and a particle size analyzer (VASCO - 1, France), respectively. SEM analysis of nanoemulsions was carried out on a scanning electron microscope (LEO, model VP 1450, Germany). Also, ultrasound (XL2020-010, USA), ultraturax (IKA, Model T25, Germany), circular dichroism (CD) spectrometer (J-815, CD spectrometer, Japan), fluorescence intensity (model 2500, Hitachi, Japan) were used for analytical assays.

Isolation and purification of LF from camel milk

Fat and casein were isolated from camel milk by centrifuge at 4500 g at 4°C for 15 min (two times) and ultracentrifuge at 30000 g for 30 min at 25°C (two times), then filtered by Whatman filter paper No. 7. LF was extracted from whey (pH 6.8) by ion-exchange chromatography (carboxymethyl Sephadex C-50 resin) [37,38]. Whey was passed through the CM column for 30 min (two times) in order to make a connection between the whey proteins and CM. After a designated time, whey was removed from the column. The unabsorbed proteins were eluted from the column with sodium phosphate buffer (10 mM, pH = 6.8). Then the column was washed with NaCl solutions of increasing molarity (0.3 and 1.2 mol/L) in a stepwise procedure. The protein solution was

desalinated by dialysis where the dialysis bag was surrounded with sucrose or polyethylene glycol (PEG)[30].

SDS PAGE analysis

Extracted LF and purchased LF standard were compared using sodium dodecyl sulfate polyacrylamide gel electrophoresis (SDS-PAGE). SDS-PAGE separates proteins conforming to their molecular weight, based on their different rates of departure through a sieving matrix (a gel) under the influence of an applied electrical field. In this method, silver staining was used to detect the band of acrylamide gel containing the protein.

SDS-PAGE shows a 80 kDa band confirming the existence of lactoperoxidase.

Gel composition is as follows: (for a 5 mL stacking 15% gel: deionized water (DDW) (2.975 mL); Tris-HCl 0.5 M, pH 6.8 (1.25 mL); SDS 10% w/v (0.05 mL); acrylamide/bis-acrylamide (30%/0.8% w/v) (0.67 mL); APS 10% w/v (0.05 mL); TEMED (0.005 mL) and for a 10 ml separating 15% gel: DDW (2.2 mL); Tris-HCl 1.5 M, pH 8.8 (2.6 mL); SDS 10% w/v (0.1 mL); acrylamide/bis-acrylamide (30%/0.8% w/v) (5 mL); APS 10% w/v (100 µL); TEMED (10 µL)). The running buffer contains: SDS 0.5 g; Tris-HCl 1.2 g; glycine 7.2 g to a final volume of 500 mL with DDW; the loading buffer contains: SDS 0.6 g; beta-mercaptoethanol 200 µL; glycerol 6 mL; Tris-HCl 1.5M, pH 6.8 (3 mL); bromophenol blue 0.005 g, at 120V and 90 minutes.

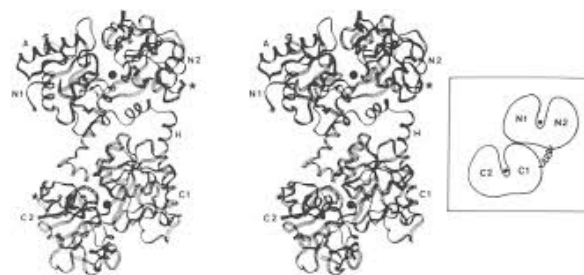


Fig. 1. Schematic diagram of the three-dimensional structure of the LF molecule. LF is lactoferrin

Coloring gel preparation: 1- Put the gel in a fixative solution and put it on a shaker with moderate speed for 30 min (water 20 mL, acetic acid 5 mL, methanol 25 mL); 2- Put the gel in methanol solution while shaking for 15 min (twice); 3- Put the gel in Hypo solution while shaking for 2 min (sodium thiosulfate 20% w/v 200 µL to a final volume of 50 mL with DDW) then wash the gel for 2 min three times with DDW; 4- Put the gel in a staining solution (silver nitrate 0.13 g, formaldehyde 100 µL to a final volume of 50 mL with DDW) in the dark for 10 min then wash again

the gel for 2 min three times with DDW; 5- Put the gel in a developing solution (sodium carbonate 3.4 g, formaldehyde 1400 μ L, sodium thiosulfate 20% w/v 800 μ L to a final volume of 50 mL with DDW) until the appearance of a protein band, drain it and put the gel in the fixative solution.

For the detection of lactoperoxidase the TMB (3, 5, 3', 5' - tetramethylbenzidine) color reaction was used in the presence of hydrogen peroxide and the purity of LF was confirmed. Briefly: 1- Prepare a solution of TMB (dissolve 5 mg of TMB powder in 1 ml DMSO in a water bath at 45°C and add 300 μ L of it to 700 μ L of sodium phosphate buffer (pH = 6)). Add 2-100 μ L of the sample to 100 μ L of TMB solution and 10 μ L hydrogen peroxide 30% and incubate at 37°C for 5 min, then read the absorbance at 450 nm using a spectrophotometer. LF concentration was determined by coomassie dye binding or Bradford assay [39]. In summary, 50 μ L of sample was added to 2.5 ml of Bradford solution (100 mg C. blue G250 dissolved in 50 mL ethanol 96%, then 100 ml of 85% phosphoric acid was added and the volume was brought to 1 L with DDW). Using BSA standard solution and measuring absorbance at 595 nm, the absorption curve was drawn with Excel 2013 and the concentration of LF was found.

100 mg Blue Kumasi LF was lyophilized and stored at -20°C in the dark until needed.

Preparation of NEP stabilized emulsions

Pre-emulsions were prepared as follows : 2% W / V surfactant (including 98% mol egg lecithin and 2% mol DPPE) and 20% V/V PFOB in DDW were stirred by a magnetic stirrer [40] for 10 min at 5000 rpm. Homogenization was carried out using an Ultra-Turex stirrer for 10 min at 12000 rpm within water-ice solution. To obtain nano-sized particles and uniform emulsions duplicate stirring in an ultrasonic stirrer for 10 min followed. The formulations prepared with each of these lipids showed a milky and uniform appearance [41].

Addition of LF to NEPs

After the preparation of NEPs, LF (selected amounts in saline phosphate buffer of 110, 55, 27.5 μ g/mL, respectively) was added to the preformed NEPs, and the residual free (unbound) LF was washed out by centrifugation at 1000 rpm for 10 min. The amount of unbound LF was determined by measuring the tryptophan fluorescence and Bradford method [39]. Control NEPs (without LF) were stored for 52 days under the same conditions [22].

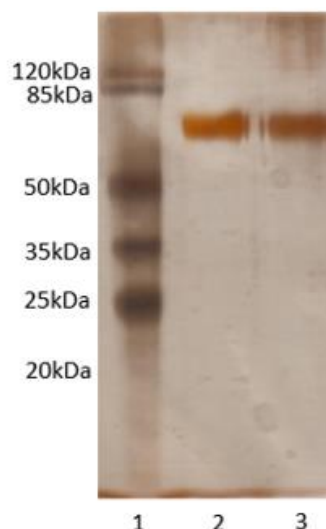


Fig. 2. SDS PAGE analysis of LF on a 15% gel with 120V and 90 min of fractions obtained in ultrafiltrated (purified) whey by ion-exchange column using saline gradient. Lane 1, 2, and 3 represent protein markers, elution peak with 0.7 mol/L NaCl and LF standard, respectively.

Entrapment efficiency (EE):

The loading efficiency was determined by centrifugation of NEPs. Following the addition of LF to NEPs, the residual free (unbound) LF was washed out by centrifugation at 1000 rpm for 10 min. The protein content of the supernatant was measured by tryptophan fluorescence and Bradford method [39] and the total amount of LF was determined spectrophotometrically.

Entrapment efficiency (in percentage) was calculated using Eq.1.

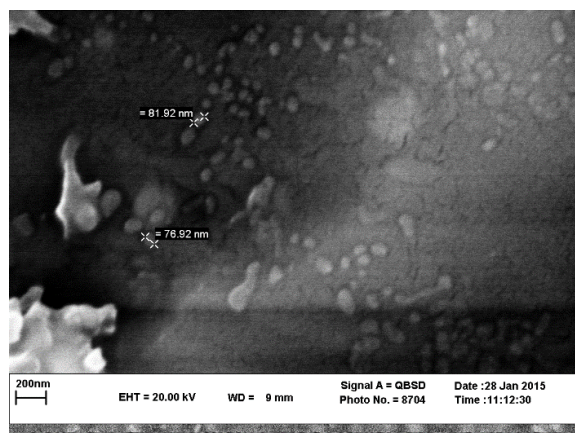
$$EE\% = \frac{(C_t - C_f)}{C_t} * 100 \quad (1)$$

where C_f is the amount of free LF and C_t is the total amount of LF present in 500 μ L of NEPs [31].

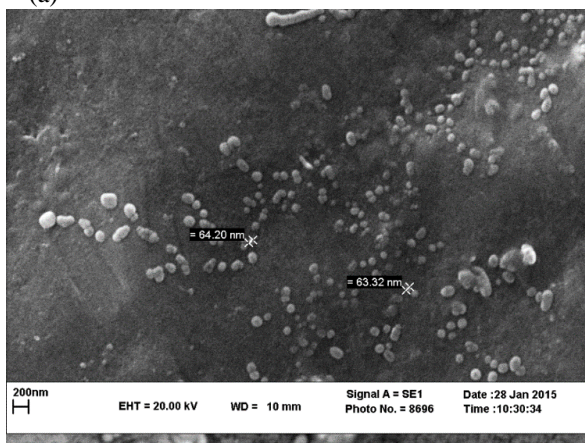
Scanning electron microscopy analyses

The scanning electron microscopy (SEM) produces a variety of signals at the solid samples surface by using a focused beam of high-energy electrons. The signals which are obtained by the interaction of electrons with the solid sample give information on the morphology, chemical composition, crystalline structure and orientation of the solid sample. Coating of samples is required to enable or improve the imaging of samples. Samples of NEPs were coated with a thin layer of conducting material (gold/palladium (Au/Pd)). Magnifications of NEPs before and after the accession of LF are shown in Fig. 3, where the shape structure of the particles is spherical. The scanning electron microphotographs of the exposed

surface of LF binding to nanoemulsions (see Fig. 3a and 3b) show the matrix structure developed during the manufacturing process and the highly homogeneous distribution of nanoemulsions diameters.



(a)



(b)

Fig. 3. Scanning electron microscopy analysis of the PFOB-NEP using 100 000 magnification (a) and inserted LF into PFOB-NEP using 50 000 magnification (b). PFOB-NEP are perfluorooctyl bromide nanoemulsion particles.

Determination of particle size

Particle size analysis is a part of particle science and it is a patented innovative technology. Particle size distribution is an important physical property for determining the behavior and nature of particles. The principles of measurement are based on dynamic light scattering (DLS) of backscattered light. DLS (also known as photon correlation spectroscopy or quasi-elastic light scattering) is a technique in physics that performs measurements in dark which can be used to characterize the size distribution profile of small particles in suspension or emulsion or of polymers which exist in the solution [42]. This method is also used to check the behavior of complex fluids such as concentrated polymer solutions. A laser is used as

monochromatic light source that is shot through a polarizer into the sample. The scattered light then goes through a second polarizer where it is collected by a photomultiplier and the resulting image is projected onto a screen [43].

Determination of zeta potential

Zeta potential shows the surface charge of particles in emulsions and suspensions so that the measurement of zeta potential serves for predicting formulation stability and interactions between particles. Optimization processing is an important and easy way to control quality. Zeta potential is the electric potential that dominates in the incision plan of a particle, which is at a tiny distance from its level, as a consequence of the measuring of the mobility distribution of a scissoring of charged particles that are under an electric field [44]. The mobility is the speed of a particle per unit electric field. In another definition, zeta potential is the potential difference between the dispersion medium and the stationary layer of fluid attached to the dispersed particle. Methods of measuring a particle's zeta potential are dependent on the nature of both the particle and the suspension or emulsion formulation.

Circular dichroism (CD) spectroscopy

Circular dichroism (CD) is dichroism involving circularly polarized light, i.e., differential absorption of left- and right-handed light. CD spectroscopy is an important technique in structural biology for examining the folding, conformational changes, and especially the secondary structures of proteins. Herein, CD was used to confirm the incorporation of LF in the nanoemulsions. This interaction produces a CD signal at the plasmon resonance frequency of the chiral protein-NEP complex.

Fluorescence spectroscopy

For the analysis of sample fluorescence, fluorescence spectroscopy (also known as fluorometry or spectrofluorometry) is used which is a type of electromagnetic spectroscopy. An emission map is measured by recording the emission spectra resulting from a range of excitation wavelengths and combining them all together. The intrinsic tryptophan fluorescence (TRP19) in LF (excitation, 280 nm; emission, 355 nm) was used to study the nature of the LF interaction with the lipid monolayer of perfluorocarbon NEPs. Fluorescence emission spectra show the quenching of endogenous

tryptophan fluorescence of LF upon insertion into the lipid monolayer of NEPs.

The effects of nanoparticles prepared in breast cancer MCF7 cells lines

The MCF-7 breast cancer cell line was obtained from Razi Institute, Ministry of Jihad-e-Keshavarzi, Mashhad, Iran. The cells were thawed to revive and recover. The recovered cells were transferred into culture flasks and were incubated with 5% carbon dioxide at 37 ° C. To investigate the effect of nanoparticles containing LF in the growth of cancer cells, three different concentrations were used. For this purpose, a day before adding the nanoparticles, the cells were transferred into 96-well plates with 200 ml of medium. After adding the nanoparticles, the cell-containing plates were incubated with 5% carbon dioxide at 37 ° C. After 24 hours the survival rate of the cells was controlled with MTT assay *in vitro*.

RESULTS AND DISCUSSION

SDS PAGE analysis

The fraction in NaCl solution (0.7mol/L) was identified as LF by SDS-PAGE analysis on a 15% gel (Fig. 2, Lane 2) and TMB color reaction was used to confirm the purity of LF. SDS-PAGE results showed (Fig. 2, Lane 2) that the identified fraction in the NaCl solution had higher purity. Following electrophoresis, the gels were stained using the silver nitrate method [45]. Silver staining of proteins on a gel increases the sensitivity by a factor of 10-100.

The comparison between line 2 (isolated protein) and line 3 (standard LF) shows that the molecular weight of the protein is 80 kDa. The amount of LF or lactoperoxidase was determined by the coloring reaction of tetramethylbenzidine (TMB) test at a later stage.

Entrapment efficiency (EE)

By measuring the amount of free (unbound) LF after centrifugation and comparison with LF present in 500 µL of NEPs by tryptophan fluorescence and Bradford method according to equation 1, the entrapment efficiency was obtained (91%).

Scanning electron microscopy analyses

Magnifications of PFOB-NEP and inserted LF into lipid bilayer nanoemulsions of 100 000 and 50 000 are depicted in Fig. 3a, 3b, respectively. The scanning electron microphotographs of the exposed surface of PFOB-NEP and inserted LF into PFOB-

NEP showed that the nanoemulsions structure remained unchanged during the manufacturing process and the highly homogeneous distribution of nanoemulsion diameters and the morphology after reunification of LF in the spherical particles have not changed.

Particle size analysis and determination of zeta potential

The mean particle diameter and the zeta potential were monitored by increasing the concentration of LF (Fig.4). No changes were observed in the mean diameter (~100 nm) of the PFC NEPs after addition of LF, but since LF is a cationic protein, as expected, by increasing the concentration of LF, the zeta potential of the NEPs increased from -18.43 mV (without LF) to 21.61 mV (110.68µg/mL LF).

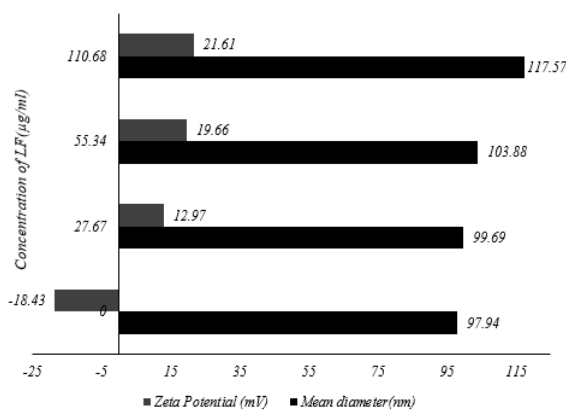


Fig. 4. Mean hydrodynamic diameter and zeta potential of NEPs before and after incorporation of LF.

Circular dichroism (CD) spectroscopy

CD spectroscopy played an important role in these studies. CD spectroscopy was used to study the structure of NEP free of LF and upon interaction with LF. As Fig. 5 shows, the nanoparticles without LF give no peak, while after accession LF creates a negative peak at a wavelength of 202. The differences in the CD spectra are indicative of the LF incorporation upon interaction with NEP.

Tryptophan fluorescence

Typically LF undergoes a blue shift (or a change in emission from 330 to 325 nm) upon insertion into lipid bilayers due to the hydrophobic membrane environment. The fluorescence of NEP associated LF was completely quenched (Fig. 6a). Fluorescence emission spectra show the quenching of endogenous tryptophan fluorescence of LF (110.68 µg/mL of LF) upon insertion into the lipid monolayer of NEPs with a PFOB core. Because tryptophan fluorescence quenching is not generally

a feature of peptide interaction with membranes, the special role of the PFOB core was tested as a mechanism for the observed fluorescence quenching upon integration into NEPs. Fig. 6b shows the percentage quenching of tryptophan fluorescence by free LF and LF with perfluorocarbon cores.

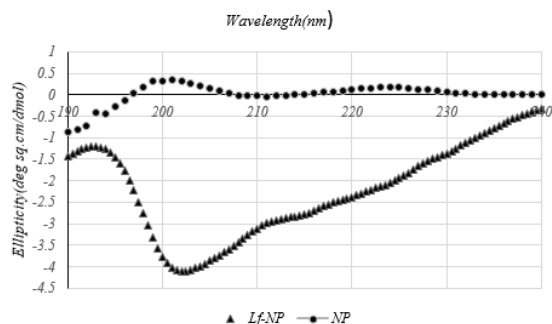
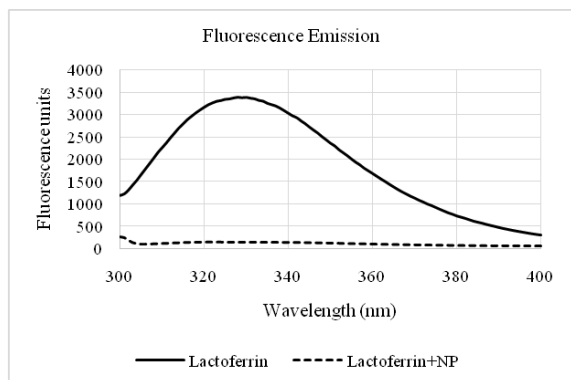
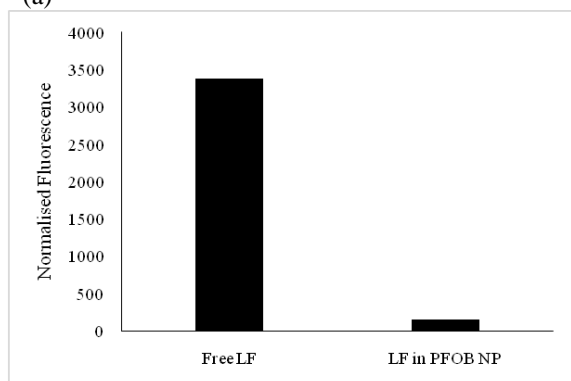


Fig. 5. Far-UV CD spectra of NEPs and LF in monolayered PFOB NEPs at 25°C. CD is circular dichroism



(a)



(b)

Fig. 6. Interaction of LF tryptophan with PFC NEPs (a) Percentage quenching of tryptophan fluorescence with free LF and LF with perfluorocarbon cores; (b) PFC in perfluorocarbons.

MTT test results in breast cancer MCF7 cell lines

Cell viability was determined as a ratio of absorbance ($A_{570 \text{ nm}}$) in treated cells relative to absorbance in control cells (DMSO) ($A_{570 \text{ nm}}$). The IC_{50} was defined as the concentration of sample

needed to reduce 50% of absorbance relative to the vehicle (DMSO)-treated control (Fig. 7).

$$\text{Cell viability (\%)} = \frac{A_{570\text{nm}}(\text{Sample})}{A_{570\text{nm}}(\text{Control DMSO})} \times 100$$

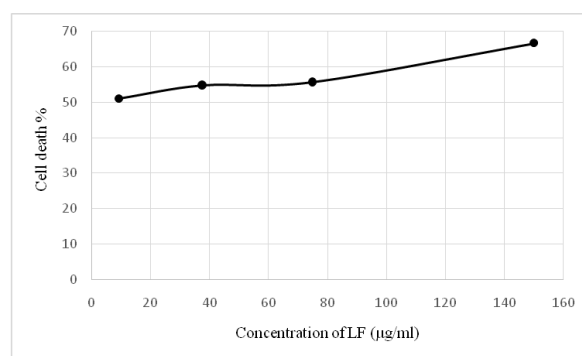


Fig. 7. Cell death % with concentration of LF in PFOB NEPs.

CONCLUSIONS

Due to the unique properties of LFs such as antimicrobial activity, immunomodulatory, and even antineoplastic properties, LF seems to have great potential in practical medicine. A lot of research has been done on it of late. Nevertheless, more research still needs to be carried out in order to obtain a better understanding of its activity and interactions and to enable the full and safe utilization of this glycoprotein. As already mentioned, due to the sensitivity of LF to proteolysis, a lot of research has been done on the use of alginate and carrageenan nanoparticles as carriers.

The purpose of this research was to design, formulate, characterize, and assess the advantage of PFOB particles as nanovehicles for LF delivery in pharmaceutical applications, e.g., the use of this combination on breast cancer cells. In this study LF was isolated from camel milk using ion-exchange chromatography.

Although LF is resistant to pH changes, to avoid breaking LF and to retain its biological activity against factors such as sonication, stirring and heat, LF was added after the formation of NEPs.

Effective connection between the NEPs and LF is mediated by electrostatic interactions between the negatively charged lipid monolayer of NEPs and the positively charged LF surface. These interactions were proved by CD and tryptophan fluorescence.

SEM analysis (Fig. 3a and 3b) of PFOB NEPs illustrates that their structural integrity is preserved even after addition of LF. The very high surface tension of PFOB NEPs, as well as the hydrophobic and lipophobic perfluorocarbon core prevent

disintegration of the NEP after LF insertion and may actually contribute to the stability and controlled release of LF from PFOB NEPs. The results showed that perfluorocarbon NEPs can be used to deliver cytolytic peptides and proteins.

The results of MTT assay showed that LF loaded on PFOB NEPs causes the death of cancer cells and with increasing LF concentration, the percentage of dead cells increased.

REFERENCES

1. A. A. Al-Alawi, L.C. Laleye, Characterization of Camel Milk Protein Isolates as Nutraceutical and Functional Ingredients. Collaborative Research Project SQU/UAEU, 2008
2. HA. Al Kanhal, *International Dairy Journal*, **20**(12), 811 (2010).
3. Y.W. Park, Bioactive components in milk and dairy products, John Wiley & Sons, 2009
4. P. Masson, J. Heremans, E.Schonne, *The Journal of Experimental Medicine*, **130**(3), 643 (1969).
5. G. Konuspayeva, B. Faye, G. Loiseau, D. Levieux, *Journal of Dairy Science*, **90**(1), 38 (2007).
6. G Konuspayeva, B Faye, G. Loiseau, *Journal of Food Composition and Analysis*, **22**(2), 95 (2009).
7. L. Adlerova, A. Bartoskova, M. Faldyna. *Veterinarni Medicina*, **53**(9), 457 (2008).
8. S. Sharma, M. Sinha, S. Kaushik, P. Kaur, T.P. Singh, *Biochemistry Research International*, Volume 2013, Article ID 271641, doi 10.1155/2013/271641 (2013).
9. P. Masson, J. Heremans, *Comparative Biochemistry and Physiology part B: Comparative Biochemistry*. **39**(1), 119 (1971).
10. V. M. Balcão, C. I. Costa, C. M. Matos, C. G. Moutinho, M. Amorim, M. E. Pintado, A. P. Gomes, M.M. Vila, J. A. Teixeira, *Food Hydrocolloids*, **32**(2), 425 (2013).
11. A.M. Al-Majali, Z.B. Ismail, Y. Al-Hami, A.Y. Nour, *International Journal of Applied Research in Veterinary Medicine*, **5**(3), 120 (2007).
12. A. Pierce, D. Legrand, J. Mazurier, *Medicine Sciences: M/S*, **25**(4), 361 (2009).
13. B. Van der Strate, L. Beljaars, G. Molema, M. Harmsen, D. Meijer, *Antiviral Research*, **52**(3), 225 (2001).
14. D. Rodriguez-Franco, L. Vazquez-Moreno, G. Ramos, *Rev. Latinoam. Microbiol.*, **47**(3), 102 (2005).
15. S.A. González-Chávez, S. Arévalo-Gallegos, Q. Rascón-Cruz, *International Journal of Antimicrobial Agents*, **33**(4), 301 (2009).
16. J.M. Torres, J.L. Concepción, J.R. Vielma, E.T. La Mucuy, LdE.de Parásitos, *Mundo Pecuario*, **2**(3), 57 (2006).
17. I.A. García-Montoya, T.S. Cendón, S. Arévalo-Gallegos, Q. Rascón-Cruz, *Biochimica et Biophysica Acta (BBA)-General Subjects*, **1820**(3), 226 (2012).
18. E.D. Weinberg, *Current Pharmaceutical Design*, **13**(8), 801 (2007).
19. F. Moradian, R. Sharbafi, A. Rafiei, *Journal of Medical and Bioengineering*, **3**(3), 203, (2014).
20. F. Berlutti, F. Pantanella, T. Natalizi, A. Frioni, R. Paesano, A. Polimeni, P.Valenti, *Molecules*, **16**(8), 6992 (2011).
21. L.H. Vorland, H. Ulvatne, J. Andersen, H. H. Haukland, Ø. Rekdal, J.S. Svendsen, T. J. Gutteberg, *Scandinavian Journal of Infectious Diseases*, **30**(5), 513 (1998).
22. J.S. Mader, J. Salsman, D.M. Conrad, D.W. Hoskin, *Molecular Cancer Therapeutics*, **4**(4), 612 (2005).
23. L.H.Vorland, *Anticancer Research*, **22**, 2703 (2002).
24. K-i. Fujita, E. Matsuda, K. Sekine, M. Iigo, H. Tsuda, *Carcinogenesis*, **25**(10), 1961 (2004).
25. K Golla, C. Bhaskar, F. Ahmed, A.K.Kondapi, *Journal of Cancer*, **4**(8), 644 (2013).
26. L. Safaeian, H. Zabolian, *ISRN pharmacology*, Volume 2014, Article ID 943523, doi 10.1155/2014/943523 (2014).
27. N.D. Embleton, J.E. Berrington, W. McGuire, C.J.Stewart, S.P. Cummings, Lactoferrin: Antimicrobial activity and therapeutic potential. Paper presented at: Seminars in Fetal and Neonatal Medicine, 2013,
28. E.M. EL-Fakharany, L, Sánchez, H.A. Al-Mehdar, E.M. Redwan, *Virology Journal*, **10**(1), 199 (2013).
29. E. Acosta, *Current Opinion in Colloid & Interface Science*, **14**(1), 3 (2009).
30. G.R.M. Raei, S. Zibaei, S.M. Jafari, A.M. Sani, *International Journal of Biological Macromolecules*, **28**, 5 (2015).
31. R. Guan, J. Ma, Y. Wu, F. Lu, C-G Xiao, H. Jiang, T. Kang, *Nanoscale Research Letters*, **7**(1):679, (2012).
32. S-J. Lee, B. Olsen, P.H. Schlesinger, N.A. Baker. *The Journal of Physical Chemistry B*, **114**(31), 10086 (2010).
33. S-J. Lee, P.H. Schlesinger, S.A. Wickline, G.M. Lanza, N.A. Baker, *The Journal of Physical Chemistry B*, **115**(51), 15271 (2011).
34. M. Chenoune, L. De Rochefort, P. Bruneval, F. Lidouren, M. Kohlhauser, A. Seemann, B. Ghaleh, M. Korn, R.-M. Dubuisson, A. B. Yahmed, X. Maître, D. Isabey, J.-D. Ricard, R. E. Kerber, L. Darrasse, A. Berdeaux, R. Tissier, *BMC Pharmacology and Toxicology*, **15**(1), 53 (2014).
35. T. Nelson, R. Mattrey, *Investigative Radiology*, **25**(9), 983 (1990).
36. C. Jacoby, S. Temme, F. Mayenfels, N.Benoit, M. P. Krafft, R.Schubert, J. Schrader, U. Flögel, *NMR in Biomedicine*. **27**(3), 261 (2014).
37. Y. Liang, X. Wang, M. Wu, W. Zhu, *International Journal of Environmental Research and Public Health*, **8**(9), 3764 (2011).
38. M. Wu, R. Wang, X. Wang, Z. Zhang, . Isolation and Purification of Bioactive Proteins from Bovine Colostrum: INTECH, Open Access Publisher; Rijeka, Croatia 2011.
39. N.J. Kruger, in: Basic Protein and Peptide Protocols (Methods in Molecular Biology, vol. 32), Humana Press, Totowa, NJ, p. 9, 1994.

40. N.R. Soman, G.M. Lanza, J.M. Heuser, P.H. Schlesinger, S.A. Wickline, *Nano Letters.*, **8**(4), 1131 (2008).
41. S. Abbas, K. Hayat, E. Karangwa, M. Bashari, X. Zhang, *Food Engineering Reviews*, **5**(3), 139 (2013).
42. B.J. Berne, R. Pecora, *Dynamic light scattering: with applications to chemistry, biology, and physics: Dover Publications, Inc., Mineola, N. Y.*, 2000,
43. J.W. Goodman, *JOSA*, **66**(11), 1145 (1976).
44. A. Wiącek, E. Chibowski, *Colloids and Surfaces A: Physicochemical and Engineering Aspects*. **159**(2), 253 (1999).
45. J.H. Morrissey, *Analytical Biochemistry*, **117**(2), 307 (1981).
46. E.N. Baker, B.F. Anderson, H.M. Baker, C.L. Day, M. Haridas, G.E. Norris, S.V. Rumball, C.A. Smith, D.H. Thomas, in: *Lactoferrin (Advances in Experimental Medicine and Biology, vol. 357)*, Springer US, 1994.

ФЛУОРОВЪГЛЕРОДНИ НАНО-СТРУКТУРИ (PFOB-NEP) КЪМ ЛАКТОФЕРИН ОТ КАМИЛСКО МЛЯКО И НЕГОВИЯТ ПРОТИВО-ТУМОРЕН ЕФЕКТ ВЪРХУ КЛЕТЪЧНА ЛИНИЯ MCF7 НА РАК НА ГЪРДАТА

Х. Р. И. Кейканлу¹, С. Зибаси^{2*}, М. Арджманд³, А. А. Сафекорди⁴

¹Департамент по химично инженерство, наука, Изследователски клон, Ислямски университет "Азад", Техеран, Иран

²Институт „Рази“, Министерство Джахад-е-Кешаварзи, Маишад, Иран

³Департамент по химично инженерство, Клон Южен Техеран, Ислямски университет „Азад“, Техеран, Иран

⁴Департамент по химично инженерство Технологичен университет „Шариф“, Техеран, Иран

Получена на 5 януари, 2016 г., приета на 14 януари, 2015 г.

(Резюме)

Поради разпространението на рака в световен мащаб е важно да се търсят нови лекарства за неговото лечение. Въпреки големия напредък, разширеното разработване на нови лекарства се обуславя от резистентността на раковите клетки към известните противоракови средства.

В настоящото изследване са изследвани биологичните свойства на лактоферин (LF) от камилско мляко и е направен опит да се запази неговата тримерна структура и да се повиши живота на LF, като се предотврати денатурирането му от протеолиза. Това се постига чрез добавяне на нано-емулсия с частици от перфлуороктил бромид (PFOB-NEP). LF се извлича от камилско мляко чрез йонообменна хроматография (карбоксиметилова Sephadex C-50 смола), а неговата чистота бе потвърдена чрез SDS-PAGE.

Перфлуоровъглеродът е биологически инертен, химически стабилен, нетоксичен и нелетлив, PFOB-NEP се приготвя от емулсия масло/вода (O/W). LF се натоварва върху нано-частиците, а след това се определят неговите характеристики и противотуморния ефект върху клетъчна линия MCF7 на рак на гърдата. Достъпът на LF до нано-частиците се доказва чрез кръгов дихроизъм и флуоресцентно спектроскопски методи. Ефективността на включване на LF в наночастиците беше около 91%. Средният диаметър на нано-частиците не се променя след включването на (~ 100 nm) а ζ -потенциалът на нано-частиците нараства от -18.43 mV (без LF) до 21.61 mV (110.68 μ g/mL LF).

On counting polynomials of certain polyomino chains

M. Imran^{1*}, S. Hayat²

¹Department of Mathematics, School of Natural Sciences (SNS), National University of Sciences and Technology (NUST), Sector H-12, Islamabad, Pakistan

²School of Mathematical Sciences, University of Science and Technology of China (USTC), Hefei, Anhui, China

Received April 24, 2015, Revised October 20, 2015

A counting polynomial $C(G, x)$ is a sequence description of a topological property so that the exponents express the extent of its partitions while the coefficients are related to the occurrence of these partitions. Omega, Sadhana and Padmakar-Ivan polynomials are extensive examples of counting polynomials which play an important role in topological description of bipartite structures as well as counts equidistance and non-equidistance edges in graphs. These polynomials count the quasi orthogonal cut (*qoc*) strips in graphs generated from bipartite chemical structures. A *qoc* strip defined with respect to any edge in a graph $G(V, E)$, represents the smallest subset of edges closed under taking opposite edges on faces.

In this article, we focus on counting polynomials of polyomino chains of different possible shapes. We derive the exact formulas of omega, Sadhana and PI polynomials for 2-parametric 4-polyomino system P_n^k for $k \geq 3, n \geq 1$. An open problem is proposed for further research in this direction.

2010 Mathematics Subject Classification: 05C12, 05C90

Keywords: Counting polynomial, omega polynomial, Sadhana polynomial, PI polynomial, Polyomino chains, k -polyomino system

INTRODUCTION AND PRELIMINARY RESULTS

A k -polyomino system is a finite 2-connected plane graph such that each interior face (also called cell) is surrounded by a regular $4k$ -cycle of length one. In other words, it is an edge-connected union of cells [12].

Counting polynomials are those polynomials having at exponent the extent of a property partition and coefficients the multiplicity/occurrence of the corresponding partition. A counting polynomial is defined as:

$$C(G, x) = \sum_c m(G, c) x^c, \quad (1)$$

Where the coefficient $m(G, c)$ are calculable by various methods, techniques and algorithms. The expression (1) was found independently by Sachs, Harary, Milić, Spialter, Hosoya, etc [5]. The corresponding topological index $P(G)$ is defined in this way:

$$C(G) = C'(G, x)|_{x=1} = \sum_c m(G, c) \times c$$

A molecular/chemical graph is a simple finite graph in which vertices denote the atoms and edges denote the chemical bonds in underlying chemical structure. This is more important to say that the hydrogen atoms are often omitted in any molecular graph. A graph can be represented by a matrix, a sequence, a polynomial and a numeric number (often called a topological index) which represents the whole graph and these representations are aimed to be uniquely defined for that graph.

Two edges $e = uv$ and $f = xy$ in $E(G)$ are said to be *codistant*, usually denoted by $e \text{ co } f$, if

$$d(x, u) = d(y, v)$$

and

$$d(x, v) = d(y, u) = d(x, u) + 1 = d(y, v) + 1$$

The relation “*co*” is reflexive as $e \text{ co } e$ is true for all edges in G , also symmetric as if $e \text{ co } f$ then $f \text{ co } e$ for all $e, f \in E(G)$ but the relation “*co*” is not necessarily transitive. Consider

$$C(e) = \{f \in E(G) : f \text{ co } e\}$$

If the relation is transitive on $C(e)$ also, then $C(e)$ is called an *orthogonal cut* “*co*” of the graph

* To whom all correspondence should be sent:

E-mail: imrandhab@gmail.com; sakander@mail.ustc.edu.cn

G . Let $e = uv$ and $f = xy$ be two edges of a graph G , which are opposite or topological parallel, and this relation is denoted by $e \text{ op } f$. A set of opposite edges, within the same face or ring, eventually forming a strip of adjacent faces/rings, is called an opposite edge strip ops, which is a quasi-orthogonal cut qoc (i.e. the transitivity relation is not necessarily obeyed). Note that “co” relation is defined in the whole graph while “op” is defined only in a face/ring.

In this article, G is considered to be simple connected graph with vertex set $V(G)$ and edge set $E(G)$, $m(G, c)$ be the number of ops of length c , $e = |E(G)|$ is the edge set cardinality of G .

The omega polynomial was introduced by Diudea et al. in 2006 on the ground of op strips. The omega polynomial is proposed to describe cycle-containing molecular structures, particularly those associated with nanostructures.

Definition 1.1. [1] Let G be a graph, then its omega polynomial denoted by $\Omega(G, x)$ in x is defined as

$$\Omega(G, x) = \sum_c m(G, c) \times x^c$$

The derivative of omega polynomial at $x = 1$ for any bipartite graph is equal to its edge set cardinality.

The Sadhana polynomial is defined based on counting opposite edge strips in any graph. This polynomial counts equidistant edges in G .

Definition 1.2. [6] Let G be a graph, then Sadhana polynomial denoted by $Sd(G, x)$ is defined as

$$Sd(G, x) = \sum_c m(G, c) \times x^{e-c}$$

The PI polynomial is defined based on counting opposite edge strips in any graph [10]. This polynomial counts non-equidistant edges in G .

Definition 1.3. [11] Let G be a graph, then PI polynomial denoted by $PI(G, x)$ is defined as

$$PI(G, x) = \sum_c m(G, c) \times c \times x^{e-c}$$

Ashrafi et al. computed Sadhana polynomial of V-phenylenic nanotube and nanotori.

Theorem 1.1. [2] Let G be the graph of V-phenylenic nanotube, then Sadhana polynomial of G is,

$$Sd(G, x) = 4 \sum_{i=1}^{\text{Max}\{m,n\}-1} x^{|E(G)-2i} + 2(|n-m|+1)x^{|E(G)-2\text{Min}\{m,n\}} + nx^{|E(G)-2m} + (m-1)x^{|E(G)-2m} + (n-1)x^{|E(G)-n}$$

All nanotubes are allotropes of carbon and are a type of fullerene. Imran et al. [9] computed omega and Sadhana polynomials of H-Naphtalenic nanotube.

Theorem 1.2. [9] The omega polynomial of H-Naphtalenic nanotube $NPHX[m, n]$, $\forall m, n \in \mathbf{N}$ is:

$$\Omega(NPHX[m, n], x) = \begin{cases} \eta + 4 \sum_{i=1}^{\lfloor \frac{n}{2} \rfloor - 1} x^{2i} + 2(n-2m+1)x^{4m}, & m \leq \lfloor \frac{n}{2} \rfloor \\ \eta + 4 \sum_{i=1}^{n-1} x^{2i} + 2(2m-n+1)x^{2n}, & m > \lfloor \frac{n}{2} \rfloor \end{cases}$$

where $\eta = nx^{3m} + mx^{2n} + (n-1)x^{2m}$.

The Sadhana polynomial of $NPHX[m, n]$, $\forall m, n \in \mathbf{N}$ is.

$$Sd(NPHX[m, n], x) = \begin{cases} \eta + 4 \sum_{i=1}^{\lfloor \frac{n}{2} \rfloor - 1} x^{15mm-2m-2i} + 2(n-2m+1)x^{15mm-6m}, & m \leq \lfloor \frac{n}{2} \rfloor \\ \eta + 4 \sum_{i=1}^{n-1} x^{15mm-2m-2i} + 2(2m-n+1)x^{15mm-2m-2n}, & m > \lfloor \frac{n}{2} \rfloor \end{cases}$$

where

$$\eta = nx^{15mm-5m} + mx^{15mm-2m-2n} + (n-1)x^{15mm-4m}.$$

The preceding results are used to compute their corresponding topological indices which provides a good model correlating the certain physico-chemical properties of these carbon allotropes.

RESULTS AND DISCUSSION

In this paper, we compute omega, Sadhana and PI polynomials of polyomino chain system P_n^k for $k = 1, 2, 3, \dots, 6$. By using these results, we present our main results of counting polynomials for polyomino chain system P_n^k for $k \geq 3, n \geq 1$. Imran et al. [8] studied some degree based topological indices of the polyomino chains. For further study of these polynomials their topological indices and various nanotubes, consult [3, 4, 9, 13, 14, 15]. These polynomials are used to predict various physico-chemical properties of certain chemical compounds.

Polyomino chains

A polyomino system is a finite 2-connected plane graph such that each interior face (or say a cell) is surrounded by a regular square of length one. In other words, it is an edge-connected union of cells in the planar square lattice. This polyomino system divides the plane into one infinite external region and a number of finite internal regions where all internal regions must be squares. A polyomino chain is a polyomino system, in which

the joining of the centers of its adjacent cells (regular squares) forms a path c_1, c_2, \dots, c_n , where c_i is the center of the i -th square. Such a polyomino chain is denoted as B_n . A square of a polyomino chain has either one or two neighboring squares. If a square has one neighboring square, it is called terminal, if it has two neighboring squares having no vertex of degree 2, it is called medial, and if it has two neighboring squares such that it has a vertex of degree 2, it is called kink. Every polyomino chain of dimension n has a unit such that it contains n number of units [16].

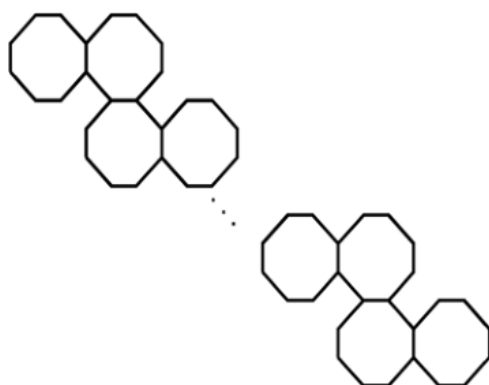


Fig. 1. A 2-polyomino system which is a zig-zag chain of 8-cycles.

Theorem 2.1.1. [7] Consider the graph of 2-polyomino system depicted in Figure 1. Then:

$$\Omega(x) = (4n - 1)x^3 + (8n + 2)x^2 \text{ and } Sd(x) = (4n - 1)x^{28n-2} + (8n + 2)x^{28n-1}.$$

We denote the polyomino chain system by P_n^k , and $k = k' + m + t$, where k' is the number of kinks, m is the number of medials and t is the number of terminals in a unit of polyomino chain. Figure 2 depicts the different polyomino chains with their units as dotted part. We call l_n, z_n, c_n, k_n, r_n and h_n the polyomino chains P_n^k for $k = 1, 2, 3, 4, 5$ and 6 respectively. Now we compute omega polynomial of these chemical graphs which count equidistance edges in these graphs.

Theorem 2.1.2. The omega polynomial of P_n^k for $k = 1, 2, 3, 4, 5, 6$ is equal to:

$$\Omega(l_n, x) = x^{n+1} + nx^2$$

$$\Omega(z_n, x) = 2x^2 + (2n - 1)x^3$$

$$\Omega(c_n, x) = (n + 1)x^2 + (n + 1)x^3 + (n - 1)x^4$$

$$\Omega(k_n, x) = (2n + 1)x^2 + nx^3 + x^4 + (n - 1)x^5$$

$$\Omega(r_n, x) = (3n + 1)x^2 + nx^3 + x^5 + (n - 1)x^6$$

$$\Omega(h_n, x) = (4n + 1)x^2 + nx^3 + x^6 + (n - 1)x^7$$

Proof. For l_n

The polyomino chain l_n is a linear chain of squares as shown in Figure 2. The number of edges in this chain graph is $3n + 1$. There are two types of ops in l_n , there are n qoc strips of length 2 and one strip of length $n + 1$. Since

$$\Omega(G, x) = \sum_c m(G, c) \times x^c$$

$$\Omega(l_n, x) = nx^2 + x^{n+1}$$

For z_n :

The chemical graph z_n is a zig-zag chain of squares as shown in Figure 2. The number of edges in this chain graph is $6n + 1$. There are also two types of ops in z_n , there are 2 qoc strips of length 2 and $2n - 1$ strips of length 3. Since

$$\Omega(G, x) = \sum_c m(G, c) \times x^c$$

$$\Omega(z_n, x) = 2x^2 + (2n - 1)x^3$$

For c_n :

The polyomino chain c_n is a polyomino chain P_n^k with $k = 3$ shown in Figure 2. The number of edges in this chain graph is $9n + 1$. This chain of dimension n has three types of qoc strips in c_n , there are $n + 1$ strips of length 2, $n + 1$ strips of length 3 and $n - 1$ strips of length 4. Now

$$\Omega(G, x) = \sum_c m(G, c) \times x^c$$

$$\Omega(c_n, x) = (n + 1)x^2 + (n + 1)x^3 + (n - 1)x^4$$

For k_n :

The number of edges in this chain graph is $12n + 1$. This chain of dimension n has four types of qoc strips in k_n , there are $2n + 1$ strips of length 2, n strips of length 3, one strip of length 4 and $n - 1$ strips of length 5. Now

$$\Omega(G, x) = \sum_c m(G, c) \times x^c$$

$$\Omega(k_n, x) = (2n + 1)x^2 + nx^3 + x^4 + (n - 1)x^5$$

For r_n :

In polyomino chain r_n , there are $15n + 1$ edges and four types of strips. There are $3n + 1$ strips of length 2, n strips of length 3, one strip of length 5 and $n - 1$ strips of length 6. We know

$$\Omega(G, x) = \sum_c m(G, c) \times x^c$$

$$\Omega(r_n, x) = (3n+1)x^2 + nx^3 + x^5 + (n-1)x^6$$

For h_n :

The polyomino chain h_n contains $18n+1$ edges and four types of strips. There are $4n+1$ strips of length 2, n strips of length 3, one strip of length 6 and $n-1$ strips of length 7. We know

$$\Omega(G, x) = \sum_c m(G, c) \times x^c$$

$$\Omega(h_n, x) = (4n+1)x^2 + nx^3 + x^6 + (n-1)x^7$$

□

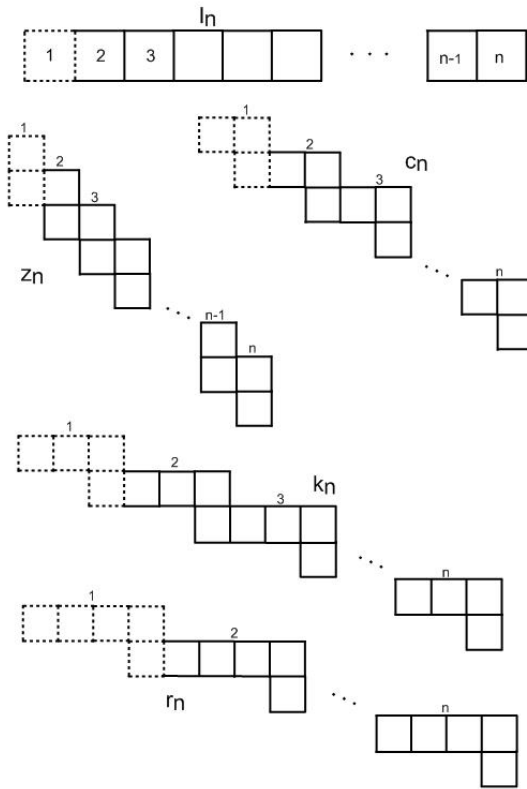


Fig. 2. Different polyomino chains.

In the following theorem, the Sadhana polynomial of P_n^k for $k=1,2,3,4,5$ and 6 is computed.

Theorem 2.1.3. The Sadhana polynomial of P_n^k for $k=1,2,3,4,5$ and 6 is as follows:

$$Sd(l_n, x) = nx^{3n-1} + x^{2n}$$

$$Sd(z_n, x) = 2x^{6n-1} + (2n-1)x^{6n-2}$$

$$Sd(c_n, x) = (n+1)x^{9n-1} + (n+1)x^{9n-2} + (n-1)x^{9n-3}$$

$$Sd(k_n, x) = (2n+1)x^{12n-1} + nx^{12n-2} + x^{12n-3} + (n-1)x^{12n-4}$$

$$Sd(r_n, x) = (3n+1)x^{15n-1} + nx^{15n-2} + x^{15n-4} + (n-1)x^{15n-5}$$

$$Sd(h_n, x) = (4n+1)x^{18n-1} + nx^{18n-2} + x^{18n-5} + (n-1)x^{18n-6}$$

The proof of this theorem is on the same lines as in case of omega polynomial, so we skip this proof.

Now we compute PI polynomial of P_n^k for $k=1,2,3,4,5,6$.

Theorem 2.1.4. Consider the polyomino system P_n^k for $k=1,2,3,4,5$ and 6. Then their PI polynomials are:

$$PI(l_n, x) = 2nx^{3n-1} + (n+1)x^{2n}$$

$$PI(z_n, x) = 4x^{6n-1} + (6n-3)x^{6n-2}$$

$$PI(c_n, x) = (2n+2)x^{9n-1} + (3n+3)x^{9n-2} + (4n-4)x^{9n-3}$$

$$PI(k_n, x) = (4n+2)x^{12n-1} + 3nx^{12n-2} + 4x^{12n-3} + (5n-5)x^{12n-4}$$

$$PI(r_n, x) = (6n+2)x^{15n-1} + 3nx^{15n-2} + 5x^{15n-4} + (6n-6)x^{15n-5}$$

$$PI(h_n, x) = (8n+4)x^{18n-1} + 3nx^{18n-2} + 6x^{18n-5} + (7n-7)x^{18n-6}$$

The proof of this result is also skipped due to similarity with proof of omega polynomial.

Polyomino chain system P_n^k

In this section, we deal with polyomino chain system P_n^k with two defining parameters k and n , where k is the sum of the number of kinks and number of terminals in a unit of any particular polyomino chain and n is the defining parameter of the chain i.e. dimension. Figure 3 shows the polyomino chain system P_n^k , with arbitrary defining parameters. The number of edges in P_n^k is $3kn+1$.

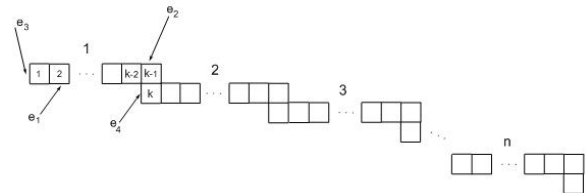


Fig. 3. General representation of P_n^k .

Table 1. Number of quasi-orthogonal strips in P_n^k for $k \geq 3, n \geq 1$.

Types of qoc's	Types of edges	Number of co-distant edges	No of qoc
C ₁	e ₁	2	$(kn-2n+1)$
C ₂	e ₂	3	n
C ₃	e ₃	k	1
C ₄	e ₄	k	$n-1$

There are four types of qoc strips in P_n^k shown in Table. In the following theorem, the omega

polynomial of P_n^k is computed.

Theorem 2.2.1. The omega polynomial of P_n^k with $k \geq 3, n \geq 1$, is as follows:

$$\Omega(P_n^k, x) = (kn - 2n + 1)x^2 + nx^3 + x^k + (n - 1)x^{k+1}$$

Proof. Let G be the graph of polyomino chain system P_n^k with $k \geq 3, n \geq 1$. Table 1 shows the number of co-distant edges and number of qoc in G . The quasi-orthogonal cuts and starting edges of strips are depicted in Fig 2. By using Table 1, the proof is mechanical. Now we apply formula and do some calculation to get our result.

$$\Omega(G, x) = \sum_c m(G, c) \times x^c$$

$$\Omega(G, x) = (kn - 2n + 1)x^2 + nx^3 + x^k + (n - 1)x^{k+1}$$

□

Now we compute Sadhana polynomial of P_n^k for $k \geq 3, n \geq 1$. Following theorem shows the Sadhana polynomial for this family of polyomino chains.

Theorem 2.2.2. Consider the graph of P_n^k with $k \geq 3, n \geq 1$. Then its Sadhana polynomial is as follows:

$$Sd(P_n^k, x) = (kn - 2n + 1)x^{3kn-1} + nx^{3kn-2} + x^{3kn-k+1} + (n - 1)x^{3kn-k}$$

Proof. Consider the graph of P_n^k with $k \geq 3, n \geq 1$. We prove it by using Table 1. We know that

$$Sd(G, x) = \sum_c m(G, c) \times x^{e-c}$$

$$Sd(P_n^k, x) = (kn - 2n + 1)x^{3kn-1} + nx^{3kn-2} + x^{3kn-k+1} + (n - 1)x^{3kn-k}$$

□

Next we compute PI polynomial of this polyomino chain system. Following theorem explains the PI polynomial of this family of polyomino chains.

Theorem 2.2.3 Consider the graph of P_n^k with $k \geq 3, n \geq 1$. Then its PI polynomial is as follows:

$$PI(P_n^k, x) = 2(kn - 2n + 1)x^{3kn-1} + 3nx^{3kn-2} + x^{kn-k+n-1} + (n - 1)x^{3kn-k}$$

Proof. Let G be the graph of P_n^k with $k \geq 3, n \geq 1$. We prove it by using data given in Table 1. We know that

$$PI(G, x) = \sum_c m(G, c) \times c \times x^{e-c}$$

$$PI(P_n^k, x) = 2(kn - 2n + 1)x^{3kn-1} + 3nx^{3kn-2} + x^{kn-k+n-1} + (n - 1)x^{3kn-k}$$

□

Open Problem

Investigate $C(G, x)$ for 3-parametric 4-polyomino system $P_r^k(n)$, where $k = k' + m + t$, and r is the number of squares between kinks inclusively in a unit and n is the dimension.

CONCLUSION AND GENERAL REMARKS

In this paper, three important counting polynomials called omega, Sadhana and PI are studied. These polynomials are useful in determining omega, Sadhana and PI topological indices which play an important role in QSAR/QSPR study. These counting polynomials play an important role in topological description of bipartite structures as well as counts equidistance and non-equidistance edges in graphs. In this paper, we studied these polynomials for polyomino chains or conducted the counting of qoc strips in these bipartite chemical graphs alternatively. An open problem is proposed for study of polyomino chains and k -polyomino system.

Acknowledgements: The authors would like to thank the referee for his/her careful reading, corrections and criticism which resulted as an improved version of this paper. This research of first author is supported by the grant of Higher Education Commission of Pakistan Ref. No. 20-367/NRPU/R&D/HEC/12/831. The second author is supported by CAS-TWAS president's fellowship at USTC China.

REFERENCES

1. M. V. Diudea, *Carpath. J. Math.*, **22**, 43 (2006).
2. A.R. Ashrafi, M. Ghorbani, M. Jalali, *Indian J. Chem.*, **47A**, 535 (2008).
3. A. Bahrami, J. Yazdani, *Dig. J. Nanomater. Biostruc.*, **3**, 265 (2008).
4. K. C. Das, F. M. Bhatti, S. G. Lee, I. Gutman, *MATCH Commun. Math. Comput. Chem.*, **65**, 753 (2011).
5. M. V. Diudea, I. Gutman, J. Lorentz, *Molecular Topology*, Nova, Huntington, 2001.
6. M. V. Diudea, S. Cigher, P. E. John, *MATCH Commun. Math. Comput. Chem.*, **60**, 237 (2008).
7. M. Ghorbani, M. Ghazi, *Dig. J. Nanomater. Biostruc.*, **5** (4), 843 (2010).
8. M. Imran, S. Hayat, M. K. Shafiq, *Optoelectron. Adv. Mater. Rapid Commun.*, **8**, 948 (2014).
9. M. Imran, S. Hayat, M. K. Shafiq, *Optoelectron. Adv. Mater. Rapid Commun.*, **8**, 1218 (2014).
10. P. V. Khadikar, *Nat. Acad. Sci. letters*, **23**, 113 (2000).

- 11.P. V. Khadikar, S. Karmarkar, V. K. Agrawal, *J. Chem. Inf. Comput. Sci.*, **41**, 931 (2001).
- 12.D. A. Klarner, Polyominoes, In: J. E. Goodman, J. O'Rourke, (eds.), Handbook of Discrete and Computational Geometry, CRC Press, Boca Raton, 1997, p.225.
- 13.A. Rajan, A. William, C. Grigorious, S. Stephen, *J. Comp. Math. Sci.*, **5**, 30 (2012).
- 14.S. Hayat, M. Imran, *J. Comput. Theor. Nanosci.*, **12**, 7 (2015).
- 15.I. Tomescu, S. Kanwal, *MATCH Commun. Math. Comput. Chem.*, **69**, 535 (2013).
- 16.Z. Yarahmadi, A. R. Ashrafi, S. Moradi, *App. Math. Lett.*, **25**, 166 (2012).
- 17.I. Yazdani, A. Bahrami, *Dig. J. Nanomater. Biostruc.*, **4**, 507 (2009).
- 18.M. Alaeiyan, A. Gilani, R. Mojarad, *Kuwait J. Sci.*, **41** (1), 85 (2014).

ВЪРХУ БРОЙНИ ПОЛИНОМИ НА НЯКОИ ПОЛИМИНО ВЕРИГИ

М. Имран¹, С. Хаят^{2*}

¹ Департамент по математика, Училище по природни науки, Национален университет по наука и техника, сектор Н-12, Исламабад, Пакистан

² Училище по математически науки, Университет по наука и техника на Китай, Хефей, Анхуй, Китай

Получена на 24 април 2015 г.; преработена на 20 октомври 2015 г.

Бройният полином $C(G, x)$ е поредица, описваща топологично свойство, така че степенните показатели изразяват размерите на неговите дялове, докато коефициентите са свързани с честотата на тези дялове. Полиномите Ω , на Sadhana и Padmakar-Ivan са разширени примери на бройни полиноми, които играят важна роля в топологичното писание на двуделни структури, както и в преброяването на еквиливантни и не еквиливантни ребра на графи. Тези полиноми преброяват квазиортогоналните отрезни (КОО) ленти в графи, генерирани от двуделни химически структури. КОО лента, дефинирана по отношение на кое и да е ребро на графа $G(V, E)$, представлява най-малката подгрупа от ребра, затворени при вземане на противоположни ребра върху лицата.

В тази статия, ние се фокусираме върху бройните полиноми на полимино вериги от различни възможни форми. Ние извеждаме точните формули на полиномите ω , на Sadhana и PI за 2-параметрична 4-полимино система P_n^k за $k \geq 3, n \geq 1$. Предложена е отворена задача за по-нататъшни изследвания в тази посока.

Evaluation of ERIC-PCR for fingerprinting Methicillin-resistant *Staphylococcus aureus* strains

S.Lin¹, L. Li¹, B. Li¹, X. Zhao^{2*}, C.Lin⁴, Y. Deng¹, Z. Xu^{1, 3*}

¹College of Light Industry and Food Sciences, South China University of Technology, Guangzhou 510640, China

²Key Laboratory for Green Chemical Process of Ministry of Education, School of Chemical Engineering and Pharmacy, Wuhan Institute of Technology, Wuhan 430073, Hubei, China

³Department of Microbial Pathogenesis, School of Dentistry, University of Maryland, Baltimore, Maryland, USA

⁴Institute of Biomedical Engineering, National Taiwan University, Taipei 10617, Taiwan

Received September 16, 2015, Revised October 17, 2015

Staphylococcus aureus (*S. aureus*) has been long recognized as a common food-borne pathogen in food safety. To study their individuality and drug resistance, a total of 179 *Staphylococci* strains were subject to the investigation. *S. aureus* was further confirmed with the detection of specific 16S rRNA and *femA* genes by multiplex-PCR. The molecular method was also used for amplification of *mecA* and *orfX* elements to identify Methicillin-resistant *S. aureus* (MRSA). Then fingerprinting for all strains was performed using ERIC-PCR. In this experiment, 179 *staphylococci* were isolated, and all of these strains were MRSA. In addition, 179 MRSA strains can be typed into 10 genotypes which have significant diversities, based on the results of ERIC-PCR. Through the above studies, a new protocol was brought out for rapid identification of MRSA using multiplex-PCR and MRSA typing using fingerprinting, which have a broad application prospect in food safety and epidemiology.

Key words: MRSA, Multiplex-PCR, ERIC-PCR, Fingerprinting

INTRODUCTION

Staphylococci are a group of gram-positive, facultative aerobic and usually unencapsulated organisms, which are responsible for various tissues infection and a multitude of diseases. *Staphylococcus aureus* are typical foodborne microorganisms, which can cause food poisoning and toxic shock, bringing serious public health burden. About 14 million people are infected due to foodborne microorganisms per year [1]. Among these public health events, food poisoning caused by *Staphylococcus aureus* accounts for a large proportion, which has become an advanced project in food safety [2-4]. Since the first methicillin-resistance *Staphylococcus aureus* (MRSA) was found in Britain in 1961, it has been spreading among the world at an alerting rate. With the wide identification of MRSA in animal husbandry and food industry, a concept was put forward that MRSA strains are a potential risk factor, not only for food itself, but for those who engage in food production and processing [5~8]. Instead of restricting the resistance, invasion and propagation of MRSA into clinical fields, these events should be expanded into food safety [9]. It

has been recognized that the infection caused by MRSA has high morbidity and mortality. According to the statistics published by CDC in 2003, hundreds of thousands of patients were hospitalized due to infection of MRSA, and the separation rate of MRSA might reach high up to 80%. The multi-drug resistance of MRSA increases the complicacy and difficulty in therapy as well as in the rapid growth of antibiotic and healthcare budget. Reducing the infection rate of MRSA has been a major challenge in clinical medicine, which decides that rapid identification and efficient typing method of MRSA are particularly crucial [10].

Increasing awareness of the risk of MRSA strains and demands for tests capable of early, cost-effective, timely, and sensitive detection of *staphylococci* with associated antibiotic resistance determinants has made these tests an urgent demand. This study used multiplex-PCR assay for identification of MRSA by detecting *Staphylococcus*-specific regions of the 16S rRNA gene, *S. aureus* specific *femA* gene and MRSA key drug-resistance gene *mecA*. Furthermore, in order to genotype MRSA strains, ERIC-PCR assay is used for fingerprinting. MRSA can be rapidly identified and genotyped using methods above.

* To whom all correspondence should be sent:

E-mail: xhzhao2006@gmail.com; zhenbo.xu@hotmail.com

MATERIALS AND METHODS

Bacterial strains

Four reference strains, including MRSA 12513 and 10864 (with *mecA*, *femA*, 16S rRNA and *orfX* positive), MSSA 10501 (with *femA*, 16S rRNA and *orfX* positive, and *mecA* negative), MRCNS A110146 (with *mecA*, 16S rRNA and *orfX* positive, and *femA* negative), MSCNS 110830 (with 16S rRNA positive, and *mecA*, *femA*, *orfX* negative) were subjected to evaluation and optimization of multiplex-PCR assay. Application of the multiplex-PCR and RAPD assays were further performed on a total of 179 *Staphylococcus* isolates, which were isolated from The First Affiliated Hospital of Jinan University (FAHJU).

Culturing condition and template DNA preparation

Genomic DNA from *S. aureus* strains used as template for PCR amplification was prepared from overnight Tryptic soy broth (TSB) cultures at 37 °C with shaking. Culture was performed according to the instruction of kits (Dongsheng Biotech, Guangzhou). Harvest 0.5-2.0ml culture in a sterile 1.5ml micro centrifuge tube by centrifuging for 1min at 12,000rpm, discard supernatant. Resuspend pellet in 200µl DS Buffer. Mix the mixture thoroughly with tip. Add 20µl Proteinase K and 220µl MS lysis buffer, mix thoroughly. Incubate at 65°C for 10min. Add 220µl EtOH, mix the mixture thoroughly with tip. Transfer the supernatant and floc to a new purify tube, centrifuging for 1 min at 12,000rpm, discard filtrate. Add 500µl PS Buffer, centrifuging for 1min at 12,000rpm, discard filtrate. Add 500µl PE Buffer, centrifuging for 1min at 12,000rpm, discard filtrate. Add 500µl PE Buffer, centrifuging for 1min at 12,000rpm, discard filtrate. Centrifuge the tube for 3 min at 12,000rpm, and transfer the spin column to a sterile 1.5ml centrifuge tube. Add 100µl TE Buffer, incubate at room temperature for 2min. At last, Centrifuge the tube for 2 min at 12,000rpm. Remove spin column, the buffer in the micro centrifuge tube contains the highly purified DNA. Stored at -20°C.

Primer design

Three targets were selected to differentiate MRSA, MSSA, MRCNS, MSCNS and non-*Staphylococcus* strains. The protocol was designed to (i) detect any staphylococcal species to the exclusion of other bacterial pathogens using as an internal control, with primers corresponding to *Staphylococcus*-specific regions of the 16S rRNA genes (C1: 5'-GATGAGTGCTAAGTGTTAGG-3' and C2: 5'-TCTACGATTACTAGCGATTC-3', with an expected 542 bp amplicon); (ii) distinguish

between *S. aureus* and CNS strains based on amplification of the *S. aureus* specific *femA* gene (F1: 5'-AAAGCTTGCTGAAGGTTATG-3' and F2: 5'-TTCTTCTTGTAGACGTTTAC-3', with an expected 823 bp amplicon) and (iii) provide an indication of the likelihood that the staphylococci present in the specimen are resistant to methicillin based on the amplification of the *mecA* gene (M1: 5'-GGCATCGTTCCAAAGAATGT-3' and M2: 5'-CCATCTTCATGTTGGAGCTTT-3', with an expected 374 bp amplicon). (iv) detect an open reading frame existing on both sides of SCCmec in order to identify MRSA strain (with *mecA*+) based on the amplification of the *orfX* gene (O1: 5'-ACCACAATCMACAGTCAT-3' and O2: 5'-CCCGCATCATTTGATGTG-3'). Besides, primer ERIC2 (5'-AAGTAAGTGACTGGGGTGAGCG-3') is used for ERIC-PCR assay. All primers mentioned above are listed in Tab.1.

Establishment of multiplex-PCR assay

Four reference strains were used to evaluate the multiplex-PCR assay, which was carried out in a total of 25 µL reaction mixture. Components for multiplex-PCR are listed in Tab.2. Primers are stored at -20°C. The stock solution of primers is 100pmol/µL. Work solution of primers is 10pmol/µL. Multiplex-PCR amplification was carried out using the thermal profile as follows: 94°C for 5 min, followed by 30 cycles of 94°C for 30 sec, annealing temperature for 30 sec, and 72°C for 1.5 min and a final extension cycle at 72°C for 7 min. Annealing temperature is presented in **Tab.1**. The amplified products (7µL/well) were analyzed by gel electrophoresis in 1.5% agarose gels and stained with ethidium bromide for 10 min. A negative control was performed using sterile water instead of DNA template.

Application of the multiplex-PCR assay on clinical strains

179 clinical staphylococci isolates, were subjected to detection by the established multiplex-PCR assay with primers pairs F1 with F2, C1 with C2, O1 with O2, and M1 with M2, and PCR amplicons were evaluated by electrophoresis as aforementioned. These experiments were replicated to ensure reproducibility.

Fingerprinting analysis by ERIC-PCR on clinical strains

179 isolated strains were genotyped using the ERIC-PCR assay, which was carried out in a total of 50 µL reaction mixture. Components for ERIC-PCR are listed in Tab.3. Primer ERIC-2 is stored at -20°C. The stock solution of primers is 100pmol/µL, while work solution is 10pmol/µL.

Table 1. Description of the primers used for amplification

Primer	Sequence (5'-3')	Target	Tm (°C)	Amplification (bp)
C1	GGACTGTTATATGGCCTTTT	16S rRNA	50	542
C2	GAGCCGTTCTTATGGACCT			
M1	GGCATCGTTCCAAAGAATGT	mecA	50	374
M2	CCATCTTCATGTTGGAGCTTT			
F1	AAAGCTTGCTGAAGGTTATG	femA	50	823
F2	TTCTTCTTGTAGACGTTTAC			
O1	ACCACAATCMACAGTCAT	orfX	50	212
O2	CCCGCATCATTGATGTG			
ERIC2	AAGTAAGTGACTGGGGTGAGCG	RAPD	25	—

Table 2. Reaction system of multiplex PCR amplification

Component	Volume (µL)
2×UTaq PCR Master Mix	12.5
Primer M1, M2; C1, C2 (each)	1
Primer F1, F2; O1, O2(each)	1.5
DNA template	1.5
ddH ₂ O	1

Table 3. ERIC-PCR amplification of insert DNA

Component	Volume (µL)
2×Uaq PCR Master Mix	25
Primer ERIC-2	3
DNA template	1
ddH ₂ O	21

ERIC-PCR amplification was carried out using the thermal profile as follows: 94°C for 4 min, followed by 35 cycles of 94°C for 1 min, annealing temperature for 2 min, and 72°C for 2 min and a final extension cycle at 72°C for 7 min [11]. Annealing temperature is presented in Tab.1. The amplified products (7µL/well) were analyzed by gel electrophoresis in 1.5% agarose gels and stained with ethidium bromide for 10 min. A negative control was performed using sterile water instead of DNA template

RESULTS AND DISCUSSION

Evaluation of the multiplex-PCR

The specific amplification generated 4 bands on agarose gel (**Fig.1**), with sizes 823 bp for *femA*, 542 bp for *16S rRNA*, 374 bp for *mecA* and 212bp for *orfX* (**Tab.1**), respectively. Marker DS2000 (track 1) was used for control. MRSA strain 12513 (track 1) and strain 10864 (track 2) showed specific amplification for *mecA*, *femA*, *16S rRNA* and *orfX*, MSSA strain 10501 (track 3) showed positive result for *femA*, *16S rRNA* and *orfX*, MRCNS 110146 (track 4) was detected to carry *mecA*, *16S rRNA* and *orfX*, MSCNS 110830 (track 5) had been found to be *16S rRNA* positive, while ddH₂O (track 6) cannot amplified any band.

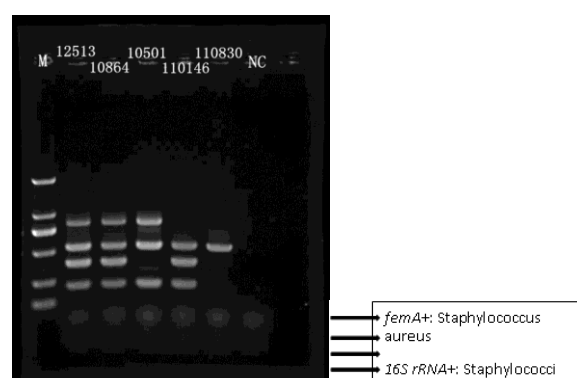


Fig. 1. Amplification results of multiplex-PCR

According to the amplification results mentioned above, the multiplex-PCR assay has fine resolution, not only to MRSA, but other *Staphylococci* such as MRCNS, MSCNS, and

MSSA etc. Besides, characters showed by multiplex-PCR, rapid identification and high specificity, for instance, may significantly increase efficiency both in clinical medicine and microbial safety in food industry.

Application of multiplex-PCR on 179 clinical strains

One hundred and seventy-nine clinical Staphylococci strains had been subjected to the application of the multiplex-PCR detection using primers F1 with F2, C1 with C2, O1 with O2, and M1 with M2 together. Multiplex-PCR and subsequent detection by electrophoresis were performed as described previously. All 179 MRSA strains yielded three bands as 374 bp, 572 bp and 823 bp amplicon, corresponding to *mecA*, 16S

rRNA and *femA*. No false positive amplification was observed, indicating the high specificity of the established multiplex-PCR assay (Fig.2).

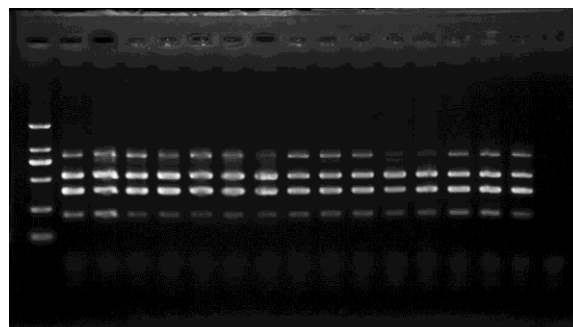


Fig.2. Part of amplification results of 179 clinical strains

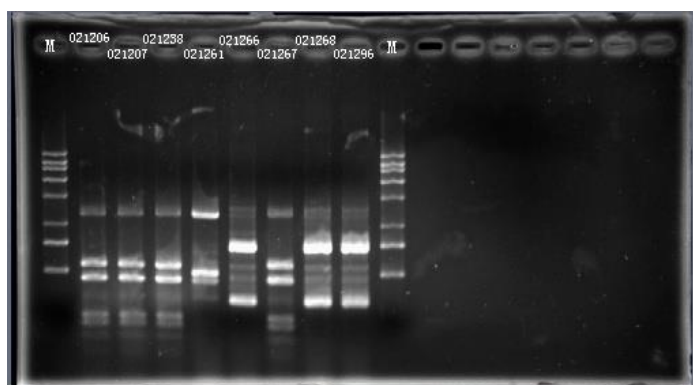
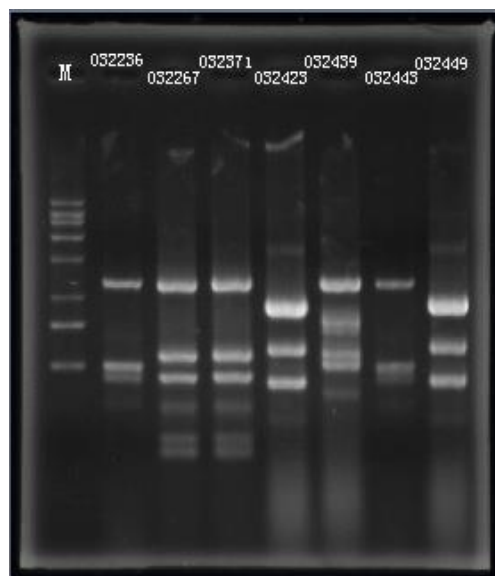
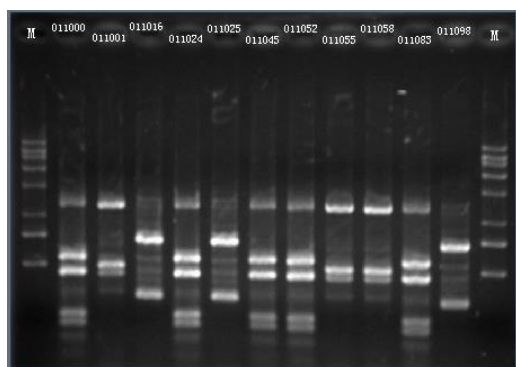


Fig. 3. The PCR amplification of part Staphylococcus aureus in primer AP1 in primer ERIC2 (continues on the next page)

Fig. 3.- continuation.

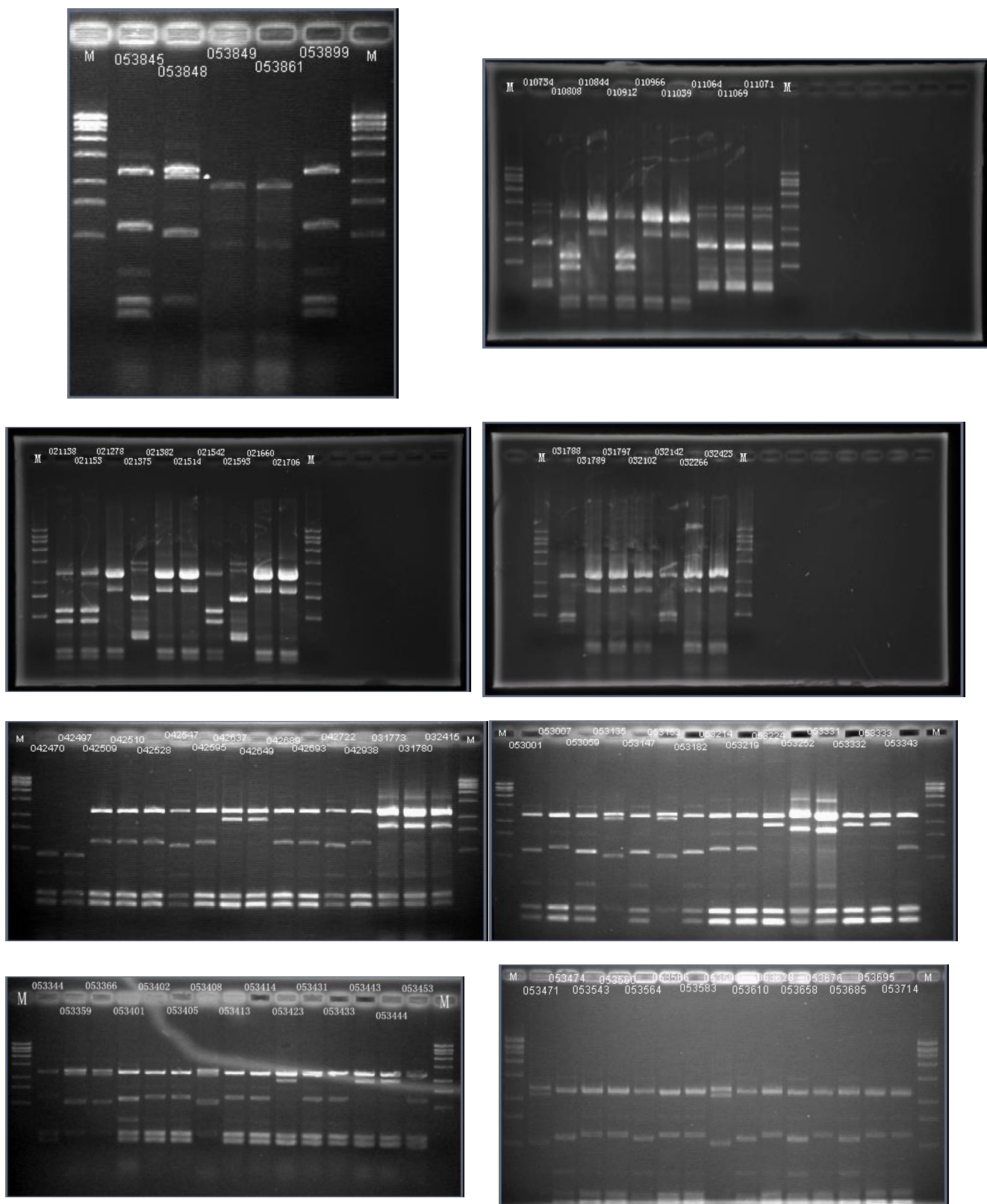


Fig. 3. The PCR amplification of part Staphylococcus aureus in primer AP1 in primer ERIC2 (continues on the next page).

Fig. 3.- continuation.

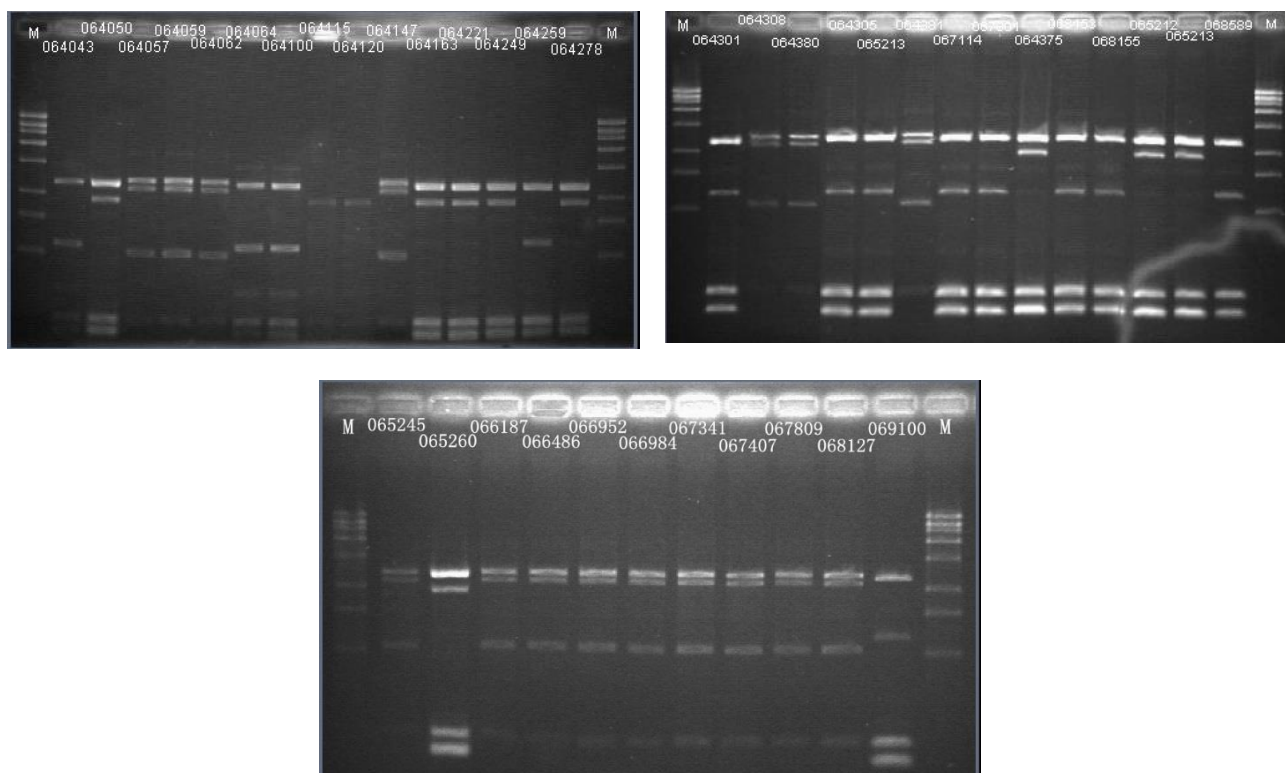


Fig. 3. The PCR amplification of part *Staphylococcus aureus* in primer AP1 in primer ERIC2

Application of Fingerprinting on 179 clinical strains

One hundred and seventy-nine clinical MRSA strains which were rapidly identified by multiplex-PCR previously, had been subjected to the application of the ERIC-PCR detection with primer ERIC2 in order to genotyping in fingerprinting. ERIC-PCR and subsequent detection by electrophoresis were performed as described previously.

Based on the results of gel electrophoresis of ERIC-PCR, complex banding patterns were amplified in 2-5 bands, ranging from 400bp-5000bp. All 179 clinical MRSA strains were successfully genotyped with ERIC-PCR assay into 10 genotypes A-J (**Fig.4**). These clinical MRSA strains were isolated in separate ward and different organs of patients. All 179 clinical MRSA strains were listed in **Tab.4**. Fingerprinting results were recorded, then with the usage of Quantity One, the similarity between 179 MRSA strains was evaluated. The DNA relatedness between 179 MRSA strains was analyzed based on the unweighted pair group method using arithmetic averages (UPGMA).

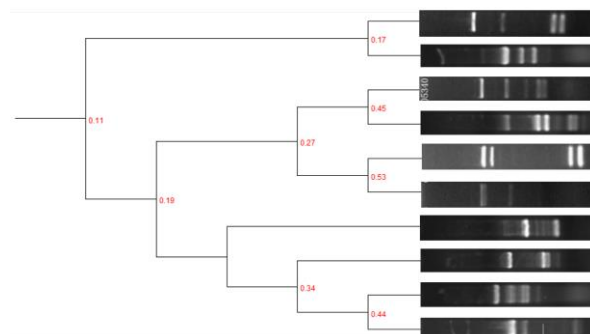


Fig. 4. Dendrogram analysis by ERIC-PCR of DNA fingerprinting results.

CONCLUSION

MRSA are currently widespread pathogens throughout the world and have prompted a heightened interest and concern for the rapid detection [12] and accurate categorization of these pathogens. Thus, rapid and accurate detection and genotyping approaches are needed to reduce risk in nosocomial infection and food industry caused by MRSA strains.

This study was aimed to use rapid identification methods based on multiplex-PCR assays for differentiation of MRSA, MSSA, MRCNS, MSCNS even non-staphylococci strains.

Table 4. Summary of typing result of 179 MRSA strains using ERIC-PCR.

Year	Source	Ward	Amount	Genotype	
2001	Blood	Orthopedics	1	C	
		General	1	B	
	Skin and parenchyma	Internal medicine	4	A	
		Surgery	1	C	
		Infection	1	A	
		Orthopedics	1	B	
	Respiratory		1	A	
		Neurology	1	B	
	Other		1	C	
		Orthopedics	1	A	
			1	C	
		Neurology	1	C	
		General	1	D	
		Surgery	1	A	
		Internal medicine	2	D	
		Urethra	Surgery	1	C
				5	A
			Internal medicine	5	D
	2002	Blood	Orthopedics	1	C
			Neurology	1	B
Urethra		Surgery	1	C	
		Internal medicine	1	D	
Respiratory			1	A	
		Surgery	1	C	
Other			1	A	
		Surgery	1	C	
			1	A	
			2	B	
2003	Skin and parenchyma	Internal medicine	5	D	
			1	E	
			1	F	

Table 4. Summary of typing result of 179 MRSA strains using ERIC-PCR. (*Continuation*).

			1	D
		Surgery	1	E
	Blood	Internal medicine	2	B
	Other	Surgery	1	A
			1	A
			5	D
		Internal medicine	4	G
			1	H
	Skin and parenchyma		3	I
			2	J
		Gynecology and obstetrics	1	D
			1	G
		Infection	1	A
		General	1	G
2004	Urethra	Internal medicine	1	A
		General	1	A
	Blood	Pediatric	1	G
		Internal medicine	1	G
		Orthopedics	1	H
			1	A
	Other		2	D
		Internal medicine	1	G
			1	H
			2	I
	Respiratory	Gynecology and obstetrics	1	I
		Pediatric	1	I
			2	G
		Internal medicine	3	H
	Skin and parenchyma		3	I
			4	J
2005		General	1	I
			1	I
	Blood	Internal medicine	1	J
			1	H

Table 4. Summary of typing result of 179 MRSA strains using ERIC-PCR. (*Continuation*).

		Infection	2	G
			1	D
		Pediatric	1	H
			1	I
			1	J
			2	G
		Neurology	2	H
			3	I
	Respiratory	General	2	G
			1	D
		Surgery	1	G
			2	I
		Orthopedics	3	G
			1	H
		Internal medicine	1	H
			1	G
		Gynecology and obstetrics	1	I
			6	G
	Urethra	Internal medicine	1	H
			1	I
			5	G
		Internal medicine	5	H
			1	J
			1	G
	Skin and parenchyma	Gynecology and obstetrics	2	H
			1	J
		Infection	1	I
			1	J
		Orthopedics	1	G
		Pediatric	1	H
			1	I
	Blood	Internal medicine	1	J
			1	J
	Respiratory	Pediatric	1	G
			1	I
2006				

Table 4. Summary of typing result of 179 MRSA strains using ERIC-PCR. (Continuation).

		1	J
	Infection	2	H
		1	G
	Surgery	2	H
		1	G
	Neurology	2	H
		1	J
	Gynecology and obstetrics	1	J
		1	G
	Internal medicine	3	H
Urethra		1	J
	Orthopedics	1	J

Then apply fingerprinting to genotyping 179 clinical MRSA strains with ERIC-PCR assay. The experiment results indicated that both multiplex-PCR and ERIC-PCR showed strength in rapid identification and superior sensitivity.

In conclusion, the multiplex-PCR assay proved to be an efficient and accurate tool to identify and separate staphylococci, such as MRSA, MSSA, MRCNS, MSCNS, even non-staphylococci (Fig.1). All of the 179 clinical strains were identified as MRSA (Fig.2). On the other side, fingerprinting using ERIC-PCR also showed excellent resolution to 179 clinical MRSA strains (Fig.3). Each DNA of the 179 clinical strains was amplified into 2-5 bands, ranging from 400bp- 5000bp. Based on this result, the 179 clinical MRSA strains were successfully genotyped into 10 genotypes A-J (Fig.4).

Dendrogram analysis shows the similarity between 10 types MRSA strains. Among 10 types, type I and A, J and H, E and D had a relatively high affinity while type G and F was rather low. The results showed that the 179 clinical MRSA strains resolute by ERIC-2 system did not have close affinity, which could be considered to be evolved isolated. Resulted from the resolution, the ERIC-PCR assay in this study provided a sensitive method in the classification of 179 clinical MRSA strains while traditional genotyping means may not possess such high sensitivity and accuracy.

In the long term, the fingerprinting approach can be applied on rapid genotyping, genetic similarity analysis [9], genetic tracking [13] and epidemiology research [14]. Based on the character

of simple, rapid and accurate, DNA fingerprinting are supposed to be listed in the common tools for genotyping.

Acknowledgements: This work was supported by the National 973-Plan of China (2012CB720800), International Science & Technology Cooperation Program of Guangdong Province (2013B051000014), National Natural Science Foundation of China (31201362 & 31101278), the National Science and Technology Support Program (2012BAD37B01), National Outstanding Doctoral Dissertation Funding (Dr. Zhenbo Xu), Guangdong Outstanding Doctoral Dissertation Funding (K3140030), the Fundamental Research Funds for the Central Universities (2012ZM0060) and Hubei Provincial Education Of Department Scientific Research Program (Q20151508).

REFERENCES

1. L. Zhang; L. Wang; W. Zhang; Z. .*Chinese Journal of Food Hygiene*, **16**(1), 35 (2004).
2. L. Chen, M. Li, Y. Wang, Y. Jin, W. Guo, *Chinese Journal of Food Hygiene*, **20**(5), 431 (2008).
3. Y.-D. Xiang, X.-A. Xu, H.-W. Xiao., *Occupation and Health.*, **21**(2), 215 (2005).
4. B. Alarcon, B. Vicedo, R. Aznar, *J Appl Microbiol*, **100**, 352 (2006).
5. O. Andreoletti, H. Budka, S.Buncic, P. Colin, J. D. Collins, A. De Koeijer, J. Griffin, A. Havelaar, J. Hope, G. Klein, H. Kruse, S. Magnino, A. M. López, J. McLauchlin, C. Nguyen-Thé, K. Noeckler, B. Noerrung, M. P. Maradona, T. Roberts, I. Vagsholm, E. Vanopdenbosch, *EFSJ*, **765**, 2 (2008).

6. E. De Boer, *Int J Food Microbiol*, **134**, 52 (2009).
7. J. Kluytmans, W. van Leeuwen, W. Goessens, R. Hollis, S. Messer, L. Herwaldt, H. Bruining, M. Heck, J. Rost, N. van Leeuwen, A. van Belkum, H. Verbrugh, *J Clin Microbiol*, **33**, 1121 (1995).
8. N. H. Kwon, K. T. Park, J. S. Moon, W. K. Jung, S. H. Kim, J. M. Kim, S. K. Hong, H. C. Koo, Y. S. Joo, Y. H. Park, *J Antimicrobial Chemotherapy*, **56**, 624 (2005).
9. Z. Xu, Study on the mechanism of the biofilm behavior and drug resistance of *Staphylococcus* in the sugar biosecurity [D]. Guangzhou: South China University of Technology, 2011.
10. Z. Xu, L. Lin, L. Shi, *Chinese Journal of Laboratory Medicine*, **31**(11), 1270 (2008).
11. A. van Belkum, J. Kluytmans, W. van Leeuwen, R. Bax, W. Quint, E. Peters, A. Fluit, C. van den Broucke-Grauls, A. van den Brule, H. Koeleman, W. Melchers, J. Meis, A. Elaichouni, M. Vaneechoutte, F. Moonens, N. Maes, M. Struelens, F. Tenover, H. Verbrugh, *J Clin Microbiol*, **33**, 1537 (1995).
12. Z. Xu, L. Li, X. Zhao, J. Chu, B. Li, L. Shi, J. Su, M.E. Shirliff, *Afr. J. Microbiol. Res.* **5**(14), 1869 (2011).
13. Z. Chunhui, Molecular epidemiological study of *Staphylococcus aureus* [D]. Tianjin: Tianjin Medical University, 2010.
1. W. Jun., L. Xi. *Clinical Medical Journal of China*, **12**(6), 1018 (2005)

ОЦЕНЯВАНЕ НА МЕТОДА ERIC-PCR ЗА ОПРЕДЕЛЯНЕ НА ПРЪСТОВИТЕ ОТПЕЧАТЪЦИ НА МЕТИЦИЛИН-РЕЗИСТЕНТЕН ЩАМОВЕ ОТ ВИДА *Staphylococcus aureus*

С. Лин¹, Л. Ли¹, Б. Ли¹, С. Жао^{2*}, С. Лин⁴, Я. Денг¹, Ж. Ксу^{1,3}

¹Колеж по лека промишленост и науки за храненето, Южнокитайски технологичен университет, Гуанчжоу 510640, Китай

²Ключова лаборатория по зелени химични процеси при Министерството на образованието, Училище по химично инженерство и фармация, Технологичен университет в Ухан, Ухан 430073, Хубей, Китай

³Департамент по микробна патогенеза, Училище по стоматология, Университет в Мериленд, Балтимор, Мериленд, САЩ

⁴Институт по биомедицинско инженерство, Национален университет в Тайван, Тайпе 10617, Тайван

Постъпила на 16 септември, 2015 г.; Приета на 17 октомври, 2015 г.

(Резюме)

Бактериите от вида *Staphylococcus aureus* (*S. aureus*) дълго са били признавани като обикновени патогени в храните. За да се изследва тяхната индивидуалност и резистентност спрямо лекарства в настоящата работа 179 стафилококови щамове са подложени на изследване. *S. aureus* са потвърдени с откриването на специфични гени 16S rRNA и femA чрез мултиплексен PCR. Използван е също така молекулен метод за усилването на елементите mecA и orfX за идентифицирането на метицилин-резистентен щам *S. aureus* (MRSA). След това са представени пръстовите отпечатьци за всички щамове при използването на техниката ERIC-PCR. В този експеримент са изолирани 179 стафилококови щамове, като всички те са MRSA. Допълнително, на основание ERIC-PCR-техниката тези 179 MRSA-щамове могат да се разпределят в 10 генотипа с значимо разнообразие. Чрез тези резултати е съставен нов протокол за бърза идентификация на MRSA чрез пръстови отпечатьци. Тези щамове имат широко приложение за безопасността на храните и епидемиологията.

BULGARIAN CHEMICAL COMMUNICATIONS

Instructions about Preparation of Manuscripts

General remarks: Manuscripts are submitted in English by e-mail or by mail (in duplicate). The text must be typed double-spaced, on A4 format paper using Times New Roman font size 12, normal character spacing. The manuscript should not exceed 15 pages (about 3500 words), including photographs, tables, drawings, formulae, etc. Authors are requested to use margins of 3 cm on all sides. For mail submission hard copies, made by a clearly legible duplication process, are requested. Manuscripts should be subdivided into labelled sections, e.g. **Introduction, Experimental, Results and Discussion**, etc.

The title page comprises headline, author's names and affiliations, abstract and key words.

Attention is drawn to the following:

a) **The title** of the manuscript should reflect concisely the purpose and findings of the work. Abbreviations, symbols, chemical formulas, references and footnotes should be avoided. If indispensable, abbreviations and formulas should be given in parentheses immediately after the respective full form.

b) **The author's** first and middle name initials, and family name in full should be given, followed by the address (or addresses) of the contributing laboratory (laboratories). **The affiliation** of the author(s) should be listed in detail (no abbreviations!). The author to whom correspondence and/or inquiries should be sent should be indicated by asterisk (*).

The abstract should be self-explanatory and intelligible without any references to the text and containing not more than 250 words. It should be followed by key words (not more than six).

References should be numbered sequentially in the order, in which they are cited in the text. The numbers in the text should be enclosed in brackets [2], [5, 6], [9–12], etc., set on the text line. References, typed with double spacing, are to be listed in numerical order on a separate sheet. All references are to be given in Latin letters. The names of the authors are given without inversion. Titles of journals must be abbreviated according to Chemical Abstracts and given in italics, the volume is typed in bold, the initial page is given and the year in parentheses. Attention is drawn to the following conventions:

a) The names of all authors of a certain publications should be given. The use of “*et al.*” in

the list of references is not acceptable.

b) Only the initials of the first and middle names should be given.

In the manuscripts, the reference to author(s) of cited works should be made without giving initials, e.g. “Bush and Smith [7] pioneered...”. If the reference carries the names of three or more authors it should be quoted as “Bush *et al.* [7]”, if Bush is the first author, or as “Bush and co-workers [7]”, if Bush is the senior author.

Footnotes should be reduced to a minimum. Each footnote should be typed double-spaced at the bottom of the page, on which its subject is first mentioned.

Tables are numbered with Arabic numerals on the left-hand top. Each table should be referred to in the text. Column headings should be as short as possible but they must define units unambiguously. The units are to be separated from the preceding symbols by a comma or brackets.

Note: The following format should be used when figures, equations, etc. are referred to the text (followed by the respective numbers): Fig., Eqns., Table, Scheme.

Schemes and figures. Each manuscript (hard copy) should contain or be accompanied by the respective illustrative material as well as by the respective figure captions in a separate file (sheet). As far as presentation of units is concerned, SI units are to be used. However, some non-SI units are also acceptable, such as °C, ml, l, etc.

The author(s) name(s), the title of the manuscript, the number of drawings, photographs, diagrams, etc., should be written in black pencil on the back of the illustrative material (hard copies) in accordance with the list enclosed. Avoid using more than 6 (12 for reviews, respectively) figures in the manuscript. Since most of the illustrative materials are to be presented as 8-cm wide pictures, attention should be paid that all axis titles, numerals, legend(s) and texts are legible.

The authors are asked to submit **the final text** (after the manuscript has been accepted for publication) in electronic form either by e-mail or mail on a 3.5” diskette (CD) using a PC Word-processor. The main text, list of references, tables and figure captions should be saved in separate files (as *.rtf or *.doc) with clearly identifiable file names. It is essential that the name and version of

the word-processing program and the format of the text files is clearly indicated. It is recommended that the pictures are presented in *.tif, *.jpg, *.cdr or *.bmp format, the equations are written using "Equation Editor" and chemical reaction schemes are written using ISIS Draw or ChemDraw programme.

The authors are required to submit the final text with a list of three individuals and their e-mail addresses that can be considered by the Editors as potential reviewers. Please, note that the reviewers should be outside the authors' own institution or organization. The Editorial Board of the journal is not obliged to accept these proposals.

EXAMPLES FOR PRESENTATION OF REFERENCES

REFERENCES

1. D. S. Newsome, *Catal. Rev.–Sci. Eng.*, **21**, 275 (1980).
2. C.-H. Lin, C.-Y. Hsu, *J. Chem. Soc. Chem. Commun.*, 1479 (1992).
3. R. G. Parr, W. Yang, *Density Functional Theory of Atoms and Molecules*, Oxford Univ. Press, New York, 1989.
4. V. Ponec, G. C. Bond, *Catalysis by Metals and Alloys* (Stud. Surf. Sci. Catal., vol. 95), Elsevier, Amsterdam, 1995.
5. G. Kadinov, S. Todorova, A. Palazov, in: *New Frontiers in Catalysis* (Proc. 10th Int. Congr. Catal., Budapest, 1992), L. Guzzi, F. Solymosi, P. Tetenyi (eds.), Akademiai Kiado, Budapest, 1993, Part C, p. 2817.
6. G. L. C. Maire, F. Garin, in: *Catalysis. Science and Technology*, J. R. Anderson, M. Boudart (eds), vol. 6, Springer-Verlag, Berlin, 1984, p. 161.
7. D. Pocknell, *GB Patent 2 207 355* (1949).
8. G. Angelov, PhD Thesis, UCTM, Sofia, 2001.
9. JCPDS International Center for Diffraction Data, Power Diffraction File, Swarthmore, PA, 1991.
10. *CA* **127**, 184 762q (1998).
11. P. Hou, H. Wise, *J. Catal.*, in press.
12. M. Sinev, private communication.
13. <http://www.chemweb.com/alchem/articles/1051611477211.html>.

CONTENTS

Book Review: "Modeling of Column Apparatus Processes", Chr. Boyadjiev, M. Doichinova, B. Boyadjiev, P. Popova - Krumova,.....	181
M. G. Varadinova, M. L. Valcheva-Traykova, Circadian misalignment and alcohol intake change the oxidative status of rat blood plasma	183
B. Ebadzadeh, A. Ramazani, V. Azizkhani, . H. Aghahosseini, S. W. Joo, A convenient green protocol for one-pot three-component synthesis of 2-amino-4H-chromene derivatives catalyzed by ilmenite (FeTiO ₃) as an efficient and reusable catalyst in water	187
W. Long, Y.K. Li , J.X. Ma, Y.B. Wang, Theoretical research of inulin's pharmacological activity by combining DFT with concept DFT methods	194
M. Parvez, M. Akram, Suffering water of Pakistan: arsenic – A major threat	203
S. A. Musavi, M. Montazerzohori, M. Nasr-Esfahani, R. Naghiha, M. Montazer Zohour, Nano-structure zinc and cadmium azide and thiocyanate complexes: Synthesis, characterization, thermal, antimicrobial and DNA interaction	209
X. Hou, J. Li, Z. Nuo, Y. Ren, C. Gao, The study on D-aminoacylase gene synthesis via chemical and enzymatic combined method	219
I. E. Kononova, D. M. Vorobiev, D. Tz. Dimitrov, A. Ts. Georgieva, V. A. Moshnikov, Room temperature acetone vapor - sensing properties of a mesoporous zinc stannate layer	225
I. Tsibranska, V. Karabojkova, J. Jeliakov, Concentration of flavonoids in ethanolic extracts from tobacco leaves through nanofiltration	232
B. Khodadadi, Nickel doping effect on the photocatalytic activity of TiO ₂ /SiO ₂ nanocomposite	238
H. Yaghoobian, S.M. Habibi-Khorassani, A. Ebrahimi, Kinetic investigation of tetrahydrobenzo[b]pyran synthesis in the presence of fructose as a catalyst via a three-component reaction: an experimental study	244
M. Pateraki, G. K. Morales-Ortiz, A. López-Guzmán, A. Fuentes-Benites , E. Cuevas-Yañez, Solventless synthesis of triazoles and bistriazoles through Copper-catalyzed alkyne-azide cycloaddition	250
H. Sevik, M. Cetin, Effects of some hormone applications on germination and morphological characters of endangered plant species <i>Lilium artvinense</i> L. Onion scales	256
M. B. Taşkın, S. Özbek, E. Demirhan, B. Özbek, BSA adsorption onto commercial activated carbon modified by microwave assisted chemical activation	261
K. I. Aleksieva, N. D. Yordanov, EPR study of gamma - irradiated homeopathic medicines	269
M. M. Ghorab, M. S. Alsaïd, Anticancer evaluation of novel quinazolines carrying a biologically active pyrimidine, triazine, benzo[d][1,3]dioxol, morpholinophenyl, quinoline, sulfonamide moieties	272
Z. Aghajani, A. A .Engashte-Vahed, Comparison of the components of the volatile oils from leaves of <i>Ziziphus jujuba</i> extracted by changing the solvent system and the separation methods	279
N. Chahmana, M. Matrakova, L. Zerroual, Physicochemical and electrochemical study of lead acid battery positive active mass (PAM) modified by the addition of bismuth	285
A. Kaur, D. Gangacharyulu, P.K. Bajpai, Kinetic studies on the NaBH ₄ /H ₂ O hydrogen storage system with CoCl ₂ as a catalyst	290
A. S. Afify, M. Ataalla, A. Hussain, M. Hassan, A. Mohammed, M. Milanova ⁴ , J.M. Tulliani, Studying the effect of doping metal ions onto a crystalline hematite-based humidity sensor for environmental control	297
H. I. Moon, Y. B. Kim, S. K. Kim, Anti-influenza A activity of C-geranyl flavonoids isolated from <i>Paulownia tomentosa</i> and <i>Maclura pomifera</i>	303
L. Yang, D. Hua, W. J. Wang, A. M. Yang, M. Y. Fu, Antioxidant activity of polysaccharides from fermented <i>Meconopsis</i> Vig. endophytic fungi	306
Ö. Altun, N. Becenen, CdSe nanomaterials: kinetics, thermodynamics, antioxidant activity and application to Denim fabric	311
H. I. Moon, D. W. Kim, S. K. Kim, S. H. Seo, Effect of 6-hydroxy-7,4'-dimethoxyflavone on antidiabetic effects in normal and streptozotocin-induced diabetic rats	317
H. R. I. Keykanlu, S. Zibaei, M. Ardjmand, A. A. Safekordi, Fluorocarbon nanostructures (PFOB-NEP) as camel milk lactoferrin and its anti-cancer effects on human breast cancer cell line MCF7	323
M. Imran, S. Hayat, On counting polynomials of certain polyomino chains	332
S. Lin, L. Li, B. Li, X. Zhao, C. Lin, Y. Deng, Z. Xu, Evaluation of ERIC-PCR for fingerprinting Methicillin-resistant <i>Staphylococcus aureus</i> strains	338
INSTRUCTIONS TO THE AUTHORS	349

СЪДЪРЖАНИЕ

М. Г. Варадинова, М. Л. Вълчева-Трайкова, Нарушеният циркаден ритъм и алкохолният прием променят оксидативния статус на кръвна плазма на плъх	186
В. Евадзаде, А. Рамазани, В. Азизхани, Х. Агахосеини, С. В. Джу, Удобен зелен протокол за едно-стадийна три-компонентна синтеза на 2-амино-4 <i>h</i> -хроменови производни, катализирани от илменит(FeTiO ₃) като ефективен и многократно употребяван катализатор във водна среда	193
В. Лонг, И. И. Ли, Дж. С. Ма, И. Б. Ванг, Теоретично изследване на фармакологината активност на инулин чрез комбинация на dft с концептуални dft-методи	202
М. Парвез, М. Акрам, Водният проблем на Пакистан: арсенът като главна заплаха	208
С. А. Мусави, М. Монтазерозохори, М. Наср-Есфяхани, Р. Нагиха, М. Монтазер Зохоур, Наноструктурирани цинков и кадмиев азид и тиоцианатни комплекси: синтеза, характеризиране, термични, антимицробни и ДНК-взаимодействия.....	218
Кс. Хоу, Дж. Ли, Жай Нуо, И. Рен, К. Гао, Синтеза на ген за D-аминоацилаза по химичен и комбиниран ензимен метод	224
И. Е. Кононова, Д. М. Воробъов, Д. Ц. Димитров, А. Ц. Георгиева, В. А. Мошников, Определяне при стайна температура на сензорните свойства на мезопорест слой от цинков станат по отношение на изпарения на ацетон	231
И. Х. Цибранска, В. И. Карабожикова, Ж. Желязков, Концентриране на флавоноиди в етанолов екстракт от тютюневи листа чрез нанопилтруване	237
Б. Ходадади, Ефект на дотиране с никел върху фотокаталитичната активност на нанокompозити от TiO ₂ /SiO ₂	243
Х. Язубиан, С.М. Хабиби-Хорасани, А. Ебрахими, Кинетично изследване на синтезата на тетрахидробензо[<i>b</i>]пиран в присъствие на фруктоза като катализатор чрез трикомпонентна реакция: експериментално изследване	249
М. Патераки, Г.К. Моралес-Ортиз, А. Лопес-Гусман, А. Фуентес-Бенитес, Е. Кувас-Янес, Синтеза без разтворител на триазоли и бис-триазоли чрез алкин-азид'ово цикло-притъкмяване, катализирано от мед	255
Х. Севик, М. Джетин, Ефекти на някои хормони върху зрението и морфологичните характеристики на застрашения растителен вид <i>Lilium artvinense</i> L. луковични люспи.....	260
М.В. Ташкън, С. Йозбек, Е. Демирхан, Б. Йозбек, Адсорбция на албумин от говежди серум (BSA) върху търговски активен въглен и модифициран с химично активиране с микровълново въздействие	268
К. И. Алексиева, Н. Д. Йорданов, ЕПР изследване на гама-облъчени хомеопатични лекарства	271
М.М. Гораб, М.С. Алсаид, Оценка на противотуморната активност на нови хиназолини, съдържащи биологично активни пиримидин, триазин, бензо [<i>d</i>][1,3] диоксол, морфолинофенил, хинолин и сулфонамиди	278
З. Агаяни, А. А. Енгаце-Вахед, Сравняване на компонентите на летливи масла от листата на <i>Ziziphus jujuba</i> чрез промяна на разтворителя и метода на разделяне	284
Н. Чахмана, М. Матракова, Л. Зеруал, Физикохимично и електрохимично изследване на положителната активна маса в оловен акумулатор, модифициран чрез добавяне на бисмут	289
А. Каур, Д. Гангачарюлу, П. К. Баджнаи, Кинетични изследвания върху системата за съхранение на водород NaBH ₄ /H ₂ O с CoCl ₂ като катализатор	296
А. Афифи, М. Атаалла, А. Хюсейн, М. Хасан, А. Мохамед, М. Миланова, Ж.М. Тюлиани, Изследване на ефекта на дотиране с метални йони на кристални влагови сензори на основата на хематит	302
Х. И. Мун, И. Б. Ким, С. К. Ким, Анти-грипна А-активност на С-геранилови флавоноиди, изолирани от <i>Paulownia tomentosa</i> и <i>Maclura pomifera</i>	305
Л. Янг, Д. Хуа, У.Дж. Уанг, А.М. Янг, М.И. Фу, Антиоксидантна активност на полизахариди от ферментирани <i>Mecopopsis</i> Vig. ендодитни фунги	310
Й. Алтун, Н. Бедженен, Наноматериали от CdSe: кинетика, термодинамика, антиоксидантна активност и приложение в депт-тъканите	316
Х. И. Мун, Д. В. Ким, С. К. Ким, С. Х. Сео, Ефект на 6-хидрокси-7,4'-диметоксифлавоин върху антидиабетичните прояви при нормални плъхове и такива с стрептозотоцин-индуциран диабет	322
Х. Р. И. Кейканлу, С. Зибаети, М. Арджаманд, А. А. Сафекорди, Флуоровъглеродни нано-структури (PFOB-NP) към лактоферин от камильско мляко и неговият противотуморен ефект върху клетъчна линия MCF7 на рак на гърдата	331
М. Имран, С. Хаят, Върху бройни полиноми на някои полимино вериги.....	337
С. Лин, Л. Ли, Б. Ли, С. Жао, С. Лин, Я. Денг, Ж. Ксу, Оценка на метода ERIC-PCR за определяне на пръстовите отпечатащи на метицилин-резистентен щамове от вида <i>Staphylococcus aureus</i>	348
ИНСТРУКЦИЯ ЗА АВТОРИТЕ	349